PERFORMANCE OF STEEL FIBRE REINFORCED CONCRETE COLUMNS UNDER SHOCK TUBE INDUCED SHOCK WAVE LOADING

by

Russell Burrell

Thesis submitted to the

Faculty of Graduate Studies and Research

in partial fulfillment of the requirements for the degree of

Master of Applied Sciences

in Civil Engineering

Under the auspices of the Ottawa-Carleton Institute for Civil Engineering

uOttawa

University of Ottawa

August 2012

© Russell Burrell, Ottawa, Canada, 2012

Abstract

It is important to ensure that vulnerable structures (federal and provincial offices, military structures, embassies, etc) are blast resistant to safeguard life and critical infrastructure. In the wake of recent malicious attacks and accidental explosions, it is becoming increasingly important to ensure that columns in structures are properly detailed to provide the ductility and continuity necessary to prevent progressive collapse. Research has shown that steel fibre reinforced concrete (SFRC) can enhance many of the properties of concrete, including improved post-cracking tensile capacity, enhanced shear resistance, and increased ductility. The enhanced properties of SFRC make it an ideal candidate for use in the blast resistant design of structures. There is limited research on the behaviour of SFRC under high strain rates, including impact and blast loading, and some of this data is conflicting, with some researchers showing that the additional ductility normally evident in SFRC is absent or reduced at high strain loading. On the other hand, other data indicates that SFRC can improve toughness and energy-absorption capacity under extreme loading conditions. This thesis presents the results of experimental research involving tests of scaled reinforced concrete columns exposed to shock wave induced impulsive loads using the University of Ottawa Shock Tube.

A total of 13 half-scale steel fibre reinforced concrete columns, 8 with normal strength steel fibre reinforced concrete (SFRC) and 5 with an ultra high performance fibre reinforced concrete (UHPFRC), were constructed and tested under simulated blast pressures. The columns were designed according to CSA A23.3 standards for both seismic and non-seismic regions, using various fibre amounts and types. Each column was exposed to similar shock wave loads in order to provide direct comparisons between seismic and non-seismically detailed columns, amount of steel fibres, type of steel fibres, and type of concrete.

The dynamic response of the columns tested in the experimental program is predicted by generating dynamic load-deformation resistance functions for SFRC and UHPFRC columns and using single degree of freedom dynamic analysis software, RCBlast. The analytical results are compared to experimental data, and shown to accurately predict the maximum mid-span displacements of the fibre reinforced concrete columns under shock wave loading.

Acknowledgements

First and foremost, I would like to thank my thesis supervisors, Dr. Hassan Aoude and Dr. Murat Saatcioglu for their continued guidance, assistance, inspiration, and financial support throughout this research project.

I would like to express my gratitude to *Baekert* for providing the steel fibres and *KING Pre-Packaged Materials* for providing the materials for the SFRC series of columns, and *CRC Tech* for providing the materials for the CRC series of columns.

I would also like to thank my fellow graduate students Mr. Eric Jacques and Mr. Alan Lloyd for their knowledge, instruction, and assistance in all phases of the experimental program, analytical calculations, and also the many tutorials they provided on the response of columns to blast loading.

Additionally many people volunteered their time to help me with the labour of the experimental program, namely Ms. Sarah De Carufel, Mr. Manuel Spiller, Mr. Mustafa Mohammed-Saeed, Mr. Nima Aghniaey, Mr. Nathan Carreiro, Ms. Lauren Toikka, and Ms. Michelle Tremblay-Boulianne. My sincerest thanks go out to all of you, all your dedication and generosity is greatly appreciated.

This thesis is dedicated to my family who, through their loving support, provided me the foundation required to achieve all that I have in my life.

Table of Contents

List of Figures

List of Tables

Notations

A	Area
A_g	Gross cross-sectional area of column
A_f	Cross-sectional area of fibre
A_s	Area of longitudinal reinforcing steel
A_{shy} / A_{shx}	Cross-sectional area of transverse reinforcement in the x/y direction
A_T	Transformed cross-sectional area of column
b	Friedlander equation decay constant
c_y / c_x	Width of concrete core parallel to y or x direction
d_b	Diameter of reinforcing steel
d_f	Diameter of fibre
DIF	dynamic increase factor accounting for material strength increase under high strain rates
DLF	Dynamic load factor determined as the ratio of dynamic and static maximum displacement
D_{max}	Maximum mid-height column displacement
D_{res}	Residual mid-height column displacement
D_{anls}	Maximum mid-height displacement of analytical prediction
E_c	Modulus of elasticity of concrete
E_s	Modulus of elasticity of steel
E_{fp}	Modulus of Elasticity of fibres
F	Equivalent single degree of freedom external force
$F(t)$	External forcing function in dynamic equation of motion
f'_c	Peak static strength of concrete
f_{cc}	Confined concrete stress
f_{ccf}	Confined steel fibre reinforced concrete stress
f_{cu}	Stress in the unconfined concrete at a strain equal to ε_{cu}.
f'_{cu}	Peak stress of unconfined concrete
f'_{cuf}	Peak stress of unconfined steel fibre reinforced concrete

f'_{dc}	Dynamic strength of concrete
f_{du}	Dynamic ultimate stress of reinforcing steel
f_{dy}	Dynamic yield stress for reinforcing steel
$f_{fctm,ax}$	Maximum tensile stress of steel fibre reinforced concrete
f_{hcc}	Stress in the transverse reinforcement at max strength of confined concrete
f'_{le}	Effective confinement pressure
$f_{l,fib}$	Confining pressure of fibres
$F_{pullout}$	Fibre pullout strength
$f_{s/Du}$	Limiting value for compression reinforcing steel stress when considering buckling
f_{sh}	Steel strain-hardening stress
f'_{td}	Dynamic tensile strength
f'_{t}	Quasi-static tensile strength
f_u	Static ultimate stress of reinforcing steel
f_y	Static yield stress of reinforcing steel
h	Height of column cross section
H^d_{EXP}	Heat of detonation of explosive
H^d_{TNT}	Heat of detonation of TNT
I'_E	Effective Confinement Index
$I'_{E\,fib}$	Effective confinement index for steel fibre reinforced concrete
I	Incident impulse over the negative phase
I_r	Reflected impulse over the positive phase
I	Incident impulse over the positive phase
k	Stiffness in dynamic equation of motion, rotational spring stiffness
K_{LM}	Load-mass factor for single degree of freedom conversion
K_L	Load factor for single degree of freedom conversion
K_m	Mass factor for single degree of freedom conversion
L	length of the column
l_f	Length of Fibre

L_{pl}	Plastic hinge length
m	Mass in dynamic equation of motion
M	Equivalent single degree of freedom mass
$\overline{m}$	Mass per unit length
$msec$	Millisecond
M_i	Incremental moment capacity of member
n	Ratio of steel modulus of elasticity to concrete modulus of elasticity
n_l	Fibre length factor
η_θ	Fibre orientation factor
N_{fibres}	Effective number of fibres per unit area
P	Axial load applied to column
$P(t)$	Incident overpressure at a time within the positive phase
p_o	ambient atmospheric pressure
P_o	concentric axial load capacity of column
P_r	reflected overpressure
P_{so}	Incident blast pressure
P_{stag}	Stagnation pressure
P_s^-	Peak negative phase blast pressure
R	Standoff distance from explosive charge
$R(u)$	Non-linear resistance term for single degree of freedom analysis
s	Spacing of transverse steel ties
s'	Clear spacing of transverse steel ties
sec	Second
t	Time
t_a	Arrival time of shock wave
t_d	Positive phase duration of shock wave
t_{df}	Ficticious duration of the blast wave
t_d^-	Negative phase duration of shock wave

t_{max}	Time to reach maximum mid-height displacement
T	Natural period of vibration
t_{anls}	time to reach maximum mid-height displacement after the start of shock wave loading predicted by single degree of freedom model
u	Displacement in dynamic equation of motion
u_{max}	Maximum displacement under dynamic loading
$\ddot{u}$	Acceleration in dynamic equation of motion
U_s	wave front velocity of shock wave
u_{st}	Equivalent static deflection
V_f	Amount of fibre by volume
W	Weight (or mass) of explosive charge
W_E	Effective (equivalent) charge weight (or mass)
W_{EXP}	Weight (or mass) of the explosive charge
w/c	Water-cement ratio
z	scaled distance determined as the standoff distance divided by the cube root of charge mass
α	Fibre Orientation Factor
Δ	Distance of eccentric load from centre of column.
$\dot{\epsilon}$	Strain rate
ϵ_o	Peak strain
$\dot{\epsilon}_s$	Quasi-static strain rate
ε_{cc}	Confined concrete strain
ε_{ccf}	Confined steel fibre reinforced concrete strain
ε_{cu}	Unconfined compressive strain of concrete
ε'_{cu}	Peak unconfined compressive strain of concrete
ε'_{cuf}	Peak unconfined compressive strain of steel fibre reinforced concrete
ε_{axial}	Initial axial strain in column due to axial load
$\varepsilon_{s/Du}$	Limiting value of strain when considering compression reinforcing steel buckling

ε_{sh}	Steel strain at strain-hardening
ε_{tot}	Total maximum strain at mid-span of column
ε_u	Ultimate strain
ε_y	Yield strain
ρ_c	Ratio of area longitudinal reinforcement in the core area of the column
ρ_{sey}	Effective sectional ratio of confinement reinforcement in the y direction
σ_c	Concrete stress
σ_{st}	material strength under static loading
τ_{bond}	Bond shear strength between the fibre and the matrix
θ	Rotation at the supports
μ	Ductility factor - the ratio of maximum displacement to yield displacement
φ	Non-dimensional mode shape
ϕ	Curvature
ω	Natural frequency of vibration

Acronyms

ASTM	American Society for Testing and Materials
C.o.V	Coefficient of Variation
CAD	Canadian Dollars
CBC	Canadian Broadcasting Corporation
CEB	Comité euro-international du béton (Euro-international Concrete Committee)
CFRP	Carbon Fibre Reinforced Polymer
CRC	Compact Reinforced Composite
CSA A23.3	Canadian Standards Association – Design of Concrete Structures
DAC	Data Acquisition Computer
DIF	Dynamic Increase Factor
DLF	Dynamic Load Factor
HSF	Hydraulic Portland / Silica Fume (Cement)
LTD	Load Transfer Device
LVDT	Linear Variable Differential Transducer
PFRC	Polymeric Fibre Reinforced Concrete
RC	Reinforced Concrete
RPC	Reactive Powder Concrete
rpm	Revolutions per minute
RSI	Residual Strength Index
SCC	Self Consolidating Concrete
SCFRC	Self Consolidating Fibre Reinforced Concrete
SDOF	Single Degree of Freedom
SFRC	Steel Fibre Reinforced Concrete
SHPB	Split Hopkinson Pressure Bar
SRP	Steel Reinforced Polymer
TNT	Tri-Nitro Toluene – an explosive composition
UFC	United Facilities Criteria
UHPFRC	Ultra High Performance Fibre Reinforced Concrete
VMA	Viscosity Modifying Admixture

1 Introduction

1.1 General

Incidents such as the Commonwealth avenue collapse in Boston, and the Bailey's crossroads collapse in Virginia have shown that the failure of key components in reinforced concrete buildings can lead to progressive collapse and devastating failures (Delatte, 2009). Events such as the Oklahoma City bombing have also demonstrated the vulnerability of existing reinforced concrete infrastructure against blast hazards, and especially the vulnerability of ground story columns in buildings, the loss of which can trigger progressive collapse. To prevent progressive collapse, ground-story columns need to be properly detailed to provide the ductility and continuity necessary to prevent failure. Currently, within Canada and abroad, there is a significant demand for engineering guidelines for mitigation of blast load effects on structures with very little experimental research completed to provide this guidance (Lloyd, 2010).

Extensive research has shown that steel fibre reinforced concrete (SFRC) can enhance many of the properties of traditional concrete, including shear resistance, confinement, and ductility (Li, 2002). The enhanced ductility, impact resistance and energy absorption capacity of SFRC make it an ideal material for use in the blast resistant design of structures (Banthia, 2008). Due to its improved properties, SFRC could potentially be used to relax required detailing, resulting in improved constructability without compromising performance. Nonetheless, existing research on SFRC subjected to high strain rates has been conflicting. Some authors have shown that additional ductility normally evident in SFRC is absent or reduced at high strain rates. Conversely, other authors have stated that fibres do assist in enhancing blast resistance.

Currently there is little information available on the performance of steel fibre reinforced concrete elements under blast loads. Experimental research is scarce due to difficulties associated with explosive testing. However, the state-of-the-art shock tube at the University of Ottawa uses simulated blast loads and simplifies the testing process. This thesis aims to provide additional research data on the behaviour of steel fibre reinforced concrete columns subjected to blast loads.

1.2 Research Objectives

The objective of this thesis is to study the performance enhancements that could be gained from the use of steel fibres in reinforced concrete columns subjected to blast loads. This objective is achieved by studying the behaviour of steel fibre reinforced concrete (SFRC), as well as ultra high performance fibre reinforced concrete (UHPFRC) columns under simulated blast loading, and comparing the response to columns constructed with traditional reinforced concrete. The details of the experimental and analytical program are summarized below.

1.2.1 Experimental Program

As part of the experimental research program, thirteen half-scale columns are tested under simulated blast loading using the shock tube testing facility at the University of Ottawa. The test series includes eight SFRC columns constructed with self-consolidating concrete (SCC) and steel fibres, as well as five UHPFRC columns, and includes specimens with and without seismic detailing.

1.2.2 Analytical Program

The analytical program involves numerical analysis aimed at predicting the response of the SFRC and UHPFRC columns tested in the experimental program. This is achieved by generating dynamic load-deformation resistance functions for SFRC and UHPFRC columns and using single degree of freedom dynamic analysis software, RCBlast.

1.3 Thesis organisation

As demonstrated in Figure 1.1, the thesis consists of seven Sections:

- Section 1 introduces the thesis and presents a literature review on the thesis subject matter;
- Section 2 provides additional background information that is relevant to the thesis including an overview of the properties of SFRC and a review of the effect of blast loads on structures;
- Section 3 summarizes the details of the experimental program, including: material properties, column properties, instrumentation and test setup;
- Section 4 presents the experimental results for the thirteen SFRC and UHPFRC columns tested in the experimental program;
- Section 5 discusses and evaluates the test data to examine the influence of various parameters on the blast response of the columns;

- Section 6 presents an analytical study aimed at predicting the dynamic response of SFRC and UHPFRC columns under blast loads. The Section compares analytically predicted displacements with experimentally recorded displacements from the columns tested in the experimental program and presents a discussion on variations between the results.
- Section 7 presents the concluding remarks regarding the research program, and provides some recommendations for future research.

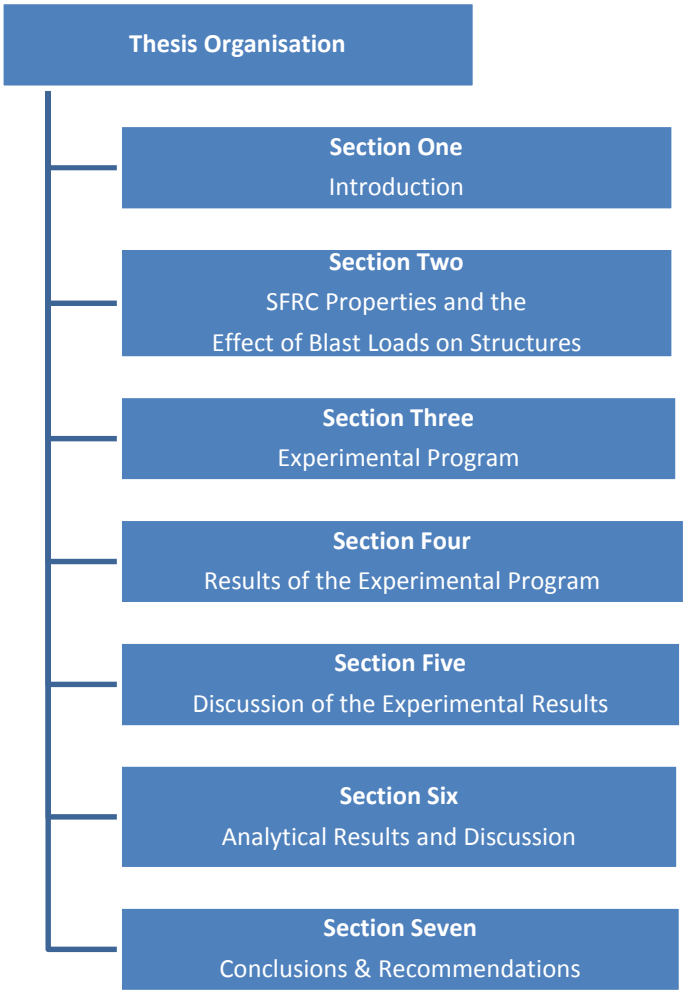

Figure 1.1 Thesis organisation

1.4 Literature Review

The section presents a literature review on the thesis research topic. After listing historical examples of explosions affecting reinforced concrete structures, the behaviour modes of reinforced concrete columns subjected to blast loading will be discussed and existing research in the literature on the blast performance of RC columns will be reviewed. Previous research on the structural behaviour of SFRC and UHPFRC subjected to impact and blast will also be summarized. Section 2 provides additional background information that is relevant to the thesis, including an overview of the properties of SFRC and a review of blast loading and its effect on structures.

1.4.1 Historical Examples of Explosion Disasters

1.4.1.1 Sunrise Propane Explosion, Toronto, Ontario, Canada, August 10th, 2008

Also known as the Toronto Propane Explosion, this event resulted from a very large propane explosion, followed by a series of explosions and the resulting fire at the Sunrise Propane Industrial Gases facility in the area of North York in Toronto, Ontario, Canada on August 10th, 2008. The explosions caused large fireballs, as shown in Figure 1.2, and damaged many homes and offices in the area. The explosions resulted in the death of one employee and forced thousands of people to evacuate their homes. The cost of clean-up was approximated to be $1.8 million. The explosion was determined to be the result of a propane leak that resulted from a hose failure during a "tank to tank" transfer from one cargo truck to another. (CBC news, 2008)

1.4.1.2 Barajas International Airport, Madrid, Spain, December 30th, 2006

This event was a terrorist attack that involved the detonation of approximately 500 kg of explosives in the concrete parking structure of Terminal 4 of the Madrid-Barajas International Airport. The Basque Nationalist and Separatist claimed responsibility for the attack. The group parked a van laden with an ammonium nitrate and hexogen mixed explosive within the reinforced concrete parking structure. The explosion demolished almost all of the five floors of the structure, as seen in Figure 1.3, and produced an estimated 40 tonnes of debris. The explosion killed 2 and injured 36 people. Prior to the explosion, authorities were warned of the device, and the airport was evacuated. The material damage was initially estimated at €30 million ($46 million CAD) (Santamaria, 2008).

1.4.1.3 AZF Plant, Toulouse, France, September 21st 2001

In this event, an explosion took place in a warehouse of the AZF Plant in Toulouse France on September 21st 2001. The plant manufactured chemicals including ammonium nitrate, chlorinated compounds and ammonium nitrate-based fertilisers. The warehouse was used as a temporary storage facility of ammonium nitrate that did not meet the quality control specifications of the plant, and the official inquiry noted that the explosion was the result of improper handling of ammonium nitrate within the warehouse (Barthelemy et al., 2001). The explosion made a crater approximately 65m by 54m in diameter with a 7m depth. The official investigation estimated that the explosion was the equivalent of approximately 20-40 tonnes of TNT. The shock waves of the explosion shattered windows within 3km of the plant. 30 people were killed as a result of the explosion, and there were up to 2242 people injured. The cost of the damage due to the explosion was estimated at €1.5 billion ($2.4 billion CAD) (Dechy et al., 2004). The aftermath of the explosion can be seen in Figure 1.4.

1.4.1.4 Arndale Shopping Centre, Manchester, United Kingdom, June 15th, 1996

On the morning of Saturday June 15th, 1996, members of the Irish Republican Army (IRA) parked a Ford cargo truck outside the Arndale Shopping Centre in the city of Manchester, UK. The size of the explosive was approximately 1500kg and was a mixture of Semtex, a military grade plastic explosive, and ammonium nitrate fertilizer. The force of the shock wave was felt up to 8km from the centre of detonation, and windows within 500m were shattered. A dozen buildings suffered major structural damage including two multi-story parking garages, with approximately 6 buildings requiring complete demolition. The city's infrastructure was also affected as there was major damage to the roads in proximity of the explosion. The damage due to the explosion was estimated at approximately £100 million ($251 million CAD). There were no casualties as local authorities were warned of the attack, which led to a mass-evacuation of the area around the explosive device (Williams et al, 2000).

1.4.1.5 Alfred P. Murrah Building, Oklahoma City, Oklahoma, April 19th 1995

The Murrah building was a nine-story conventionally reinforced concrete structure that was constructed in the mid-1970s. On April 19th, 1995 a transport truck with approximately 1800kg equivalent TNT explosive was parked outside the structure, centered approximately 4m from one of the main support columns of the façade, and exploded. Due to the proximity of the explosion,

it is generally believed that this column was shattered by the blast, and absent of any alternative load path, this directly led to the loss of four bays above the column. Of a total of 20 bays in the footprint of the structure, 10 collapsed over the full height of the building due to progressive collapse (see Figure 1.5). The incident resulted in the deaths of 168 people, and injured more than 680. The estimates of the damage were approximately $652 million (USD). 90% of the casualties are attributed to the collapse of the structure (Schmidt webinar, 2010). The failure of the Murrah building, led to the development of new structural design guidelines to resist progressive collapse (Osteraas, 2006).

Figure 1.2 Fireball of the Sunrise propane explosion as seen from midtown Toronto.

(http://www.cbc.ca/news/canada/story/2008/08/10/propane-fire.html)

Figure 1.3 Effects of the 500kg explosive on the RC parking structure of Terminal 4

(http://en.wikipedia.org/wiki/2006_Madrid-Barajas_Airport_bombing)

Figure 1.4 Aftermath of the AZF Plant explosion

(Dechy et al. 2004)

Figure 1.5 Aftermath of the Murrah Building bombing

(http://en.wikipedia.org/wiki/Oklahoma_City_bombing#cite_note-UnderstandingTerror106-4)

1.4.2 Behaviour of Reinforced Concrete Columns under Blast Loads

Blast loads on structures can produce both local and global structural responses, which depend mainly on loading rate, orientation of the structure with respect to blast wave propagation, and boundary conditions of the structural elements. Local responses in reinforced concrete cause scabbing and spalling, which can produce secondary fragments; while global responses are associated with different failure modes (Ngo et al., 2007). For the case of this research, only failure modes of columns will be discussed, as the primary focus is columns as opposed to entire structures.

1.4.2.1 Modes of Behaviour

Reinforced concrete structures are designed to crack but behave elastically under gravity and wind loads, but typically designed to behave inelastically (while dissipating energy in a ductile manner) in the case of strong earthquakes. Similarly under blast loading, if the blast pressure is weak, due to low charge or long standoff distance, the column may be expected to behave in an elastic manner. However if the blast load is sufficiently large, inelastic demands may be imposed and thus ductile dissipation of the blast energy may be required (Saatcioglu et al., 2011). Thus, under blast loading, a reinforced concrete column may either:

- Respond elastically;
- Respond inelastically while dissipating energy in a ductile manner (retaining most of its original strength but with associated permanent deformations);
- Respond inelastically but in a brittle manner and fail (due to crushing of concrete or buckling/rupture of steel).

The first two modes of response are required for the safe design of structures to blast loads. If the column does not have sufficient strength and ductility, failure may occur, resulting in local or progressive collapse of the structure (Saatcioglu et al., 2011).

1.4.2.2 Flexural Behaviour in Columns Subjected to Blast Loads

Flexure occurs in columns subjected to blast loads as the governing loads will impinge the columns laterally. Most building columns have some level of end-restraint and thus under external blast pressure develop negative bending near the ends and positive bending on the opposite face (Saatcioglu et al., 2011). Flexural failure will occur after the formation of a

sufficient number of plastic hinges (one in the centre for simply supported members, on one at each support and one in the centre for members fixed on each end). Figure 1.6 shows the development of plastic hinges due to blast loads.

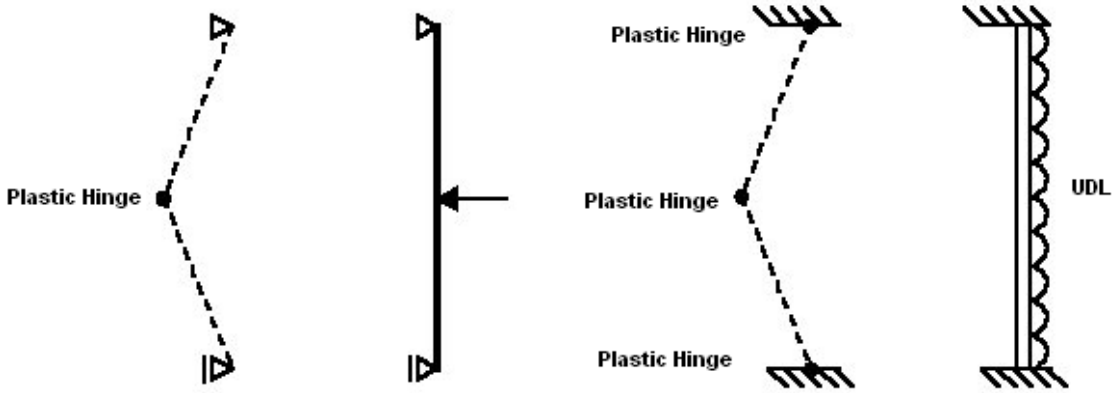

Figure 1.6 Development of plastic hinges due to blast loads

1.4.2.3 Shear Behaviour in Columns Subjected to Blast Loads

Several types of shear failures may occur for columns subjected to blast loads. Diagonal tension and diagonal compression shear are associated with flexural behaviour of structural elements, and should be considered for columns subjected to blast loads. Direct shear is associated with severe short duration dynamic loads, and consequently is very important for columns subjected to blast loading, as they are caused by high shear inertia forces that do not exist under static or slow dynamic loads. Should this shear failure occur, it will be very early in the structural response and prior to any significant bending deformation (Crawford et al. 1999).

1.4.2.4 Effect of Confinement in Columns Subjected to Blast Loads

The dynamic nature of blast loading requires columns to be capable of maintaining inelastic capacity without collapse. Extensive research has shown that the use of careful detailing in the form of closely spaced hoops and ties enhances concrete confinement and can improve the energy dissipation capacity and ductility of reinforced concrete columns subjected to earthquake loading. Similarly, some researchers have proposed that the use of seismic detailing is one possible strategy to enhance the blast performance of columns (see next section).

1.4.3 Studies in the Literature on the Blast Behaviour of RC Columns

1.4.3.1 Response of Earthquake Resistant Reinforced-Concrete Buildings to Blast Loading (Saatcioglu et al., 2009).

Saatcioglu et al. (2009) investigated the effect of seismic detailing on the blast response of 10-story moment-resistant frames subjected to a variety of charge and standoff-distance blast combinations. Using SDOF analysis the overall performance, ductility and drift demands of the buildings were compared. The results showed that the use of seismic detailing in columns improves blast performance in terms of ground-story column performance, and can reduce the potential for progressive collapse.

1.4.3.2 Residual Strength of Blast Damaged Reinforced Concrete Columns (Bao and Li, 2010).

Bao and Li (2009) used numerical finite element modelling (using program LS-DYNA) to evaluate the dynamic responses of reinforced concrete columns to blast loads. The results of the finite element models were verified with a related experimental program on columns tested using a hydraulic-based blast simulator. The analytical and experimental program included 12 RC columns with and without seismic and with varying amounts of longitudinal reinforcement.

The results of the analytical study demonstrated that seismically detailed columns had significantly less deflection than their conventional counterparts. Similar observations were made during the experimental program, and the results were consistent with the authors' predication that the improved confinement in columns with seismic detailing improves resistance and can significantly reduce the degree of direct damage due to blast loads.

After the blast tests, the columns were once again subjected to axial loading in order to evaluate their residual axial strength. In terms of residual axial capacity, the results indicated that the capacity reduces significantly for columns with lower transverse reinforcement ratio (Bao and Li, 2010). In the case of longitudinal reinforcement, the results showed that columns with greater longitudinal reinforcement ratios had reduced mid-height displacements and increased residual axial capacity when subjected to blast. This is to be expected since increasing longitudinal reinforcement ratio provides columns with greater nominal moment capacity and axial strength.

The authors also studied the effect level of axial load of the behaviour of columns under blast loads. The results on columns tested with axial load ratio ranging from 0.1 to 0.4 showed that when the impulsive loading is small, the mid-height displacement of the column with larger axial loads reduces, due to the effect of axial load on increasing moment capacity and shear strength. However, the results showed that after a critical impulse was reached, the mid-height displacement of the column would also greatly increase with increasing axial loads. The authors explained that when columns under flexure experience large deflection, axial loads will amplify the lateral deflection and internal moment due to P–Δ effects. The effect of axial load ratio was found to be more critical in the case of columns with low transverse reinforcement ratio (Bao and Li, 2010).

1.4.3.3 Performance of Reinforced Concrete Columns under Simulated Blast Loading (Lloyd, 2010).

Lloyd (2010) conducted an experimental research programme on 13 half-scale RC columns exposed to simulated blast loads using the University of Ottawa shock tube. The columns were designed according to CSA A23.3 for both seismic and non-seismic zones. Eleven of the columns had rectangular cross-section with dimensions 100 mm by 150 mm, and were 1980 mm in unsupported length. The two remaining columns had 150 mm by 150 mm cross-section with the same height as the rectangular columns. Longitudinal reinforcement consisted of 4-10M reinforcing bars, and transverse hoops having 6.3mm diameter, were placed uniformly, with columns identified for seismic zones having twice the amount of hoops. The columns were axially loaded and then tested with shockwave lateral loading along the 150mm long surface of the column (Lloyd, 2010).

The columns were subjected to various shock loads to test elastic and plastic behaviour. Multiple tests were done in the elastic range, followed by one destructive test. Seismic and non-seismic detailed columns were tested under the same conditions for comparison. The reflected pressure-time history was measured in the shock tube using pressure sensors and a high-speed digital oscilloscope, and displacements at mid-height of the columns was measured using a linear piezoelectric potentiometer (Lloyd, 2010).

The results of the experiment showed that there were large standard deviations in the displacements of the columns at mid-height, which made it difficult to conclude if there are significant differences in behaviour between the seismic and non-seismic detailed columns. It should be noted that the columns in this study had relatively small cross-sections; the author concluded that in the case of slender columns with small cross-section and high slenderness ratios, the confinement of core concrete with seismic detailing may not contribute significantly to response under shockwave loading (Lloyd, 2010). It was concluded that future experiments should focus on non-slender columns with larger core concrete areas in order to compare the effects of transverse reinforcement on the response of columns with and without seismic detailing (Lloyd 2010).

1.4.3.4 Behaviour of Steel reinforced Polymer (SRP) Strengthened RC Members under Blast Load (Carriere et al., 2009)

This experimental programme was conducted in order to study the potential of using SRP to strengthen RC members against blast loading. For the tests, ten concrete members with 150mm by 150mm cross-section and having a total length of 2100 mm (unsupported length of 1500mm) were constructed using an average 39.1 MPa concrete. The members were reinforced with four 6mm diameter reinforcing bars, and 6mm diameter transverse reinforcement spaced at 100mm. Of the ten members, 5 were strengthened using SRP sheets (Carriere et al. 2009). A total of six explosives tests were performed. For the first four, both an SRP-strengthened and non-strengthened (control) member were tested simultaneously. Each test used a different amount of C4 explosive, which resulted in different blast overpressures. For the final two tests, an axial load was applied to the members (to both control and strengthened members). The results of the tests were recorded using strain gauges mounted on the reinforcement inside the concrete members, linear variable displacement transducers, and Free Field Blast Pressure Probes to measure the resulting pressure-time histories of the varying amounts of C4 explosive (Carriere et al. 2009). The varying amounts of C4 explosive (from 15kg-50kg) were placed at a distance of 2m from the members. The damage sustained by the members was directly related to the effect of the blast overpressures. It was observed that a difference of 2.5kg of C4 explosive resulted in a transition from survival to total failure; flexural cracks at mid-span and supports became wider, showing possible yield of flexural reinforcement and the formation of plastic hinges at blasts corresponding to between 15kg and 17.5kg of C4 explosive. At a 50kg charge of C4 explosive,

the member broke into four pieces with the reinforcing steel fracturing in tension. It was also determined that RC members with axial load exhibit more severe damage in comparison to the members without axial load at the supports, due to the fact that axial compression strain and flexural compression strain from the blast load exceed the ultimate strains of the members at the supports (Carriere et al. 2009).

1.4.4 Quarter-Scale Building / Column Experiments (Woodson and Baylot, 2004)

The objective of this experimental programme was to better understand the response of RC structures and columns to blast effects. This was done by the construction of two-story, 4 bay, quarter-scale RC structure used to model a portion of a typical flat-plate structural system, some with walls (cladding), and others without to examine the effects on the columns. The central columns of the structure were axially loaded by dead weights. For the tests, 7.10kg of C4 explosive was used. The first experiment involved no cladding with the explosive charge being placed near the ground at 1.52m to the face of the central front column. Due to minor damage in this experiment, the standoff distance was changed to 1.07m for the remainder of the tests. The test was repeated at the reduced standoff distance, and the central columns sustained a permanent displacement of 6.4mm, but maintained the ability to carry the dead weight. The test was repeated for a fully clad structure with masonry walls. While it was determined that the central columns failed, the load was transferred by means of the edge beams to the corner columns, and thus total collapse was prevented. The final test involved the upper floor having cladding, and the bottom floor being open. The column of the lower, un-cladded floor sustained less damage, similar to the first experiment (Woodson and Baylot, 2004). The paper concluded that the experiments were successful in demonstrating the response of RC frame structures to blast effects, and showed that the presence of cladding played a large role on the impulse load applied to a column (Woodson and Baylot, 2004). This is an important finding for the analysis of columns under blast loads, as it highlights the role of blast wave wraparound in reducing the blast loads on columns.

1.4.4.1 Composite Retrofits to Increase the Blast Resistance of Reinforced Concrete Buildings (Crawford et al., 2001)

This research study described a blast retrofit procedure which involves the use of an advanced composites (CFRP) wrap technique for retrofitting RC columns with weak lateral resistance.

Tests and analytic studies were conducted to verify the suitability of the retrofits. The program focused on charge sizes and standoffs that would cause potential structural collapse. Full-scale experimental tests were conducted on columns representing columns in a conventional 4-story office building on the East Coast of the United States, a zone of low seismic activity. Blast tests were conducted on retrofitted and control specimens. For the specified blast loads, the results demonstrated that the conventional columns did not have sufficient moment capacity to meet deflection limits, nor the required amount of transverse reinforcement necessary to meet the required shear demand. It was determined that the conventional columns failed primarily in shear at the top and bottom, and the measured mid-height displacements agreed with the displacements from the numerical model. For the retrofitted column, both shear and moment capacities were enhanced. (Crawford et al., 2001). Under retrofit, the column appeared to remain elastic, and there was no apparent permanent deflection, which is a significant improvement compared to the conventional column. Consequently, the research study concluded that retrofitting RC columns with CFRP is an efficient means to ensure survivability of buildings subjected to blast loads (Crawford et al., 2001).

1.4.5 SFRC under Impact and Blast Loads

1.4.5.1 General

The enhanced ductility and energy absorption capacity of SFRC make it an ideal material for use in the impact and blast resistant design of structures. While we have significant knowledge and understanding of the properties and behaviour of SFRC subjected to quasi-static loading, the behaviour and properties of SFRC under high-strain loading is not completely understood. Table 1.1 summarizes some of the published research that has focussed on the impact and blast behaviour of SFRC.

No standardized test exists for testing SFRC under impact loading, however several researchers have studied the behaviour of SFRC using *Pendulum*, *Split Hopkinson Pressure Bar* (SHPB) and *Drop-Weight* tests. It is noted that there is very limited published data on the blast behaviour of SFRC structural components (and there is no published research in the case of columns).

Although there has been important research on the impact and blast behaviour of SFRC, data and conclusions in the literature are conflicting. Some research shows that the use of SFRC can improve behaviour under extreme dynamic loading, while other research shows that the ductility and toughness normally present in SFRC under static loading is absent or reduced at high-strain loading. The sections that follow detail some of the research studies listed in Table 1.1.

Table 1.1 Published research on the impact and blast behaviour of SFRC

Authors	Type of testing	Main conclusions
Naaman & Gopalaratnam (1983) Gopalaratnam & Shah (1986) Banthia et al. (1996)	▪ Impact testing of SFRC with instrumented pendulum and modified pendulum setups	▪ Behaviour of SFRC is significantly dependant on strain rate. ▪ Impact behaviour is improved for SFRC ▪ Impact behaviour is affected by fibre content and fibre properties such as aspect ratio (l_f/d_f).
Lok and Zhao (2004)	▪ Impact testing of SFRC with Split Hopkinson Pressure Bar (SHPB) setup	▪ Behaviour of SFRC is significantly dependant on strain rate. ▪ At low and moderate strain rates SFRC exhibits good ductility. ▪ At higher strain rates ductility of SFRC shows reduced ductility.
Wang et al. (2007)	▪ Impact testing of SFRC with Split Hopkinson Pressure Bar (SHPB) setup	▪ Behaviour of SFRC is significantly dependant on strain rate. ▪ Impact behaviour is improved for SFRC in terms of peak stress and strain, however post-peak ductility seems to reduce for SFRC at high-strain rates. ▪ Impact behaviour is affected by fibre content.
Bindiganavile et al. (2002)	▪ Impact testing of SFRC with drop-weight testing ▪ Impact testing of UHPFRC with drop-weight testing	▪ Behaviour of SFRC is significantly dependant on strain rate. ▪ Significant drop in the toughness of SFRC at high-strain rates. ▪ UHPFRC is less strain-sensitive and shows improved performance when compared to SFRC.
Lok and Xiao (1999)	▪ Blast testing on SFRC slab panels using live explosive testing	▪ SFRC panels showed improved damage tolerance and integrity when subjected to blast loading.
Magnusson & Hallgren (2003)	▪ Blast testing on SFRC beams using air-blast loading	▪ Positive influence of fibre reinforcement is reduced under air-blast loading when compared to static loading. ▪ Longer fibres are less effective under dynamic loading.
Cavill et al. (2006)	▪ Blast testing on UHPFRC panels using live explosive testing	▪ Panels were able to withstand large deflections with no permanent deformations and little observable damage.

1.4.5.2 SFRC under Lower-Velocity Impact Tests

Gopalaratnam and Shah (1986) used an instrumented *Pendulum* (*Charpy*) impact machine to study the behaviour of SFRC flexural beam specimens reinforced with smooth steel fibres under varying strain-rates. The tests determined that the Dynamic Increase Factor (DIF) for SFRC is dependent on the strain rate and fibre volume fraction (see Figure 1.7 (a)), as well as the volume and aspect ratio (l_f/d_f) of the fibres (see Figure 1.7 (b)). Similar conclusions were found in an experiment by Naaman and Gopalaratnam (1983). Gopalaratnam and Shah (1986) postulated that changes in the cracking process at the static and dynamic rates are primarily responsible for the rate sensitive behaviour of SFRC since the strain rate sensitivity in cement-based composites is related to crack growth.

(a)

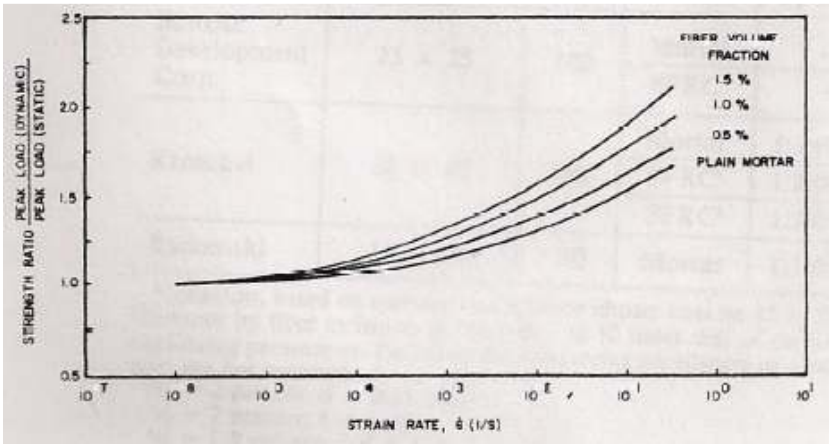

(b)

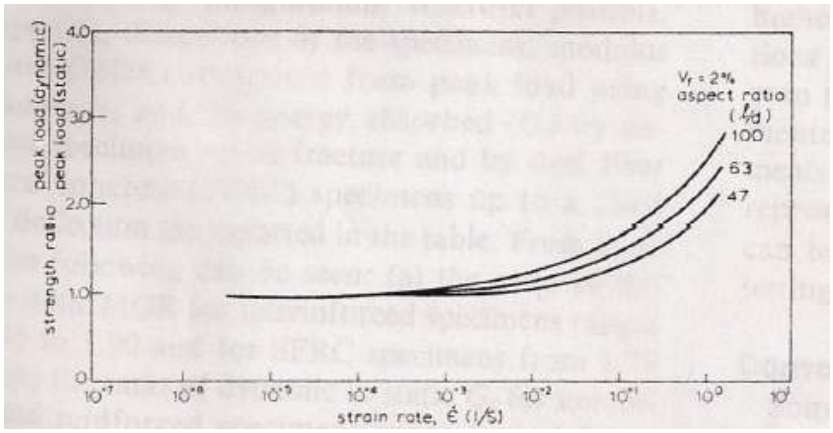

Figure 1.7 (a) DIF of SFRC vs. strain rate for various fibre volumes and (b) comparison of DIF of SFRC vs. strain rate in relation to the aspect ratio of the fibres

(Gopalaratnam and Shah, 1986)

Banthia et al. (1996) also studied the impact behaviour of SFRC using a modified pendulum test and found that addition of fibres results in improved fracture energy and toughness. The results showed that the behaviour was influenced by fibre type and fibre content.

A further test on dynamic behaviour of SFRC was conducted by Rostasy and Hartwich (1985) using a *Schenck Hydropulse Actuator* of 630kN capacity and a maximum stroke rate of 1m/s. Using this Machine, the reported dynamic rate was $\approx 170.10^{-3} sec^{-1}$. The authors compared both hooked and straight fibres with varying fibre volumes ranging from 0.75% to 1.5%. The experiment found DIFs varying between 1.2 and 1.23 for this load rate. However, converse to the study by Gopalaratnam and Shah (1983), this study reported that the increase of strength is neither influenced by fibre addition nor by the type of fibre. However it should be noted that the dynamic strain rate is approximately half the strain rate used by Gopalaratnam and Shah (1983) which could account for the difference in conclusions from the two experiments.

Rostasy and Hartwich (1985) also analysed the post-peak behaviour of SFRC when compared to plain concrete. They concluded that the post-peak behaviour is strongly influenced by fibre addition, and that "deformational energy" (area under the dynamic stress-strain curve) increases markedly with the amount of fibre addition and with the strain rate. This occurs in both plain concrete and SFRC, but more so in SFRC as can be seen in Figure 1.8.

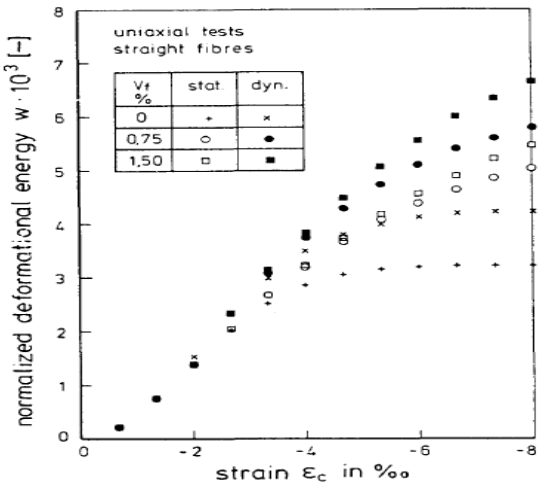

Figure 1.8 Comparison of deformational energy of SFRC with varying fibre volumes vs. strain

(Rostasy and Hartwich 1985)

1.4.5.3 SFRC under Higher-velocity Impact Tests

The *Split Hopkinson Pressure Bar* (SHPB) Impact test involves launching a standardized striker bar at high velocity at a material specimen in order to determine its behaviour at very high strain rates. Lok and Zhao (2004) tested SFRC specimens at strain rates varying from ≈20 sec^{-1} up to ≈100 sec^{-1} using a SHPB test setup. The experimental setup for the SHPB test and the dimensions of the striker bar can be seen in Figure 1.9.

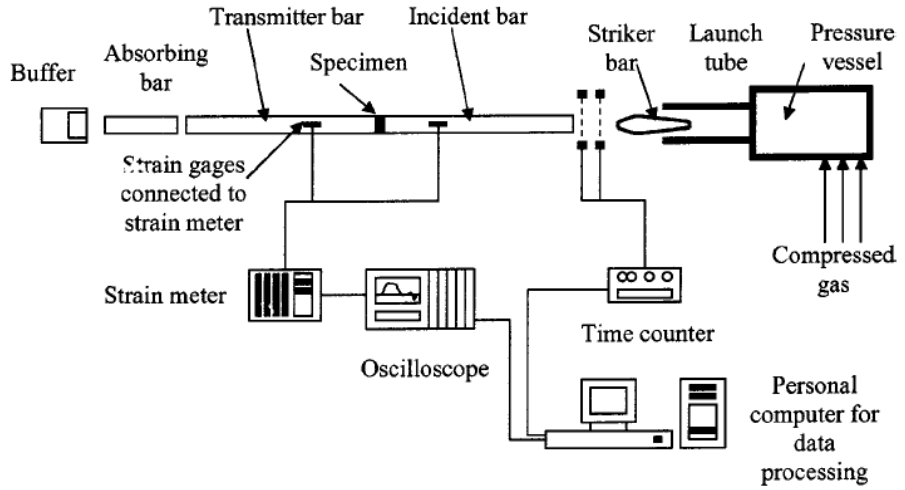

Figure 1.9 Setup for Split Hopkinson pressure bar test

(Lok and Zhao, 2004)

The test specimens were constructed with SFRC using hooked-end steel fibres, and a fibre content of 0.6% by volume. The authors remarked that while SFRC exhibits good post-peak ductility if tested under quasi-static or low strain-rates, post-peak ductility was absent at higher strain-rates. For the specimens tested at a strain rate of 20 sec^{-1}, there was distinct mobilization of the steel fibres in providing ductility; however specimens tested at a strain rate above 50 sec^{-1} showed reduced ductility enhancement. This finding coincides with a previous experimental program reported by Zhao et al. (2001), where SFRC was tested at a strain rate of 50 sec^{-1}. The authors noted that this finding is of importance for structures subject to blast loading where strain rates can range from approximately 100 sec^{-1} to 10,000 sec^{-1}. It should be noted that the fibre content in the samples of this study was relatively low. As reported by other authors, the behaviour of SFRC under dynamic loading is dependent on the fibre content. In addition to this, the quasi-static strain rate reported by Lok and Zhao was 2×10^{-5} sec^{-1}. This is approximately 7

times the rate that is specified for quasi-static loading by CEB and could skew the results of the DIF.

A further SHPB test on SFRC was conducted by Wang et al. (2007). In this study, the samples were constructed with straight fibres at volume contents of 0, 3.0%, and 6.0% fibres, and were tested under strain rates from 42 sec^{-1} to 99 sec^{-1}. The authors noted that the behaviour of SFRC is significantly sensitive to strain rate with results demonstrating that the peak stress, peak strain, and slope of the descending portion of the stress-strain curve all increase with increases in strain rate. The findings also demonstrated that the increase in peak strain with increasing strain-rate is more significant for specimens with higher fibre contents. The authors noted that the addition of fibres resulted in improvements in overall toughness and behaviour. However, when comparing the descending branch of the stress-strain curves, it is noted that the slopes are greater for the SFRC samples when compared to the companion plain concrete samples (see Figure 1.10).

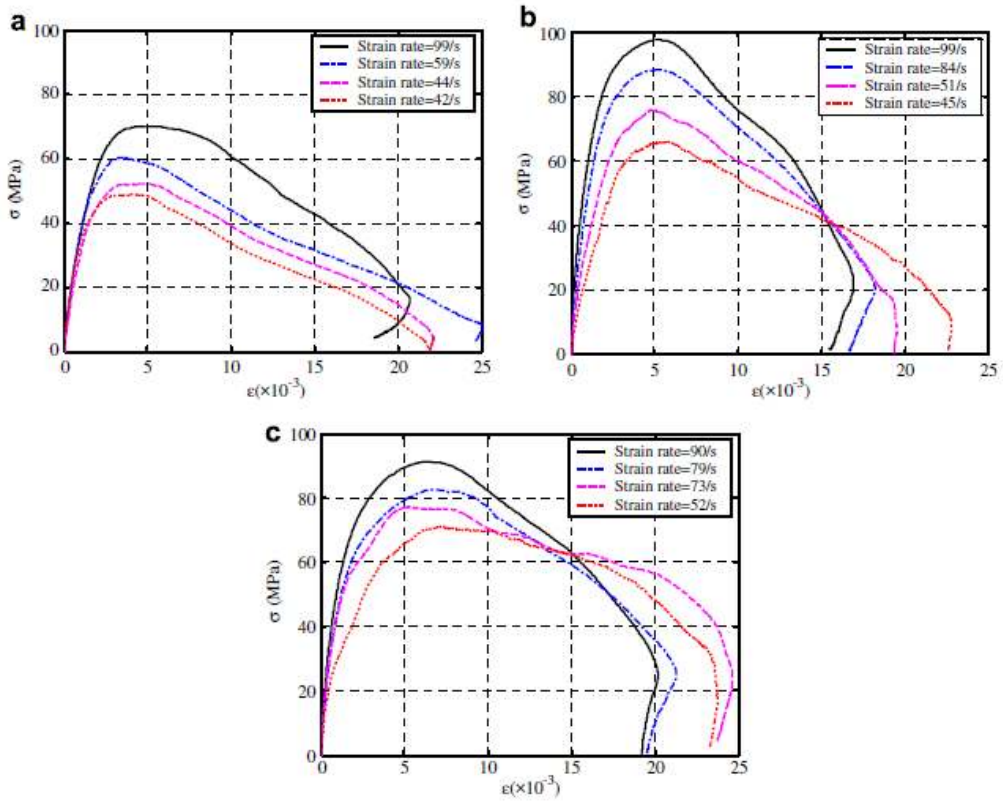

Figure 1.10 Dynamic stress-strain curves of SFRC a) 0%, b) 3%, and c) 6% fibres by volume.

(Wang et al., 2007)

1.4.5.4 SFRC under Drop-weight Tests

Bindiganavile et al. (2002) studied the performance of normal steel fibre reinforced concrete (SFRC) and ultra high-performance fibre reinforced concrete (UHPFRC) under impact loading using a drop-weight testing device. While the authors found UHPFRC to perform very well at high-strain rates (see section 1.4.6), they observed a significant drop in the toughness of the SFRC samples as the loading rate increased. In accordance with previous findings, the authors of this study reported that SFRC composites can fracture across cracks at higher strain rates, consequently producing brittle failures.

1.4.5.5 Blast Tests on SFRC (Lok and Xiao, 1999)

Experimental data on the behaviour of SFRC under blast loading is very scarce. However some limited research has been conducted on the behaviour of SFRC slab panels and beams. Lok and Xiao (1999) completed a series of tests of SFRC panels to varying blast overpressures. The panels were made with hooked-end steel fibres with fibre contents varying from 0.5%-1.5%, and varying aspect ratios (33.4, 60, and 75). The panels were exposed to hemispherical blast waves from different charge weights of TNT (8kg, 20kg, and 40kg). The blast wave overpressures were measured by pressure transducers mounted in front of two of the supports, and a damped plunger was positioned to measure the maximum displacement of the panels (see "measuring device" in Figure 1.11). It is noted that the panels had varying boundary conditions (simply-supported and fully fixed).

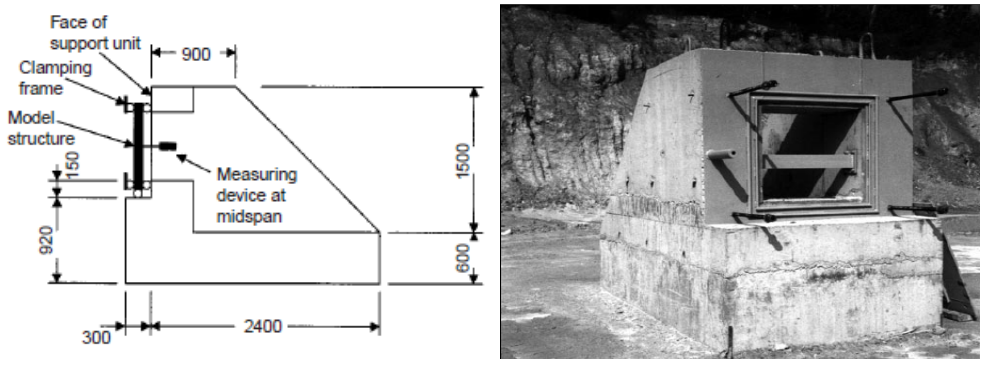

Figure 1.11 Detail of setup used for blast tests on SFRC panels.

(Lok and Xiao, 1999)

Prior to the experiments, the SFRC panels were studied analytically using an equivalent single degree of freedom (SDOF) model. To evaluate the model, Lok and Xiao (1999) took the

dynamic increase factor (DIF) for the SFRC panels to be 1.4, but remarked that for SFRC structures, the DIF could be higher than 1.4 - perhaps as high as 1.6 - owing the increase to the crack-resisting and enhanced post-peak properties of the material. The maximum deflections of the panels under blast loading from the TNT charges were then compared to the computed values of the SDOF models. The average computed results of the SDOF models overestimated the experimental data in all cases. For the simply-supported boundary condition, this overestimation was approximately 10%-20% and for the fully-fixed boundary condition, the computed permanent deflections were on average about four times higher when compared to the experimental data (Lok and Xiao, 1999). This result could be due to an improper estimation of the DIF for SFRC. Also as shown in Figure 1.12, there is a gap between the panel and the support which could lead to wrap around of the blast wave that could lead to reduced pressures on the panel. This effect was not discussed in the paper. Lok and Xiao (1999) conclude that dynamic material properties and the influence of strain rate, for SFRC, have important implications but may be too complex for incorporation into a simple model. The authors noted that more research needs to be conducted to quantify the DIF and other factors used in the SDOF representation of SFRC structures subjected to blast (Lok and Xiao 1999). Although the authors did not report a comparison between the experimental data for the SFRC and concrete specimens, they noted that the SFRC panels demonstrated improved damage tolerance. It can be clearly seen in Figure 1.12 when compared to the plain concrete panel, the SFRC panel reduced the amount of fractured concrete under the same blast pressure.

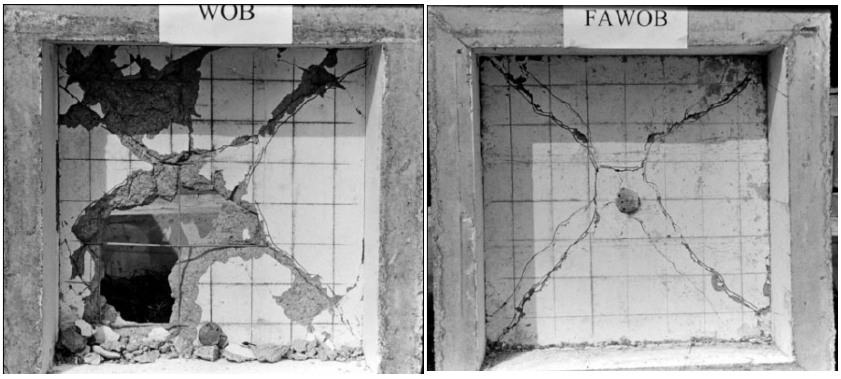

Figure 1.12 Failure pattern of panels reinforced with weldmesh only (left), and with weldmesh and 0.6% fibres.

(Lok and Xiao, 1999)

1.4.5.6 Blast Tests on SFRC Beams (Magnusson and Hallgren, 2003)

Magnusson and Hallgren (2003) tested a large series of SFRC beams under quasi-static and air-blast loading. Both regular and high-strength concrete mixes were reinforced with hooked-end fibres having lengths of 30 mm and 60 mm, and an aspect ratio of 80. It should be noted that there was no mention of traditional longitudinal and transverse reinforcing steel reinforcement in the beams. The dynamic testing was conducted using a shock tube with a rectangular inner cross section, and air-blast loading was achieved by the detonation of a spherical plastic explosive placed 10m from the beam within the centre of the shock tube. The tests determined that the positive influence of fibre reinforcement is reduced under air-blast loading when compared to static loading. It was also noted that longer fibres were less effective under dynamic loading; the authors thus postulated that it may be beneficial to use shorter fibres with smaller aspect ratios.

1.4.6 UHPFRC under Impact and Blast Loads

Ultra high performance fibre reinforced concrete (UHPFRC) is a general term, but is essentially ultra-high strength concrete reinforced with high volumes of short steel fibres. This section presents results from impact and blast tests on Compact-Reinforced Concrete (CRC) and Reactive Powder Concrete (RPC), two UHPFRC products developed and marketed by *CRC Technology* (Denmark) and *Lafarge Cement* respectively (further details regarding these materials is provided in Section 2).

1.4.6.1 CRC Impact Tests (Bindiganavile et al., 2002)

In preparation for impact load tests, Bindiganavile et al. (2002) conducted quasi-static flexure tests on CRC specimens in accordance with ASTM C1018 and ASTM C 1399. 100 mm square by 350mm long beams were cast of the mix proportions presented in Table 1.2. Conducting the flexure tests allowed for the measurement of the post peak residual strength capacity from the Residual Strength Index (RSI) of the ASTM C 1399. Following the flexure tests, the broken halves were cored to yield four cylinders that were tested in compression. The value determined was exceptionally high, and is attributed to the presence of the large volume fraction of steel fibres. The results of the quasi-static flexure tests are shown in Table 1.3, and the load-deflection curves including post-peak behaviour are shown in Figure 1.13.

Table 1.2 Mix proportions used for CRC quasi-static and impact tests (Bindiganavile et al., 2002)

Constituent	Cement	Silica fume	SP	Quartz Sand			Water	Fiber
				0-0.25 mm	0.25- 1 mm	1-4 mm		
Proportion (kg/m^3)	750	179	21	189	383	613	150	457

Table 1.3 Quasi-static flexure tests results (Bindiganavile et al., 2002)

ASTM C 78 & JSCE SF4	Peak Load	Toughness	Toughness Factor
	53 kN	69.2 J	10.38 MPa
ASTM C 1399	MOR	RS	RSI
	16 MPa	10.07 MPa	63 %

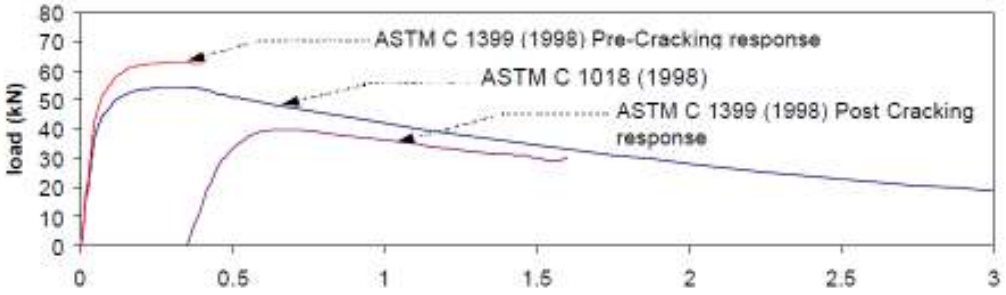

Figure 1.13 Flexural behaviour of CRC

(Bindiganavile et al., 2002)

Using the same mix proportions as in Table 1.2, Bindiganavile et al. (2002) studied the impact behaviour of CRC in order to determine the material's properties at high rates of strain. The results from the impact tests at varying drop-heights are shown in Figure 1.14.

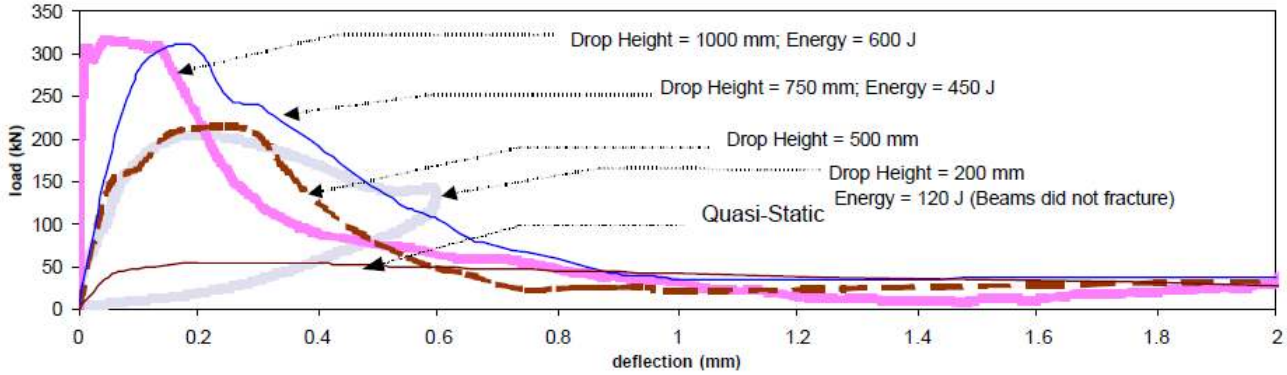

Figure 1.14 Comparison of impact load deflection plots for CRC

(Bindiganavile et al., 2002)

Using the area under the curves presented in Figure 1.14, the dynamic toughness (Joules) can be plotted, as shown in Figure 1.15. While the authors found that the toughness of traditional SFRC decreases as the drop height further increases, CRC shows an opposite trend, with increased energy absorption. The results demonstrate that CRC is not immediately brittle at higher strain rates as previously reported for SFRC by Lok and Xiao (2004), and retains its post-peak ductility. However, CRC does become brittle at a very large drop height, which implies that brittle behaviour, a characteristic of high stress rate response, manifests itself only at larger stress rates for ultra-high strength systems such as CRC. Bindiganavile et al. (2002) conclude that under high impact, the high strength matrix achieves higher peak loads, and while brittleness would be expected for a plain matrix, post-peak energy dissipation becomes possible with the addition of steel fibres.

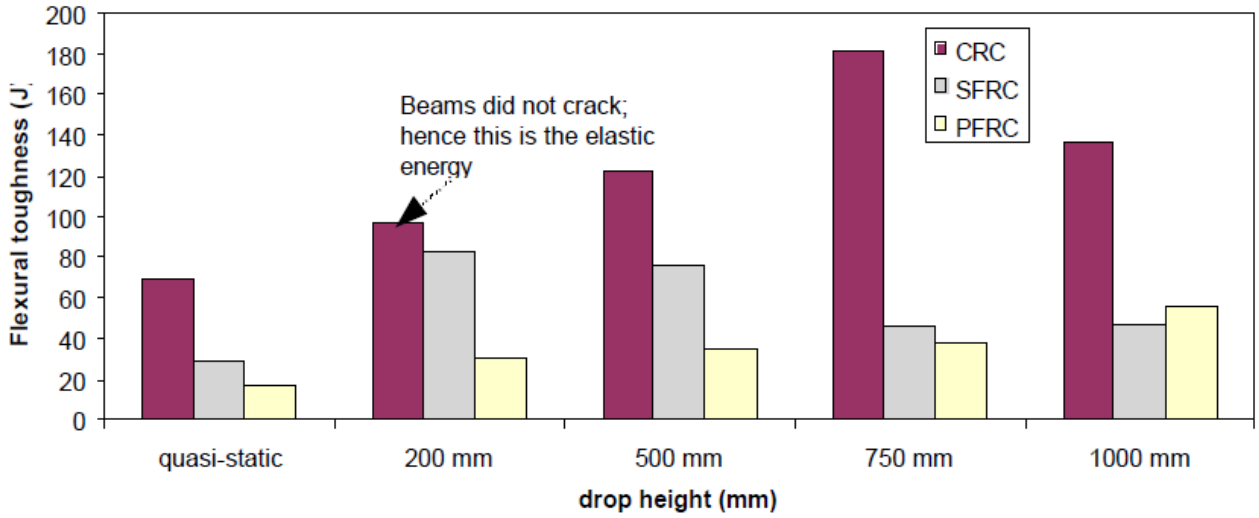

Figure 1.15 Toughness of CRC, SFRC, and PFRC

(Bindiganavile et al., 2002)

Using the results of the experimental programme, the dynamic impact factors were plotted as a function of drop height in for SFRC, Polymeric Fibre Reinforced Concrete (PFRC), and CRC. As shown in figure Figure 1.16, CRC is less strain-rate sensitive than typical SFRC, as demonstrated by the location of the rapidly ascending portion of the bi-linear curves occurring at higher stress rates. This is a phenomenon that is characteristic of high-strength materials. The

authors of this study concluded that CRC is an ideal building material for use in structures of military and strategic importance subject to impact loads (Bindiganavile et al. 2002).

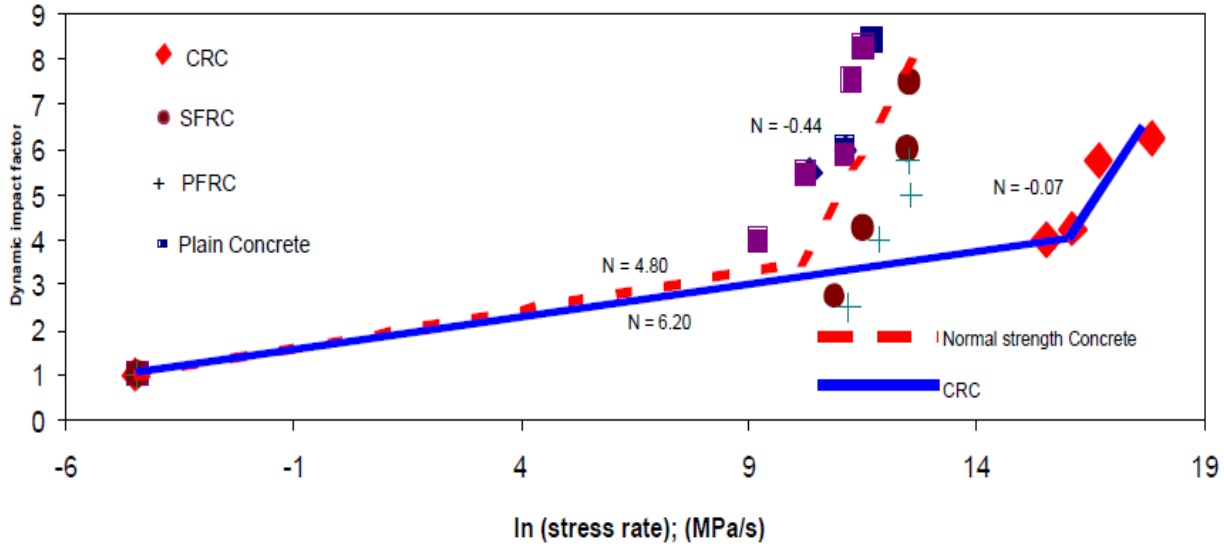

Figure 1.16 Dynamic Impact Factors for CRC, SFRC, PFRC, and plain concrete

(Bindiganavile et al., 2002)

1.4.6.2 *Ductal* Blast Tests (Cavill et al., 2006)

Cavill et al. (2006) conducted conventional explosive tests on seven panels constructed of *Ductal*, a proprietary name for an UHPFRC. The panels were designed 2 m by 1m, with varying thicknesses of 50 mm 75 mm and 100 mm, and five of the panels contained an identical arrangement of high strength pre-stressing strands; however the exact design of the panels were not detailed as they are considered confidential. The panels were set up at varying stand-off distances from the centre of detonation at 30 m, 40 m and 50 m, which caused calculated reflected pressures of 2000 kPa, 800 kPa, and 400 kPa respectively. Deflections were recorded on five panels using a simple pen on paper apparatus.

a) 100 mm panel, R=30 m b) 50 mm panel, R=50 m

Figure 1.17 *Ductal* protective panel tests

(Cavill et al., 2006)

Figure 1.17 a) shows the results of the blast test on a 100 mm thick, stressed panel, placed at 30 m from the centre of detonation. The authors note that this panel had deflected inwards 50 mm, then outwards 37 mm, and then returned to its original position with no permanent deformation or any observable damage. Figure 1.17 b) shows the results of a 50 mm thick, stressed panel placed at 50 m from the centre of detonation. The authors also note that this panel withstood significant deflection and had no permanent deflection, and only the shallow crack shown in the photo was observed. Overall, the test data and observations demonstrated that the *Ductal* panels performed remarkably well, displaying high ductility and no signs of fragmentation; also the stressed panels were able to absorb substantial energy through their ability to sustain considerable deflection up to span/28 (Cavill et al. 2006).

1.5 Conclusions from Literature Review

1. Historical examples demonstrate the dynamic and uncertain nature of blast loading that requires columns to be capable of maintaining inelastic capacity without collapse from extreme loading in any direction. The addition of randomly oriented steel fibres to typical concrete can improve many of the properties of concrete, including ductility, which is expected to improve the material's performance to blast loads.

2. There is no consensus in the literature as to whether steel fibres truly enhance the dynamic properties of concrete. Low-velocity impact tests have shown that SFRC has a greater capacity under dynamic loads than typical concrete. These tests have also shown that the amount and type of fibre plays a role in their dynamic capacity. Higher-velocity impact tests have shown that post-peak ductility is absent at high-strain rates. However, blast tests of SFRC panels demonstrated increased damage resistance when compared to typical concrete.

3. Ultra-high performance fibre reinforced concrete (UHPFRC) is a new class of material that can have compressive strengths between 150-400 MPa, high tensile strengths and good ductility. There is little published research available on the dynamic capacity of UHPFRC, however the limited research indicates that UHPFRC has good impact and blast resistance

4. While many researchers report that fibre reinforcement can be an effective way of enhancing concrete's resistance to impact and blast loads, significant issues remain unresolved and data in the literature is conflicting. There is no consensus on whether the addition of steel fibres does indeed provide the added ductility required in structures exposed to blast loads. Consequently there is a need for further research in this area, and should include effect of concrete type and strength, as well as effect of fibre type, content, and aspect ratio to determine the optimal properties required for blast resistance.

2 SFRC Properties and Effects of Blast Loads on Structures

2.1 Section Overview

This Section provides additional background information that is relevant to the thesis for the development of an analytical model, including an overview of the properties of SFRC and a review of the effects of blast loads on structures.

Section 2.2 begins by introducing steel fibre reinforced concrete (SFRC). Parameters affecting the performance of SFRC will be reviewed and the behaviour of SFRC in compression and tension will be discussed. The section will also discuss the potential of using self-consolidating fibre reinforced concrete (SCFRC) and ultra-high performance fibre reinforced concrete (UHPFRC) as an alternative to traditional SFRC.

Section 2.3 reviews blast phenomena and the modelling of blast wave parameters. The single degree of freedom (SDOF) system approach for modelling the structural response of RC elements subjected to blast loads will also be discussed. The section will also review the dynamic material properties of reinforced concrete and SFRC.

2.2 Overview of the Properties of SFRC

2.2.1 Introduction to Steel Fibre Reinforced Concrete

Steel fibre reinforced concrete (SFRC) is a material whose components include the traditional constituents of Portland cement concrete (namely, hydraulic cement, fine and coarse aggregates, admixtures) and a dispersion of randomly oriented short discrete steel fibres (Aoude, 2007).

Plain concrete is very weak and brittle in tension, especially when compared to its behaviour under compressive forces. The addition of steel fibres transforms this behaviour and results in significant improvements in tensile post-cracking strength and toughness. Similarly the addition of fibres can improve the toughness and ductility of concrete in compression. The improvement in behaviour results from the ability of the fibres to bridge and control the formation of cracks in concrete.

Current widespread use of steel fibres has mostly been limited to non-structural applications (e.g. industrial slabs), where the fibres are used as an alternative or supplement to traditional steel bars or wire-mesh reinforcement used to control cracking. However, the use of steel fibres may be beneficial to improve the structural behaviour of reinforced concrete elements. For example, the use of steel fibres can potentially be used to replace transverse reinforcement in beams and columns (Aoude, 2007). Similarly, the addition of steel fibres improves the ductility and toughness of concrete and thus may be beneficial in seismic and blast applications.

Steel fibres have various configurations and are shaped in such a way as to improve pullout resistance from the cement matrix through mechanical clamping. Two of the most popular configurations include hooked-end and crimped fibres (see Figure 2.1). In the case of hooked-end fibres, the energy required to deform the hooks provides added resistance to pullout, while additional resistance is provided through the use of a continuously deformed shape in the case of crimped fibres. Hooked-end steel fibres represent the most widely used fibre typology in the construction industry and in published research studies. The fibres are manufactured by *Bekaert* under the *Dramix* brand.

(a) Crimped steel fibres

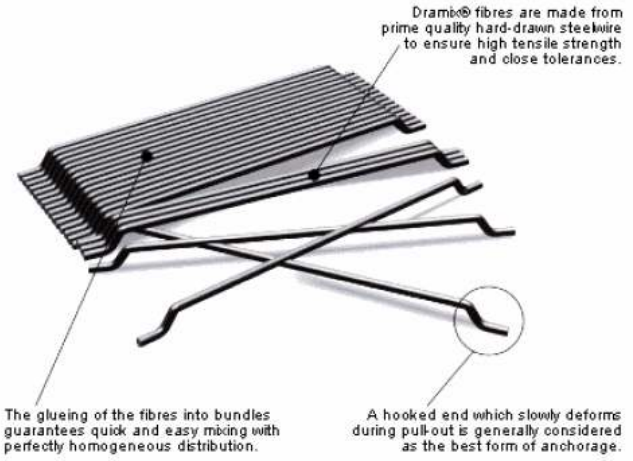

(b) Hooked-end steel fibres (Dramix Brand)

Figure 2.1 Examples of crimped and hooked-end steel fibres

2.2.2 Parameters Affecting the Performance of Steel Fibres

When considering the addition of steel fibres to a concrete mix, the principle characteristics that will influence the performance of SFRC are: fibre aspect ratio, fibre content, fibre pullout strength, and fibre orientation factor.

2.2.2.1 Fibre Aspect Ratio & Fibre Content

When considering the addition of steel fibres to a concrete two of the principle characteristics that will influence performance are the aspect ratio and fibre content (or volume of fibres in the concrete mix). The aspect ratio is given as:

$$Aspect\ Ratio = l_f/d_f \qquad [2.1]$$

where l_f is the length of the fibre, and d_f is the diameter of the fibre. Typically steel fibres have lengths that range between 10 and 60 mm and have circular cross sections with diameters in the range of 0.2 to 1 mm. Most steel fibres have aspect ratios that are less than 80. Increasing the aspect ratio of the fibres has been noted to improve the mechanical properties of SFRC (Gopalaratnam and Shah, 1986). It should be noted that as the fibre aspect ratio increases, workability in the fresh state tends to be reduced. As such there exists a trade-off between improved mechanical properties and ease of placement when selecting fibre aspect ratio.

2.2.2.2 Fibre Content

In terms of fibre proportion within a concrete mix, most literature refers to the percentage of fibres by volume expressed in the literature by the symbol V_f. The use of 78 kg/m^3 of fibres results in 1% of fibres per volume of concrete. Typical fibre contents range from 0.25% to 1.5%, with non-structural applications typically requiring fibre contents of 0.5% or less, while quantities greater than 0.5% are typically required for most structural applications (Aoude, 2007). It should be noted that increasing fibre content beyond certain limits in traditional concrete (typically above 1%) can cause problems during mixing and placement.

2.2.2.3 Fibre Pullout Strength

Naaman and Najm (1991) reported that it is generally agreed that the fibres contribute primarily to the post-cracking response SFRC through the ability of the randomly oriented fibres to bridge cracks and provide resistance to crack opening. The pull-out strength of steel fibres in concrete

is related to several factors, namely the adhesion between the fibres and matrix (bond), the mechanical component provided by the fibre deformations (hooks, crimps, etc.), and friction (Naaman and Najm, 1991).

Bond is an essential parameter when considering the pullout strength of steel fibres and is the primary mechanism affecting the pullout strength of straight smooth steel fibres. The bond shear strength between the fibre and the matrix (τ_{bond}) is directly related to the concrete matrix strength (Aoude, 2007); the higher the strength of the matrix, the higher the bond strength. For a straight smooth steel fibre the pullout strength, $F_{pullout}$ can be obtained using:

$$F_{pullout} = \tau_{bond} \times \pi \times d_f \times \frac{l_f}{2} \qquad [2.2]$$

For straight fibres the pullout stages involve partial and full debonding followed by frictional pullout (see pullout of smooth fibre in Figure 2.2). As discussed previously, hooked-end fibres provide improved performance when compared to straight smooth fibres. After initial debonding, the hook must straighten before the frictional pullout stage, resulting in an improvement in pullout strength.

Naaman and Najm (1991) conducted an experimental program studied the pull-out load (force) vs. end slip (displacement) relationship of smooth and hooked-end fibres. In the case of hooked-end fibres, the ascending portion of the load-slip curve has two parts; linear and non-linear. The slope of the linear portion is similar in magnitude to the slope for smooth fibres, as seen in Figure 2.2. However, the peak load can be in the magnitude of 3-4 times higher, and the slip at the peak load can be in the magnitude of 100 times greater (Naaman and Najm, 1991), demonstrating that the mechanical contribution of the hooks plays a significant role in the pullout behaviour. The study also observed that the mechanical contribution is only developed at large slips, which means the mechanical contribution to the matrix is only available after cracking of the matrix. This implies that the contribution of smooth or deformed fibres to first cracking strength is of the same order of magnitude and that the mechanical contribution of the hook is independent of concrete matrix strength (Naaman and Najm, 1991).

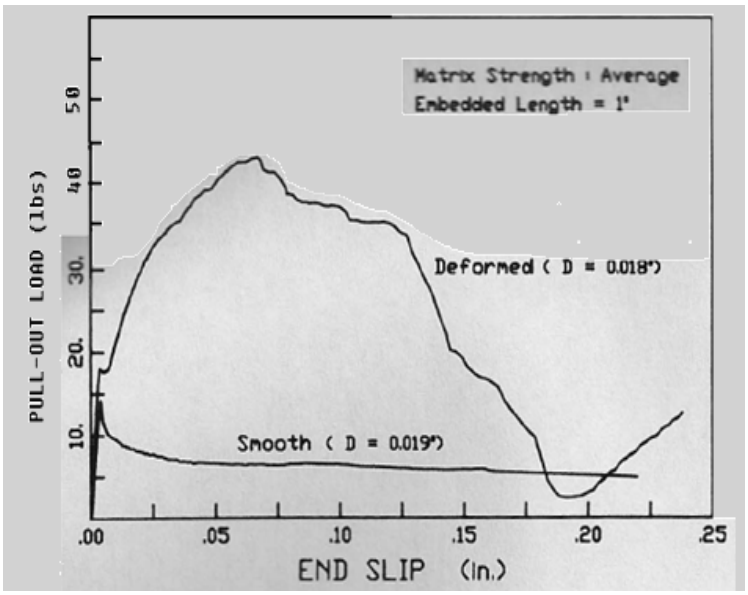

Figure 2.2 Comparison of pullout curves for hooked and smooth fibres

(Naaman and Najm, 1991)

The idealized pullout – end displacement curve for hooked end steel fibres is shown in Figure 2.3; it demonstrates the contribution of the deformed shape on the overall pullout behaviour at various stages in the pullout. After initial debonding, the hook must first straighten in order to slip through the matrix and pullout; this is the mechanical contribution provided by the hooked end (see Figure 2.4).

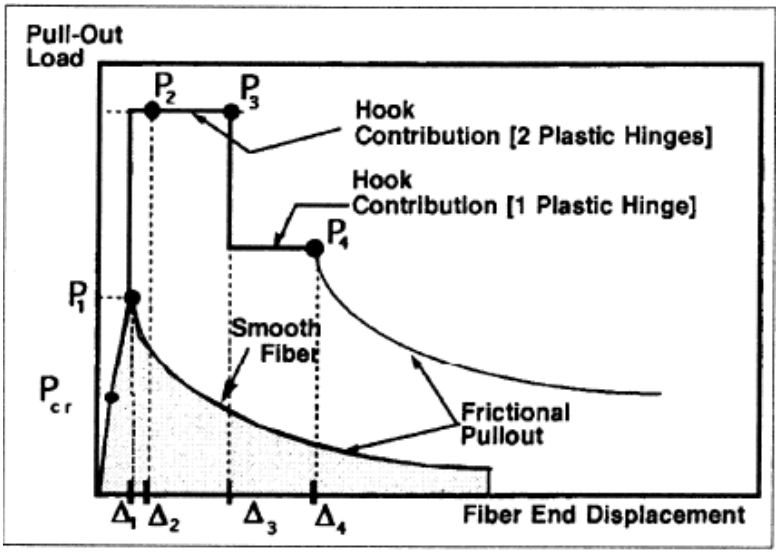

Figure 2.3 Idealized pullout load vs. fibre end displacement for smooth and hooked-end fibres

(Alwan et al., 1991)

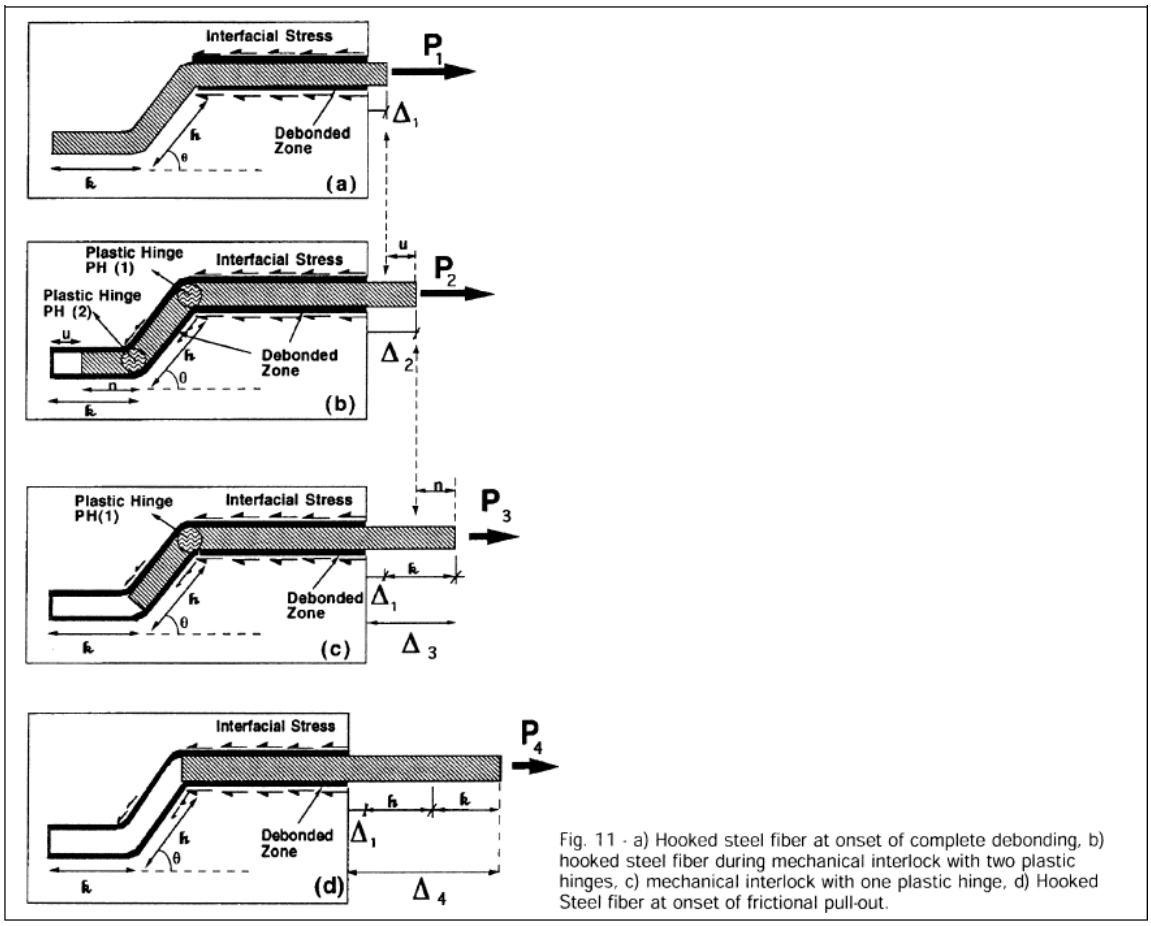

Fig. 11 - a) Hooked steel fiber at onset of complete debonding, b) hooked steel fiber during mechanical interlock with two plastic hinges, c) mechanical interlock with one plastic hinge, d) Hooked Steel fiber at onset of frictional pull-out.

Figure 2.4 Representation of hooked end steel fibre debonding, and of the curve in Figure 2.3

(Alwan et al., 1991)

2.2.2.4 Fibre Orientation Factor

The fibre orientation factor, expressed as the symbol α in the literature, is used to account for the orientation of the fibres crossing any arbitrary cracking plane (Aoude, 2007). Fibres used for concrete reinforcement are randomly oriented within the matrix during the mixing process, and only a certain amount will be effective in bridging the gap across cracks in the concrete. The fibre orientation factor, α, is used to describe the amount of effective fibres in the cracked region.

For fibres that are not limited by boundary conditions (i.e. fibres that can rotate freely about their center of gravity) a value of $\alpha = 0.5$ has been recommended. This value is derived by integrating the fibre pull-out length over all possible orientation angles (see Figure 2.5); for fibres that have one boundary condition, a value of $\alpha = 0.6$, and for fibres with 2 boundary conditions a value of

0.84 has been recommended (Dupont and Vandewalle, 2005). Boundary conditions occur when the fibres are close to the mould and no longer able to rotate freely as a result.

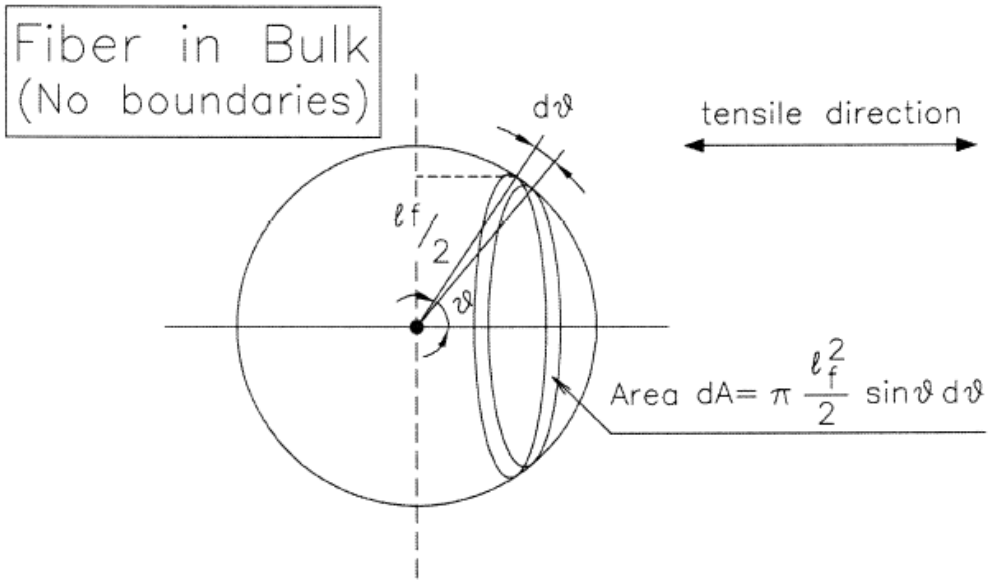

Figure 2.5 Derivation of the Fibre Orientation Factor

(Dupont and Vandewalle, 2005)

2.2.2.5 Effective Number of Fibres

The effective number of fibres per unit area, N_{fibres}, can be described as:

$$N_{fibres} = \frac{V_f}{A_f} \times \alpha \times n_l \qquad [2.3]$$

where A_f is the cross-sectional area of the fibre and n_l is the length factor (Aoude, 2007). The length factor is used to describe varying embedment lengths of fibres across cracks. Fibres will be the most effective if exactly half of its total length is on each side of the gap; however, this is not always the case. Average effectiveness is described as having one quarter of the fibre on one side of the crack. This leads to a length factor of n_l= 0.5 (Aoude, 2007).

2.2.3 Mechanical Properties of SFRC

2.2.3.1 SFRC under Compression

While SFRC has been noted to give only a negligible increase in compressive strength, the addition of steel fibre reinforcement does increase the post-peak behaviour of concrete in compression. Nataraja et al. (1999) tested a series of SFRC cylinders with a goal of developing a stress-strain model for SFRC in compression. Their observations and conclusions include that while the maximum compressive strength is essentially the same between SFRC and regular concrete, the post-peak stress-strain behaviour shows significant improvements with results demonstrating that SFRC has a higher toughness than regular concrete in compression. This finding has also been observed in many other experimental studies in the literature (Li, 2002). When concrete cylinders are subjected to compressive forces to, the sides will expand outward in a direction perpendicular to the applied force, in accordance with Poisson's ratio. The outward expansions induce tensile forces within the sample that would normally cause regular concrete to fail in a brittle manner. The addition of steel fibre reinforcement increases the resistance to these internal forces. Figure 2.6 shows stress-strain curves for a 50MPa concrete reinforced with 30 mm long hooked-end steel fibres at 0%, 1% and 1.5% fibres by volume of concrete from a study conducted by Aoude (2007).

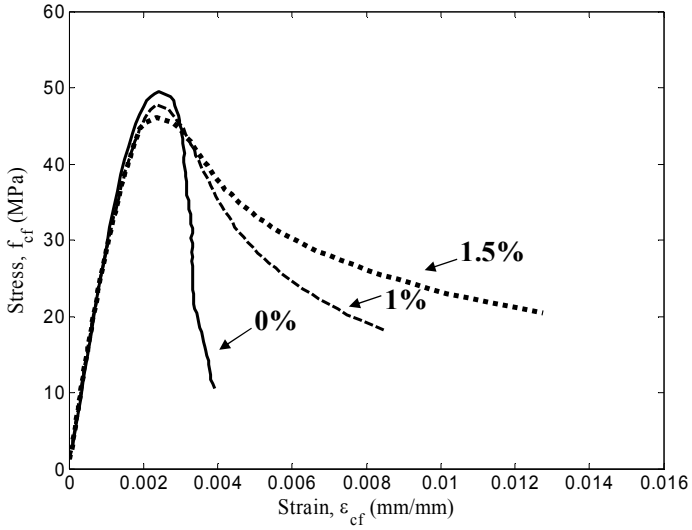

Figure 2.6 Typical stress-strain response of SFRC tested under compression

(Aoude, 2007)

2.2.3.2 SFRC under Tension

Behaviour of concrete is very weak and brittle in tension. The addition of steel fibres transforms this behaviour and allows concrete to carry tensile stresses after cracking and improves post-cracking toughness. The direct tensile strength of SFRC can be experimentally studied using dog-bone shaped specimens. Figure 2.7 shows typical stress-displacement curves of SFRC tested in direct tension. Although increases in peak tensile strength can result, the more important enhancement is in post-cracking strength and ductility.

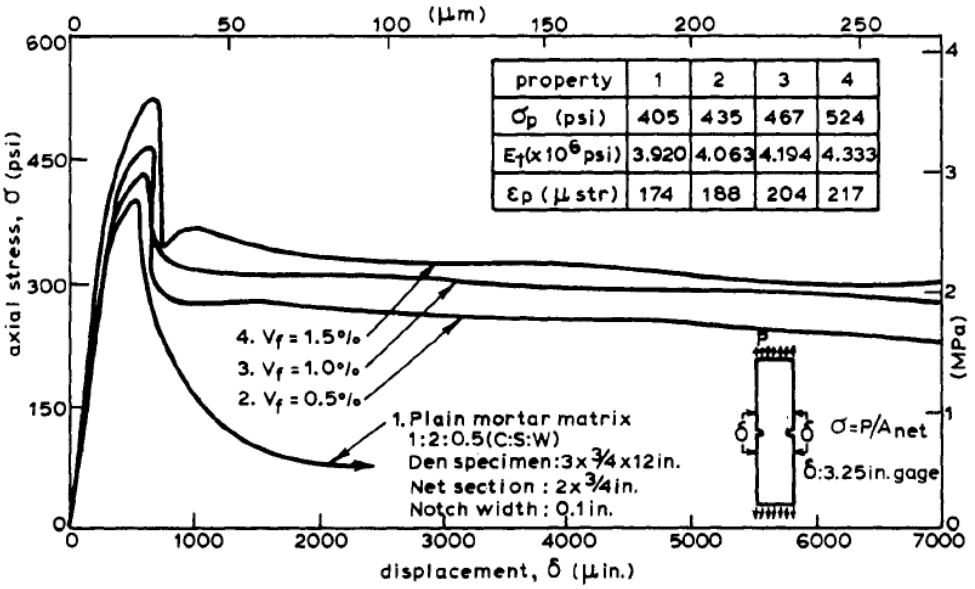

Figure 2.7 Results of stress-displacement curves from direct tension tests

(Lee, 1993)

It is noted that direct tensile tests using dog-bone specimens are difficult to run, can show high scatter in test results and lack standardized testing procedures. As a result, indirect testing methodologies are typically used to quantify the post-cracking properties of SFRC. In North America, the ASTM C1609 flexural toughness test method has been adopted as the standardized test method for SFRC. In this test, four-point loading is applied to a 100 × 100 × 350 mm beam. The load displacement curve is then used to compute various toughness indices to assess the post-cracking properties of SFRC (ASTM, 2010).

2.2.4 Steel Fibres as a Method to Replace Transverse Reinforcement

The potential of using SFRC in structural applications has not yet fully garnered acceptance for load carrying elements. One of the main reasons returns to the lack of reliable prediction models and the lack of detailed design guidelines for engineers. Other reasons include the high initial cost of SFRC and the conservative nature of the construction industry (Li, 2002). This is why the most common application for SFRC is currently as a surfacing material to assist in crack control. Despite this fact, several researchers have discussed the ability of SFRC to replace traditional transverse steel reinforcement in beams and columns.

2.2.4.1 Ability of Steel Fibres to Replace Transverse (Shear) Reinforcement in Beams

The addition of steel fibres results in enhancements in diagonal tension capacity and post-cracking resistance of concrete, which in turn improves shear and flexural capacity. Extensive research over the past three decades has shown that the use of SFRC in beams results in improvements in shear capacity and overall ductility. As an example consider the results of a series of tests was performed by Colajanni et al. (2008) that compared the behaviour of plain concrete and SFRC beams under flexure. Three types of beams were produced as the basis of the comparison: regular concrete beams without stirrups, SFRC beams without stirrups, and SFRC beams with stirrups. The SFRC was mixed with hooked end steel fibres with a volume of steel fibres of 1% (V_f=1%). All beams had flexural reinforcement in the form of 2-20M longitudinal bars. The test results, as seen in Figure 2.8, showed that for all SFRC specimens the presence of fibres increases the shear capacity when compared to the control specimens made of plain concrete. In the case of these tests, when diagonal tension shear was the failure mode, SFRC specimens had a maximum load of 158% higher than that of regular concrete, and when the failure mode was shear-compression failure, the SFRC specimens had a maximum load 96% higher. The experiments also showed that the combined use of SFRC and stirrups resulted in ductile flexural response (Colajanni et al., 2008). It should be noted that research has also shown that the use of steel fibres can promote flexural failure and ductility in beams constructed without stirrups. Therefore, if added in sufficient quantity, the inclusion of fibres can replace traditional transverse reinforcement in beams (Parra-Montesinos, 2006).

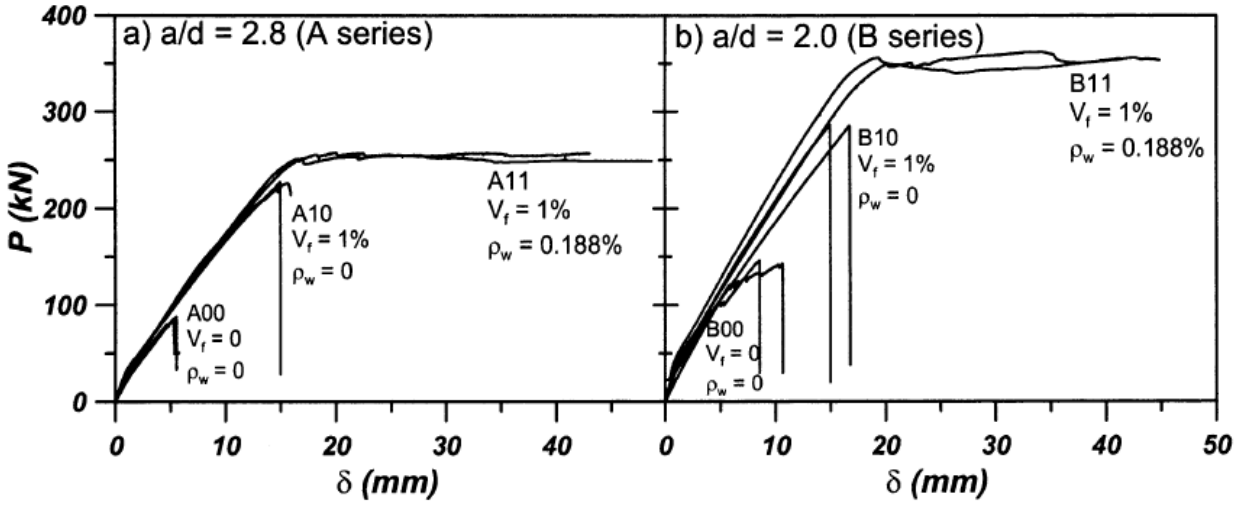

Figure 2.8 Load vs Displacement curves for SFRC beams under flexure loads

(Colajanni et al. 2008)

2.2.4.2 Ability of Steel Fibres to Replace Transverse Reinforcement in Columns

Aoude et al. (2009) tested concrete columns under pure axial load with varying amounts of hooked-end steel fibres ($0\% \leq V_f \leq 1.5\%$), and with different confinement details, with spacing of the hoops varying from 240mm to 65mm (see Figure 2.9). The results demonstrated that the addition of 1% by volume (V_f =1%) of steel fibres in a column with minimum confinement reinforcement resulted in a column that had a level of performance that surpassed a specimen with double the amount of hoops (s=240mm vs. s=120mm), as can be seen in Figure 2.10. In addition to this, the SFRC specimens showed higher peak loads and improved post-peak response (Aoude et al. 2009).

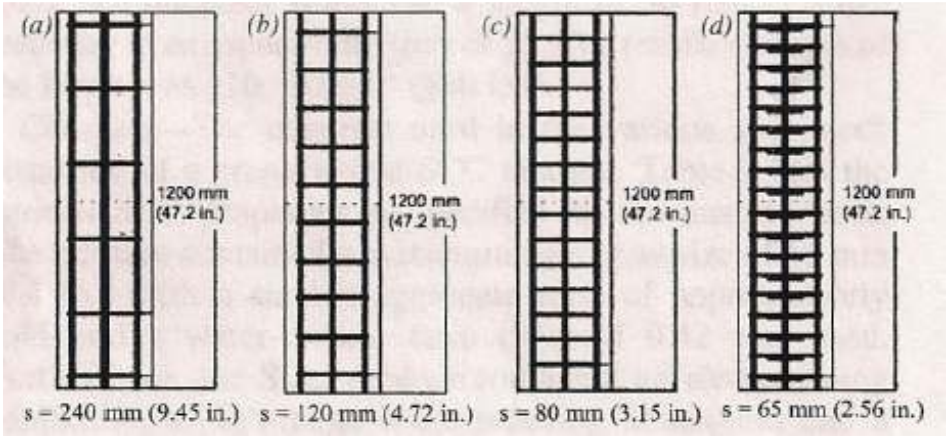

Figure 2.9 Column confinement details in test series of Aoude et al. (2009)

(Aoude et al. 2009)

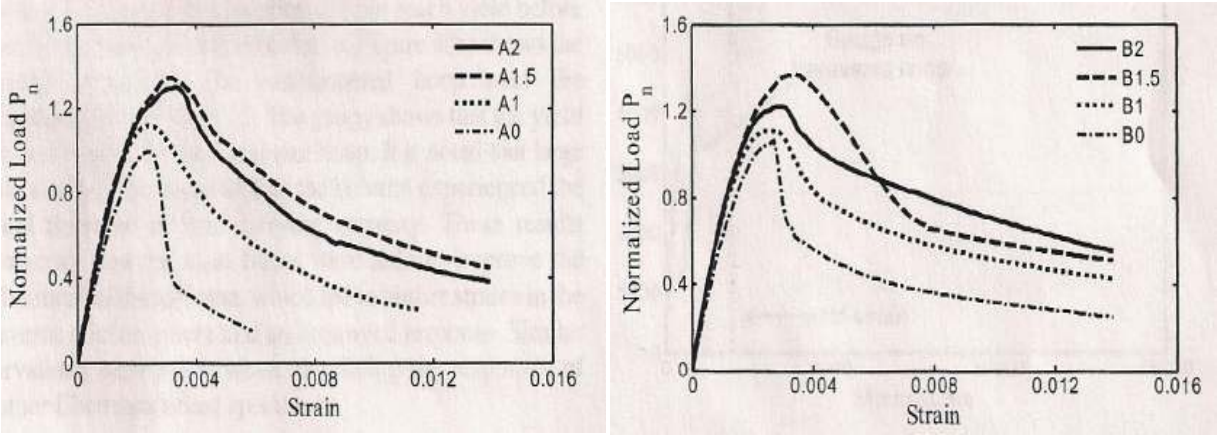

Figure 2.10 Normalized load vs. Strain of SFRC columns *.

(Aoude et al. 2009)

**The figure on the left represent the results of the axially loaded column in Figure 2.9 (a), and the figure on the right from Figure 2.9 (b). The numbers represent the amount of fibres by volume (example: B2 is B-series column with Vf=2%)*

Consequently, the use of SFRC in structural elements such as columns and beams can permit a reduction in the amount of transverse reinforcement. This would lead to improved constructability (Aoude et al. 2009), especially in high seismic risk regions where very closely spaced transverse reinforcement is required to resist seismic loading. Although the use of SFRC may result in increased material costs, the reduction of transverse reinforcing steel and improvements in constructability can potentially reduce overall construction costs.

2.2.5 Combined Use of SCC and Steel Fibres

The addition of steel fibres to a traditional concrete mix reduces workability and can cause problems during placement, particularly at higher fibre contents. One innovative solution to this problem lies in the combined use of self-consolidating concrete (SCC) and steel fibres. SCC is a highly flowable, non-segregating concrete that can be spread into place under its own weight. These properties are achieved by limiting coarse aggregate size, specifying higher fine-to-coarse aggregate ratios and using mineral and chemical admixtures (fly ash, super-plasticizers and viscosity modifying agents) (Liao et al., 2006). It should be noted that even in the case of SCC, the addition of fibres improves performance only within a limited range of fibre properties and volume fractions, with researchers demonstrating that higher aspect ratios and volume fractions can result in reduced flowability and the eventual loss of self-consolidating properties (Grunewald, 2004).

2.2.6 Ultra High Performance Fibre Reinforced Concrete (UHPFRC)

Ultra high performance fibre reinforced concretes (UHPFRC) are a new and innovative class of concrete material. When compared to traditional SFRC, they exhibit superior properties such as increased strength, durability, and long term stability; hence the name *Ultra-High Performance*. The formulation of the material includes Portland cement, silica fume, quartz flour, fine silica sand, high range water reducer, water, and steel fibres. It is noted that UHPFRC are also differentiated from tradition SFRC due to the fact that they contain no coarse aggregate. Of the granular materials, the fine sand has the largest particle size, which is generally between 150-600 μm. The silica fume has a small enough diameter to fill the interstitial voids between the cement and crushed quartz particles. These small particle sizes of the granular materials lead to an excellent interface between the paste and the steel fibres, which give UHPFRC its increased properties. Due to the use of the high range water reducer and optimized granular packing, UHPFRC have very low *w/c* ratios and still have sufficient workability (Graybeal, 2006). In addition, UHPFRC have been documented to have compressive strengths of up to 230 MPa and flexural strengths of up to 50 MPa (Perry, 2010). Examples of concretes in this class are Compact Reinforced Composite (CRC), produced by *CRC Technology*, Denmark, or Reactive Powder Concrete (RPC) that has been patented by *Lafarge Cement* and is available on the market as a product known as *Ductal*.

2.2.6.1 Compact Reinforced Composite (CRC)

2.2.6.1.1 General

CRC is a proprietary UHPFRC developed in 1986 at the Cement & Concrete Laboratory of Aalborg Portland, Denmark in 1986 (Aarup, 2004). CRC combines very high compressive strengths, between 150-400MPa, and some ductility since the matrix combines large contents of steel fibres, usually between 2-6%. The high compressive strengths are achieved using a very large amount of microsilica, and water/binder ratios of 0.16 or lower. Due to the large amount of steel fibres, elements constructed of CRC are ductile when compared to high strength concretes. Due to the high performance of CRC, the material was designed for applications in heavily loaded structures such as long span bridges, columns in high-rise structures, or structures exposed to seismic loads (Aarup, 2004). However, most current applications for the material include staircases and balcony slabs. It is expected that high performance of CRC in

compression and tension when compared to typical concrete and SFRC, will make it an ideal material for use in the blast resistant design of structures.

2.2.6.1.2 Behaviour of CRC in Tension

In his PhD thesis, Nielsen (1995) tested samples of CRC under unaxial tension. The findings are derived from force–crack width opening data obtained from notched specimens. The samples were constructed of CRC with varying fibre contents and types, using a square cross-section of 50 mm × 50 mm, and having a height of 55 mm. Three different types of fibres were used including OL12/.40, OL 6/.15 high carbon, and OL 13/.15 high carbon (the nomenclature indicates the aspect ratio, l_f/d_f of the fibres). All fibres were smooth and straight. In addition, the amounts of each fibre type was varied, using mixes of 0%, 3%, 6%, and 9% steel fibres by volume. Figure 2.11 shows the results from the stress-crack width opening tests on the specimens; note that the stress is normalized by the cracking stress of the matrix, thus all figures start at (0,1). The authors note that after the deformations localize in the notched cross-section, the material cracks followed by a strain hardening phenomenon. A first peak is observed, and interpreted as initial cracking of the matrix, defined by the cracking stress of approximately 7 MPa regardless of fibre type and amounts. A subsequent peak is then termed the post-cracking stress and is attributed to the steel fibres bridging the crack. The peak post-cracking strength and strain is dependent on fibre type, and more significantly, the volume of fibres in the matrix.

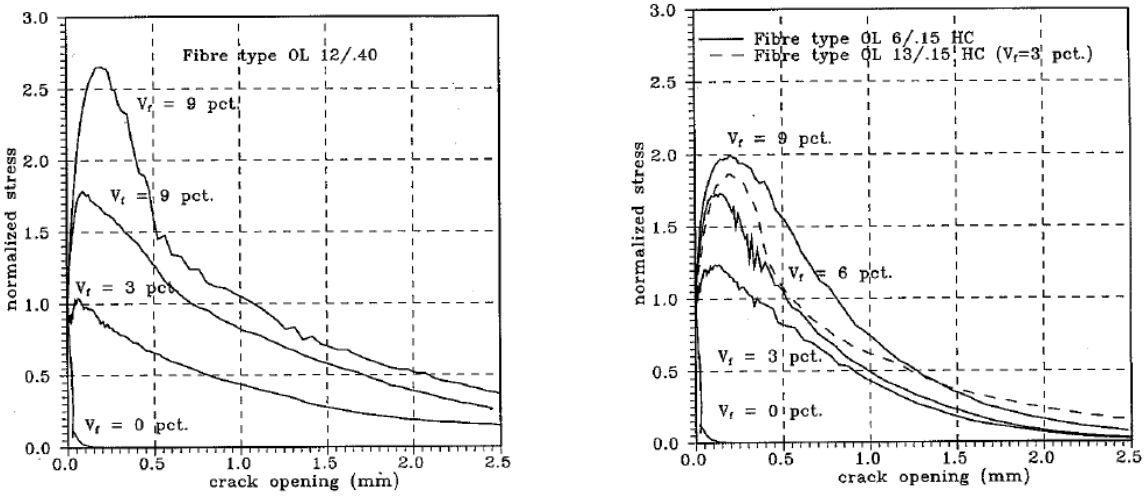

Figure 2.11 Normalized Stress vs. crack opening diagram for uniaxial tension

(Nielsen, 1995)

Bindiganavile et al. (2002) report similar findings for quasi-static testing of CRC. Splitting tensile tests carried out on 50mm diameter cylinders yielded values of 20MPa, which is exceptionally good considering that typical concrete has compressive strengths in the range of 20-40MPa, and are considered to have no tensile capacity.

2.2.6.2 Behaviour of CRC in Compression

Nielsen (1995) also completed a series of uniaxial compression tests on 45 mm diameter by 90 mm in height cylinders. The size of the cylinders was selected due to the limitations of the testing machine, and the high compressive strength of CRC. Once again, Nielsen (1995) tested various batches of CRC using various types and amounts of steel fibres. All fibres were smooth and straight, and similarly to the tension tests, included OL 12/0.40, OL 6/.15 high carbon, and OL 13/015 high carbon fibres and varying fibre contents (0%, 3%, 6%, and 9% by volume). The typical results of these tests are shown in Figure 2.12.

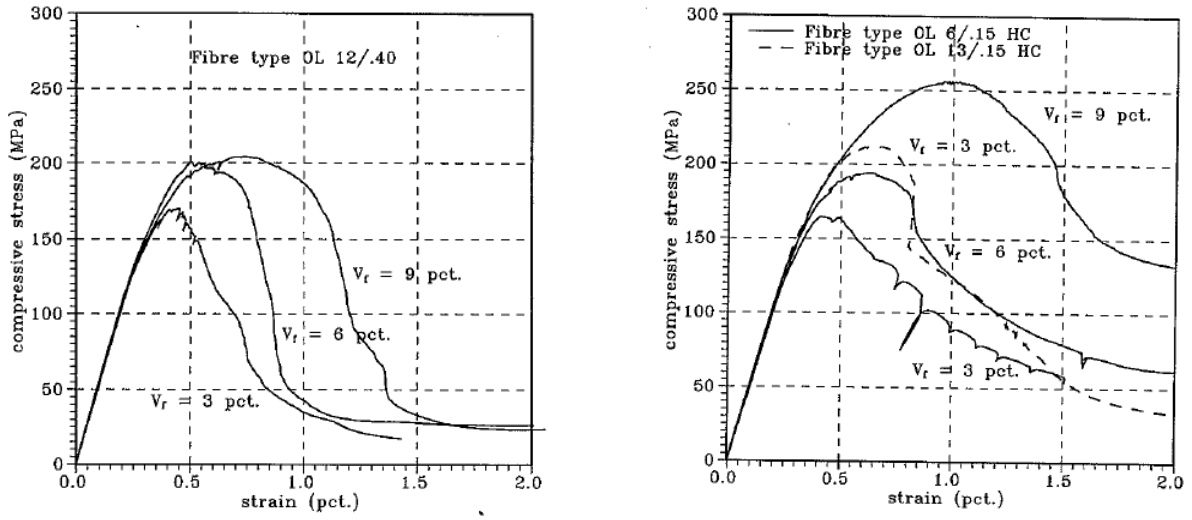

Figure 2.12 Typical Stress-strain curves of CRC under uniaxial compression

(Nielsen, 1995)

The results of this test show that regardless of fibre content and type, all samples have the same initial modulus of elasticity. However, the peaks of the curves are highly influenced by the amount of fibres: not only is the peak strength greater with higher amounts of fibre, but the corresponding strain is greater as well. The differences has a greater influence on the slope of the descending branch of the curves, the smaller aspect ratio fibre (OL 12/.40) descends with a steeper slope than the other two types (Nielsen, 1995).

2.3 Blast Loading and Structural Response

2.3.1 Explosions at Atmospheric Pressure

An explosion, in essence, is defined as a sudden release of energy (Ngo et al., 2007). Explosions can be categorized as physical, nuclear, or chemical. Examples of physical explosions include the energy released from the puncture of a compressed gas cylinder. Nuclear explosions involve the rapid release of energy due to a high speed nuclear reaction, the formation of different atomic particles by the redistribution of protons and neutrons within the interacting nuclei. Chemical explosions involve the rapid oxidation of mainly carbon and hydrogen atoms. Most conventional explosions are categorized as chemical from sources such as TNT or military munitions (Ngo et al., 2007). When an explosive detonates, the resulting explosion is essentially the rapid expansion of hot gases. The term detonation refers to a very rapid and stable chemical reaction produced within the explosive. Figure 2.13 (a) shows the effects of explosion immediately after detonation of a nuclear device. Figure 2.13 (b) shows the same detonation, but is used to highlight the different phenomena associated with explosions.

(a) 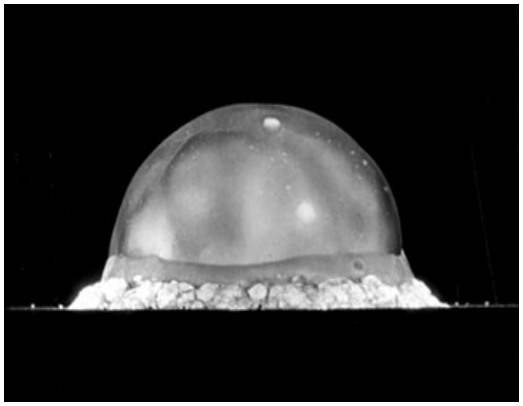 (b) 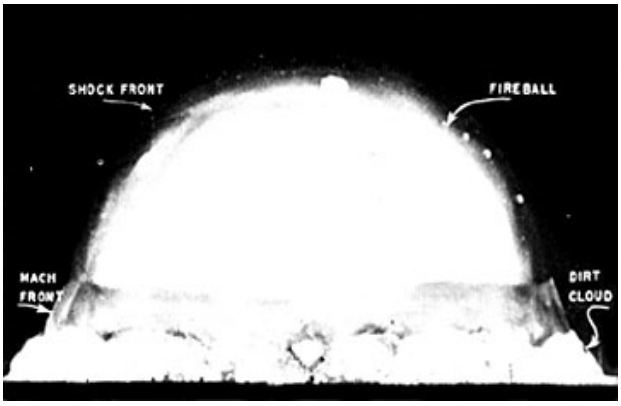

Figure 2.13 (a) Detonation of a nuclear device and (b) phenomena associated with explosions (right).

(Glasstone, 1962)

While the figure shows a nuclear explosion, the same phenomena occur within conventional explosions, just at a much smaller scale. The effects are a fireball, projectiles (known as fragmentation), and shock front (also termed blast wave).

2.3.2 Blast Wave

During an explosion, the formation of hot, high pressure gases results in a shock wave which propagates outwards from the centre of detonation at a velocity greater than the speed of sound.

The spherical blast wave produces an almost instantaneous increase in blast pressure above ambient pressure followed by an exponentially decreasing pressure as the wave travels away from the point of detonation. For explosions that occur outside a structure, it is this blast wave that has the most significant impact, as opposed to the fireball or impacts from small projectiles (Lloyd, 2010).

2.3.3 Analytical Prediction of Blast Wave Parameters

2.3.3.1 TNT Equivalency

The majority of blast data presented in the literature is expressed as the output of very common explosive trinitrotoluene (TNT). These data can then be related to other explosives by converting the explosive in question to an equivalent mass of TNT. For blast resistant design, the effects of energy output of an explosive material relative to that of TNT can be expressed as a function of the heat of detonation, as shown in Equation 2.4 (UFC-3-340-02, 2008). The TNT equivalence of a given explosive is expressed as:

$$W_E = \frac{H_{EXP}^d}{H_{TNT}^d} W_{EXP} \qquad [2.4]$$

where W_E is the effective (equivalent) charge weight (or mass), W_{EXP} is the weight (or mass) of the explosive charge, H_{EXP}^d is the heat of detonation of explosive in question and H_{TNT}^d is the heat of detonation of TNT.

The free-air equivalent weight of a particular explosive is the weight of the standard explosive (TNT) required to produce a selected shock wave parameter of magnitude equal to that produced by a unit weight of the explosive in question. TNT equivalencies for standard explosives are shown in Table 2.1 (DAHS, 2002).

Table 2.1 Equivalent TNT masses for Airblast in free-air (DAHS, 2002)

Explosive	Density Mg/m3	Equivalent Mass for Pressure	Equivalent Mass for Impulse	Pressure Range MPa
Amatol (50/50)	1.59	0.97	0.87	NA1
Ammonia Dynamite (50 percent Strength)	NA1	0.90	0.902	NA1
Ammonia Dynamite (20 percent Strength)	NA1	0.70	0.702	NA1
ANFO (94/6 Ammonium Nitrate/Fuel Oil)	NA1	0.87	0.872	0.03 to 6.90
AFX-644	1.75	0.732	0.732	NA1
AFX-920	1.59	1.012	1.012	NA1
AFX-931	1.61	1.042	1.042	NA1
Composition A-3	1.65	1.09	1.07	0.03 to 0.35
Composition B	1.65	1.11 1.20	0.98 1.30	0.03 to 0.35 0.69 to 6.90
Composition C-3	1.60	1.05	1.09	NA1
Composition C-4	1.59	1.20 1.37	1.19 1.19	0.07 to 1.38 1.38 to 20.70
PETN	1.77	1.27	1.272	0.03 to 0.69
Picrotol (52/48 Ex D/TNT)	1.63	0.90	0.93	0.03 to 4.10
RDX	NA1	1.10	1.102	NA1
RDX/Wax (98/2)	1.92	1.16	1.162	NA1
RDX/AL/Wax (74/21/5)	NA1	1.30	1.302	NA1
TATB	NA1	1.00	1.002	NA1
Tetryl	1.73	1.07	1.072	0.02 to 0.14
Tetrytol (75/25 Tetryl/TNT)	1.59	1.06	1.062	NA1
TNETB	1.69	1.13	0.96	0.03 to 0.69
TNETB/AL (90/10) (78/22) (65/35)	1.75 1.18 1.23	1.23 1.32 1.38	1.11 1.322 1.382	0.03 to 0.69 NA1 NA1
TNT	1.63	1.00	1.00	Standard
Torpex	1.85	1.23	1.28	0.01 to 0.30
Tritonal (80/20 TNT/AL)	1.72	1.07	0.96	0.03 to 0.69

1NA - Data not available. 2Value is estimated.

2.3.3.2 Blast Wave Scaling Laws

Scaling the properties of blast waves is an important tool for the analytical determination of their parameters. The scaling laws are used to predict the properties of blast waves of various sized explosions based on tests at a much smaller scale. The most common blast scaling law is known as the *Hopkinson-Cranz* or *cube-root* scaling. This law was first formulated by Hopkinson in 1915, and then independently by Cranz in 1926. The law states that "self-similar blast waves are produced at identical scaled distances when two explosive charges of similar geometry and of the same explosive, but of different sizes, are detonated in the same atmosphere" (Baker et al., 1983).

If the same overpressure is to be produced by two charges of different mass, W_1 and W_2, then in accordance with the Hopkinson-Cranz scaling law it can be shown that:

$$\frac{R_1}{R_2} = \left(\frac{W_1}{W_2}\right)^{1/3} \qquad [2.5]$$

where R_1 is the range at which an overpressure is produced by the charge of mass W_1, and R_2 is the range at which an overpressure is produced by the charge of mass W_2. This scaling law leads to the specification of the scaled distance, z:

$$z = \frac{R}{\sqrt[3]{W}} \qquad [2.6]$$

where R is the standoff distance, or distance between the centre of the charge and the point of a given blast wave parameter, and W is the charge mass.

2.3.3.3 Blast Wave Parameters

The primary parameters used to define blast loading are the blast overpressure, duration and impulse. For an observer at any point away from the initial detonation, the pressure-time history of the blast wave can be characterised by the chart in Figure 2.14. After detonation, the blast wave almost instantaneously increases ambient pressure (this increase in pressure is termed the side-on pressure). In accordance with Figure 2.14, the shock front arrives at a given location at

the Time of Arrival (t_a), and the ambient pressure is increased to the side-on blast pressure (P_{so}). This pressure then decays over time and returns to ambient pressure; this is known as the positive phase duration (t_d). Meanwhile, a negative suction phase follows as the atmospheric pressure is trying to return to the area of the detonation. The negative pressure which results is termed the negative phase of amplitude P_s^-. In terms of structural design, this phenomenon will lead to a reversal of the loading direction. The negative phase generally has a longer duration than the positive phase, and is known as the negative phase duration (t_d^-). An important blast parameter is the blast wave impulse, which is the area underneath the Pressure-Time history curve for either the positive (I) or negative phase (I^-).

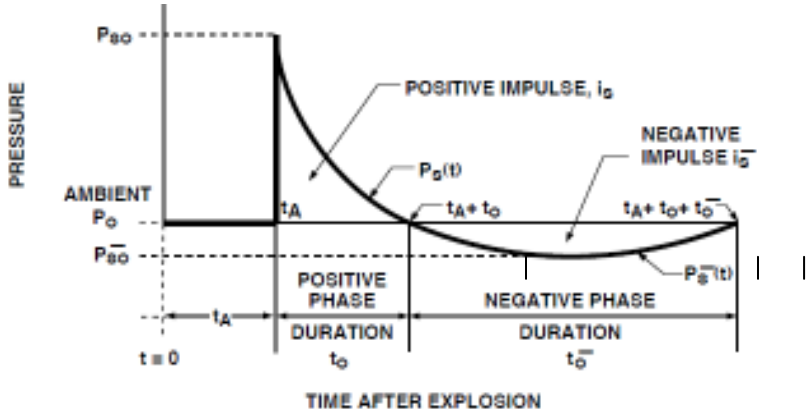

Figure 2.14 Idealized pressure-time history of a shock wave

(DAHS, 2002)

2.3.3.4 Blast Wave Pressure Profiles

The pressure-time history as shown in Figure 2.14 is typically described as an exponential function known as the Friedlander equation and is expressed in the form:

$$P(t) = P_{so}\left(1 - \frac{t}{t_d}\right)e^{\frac{b \cdot t}{t_d}} \qquad [2.7]$$

where b is the waveform parameter (decay constant), which is a function of the peak overpressure, P_{so} and scaled distance, z. As the impulse of the blast wave is defined as the area under the pressure-time history, it can be described as:

$$I = \int_{t_a}^{t_a+t_d} \left(P_{so}(t)\right)dt \qquad [2.8]$$

2.3.4 Categories of Blast loads on Structures

Blast loads on structures are caused by the overpressures of the shock waves, and are divided in to two main categories based on the location of the explosive in relation to the structure: confined explosions, which generally occur when the explosive is contained within a structure, and unconfined explosions that occur when the explosive is outside the structure. These two main categories can then be sub-divided into further sub-categories based on how the blast wave strikes, or is affected by the structural member(s), as shown in the Figure 2.15.

2.3.4.1 Confined Explosions

Confined explosions generally occur within structures or other types of containment vessels, examples include gas explosions within homes or apartment buildings, or terrorist attacks where the bomber is able to detonate a device within a structure. For structural analysis, these are sub-divided in to three major categories: fully vented explosions, partially confined explosions, and fully confined explosions.

2.3.4.2 Unconfined Explosions

Unconfined explosions are generally explosions that occur in an open environment. They are sub-divided in to three major categories: free air burst explosions, air burst explosions, and surface burst explosions.

Free air burst explosions occur in free air, well above the surface of the earth and are generally produced by military air-to-surface or air-to air munitions. They result in a spherical shock wave that propagates equally in all directions away from the center of detonation, striking the structure without any intermediate amplification due to superposition of waves (UFC-3-340-02, 2008). Air burst explosions occur when the centre of detonation of the blast wave is located at a distance above the ground such that reflections of the blast wave occur with the ground prior to the wave impinging the structure (UFC 3-340-02, 2008). Surface burst explosions occur when the center of detonation is located on or very close to the ground surface. This results in a hemispherical blast wave that is immediately amplified due to the initial reflections with the ground, which cause superposition of the blast waves (UFC 3-340-02, 2008).

Explosions that occur extremely close to a structure impose a highly impulsive, high intensity pressure load over a localized region of the structure, while increasing the standoff distance produces a lower-intensity longer duration uniform pressure distribution over the entire structure (Ngo et al. 2007). The former are termed “close-in explosions” while the latter are termed “far-field explosions” (Braimah, 2010). The remainder of this thesis will focus on far-field blast loading as shock tube induced loads create a uniform overpressure across the entire surface of the tested column.

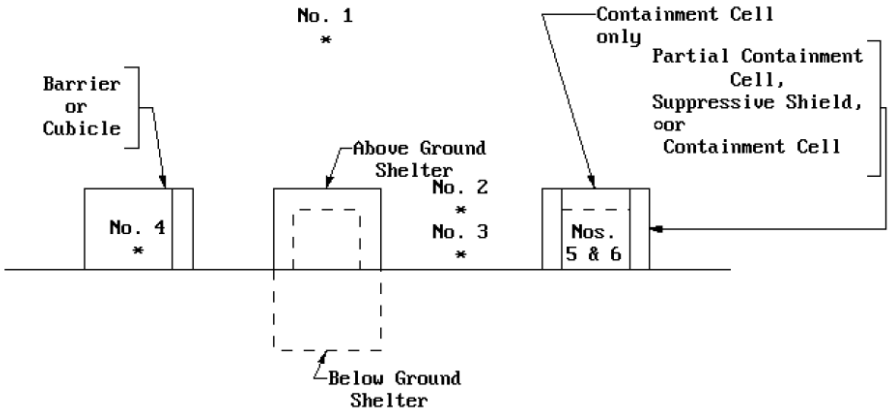

BLAST LOADING CATEGORIES			
CHARGE CONFINEMENT	CATEGORY	PRESSURE LOADS	PROTECTIVE STRUCTURE
Unconfined Explosions	1. Free Air Burst 2. Air Burst 3. Surface Burst	a. Unreflected b. Reflected b. Reflected	Shelter
Confined Explosions	4. Fully Vented	c. Internal Shock d. Leakage	Cubicle
	5. Partially Confined	c. Internal Shock e. Internal Gas d. Leakage	Partial Containment Cell or Suppressive Shield
	6. Fully Confined	c. Internal Shock e. Internal Gas	Full Containment Cell

Figure 2.15 Blast loading categories

*The * denotes the location of centre of detonation.*

(UFC-3-340-02, 2008)

2.3.5 Reflection of Blast Waves & Front Face Blast Loading of Structures

Considering the blast wave generated by the explosive impinging the structure in Figure 2.16, and considering the idealized curve shown in Figure 2.14, a blast wave will impact the front face of the structure at the time of arrival, t_a. The blast wave is instantaneously reflected. This causes the forward moving air molecules of the blast wave to be held against the surface, and further compressed, which induces a reflected overpressure on the face of the structure. This reflected blast overpressure, P_r, is of higher magnitude than the incident overpressure. Reflected overpressures only occur on the front face of structures (facing direction of blast), as the wave is unable to immediately diffract around the edges of the structure. Consequently reflected overpressures are of a greater magnitude than the side-on pressures for equivalent charge masses and standoff distances (Braimah, 2010). The peak reflected pressure can be derived from the peak static overpressure and ambient pressure as:

$$P_r = 2P_s\left[\frac{7p_0+4P_{so}}{7p_0+P_{so}}\right] \qquad [2.9]$$

where P_r is the peak reflected blast overpressure; P_{so} is the peak incident overpressure; and p_0 is pressure at ambient. The peak reflected blast overpressure then decays to the stagnation pressure (P_{stag}) as a rarefaction wave sweeps across the front face from the edges towards the centre.

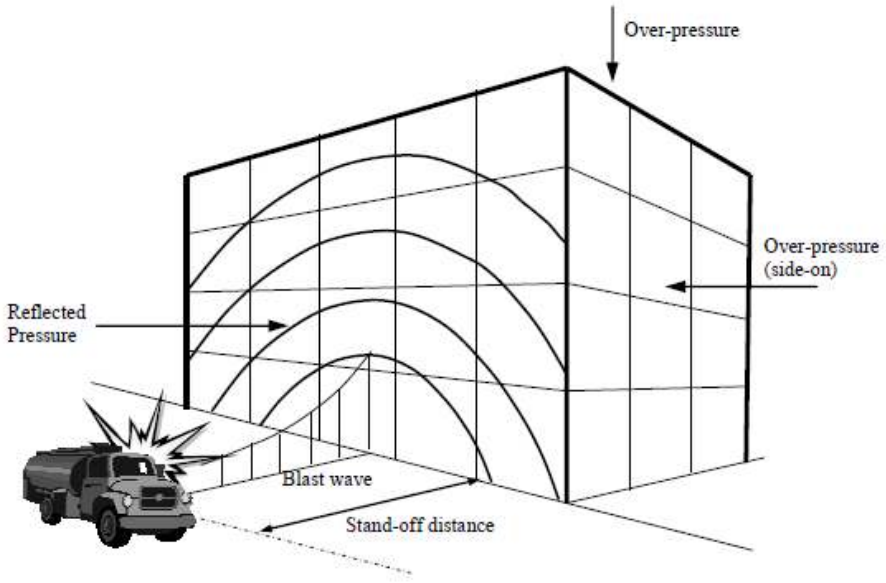

Figure 2.16 Blast loads on Structures

(Ngo et al,. 2007)

2.3.6 Single Degree of Freedom (SDOF) System Approach

The Single Degree of Freedom (SDOF) system approach, as proposed by Biggs (1964) is the most widely accepted method of the analysis of structural response to blast loads, and is used in most texts on the subject (Baker et al. 1983, Kinney and Graham, 1985, Smith and Hetherington 1994, Ngo et al. 2007, UFC 3-340-02). The approach is detailed in the sections that follow.

2.3.6.1 Equivalent SDOF system

In the equivalent SDOF approach, the structure is idealized by an equivalent system of a concentrated mass attached to a massless spring, as shown in Figure 2.17, representing the resistance of the structure against deformation.

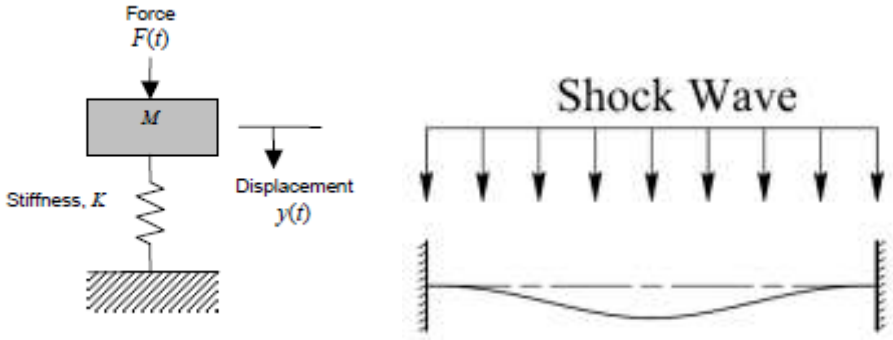

Figure 2.17 An idealised SDOF system (left) with a representation of the actual member (right)

(Lloyd, 2010)

The equation of motion for an object with mass *m,* stiffness *k,* which is loaded under the effect of external function *F(t)* is expressed in Equation 2.10, where $\ddot{u}(t)$ is acceleration and $u(t)$ is displacement of the object at time t:

$$m\ddot{u}(t) + ku(t) = F(t) \qquad [2.10]$$

It is noted that the damping coefficient is normally ignored as it has little effect on the equation of motion during the first cycle up to maximum displacement (UFC 03-340-02, 2008; Lloyd, 2010).

To simplify analysis, the first positive phase of the blast load profile can be idealized as a triangular pulse load with the same peak pressure and same impulse as that of the exponential

positive phase of the shock-wave. An example of the simplified, idealized triangular load of the positive phase of a shock wave used for design of structural members can be seen in Figure 2.18.

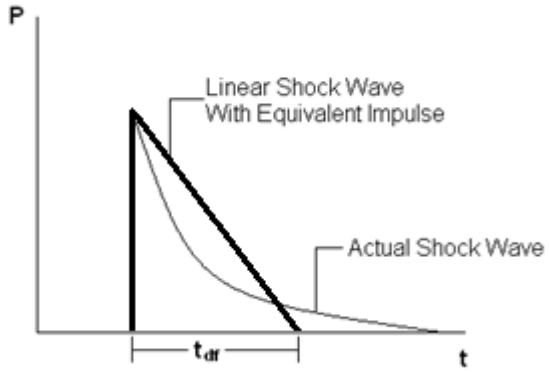

Figure 2.18 Triangular Blast Load

Consequently a fictitious duration of the blast-wave is calculated as:

$$t_{df} = \frac{2I}{P_r} \qquad [2.11]$$

where t_{df} is the fictitious duration, I is the impulse of the blast wave, and P_r is the peak overpressure of the blast wave. The resulting idealized pressure time-history $P_r(t)$ is defined as:

$$P_r(t) = P_r\left(1 - \frac{t}{t_{df}}\right) \qquad [2.12]$$

Replacing the right side of Equation 2.12 with $AP_r(t)$, where A is the area exposed to blast loading and $P_r(t)$ is the time variant forcing function, results in the following second order differential equation:

$$m\ddot{u}(t) + ku(t) = AP_r\left(1 - \frac{t}{t_d}\right) \qquad [2.13]$$

Using the above dynamic equation of motion, for an elastic member it can be shown that the displacement at any time during the forced vibration phase ($0 \leq t \leq t_d$) has the following general closed-form solution (Biggs, 1964):

$$u(t) = \frac{AP_r}{k}(1 - \cos \omega t) + \frac{AP_r}{kt_d}\left(\frac{\sin \omega t}{\omega} - t\right) \quad [2.14]$$

where ω is the natural frequency of vibration of the equivalent SDOF, and T is the natural period of the structure, expressed as:

$$\omega = \frac{2\pi}{T} = \sqrt{\frac{k}{m}} \quad [2.15]$$

2.3.6.2 Modelling Structures as Equivalent SDOF systems

The most prevalent method for the analysis of structures subjected to blast loading is the Biggs (1964) method of the equivalent SDOF. In this method, member properties of mass, stiffness, and loading are converted using deformed shape factors. When the properties are multiplied by their corresponding transformation factors, the parameters of the equivalent SDOF system are obtained. In accordance with Biggs (1964), the equivalent mass is given by

$$M = \int_0^L \bar{m}\varphi^2(x)dx \quad [2.16]$$

where M is the equivalent mass; $\bar{m}$ is the mass per unit length; and $\varphi^2(x)$ is the assumed shape function. The mass factor (K_m) then becomes the ratio of equivalent mass to the actual total mass of the structural element:

$$K_m = \frac{M}{mass\ of\ column} \quad [2.17]$$

Similarly, for a structure with concentrated forces of for distributed loads, the equivalent force on the idealized system is given by:

$$F = \int_0^L F(t)\varphi(x)dx \qquad [2.18]$$

where $F(t)$ is the loading function on the system. The load factor is defined as the ratio of equivalent force to the actual total force:

$$K_L = \frac{F_e}{F(t)} \qquad [2.19]$$

It is convenient to define a single load mass factor, K_{LM}, as the ratio of the mass factor to the load factor:

$$K_{LM} = \frac{K_M}{K_L} \qquad [2.20]$$

Biggs (1964) developed a table of transformation factors that are commonly used for the analysis of structural members subjected to blast loads, as shown in Table 2.2. The equivalent SDOF equation of motion incorporating K_{LM} is shown in Equation 2.21.

$$K_{LM}m\ddot{u}(t) + ku(t) = AP_r(t) \qquad [2.21]$$

Replacing the spring force, $ku(t)$ with a non-linear resistance term, $R(u)$ the following non-linear SDOF equation of motion is obtained:

$$K_{LM}m\ddot{u}(t) + R(u) = AP_r(t) \qquad [2.22]$$

Table 2.2 Load and Mass Transformation Factors (UFC-3-340-02, 2008)

Edge Conditions and Loading Diagrams	Range of Behavior	Load Factor K_L	Mass Factor K_M	Load-Mass Factor K_{LM}
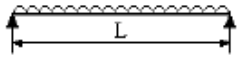	Elastic	0.64	0.50	0.78
	Plastic	0.50	0.33	0.66
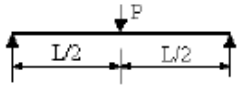	Elastic	1.0	0.49	0.49
	Plastic	1.0	0.33	0.33
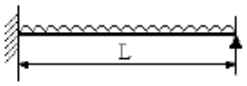	Elastic	0.58	0.45	0.78
	Elasto-Plastic	0.64	0.50	0.78
	Plastic	0.50	0.33	0.66
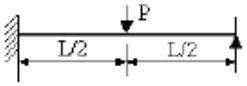	Elastic	1.0	0.43	0.43
	Elasto-Plastic	1.0	0.49	0.49
	Plastic	1.0	0.33	0.33
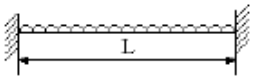	Elastic	0.53	0.41	0.77
	Elasto-Plastic	0.64	0.50	0.78
	Plastic	0.50	0.33	0.66
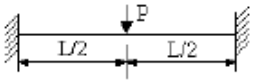	Elastic	1.0	0.37	0.37
	Plastic	1.0	0.33	0.33
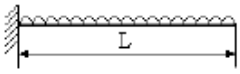	Elastic	0.40	0.26	0.65
	Plastic	0.50	0.33	0.66
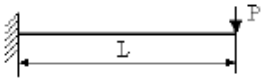	Elastic	1.0	0.24	0.24
	Plastic	1.0	0.33	0.33
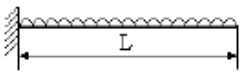	Elastic	0.40	0.26	0.65
	Plastic	0.50	0.33	0.66
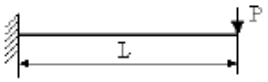	Elastic	1.0	0.24	0.24
	Plastic	1.0	0.33	0.33
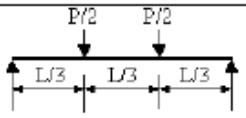	Elastic	0.87	0.52	0.60
	Plastic	1.0	0.56	0.56

2.3.6.3 Dynamic Load Factor and Types of Response

In order to relate the dynamic system into an equivalent static system the Dynamic Load Factor can be used. The Dynamic Load Factor (DLF) is defined by Biggs (1964) as the ratio of the dynamic deflection at any time to the deflection which would have resulted from the static application of the load *F*. Consequently, the DLF that relates maximum deflection under dynamic loading (u_{max}) to equivalent static deflection (u_{st}) can be expressed as:

$$DLF = \frac{u_{max}}{u_{st}} \qquad [2.23]$$

Using the solution of Equation 2.21 and the static displacement, the DLF for an equivalent SDOF system can be determined.

The resulting structural response is influenced significantly by ωt_d.

- $\omega t_d < 0.4$: impulsive loading regime;
- $0.4 < \omega t_d < 40$: dynamic loading regime; and
- $\omega t_d > 40$: quasi static loading.

2.3.6.4 Force-deformation Characteristics

The inputs required to perform dynamic analysis are the resistance function, $R(u)$, and the load-mass transformation factor, K_{LM} of the member. Since resistance and displacement are related, non-linear analysis methods need to be used to determine the resistance function (Jacques et al., 2011). For dynamic analysis, the force-deformation relationships used to generate member resistance should include the effect of strain-rate loading on the dynamic material properties. An example of a force-displacement resistance curve is shown in Figure 2.19. Simplified bi-linear resistance functions such as those presented in UFC 02-340-02 (2008) can also be used but typically yield approximate results when compared to non-linear analysis techniques. The UFC-3-340-02 (2008) presents a number of tables and figures in order to determine the maximum response of structural elements to a variety of idealized loads. The example shown in Figure 2.21 is the maximum response of the elasto-plastic SDOF system to a triangular load.

It should be noted that using simplified resistance functions in the blast analysis of reinforced concrete members has several shortfalls as summarized by Jacques et al. (2012):

- The idealization of mode shapes does not capture the effect of progression of plastic behaviour on dynamic response;
- The assumption of zero stiffness resistance after yield does not account for important effects on resistance such as concrete confinement, strain hardening, bar buckling, concrete crushing, etc;
- The method ignores important effects such as: axial load changes during response, non-ideal support conditions and yield penetration into adjacent members;
- There is no guidance on analysis incorporating advanced materials (e.g. externally bonded FRP, and for the case of this research SFRC and UHPFRC).

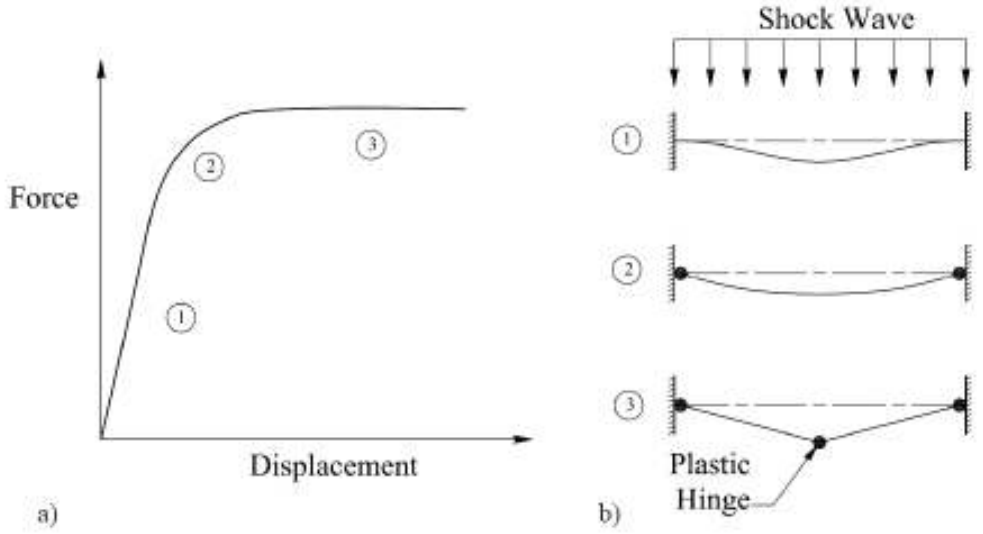

Figure 2.19 a) Force displacement function and b) Progression of damage through three mode shapes

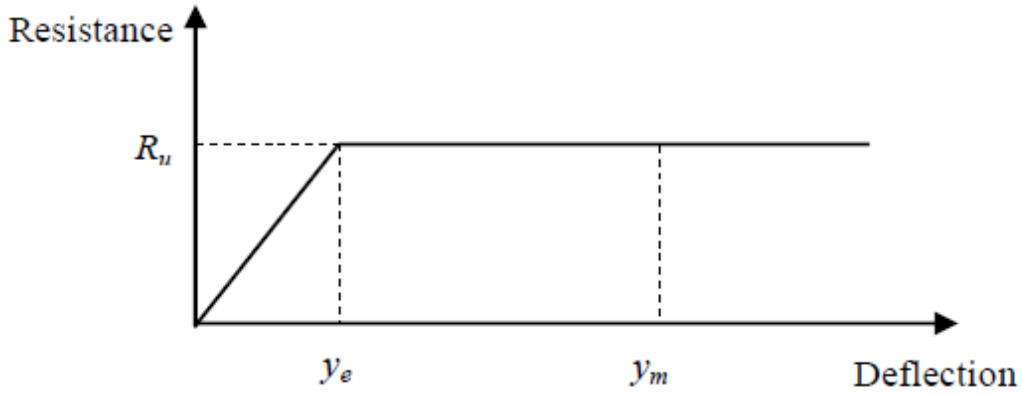

Figure 2.20 Idealized Resistance Function

(Ngo et al 2007)

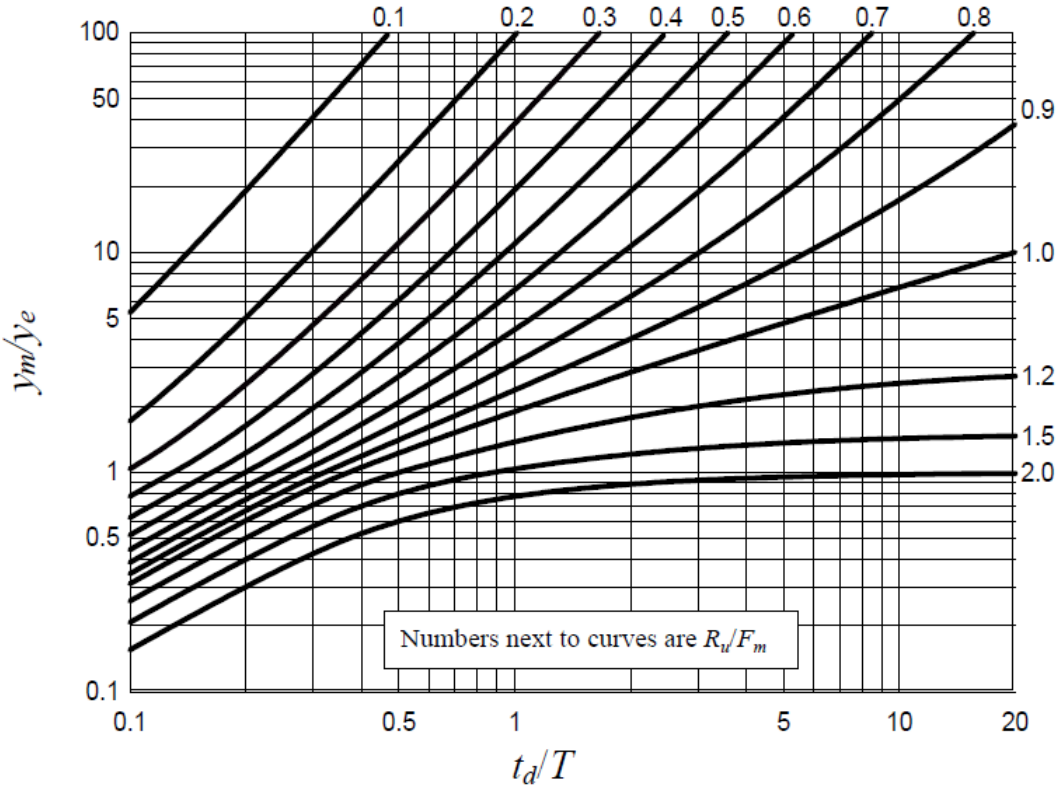

Figure 2.21 Maximum response of the elasto-plastic SDOF system to a triangular load

(UFC-3-340-02, 2008)

2.3.6.5 Blast Performance Criteria

Blast performance of a reinforced concrete structure can be interpreted based on maximum displacement u_{max} and can be assessed based on a ductility ratio:

$$\mu = u_{max}/u_{yield} \quad [2.24]$$

where μ is the ductility factor and u_y is the yield displacement.

Alternatively a deflection ratio (defined as u_{max}/L) or support rotation (θ) can be used (Jacques, 2011). The UFC 03-340-02 (2008) and the ASCE (1999) suggest performance criteria based on support rotation and deflection ratio, respectively. Table 2.3 shows performance levels and associated limits from UFC 03-340-02 (2008).

Table 2.3 Performance levels and associated deformation limits (UFC-3-340-02, 2008)

Component Level Damage	Description of Component Damage	Building Level of Protection	Limit for Reinforced Concrete Element in Flexure
Superficial Damage	Component has no visible permanent damage	High	$\mu \leq 1$
Moderate Damage	Component has some permanent deflection. It is generally repairable, if necessary, although replacement may be more economical and aesthetic	Medium	$\mu > 1$ $\theta \leq 2°$
Heavy Damage	Component has not failed, but it has significant permanent deflections causing it to be irreparable	Low	$2° < \theta \leq 5°$
Hazardous Failure	Component has failed, and debris velocities range from insignificant to very significant	Very low	$5° < \theta \leq 10°$
Blowout	Component is overwhelmed by the blast load causing debris with significant velocities	Below antiterrorism standards	$\theta > 10°$

2.3.7 Dynamic Material Properties

2.3.7.1 General

Structures are often subject to dynamic loading, whether it is due to wind gusts, earthquakes, machine vibration, impact from missiles and projectiles, or blast loads. Each of these types of loads varies with time, and, as a consequence, varies the rate of strain to which the structural material is subjected (see Figure 2.22). For reinforced concrete structures subjected to blast loads, both the dynamic strength of concrete, as well as the dynamic strength of the reinforcing steel can increase significantly due to strain rate effects. It is therefore critical to account for strain effects in the analysis of reinforced concrete members subjected to blast as the dynamic material properties affect member strength and stiffness.

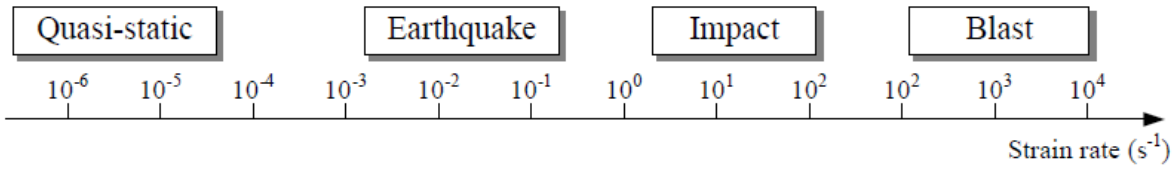

Figure 2.22 Strain rates associated with different types of loading

(Ngo et al., 2007)

There are various ways to test a material's dynamic properties including drop weight, pendulum, firing of projectiles, and detonating explosives. These tests can be instrumented in order to test material's dynamic compressive strength at varying strain rates. The ratio between the dynamic strength of a material to that of its static strength is termed the Dynamic Increase Factor (DIF), and is an important parameter used to calculate the resistance of elements subjected to dynamic loads. The DIF of concrete is a function of the strain rate, $\dot{\epsilon}$, and is given by:

$$\dot{\epsilon} = \frac{\epsilon_o}{t_E} \qquad [2.25]$$

For steel, the strain rate is given by:

$$\dot{\epsilon} = \frac{f_{dy}}{E_s t_E} \qquad [2.26]$$

where ϵ_o is the peak strain of concrete, t_E is the time required to yield reinforcement, and f_{dy} is the dynamic yield strength of steel. (Saatcioglu et al., 2011)

2.3.7.2 Dynamic Increase Factor for Concrete

When subjected to a dynamic load, concrete exhibits a higher peak load than under static load in both compression and tension (see Figure 2.23). It is noted that dynamic response is characterized by two distinct regions: at lower strain rates the relative increase in stress remains relatively low, however at higher strain rates a sharp transition occurs with a rapid increase in DIF with increasing strain rate.

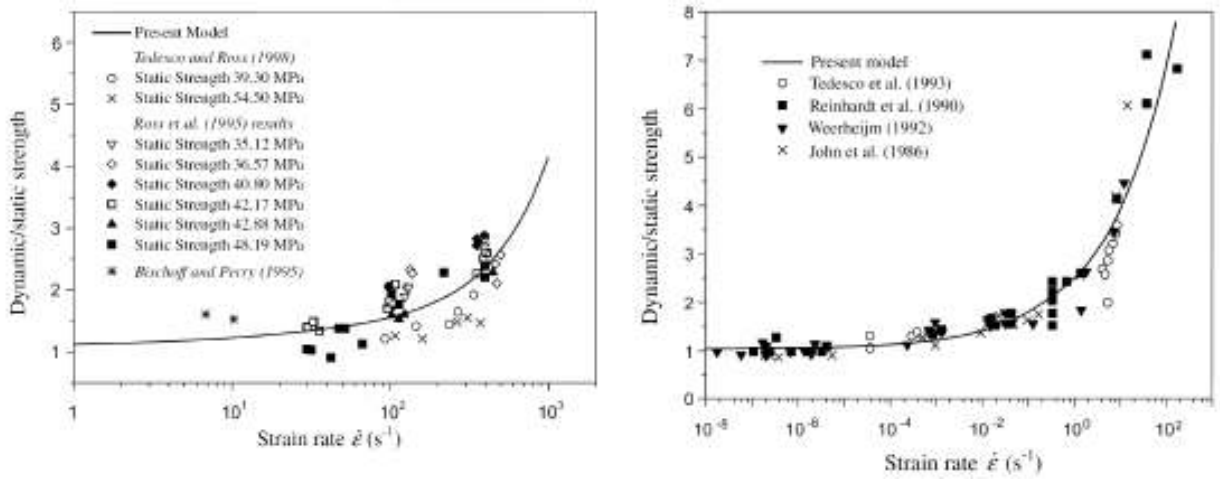

Figure 2.23 Effect of strain rate on DIF of concrete in compression (left) and tension (right)

(Lu and Xu, 2004)

The most comprehensive model for strain rate enhancement of concrete, both in tension and compression is presented by the Comité Euro-international du Béton (CEB – Euro-International Concrete Committee) Model Code. For concrete in compression the model is as follows (Malvar and Crawford, 1998):

$$DIF = \frac{f'_{dc}}{f'_c} = \left(\frac{\dot{\epsilon}}{\dot{\epsilon}_s}\right)^{1.026\alpha_s}, \quad \dot{\epsilon} \leq 30s^{-1} \qquad [2.27]$$

$$DIF = \frac{f'_{dc}}{f'_c} = \gamma\left(\frac{\dot{\epsilon}}{\dot{\epsilon}_s}\right)^{1/3}, \quad \dot{\epsilon} > 30s^{-1} \qquad [2.28]$$

where f'_{dc} is the dynamic compressive strength at strain rate $\dot{\epsilon}$, f'_c is the static compressive strength at quasi-static strain rate $\dot{\epsilon}_s$, $\dot{\epsilon}$ is the strain rate in the range of 30×10^{-6} to 300 sec^{-1} , $\dot{\epsilon}_s$ is the static strain rate (30×10^{-6} sec^{-1}) , f'_{co} = 10 MPa, and:

$$\text{Log } \gamma = 6.156\alpha_s - 2 \qquad [2.29]$$

$$\alpha_s = \frac{1}{\left(5 + \frac{9f'_c}{f'_{co}}\right)} \qquad [2.30]$$

A similar model for concrete under dynamic tension is given by the CEB Model Code as (Malvar and Ross, 1998):

$$DIF = \frac{f'_{td}}{f'_t} = \left(\frac{\dot{\epsilon}}{\dot{\epsilon}_s}\right)^{1.016\delta}, \quad \dot{\epsilon} \leq 30s^{-1} \qquad [2.31]$$

$$DIF = \frac{f'_{td}}{f'_t} = \beta\left(\frac{\dot{\epsilon}}{\dot{\epsilon}_s}\right)^{1/3}, \quad \dot{\epsilon} > 30s^{-1} \qquad [2.32]$$

where f'_{td} is the dynamic tensile strength at strain rate $\dot{\epsilon}$, f'_t is the static tensile strength at quasi-static strain rate $\dot{\epsilon}_s$, $\dot{\epsilon}$ is the strain rate in the range of 30×10^{-6} to 300 s^{-1}, $\dot{\epsilon}_s$ is the static strain rate (30×10^{-6} s^{-1}) , f_{co} = 10 MPa, and:

$$\text{Log } \beta = 7.11\,\delta - 2.33 \qquad [2.33]$$

$$\delta = \frac{1}{\left(10 + \frac{6f'_c}{f_{co}}\right)} \qquad [2.34]$$

The resulting CEB model curves are bi-linear, with a change in slope occurring at a strain rate of 30 sec^{-1}. This demonstrates that there is a significantly large increase in material strength at higher strain rates (greater than $30s^{-1}$).

There is no conclusive research on the effect of concrete compressive strength on the DIF of concrete (Saatcioglu et al., 2011), however some researchers have reported that as the concrete compressive strength increases, the DIF lowers (Hughes and Watson, 1978). Figure 2.23 shows the relative increase in compressive stress as a function of strain rate from a number of studies reported in the literature, with various series of data reported in terms of compressive strength.

Although a slight trend is noticeable, the data in the literature shows high scatter. It is noted that the CEB model does account for the effect of compressive strength when calculating DIF (the CEB-predicted DIF values for 20 MPa, 60 MPa and 100 MPa are shown in Figure 2.23).

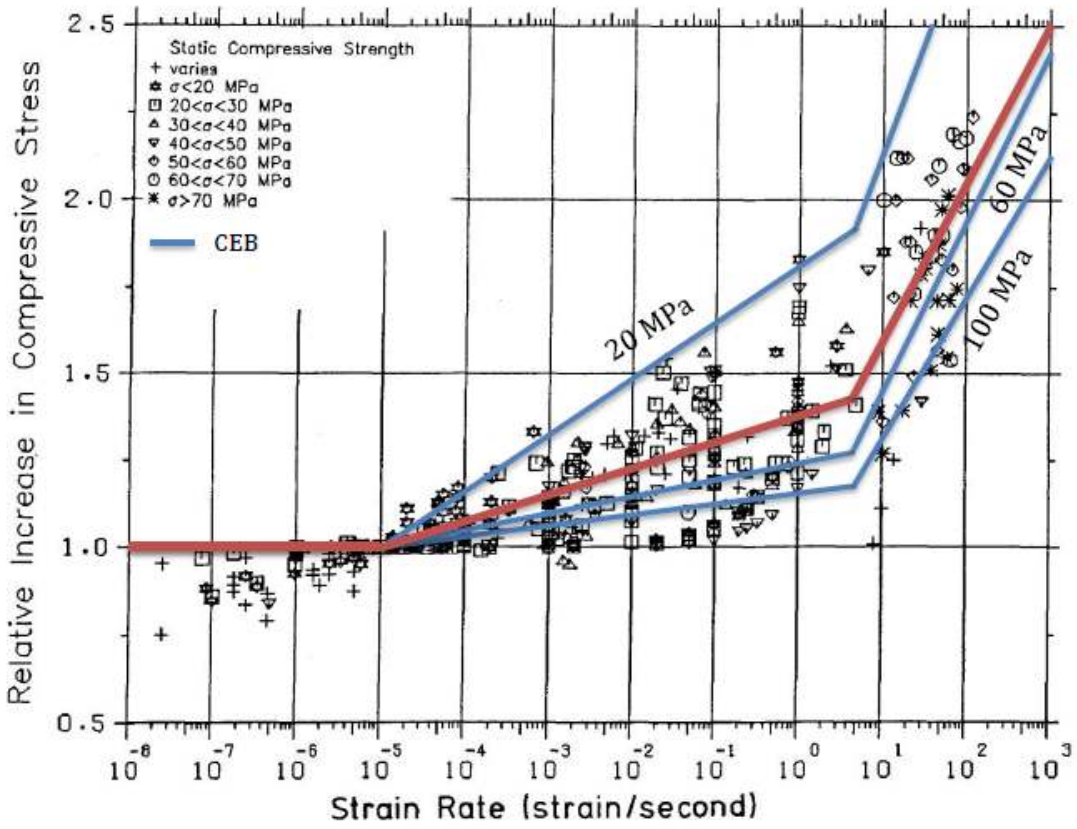

Figure 2.24 Effect of concrete compressive strength on DIF

(Saatcioglu et al., 2011)

Table 2.4 shows the currently accepted DIFs for reinforced concrete design (concrete and reinforcing bars) from the UFC-3-340-02 (2008). For analytical purposes, DIFs are applied across the entirety of the material's stress strain curve, as shown in Figure 2.25.

Table 2.4 Dynamic Increase Factors for Design of Reinforced Concrete Elements (UFC-3-340-02, 2008)

TYPE OF STRESS	FAR DESIGN RANGE			CLOSE-IN DESIGN RANGE		
	Reinforcing Bars		Concrete	Reinforcing Bars		Concrete
	f_{dy}/f_y	f_{du}/f_u	f'_{dc}/f'_c	f_{dy}/f_y	f_{du}/f_u	f'_{dc}/f'_c
Bending	1.17	1.05	1.19	1.23	1.05	1.25
Diagonal Tension	1.00	------	1.00	1.10	1.00	1.00
Direct Shear	1.10	1.00	1.10	1.10	1.00	1.10
Bond	1.17	1.05	1.00	1.23	1.05	1.00
Compression	1.10	------	1.12	1.13	------	1.16

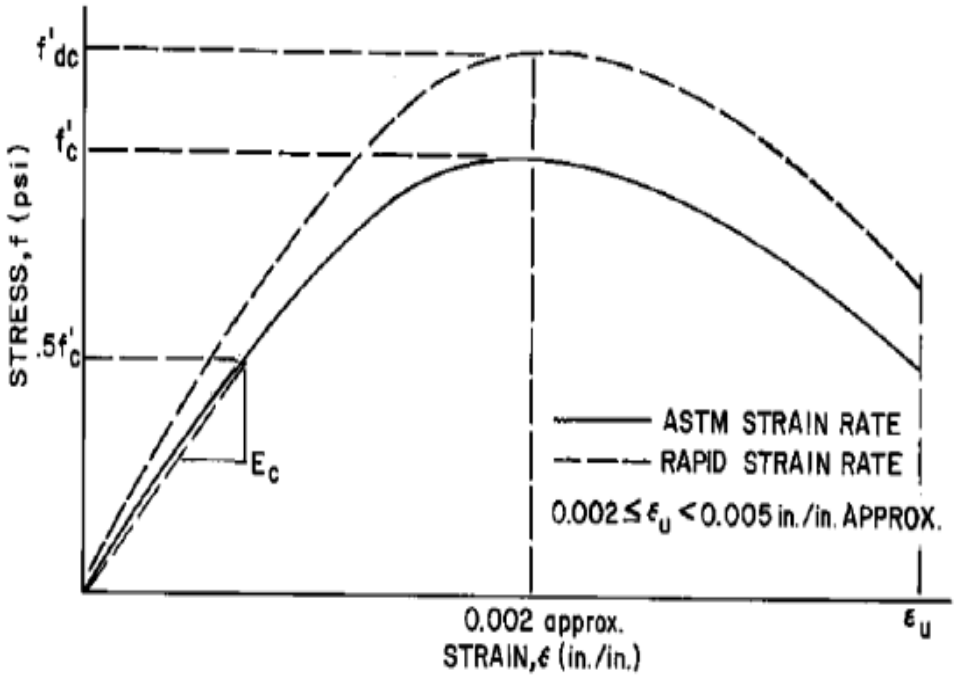

Figure 2.25 Typical stress-strain curves for concrete at quasi-static and dynamic strain rates

(UFC 03-340-02, 2008)

2.3.7.3 Dynamic Increase Factor for Reinforcing Steel

Similarly to concrete, the yield and ultimate stresses of reinforcing steel increase with strain rate. The increase in the yield stress is substantially greater than that of the ultimate stress. The dynamic increase factors of the reinforcing steel can be represented by the following equations:

$$DIF = \left(\frac{\dot{\varepsilon}}{10^{-4}}\right)^{\alpha} \quad [2.35]$$

where for the yield stress, α is given as:

$$\alpha = 0.074 - 0.04\frac{f_y}{414} \quad [2.36]$$

And for the ultimate stress, α is given as:

$$\alpha = 0.019 - 0.009\frac{f_y}{414} \quad [2.37]$$

Figure 2.26 shows the effects of the DIF on typical reinforcing steel. Note that the modulus of elasticity remains unchanged, and the DIF has less effect after ultimate stress.

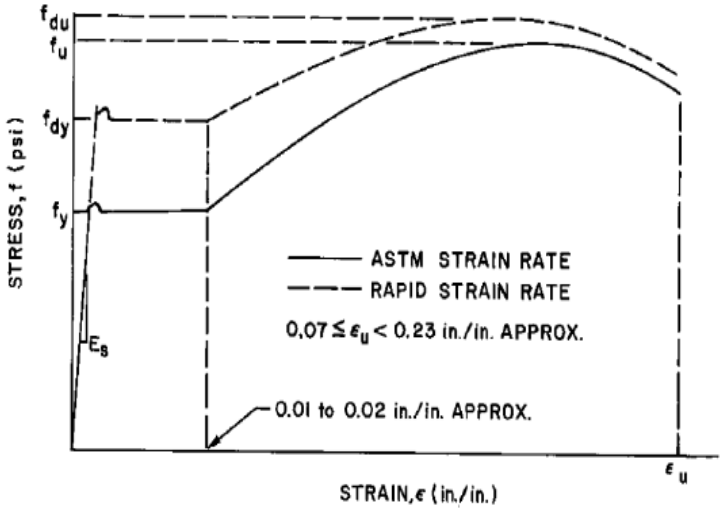

Figure 2.26 Typical stress-strain curves for steel at quasi-static and dynamic strain rates

(UFC 03-340-02, 2008)

2.3.7.4 Dynamic Increase Factor for SFRC

The determination of the DIF for SFRC can be done by taking the ratio of SFRC strength at dynamic loading to its strength at quasi-static loading by means of drop weight, pendulum, split hopskin pressure bar, or explosive testing. Table 2.5 gives a summary of DIFs for SFRC reported in the literature. It is noted that the reported data shows high-scatter. It should also be noted that studies have indicated that when compared to high-strength concrete, high-strength SFRC may have reduced DIF at high-strain rates. Wang et al. (2012) evaluated the mechanical properties of high-strength concrete and high-strength SFRC under high strain-rate compressive loading, and concluded that the CEB model overestimates the DIF for high strength SFRC.

Table 2.5 List of Dynamic Increase Factors as reported in the literature.

Reference	Material	V_f (%)	Aspect Ratio (l/d)	Fibre type	Reported Quasi-Static Strain Rate (s^{-1})	Dynamic Strain Rate (s^{-1})	DIF
Gopalaratnam and Shah 1983	Mortar				1.00E-06	0.30	1.65
	Concrete				1.00E-06	0.30	1.50
	SFRC	0.50	63	Straight	1.00E-06	0.30	1.79
	SFRC	1.00	63	Straight	1.00E-06	0.30	1.99
	SFRC	1.50	63	Straight	1.00E-06	0.30	2.11
Rostasy and Hartwhich 1985	SFRC	0.75	62.5	Straight	3.80E-05	0.17	1.20
	SFRC	1.50	62.5	Straight	3.80E-05	0.17	1.23
	SFRC	0.75	60	Hooked End	3.80E-05	0.17	1.23
	SFRC	1.50	60	Hooked End	3.80E-05	0.17	1.22
Naaman and Gopalaratnam 1983	SFRC	3.00	47	Straight	5.00E-06	1.20	2.50
	SFRC	2.00	47	Straight	5.00E-06	1.20	1.80
	SFRC	1.00	47	Straight	5.00E-06	1.20	1.70
Lok and Zhao 2004	SFRC	0.60	65	Hooked End	2.00E-05	25.80	1.17
	SFRC	0.60	65	Hooked End	2.00E-05	20.10	1.19
	SFRC	0.60	65	Hooked End	2.00E-05	19.80	1.19
	SFRC	0.60	65	Hooked End	2.00E-05	32.10	1.02
	SFRC	0.60	65	Hooked End	2.00E-05	25.20	1.25
	SFRC	0.60	65	Hooked End	2.00E-05	52.30	1.48
	SFRC	0.60	65	Hooked End	2.00E-05	65.80	1.38
	SFRC	0.60	65	Hooked End	2.00E-05	51.70	1.38
	SFRC	0.60	65	Hooked End	2.00E-05	63.30	1.40
	SFRC	0.60	65	Hooked End	2.00E-05	57.40	1.50
	SFRC	0.60	65	Hooked End	2.00E-05	57.10	1.46
	SFRC	0.60	65	Hooked End	2.00E-05	74.50	1.58
	SFRC	0.60	65	Hooked End	2.00E-05	97.80	1.75
	SFRC	0.60	65	Hooked End	2.00E-05	103.00	1.71
	SFRC	0.60	65	Hooked End	2.00E-05	94.60	1.70

2.3.8 University of Ottawa Shock Tube

2.3.8.1 General

The University of Ottawa shock tube was designed, constructed, and commissioned by Baker Engineering and Risk Consultants. It is used to subject structural components such as columns, walls, and slabs to simulated blast loads using a pressure driven shock tube. The shock waves generated by the shock tube closely simulate the blast waves produced by the hemispherical free air surface bursts of high explosives (Lloyd et al., 2010).

2.3.8.2 Components

The University of Ottawa shock tube, as seen in Figure 2.27, consists of four main components, a variable length driver section, a spool section, an expansion section and a rigid end test frame. The variable driver section is the main pressure vessel responsible for generating shock waves, and comprised of a series of bolted together cylindrical pressure vessels. The driver section length is variable from 305mm to 5185mm, and the length can be adjusted based on the required shock wave parameters (Lloyd et al., 2010).

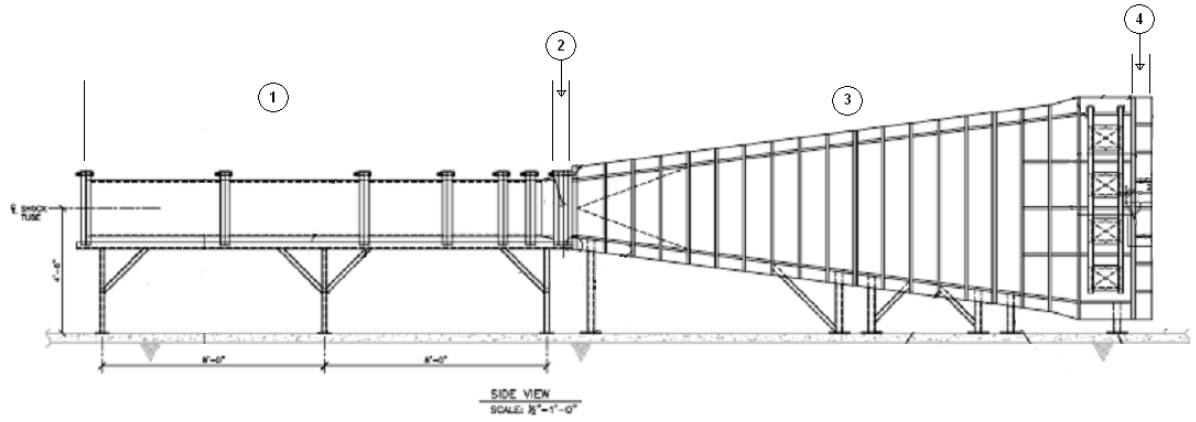

Figure 2.27 Shock tube components: 1) Variable driver length section, 2) Spool section, 3) Expansion section and 4) Rigid end test frame section.

The spool section is comprised of a double diaphragm firing system, which is responsible for the control of the shock tube firing. The diaphragms used in the spool section are composed of sheets of grade 1100 aluminum foil of varying thickness. The driver and spool sections are pressurized independently, with the driver section pressurized to the desired firing pressure, and the spool section pressurized to approximately half this pressure. The difference in pressure

must be kept below the diaphragms' rupture strength. Once the driver section has reached the triggering pressure, the spool section is vented, which causes the rupture of the diaphragms and the rapid expansion of compressed air into the expansion section of the shock tube. It is the rapid expansion of compressed air that induces the shock loads on the structural elements contained within the rigid test frame section (Lloyd et al., 2010).

The expansion section increases from 597 mm in diameter (spool section) to 2032 mm × 2032 mm square opening of the rigid test frame over a length of 6096 mm. This is done to ensure that the shock wave generated by the expansion of gases is planar: uniform across the entire surface of the structural element being tested. Twelve sliding pressure relief vents are located at the end of the expansion section that slide open when the shock wave reaches the rigid end test frame section, which allow for the creation of a negative phase in the pressure-time history as the compressed air exits the shock tube. The rigid end test frame is constructed with stiffened steel plates with 20 × 19 mm diameter holes for connecting structural elements to the shock tube (Lloyd et al., 2010).

2.3.8.3 Instrumentation

The shock tube facility is complemented by a suite of data acquisition equipment, including high speed oscilloscopes, pressure sensors, displacement transducers, accelerometers, strain gauges, and high speed video camera (Lloyd et al., 2010). The instrumentation is triggered when the shock wave reaches one of the reflected pressure sensors located near the end of the expansion section.

2.3.8.4 Shock Waves

As discussed previously, the sudden release of hot gases from the chemical reaction of a high explosive causes a pressure differential between the hot gases and the surrounding atmosphere. This, in turn, causes a blast wave to propagate outward from the centre of detonation. The University of Ottawa shock tube simulates blast waves using a physical release of energy by the rapid expansion of air that is initially pressurized and then suddenly released. The shock waves generated with the shock tube closely resemble explosive driven shock waves (Lloyd et al., 2010).

The operating range of the shock tube is defined by the peak reflected pressure, peak reflected impulse, and the positive phase duration. The peak reflected shock wave pressure is controlled by the initial pressure within the driver section, and the positive phase duration is controlled by the variable driver length. The maximum reflected pressure that can be imparted to a specimen is 100 kPa. The longer the driver length, the longer the phase duration, as there is more air used in the creation of the shock front. The impulse of the blast wave is a function of the reflected pressure and positive phase duration, and consequently it can be modified by varying these parameters. Typical values for reflected pressures with associated shock tube driver lengths are shown in Table 2.6. A typical pressure and impulse time history plot generated by the shock tube is shown in Figure 2.28.

Table 2.6 Maximum shock tube reflected pressure and impulse for 5 driver lengths (Lloyd et al. 2010)

			Approximate Equivalent TNT (Hemispherical-Reflected)		
Driver Length	Reflected Pressure	Reflected Impulse	Mass	Standoff	Scaled Distance
(mm)	(kPa)	(kPa-ms)	(kg)	(m)	(m/kg$^{1/3}$)
305	78	217	8	12	6.0
915	92	410	42	18	5.2
1830	100	840	290	33	5.0
3355	103	1760	2500	67	4.9
4880	104	2690	10000	106	4.9

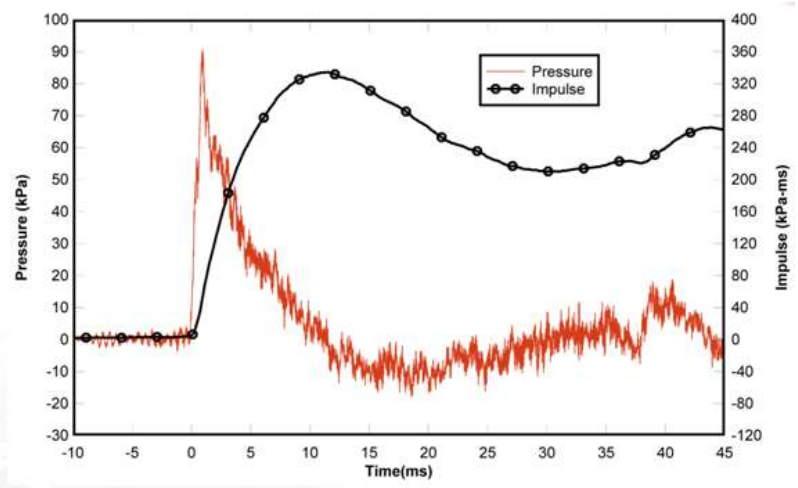

Figure 2.28 Sample Pressure and Imulse time hsirtories generated by the University of Ottawa shock tube

(Lloyd et al., 2010)

2.4 Section Conclusions:

Based on the information presented in this Section, the following conclusions can be made:

1. The use of fibres improves properties of concrete including post-peak ductility in compression, tensile capacity, flexural toughness, and post-cracking resistance. In reinforced concrete structures, the use of SFRC can partially substitute for traditional transverse reinforcement. The introduction of steel fibres into a concrete mix will reduce workability; however an innovative solution to this problem is to add steel fibres to self-consolidating concrete.

2. The effects of high strain rates on reinforced concrete have long been established, and high strain rates produce an inherent increased strength in the material, modeled as the dynamic increase factor (DIF). However, higher strength concrete typically leads to a smaller DIF. There are no established DIF values used for SFRC or CRC. However, the introduction of steel fibres and the use of high-strength SFRC such as CRC may reduce the DIF when compared to the strength increases observed in typical concrete.

3. Blast load pressure profiles can be idealized, and the response of individual elements to blast loads can be predicted with the use of single degree of freedom dynamic analysis. The analysis requires an understanding of the behaviour of the material, and its behaviour at high strain rates.

4. The University of Ottawa shock tube is a good device for simulating blast loads on structural components due to its simplicity for the users, and ease of gathering required data both during and after simulated blast testing.

3 Experimental Program

3.1 General

Reinforced concrete columns are elements that are critical to ensuring the overall strength and stability of buildings. The failure of a ground story column can trigger progressive collapse as the upper story beams and columns lose their supports. This experimental program aims at studying the behaviour of half-scale steel fibre reinforced concrete (SFRC) and ultra-high performance fibre reinforced concrete (UHPFRC) columns subjected to simulated blast loading using the University of Ottawa Shock Tube. The experimental program involves the construction and testing of thirteen column specimens. This section summarizes the details regarding specimen and material properties.

3.2 Description of Test Specimens

A total of thirteen column specimens were tested in this experimental program. Eight SFRC columns were constructed with self-consolidating concrete (SCC) and reinforced with steel fibre at contents ranging from 0% to 1.5% by volume of concrete. In addition, five UHPFRC columns made of compact reinforced composite (CRC) and reinforced with steel fibre at contents ranging from 2% to 6% by volume were constructed. Table 3.1 summarizes the properties of the various specimens. As shown in Figure 3.1, the columns had a square cross-section of 152.4 mm × 152.4 mm (6 in. × 6 in.) and a total height of 2468 mm (8 ft.); it is noted that the size of the columns was dictated by the capacity of the shock-tube. The longitudinal reinforcement consisted of 4-10M bars (fy = 480 MPa) and had 90° hooks extending 75mm at each extremity to ensure full development of the reinforcement into the support region. The transverse reinforcement consisted of smooth 6.3mm diameter ties (fy = 600 MPa) with 135° hook extensions and the clear concrete cover was kept constant at 5 mm. The columns with transverse tie spacing (s) of 75 mm were designed and detailed according to the requirements for moderately ductile columns in the CSA-A23.3-04 Standard, and columns with tie spacing of 38 mm were designed as ductile columns in accordance with the special provisions for seismic design of the same standard. The column nomenclature specifies the type of concrete, the fibre content (in % by volume of concrete) and the tie spacing used in each column. For example

column SCC-0.5%-75 refers to a column constructed with SCC, reinforced with 0.5% fibres and containing ties at a spacing of 75 mm.

Table 3.1 Properties of test specimens

Series	Columns	Concrete mix	Cross-Section	Transverse Reinforcement Spacing (s)	Transverse Reinforcing Steel Ties	Longitudinal Reinforcing Steel Bars	Fibre Type	Fibre Content (%)
SFRC	SCC-0%-75	KING SCC	152 mm × 152 mm	75 mm	6.3 mm dia. f_y = 600MPa	4 – 10M bars ρ = 1.72% f_y = 480MPa	ZP-305	0.00
	SCC-0.5%-75							0.50
	SCC-0.75%-75							0.75
	SCC-1%-75							1.00
	SCC-1.5%-75							1.50
	SCC-0.75%HS-75						BP-80/30	0.75
	SCC-0%-38			38 mm			ZP-305	0.00
	SCC-0.5%-38							0.50
CRC	CRC-2%-75	CRC Joint Cast		75 mm			OL 12/.40	2.00
	CRC-4%-75							4.00
	CRC-6%-75							6.00
	CRC-2%-38			38 mm				2.00
	CRC-4%-38							4.00

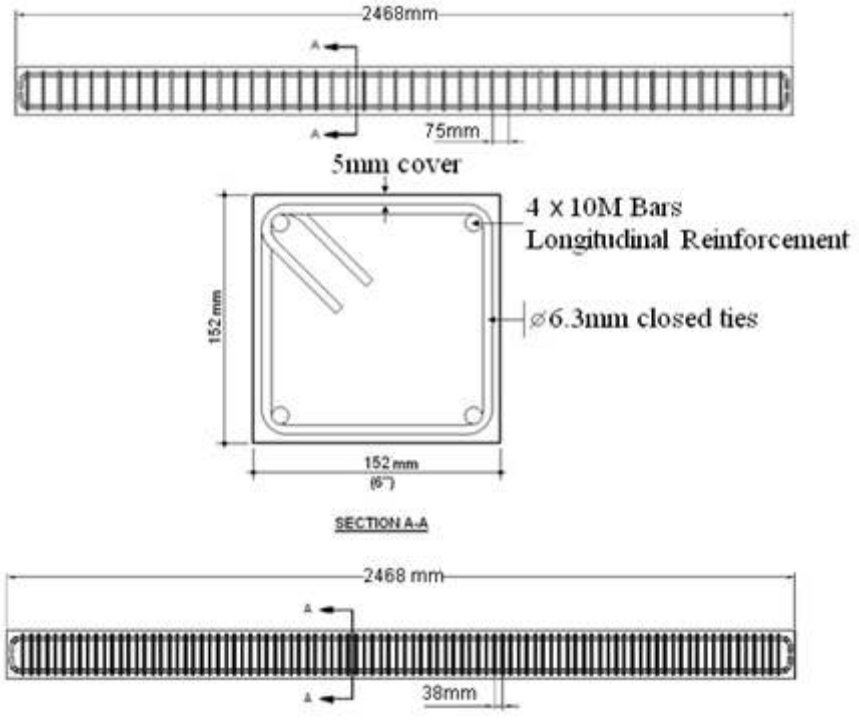

Figure 3.1 Design of (top) non-seismic and (bottom) seismically-detailed columns*

**Note that the cross section does not change, simply the tie spacing.*

3.3 Materials

3.3.1 Reinforcing Steel (Reinforcing steel)

The longitudinal deformed reinforcing bars used in this experimental program were size 10M for all columns. Transverse steel ties were fabricated from 6.3 mm diameter non-deformed steel wire. Standard tensile coupon tests were performed on two samples for both the 10M bars and 6.3 mm diameter wire using a 600 kN MTS testing machine located at the University of Ottawa Structures Laboratory, as shown in Figure 3.2. The average stress-strain relationships for the longitudinal and transverse steel are shown in Figure 3.3. Table 3.2 and Table 3.3 summarize the properties of the reinforcing steel bars.

Figure 3.2 MTS testing machine

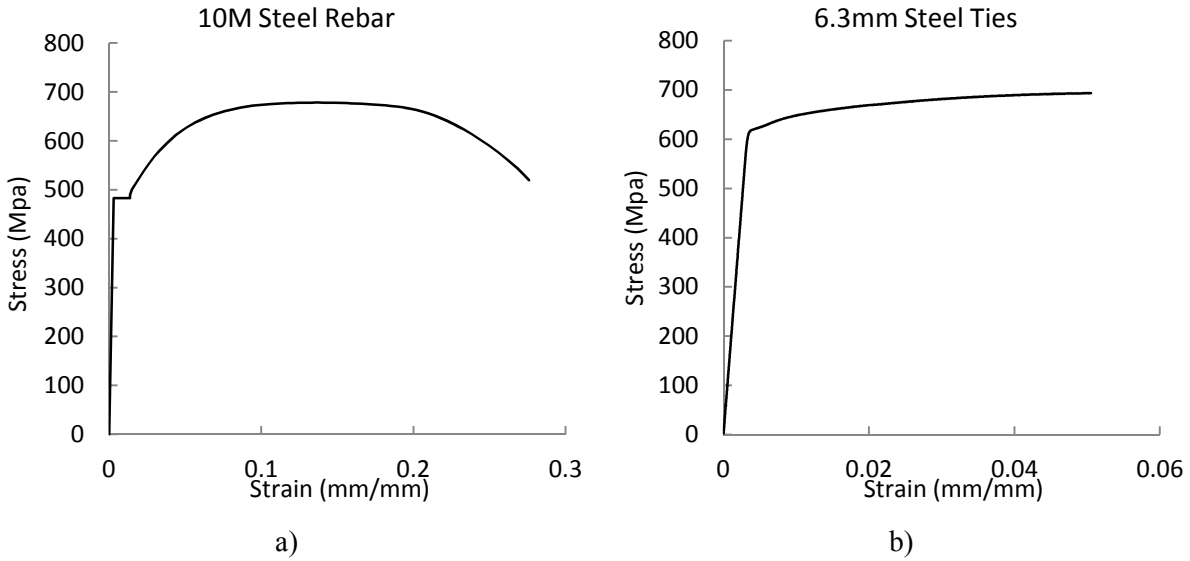

Figure 3.3 a) Stress-strain relationship for 10M bars, and b) stress-strain relationship for 6.3 mm diameter steel wire.

3.3.2 Steel Fibres

Three types of steel fibres were used in this experimental program. Six of the eight SFRC columns contained Dramix ZP305 fibres, whereas one column contained Dramix BP-80/30 fibres (noted as HS in the column nomenclature). Both of these types of fibres were 30 mm long with hooked ends and bundled by dissolvable glue as shown in Figure 3.4. The ZP305 fibres are made of normal strength steel wire with a tensile strength of 1100 MPa and have an aspect-ratio (l_f/d_f) of 55. The BP-80/30 fibres have a higher tensile strength of approximately 2300 MPa and have a higher aspect-ratio (l_f/d_f) of 80. It is noted that this second fibre type is more often employed in high strength concrete or extreme load applications.

All CRC columns contained OL-12/.40 fibres. In contrast to the Dramix fibres, the OL-12/.40 fibres are a smooth, straight fibre made of low carbon steel wire with a tensile strength of 1350 MPa and have an aspect ratio (l_f/d_f) of 30. These fibres are the typical fibres provided by CRC Technology for use with the CRC Joint Cast product.

Different amounts of fibres were used in reinforcing the specimens in order to examine the effect of varying fibre content on the blast resistance of columns. The Dramix and OL fibres are manufactured by Bekaert Corporation (Belgium) and Stratec GMBH (Germany) respectively. The properties of the steel fibres used in this study are summarized in Table 3.4.

a) ZP-305 b) RC-80/30-BP c) OL-12/.40

Figure 3.4 Dramix fibres used in this study

Table 3.2 Properties of 10M bars

Yield		Strain Hardening		Ultimate		Rupture	
f_y (MPa) [std. dev.]	ε_y (mm/mm) [std. dev.]	f_{sh} (MPa) [std. dev.]	ε_{sh} (mm/mm) [std. dev.]	f_u (MPa) [std. dev.]	ε_u (mm/mm) [std. dev.]	f_r (MPa) [std. dev.]	ε_r (mm/mm) [std. dev.]
483 [0.84]	0.0029 [0.00014]	483 [0.84]	0.0137 [0.00024]	678 [0.43]	0.1368 [0.00970]	505 [4.27]	0.2802 [0.00584]

Table 3.3 Properties of 6.3 mm diameter non-deformed steel wire

Yield		Ultimate		Rupture	
f_y (MPa) [std. dev.]	ε_y (mm/mm) [std. dev.]	f_u (MPa) [std. dev.]	ε_u (mm/mm) [std. dev.]	f_r (MPa) [std. dev.]	ε_r (mm/mm) [std. dev.]
604 [3.72]	0.0033 [0.00007]	694 [9.22]	0.0607 [0.01258]	689 [9.97]	0.0706 [0.01695]

Table 3.4 Fibre properties

Fibre type	Length l_f (mm)	Diameter d_f (mm)	Aspect ratio l_f/d_f (mm/mm)	Tensile strength f_{fy} (MPa)	Note.
ZP-305	30	0.55	55	1100	Hooked-end Low Carbon
BP-80/30	30	0.38	79	2300	Hooked-end High Carbon
OL-12/.40	12	0.40	30	1350	Smooth, straight Low Carbon

3.3.3 Concrete

The concrete for all columns was mixed at the University of Ottawa Pomerleau Concrete Laboratory. A pre-packaged SCC mix (KING SCC) was used in the construction of the eight SFRC specimens. The five UHPFRC specimens were constructed with compact reinforced concrete (CRC Joint Cast).

3.3.3.1 SFRC (KING SCC)

One of the disadvantages associated with the use of SFRC is that the addition of fibres to a regular concrete mix can cause problems in workability, particularly when higher fibre contents are used. To improve workability a SCC mix was selected for this study. The SCC mix consisted of a pre-packaged, self-consolidating concrete mix with a specified strength of 50 MPa (KING SCC, KING Packaged Materials Company). The mix contained a maximum aggregate size of 10 mm with a sand-total aggregate ratio of approximately 0.55 and a water-cement ratio of approximately 0.42. Furthermore, the SCC product contained an air-entraining admixture, a superplasticizer and a viscosity modifying admixture (VMA). The admixtures are incorporated into the blend in the form of dry powder. Table 3.5 lists the mix properties as specified by the manufacturer. This mix was used in eight of the specimens of the experimental program; two "control" specimens contained no fibres, while the remaining columns were constructed with SCC and steel fibres at contents ranging from 0.5% to 1.5% fibres by volume of concrete, and included either the ZP-305 or the BP-80/30 fibres.

Table 3.5 KING SCC composition

Component	*Content*
HSF Cement	500 (kg/m^3)
Water-cement ratio	0.42
Coarse Aggregate	765 (kg/m^3)
Fine aggregate	915 (kg/m^3)
Ratio Fine/Total Aggregate	0.55
Mass Density	2300 (kg/m^3)
Air Content	7 (%)

3.3.3.2 UHPFRC (CRC Joint Cast)

The five UHPFRC columns in this experimental program were constructed with CRC Joint Cast. CRC is a proprietary brand name for an UHPFRC produced by CRC Technology, Denmark. The mix used for CRC Joint Cast contained a maximum aggregate size of 4 mm. The *Densit Binder* consists of approximately 20% microsilica and the remainder is typical Portland cement with a superplasticizer in the form of a dry powder (Nielsen 1995). The constituents of CRC are listed in Table 3.6. The batches used to construct the 5 CRC columns ranged from 2% to 6% of OL-12/.40 fibres by volume of concrete.

Table 3.6 Constituents of CRC Joint Cast mix with 6% steel fibres by volume.

Ingredient	*Fraction by Weight (%)*	*Density (kg/m^3)*	*Content (kg/m^3 concrete)*
Densit Binder	34	Cement: 3150 Microsilica: 2250	1146
Quartz Sand			
0 – 0.25 mm	7	2640	236
0.25 – 1 mm	12	2640	404
1 – 4 mm	24	2740	809
Water	6	1000	202
Water-binder ratio			0.18
Steel Fibres	17	7500	573

3.4 Construction of Test Specimens

The construction of the test specimens was completed in five stages at the University of Ottawa Structures Laboratory. These stages included bending of steel ties, assembly of steel reinforcement cages, application of electrical resistance strain gauges on the steel cages, construction of form work, and casting of concrete. The reinforcing steel and the concrete were both provided by local companies. Bending of the steel ties was done with a hand bending jig designed to provide exact dimensions of the steel ties. The *6.3 mm* wire was first cut to the length needed for each size ties. Three *90* ° bends and two *135* ° bends were provided for each tie. Assembly of the steel cages was done by first marking out tie spacing on each of the four

longitudinal reinforcing bars per column. The transverse reinforcement was then placed on the steel bars and tied in place using quick tie wires. Figure 3.5 and Figure 3.6 show typical cages with and without seismic detailing after construction. Strain gauges were applied to the longitudinal steel and to select transverse ties in prescribed locations (see Figure 3.7). Formwork was constructed using ¾'' thick plywood and assembled in a manner such that the columns could be cast horizontally.

Figure 3.5 Typical (left) hoops and spacing of ties in (left) non-seismic and (right) seismic columns

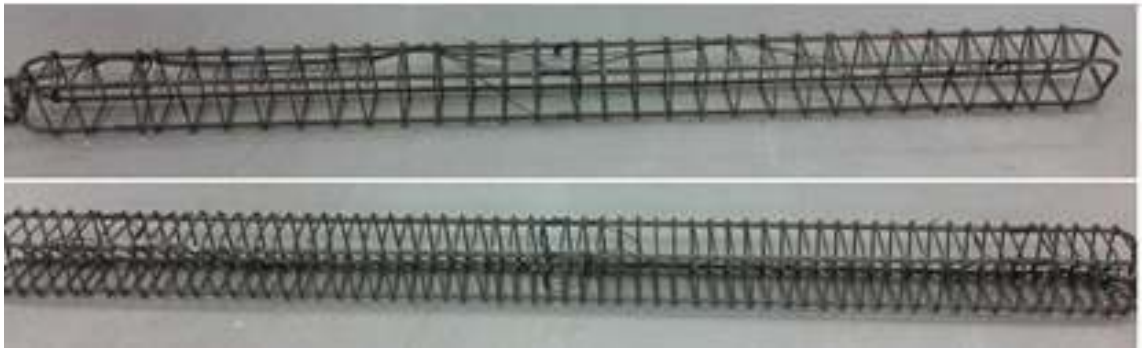

Figure 3.6 Typical cages with (top) non-seismic and (bottom) seismic detailing

Figure 3.7 Typical cage showing strain gauge instrumentation

3.4.1 Casting

3.4.1.1 Effect of Mixer Type

Prior to casting the columns, different types of mixers (as shown in Figure 3.8) were tested to assess the effect of mixer type on the fresh-state properties of SFRC and CRC. For the SFRC mixes, three different mixers were tested in the initial trial series. The first was a 420 volt electric multiflow pan mixer that uses 3 fixed paddle blades that are arranged in such a way as to create a forced mixing action as the pan revolves at high velocity (when compared to typical drum mixers). A side scraper blade is also used to ensure that material does not build up on the side of the pan. When working properly, this mixer was the ideal mixer for both SFRC due to its ability to force material at high velocity in to defined flow path that resulted in excellent distribution of the steel fibres, and uniformity of the final mix (up to 1.5%). The second was a portable gas powered rotating drum mixer. The mixing action in this type of mixer was provided by small ledges on the interior of the drum that would lift the material to a certain point, and then allow it to be dropped to the base of the drum. However, this mixer was limited due to its slower mixing rate (≈30 rpm) and its smaller mix capacity. While most mixes were satisfactory, this type of mixer occasionally did not produce an ideal mix uniformity at the end of the specified mixing time, particularly at higher fibre contents (1% and above) or when fibres with higher aspect ratio were used (e.g. BP 80/30 fibres). The third type of mixer tested was a mortar mixer that used large, vertically-rotating paddles. However, this type of mixer was not ideal due to its small drum capacity, and did not produce uniform and consistent mixes. Based on the results of this trial series the pan mixer was selected for casting the SFRC columns. Unfortunately, during part of the experimental program the pan mixer was unavailable and therefore a pair of drum mixers (as shown in Figure 3.8(b)) were used in casting three of the SFRC columns (SCC-0.75%-75, SCC-1.5%-75, SCC-0.75%HS-75). The pan mixer and mortar mixer were also used to assess the effect of mixer type on the fresh-state properties of CRC. The results showed that the forced mixing action provided by the pan mixer was required to produce a uniform CRC mix, particularly at higher fibre contents (4% and 6%). Based on the results of the trial series, all the CRC batches were mixed using the pan mixer. Table 3.7 lists the mixer type used for casting the various columns.

Table 3.7 Mixer type used for casting columns.

	SCC-0%-75	SCC-0%-38	SCC-0.5%-75	SCC-0.5%-38	SCC-1%-75	SCC-1.5%-75	SCC-0.75%-75	SCC-0.75%HS-75	CRC-2%-75	CRC-2%-38	CRC-4%-75	CRC-4%-38	CRC-6%-75
Pan Mixer	✓	✓	✓	✓	✓				✓	✓	✓	✓	✓
Drum Mixer						✓	✓	✓					

a) Pan Mixer

b) Drum Mixers

c) Mortar mixer

Figure 3.8 Mixers used in the experimental program.

3.4.1.2 Mixing Procedure SFRC

The SFRC mixes were prepared by adding the required amount of prepackaged ready-mix KING-SCC to the mixer, dry mixing for 30 seconds, and then pouring the water in several stages. The first half of the mix water was added and allowed to mix for 1 minute, then the remaining water was added in 4 steps at 60 second intervals. After the initial SCC mixing steps, steel fibres were added gradually and mixed until uniform distribution was attained. Note that this mixing procedure was used regardless of mixer type.

3.4.1.3 Mixing Procedure CRC

For the CRC mixtures, before the first batch was mixed, the electric pan mixer was wetted and then any remaining free water was removed. The required amount of pre-packaged CRC was added to the mixes, and dry-mixed for 30 seconds. The water was then added slowly without stopping the mixer. After 10 minutes, when the superplasticizer was sufficiently activated, the fibres were distributed evenly in the mixer over a period of approximately 1 minute. All ingredients were then mixed together for an additional 5 minutes.

3.4.1.4 Casting and Curing

After mixing was complete, the concrete was poured from the mixer into a wetted wheel barrow, and then transferred from the wheel barrow to the forms using plastic buckets. Figure 3.9 shows the placing and curing procedures used in this experimental program. Due to the confined areas for concrete consolidation, all specimens were vibrated to ensure proper placing using a 25 mm (1 in) vibrator until the ingredients were visibly consolidated. Once pouring was complete and the concrete surface was levelled with trowels, the specimens were covered with moist burlap, and plastic sheeting. The specimens were allowed to cure for seven days in these conditions. On the seventh day, the columns were removed from their forms and air-cured in the laboratory until the day of testing.

3.4.2 Fresh state properties

The ASTM C1611 Slump Flow of Self-Consolidating Concrete test was completed on all batches of concrete used in this experimental program to examine the workability of the mixes. Visual inspection was used to examine uniformity of the mix and to assess if segregation occurred. The diameter of the spread concrete was measured in two perpendicular directions, averaged, and recorded as slump flow. Figure 3.10 and Figure 3.11 list the measured slump flow

diameters the SCC KING and CRC mixtures, respectively. The type and the content of steel fibres affected workability, as noted in the slump flow test results. Increasing the fibre content reduced the slump-flow diameters, and consequently the workability, of both the SFRC and CRC mixes. All mixes were sufficiently workable for typical construction, but mixes with high levels of fibre (1% and above for SFRC, 6% for CRC) were no longer self-consolidating. Aoude et al. (2009) determined that 1.5% fibre content is an upper limit for a semi-workable self-consolidating mix using the KING-SCC material. The flowability of the KING-SCC mixtures was also significantly influenced by fibre type, with recorded slump flow values declining in the case of using steel fibre with larger aspect ratio (l_f/d_f) such as in case of Dramix BP 80/30 fibre. While good workability was attained when normal strength fibres were used at moderate fibre contents (up to 1.5%), the use of 0.75% of BP80/30 fibres significantly reduced workability owing to the higher aspect ratio of this fibre (some non-uniformity and segregation was observed visually for this mix).

Figure 3.9 Placing concrete and curing the columns

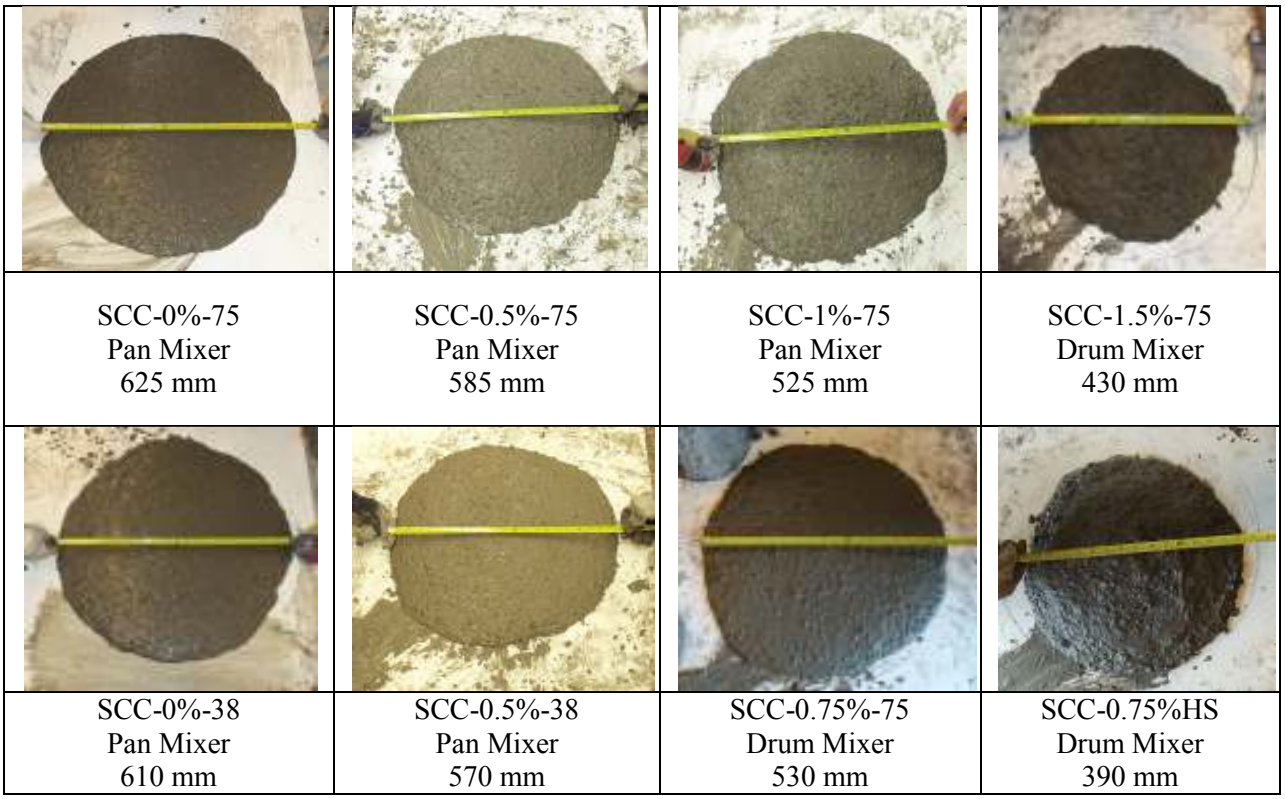

SCC-0%-75 Pan Mixer 625 mm	SCC-0.5%-75 Pan Mixer 585 mm	SCC-1%-75 Pan Mixer 525 mm	SCC-1.5%-75 Drum Mixer 430 mm
SCC-0%-38 Pan Mixer 610 mm	SCC-0.5%-38 Pan Mixer 570 mm	SCC-0.75%-75 Drum Mixer 530 mm	SCC-0.75%HS Drum Mixer 390 mm

Figure 3.10 Photos of slump flow test results for KING-SCC, including mixer type and average slump flow diameters

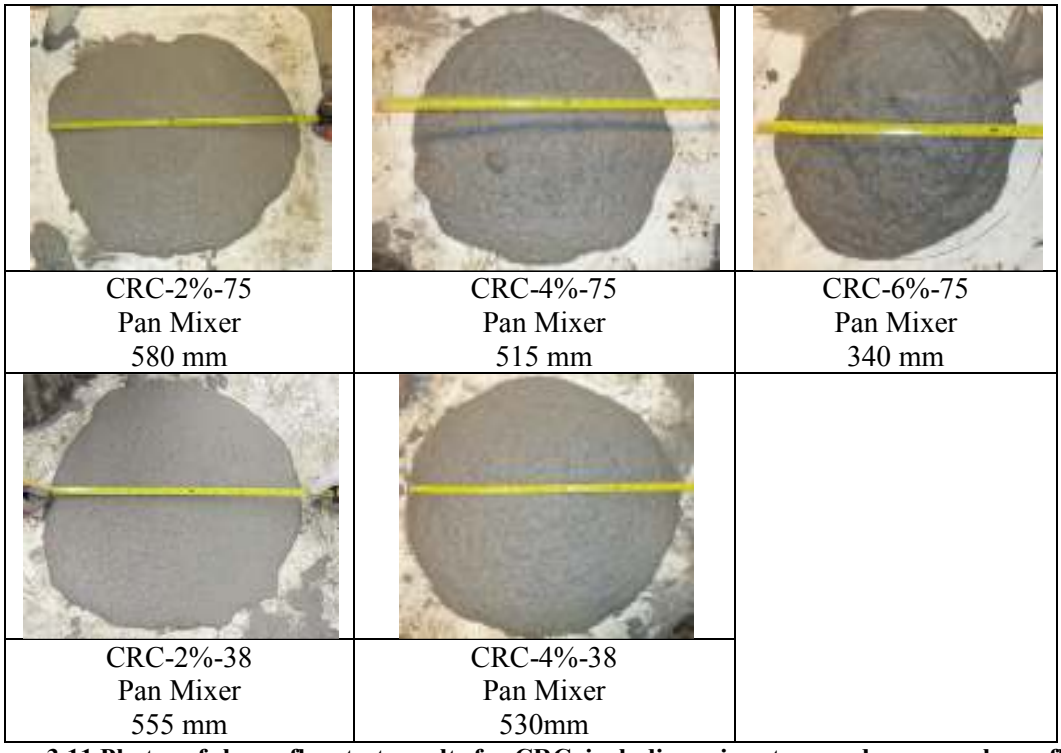

CRC-2%-75 Pan Mixer 580 mm	CRC-4%-75 Pan Mixer 515 mm	CRC-6%-75 Pan Mixer 340 mm
CRC-2%-38 Pan Mixer 555 mm	CRC-4%-38 Pan Mixer 530mm	

Figure 3.11 Photos of slump flow test results for CRC, including mixer type and average slump flow diameters

3.4.3 Hardened State Concrete Properties

A series of concrete cylinders and flexural beams were prepared during the mixing of the concrete, and cured in similar conditions as the specimens themselves. Cylinders casted from each batch were tested to determine the compressive strength of concrete within the columns by testing standard cylinders of 100 mm diameter by 200 mm height. The average compressive strength of each batch, as listed in Table 3.8, was obtained by testing cylinders at the Structures Laboratory at University of Ottawa [Figure 3.12 (a)]. Another series of compressive strength tests were carried out on a similar set of cylinders to plot the full stress-strain relationship of the materials under compression. All stress-strain curves of the CRC cylinders were determined using equipment at the Jamieson Structures Laboratory at McGill University [Figure 3.12 (b)] due to their high compressive strengths. The compressive stress-strain curves are shown in Figure 3.13. Four-point bending tests were used to determine the flexural toughness of SCC batches, in accordance with ASTM C1609 standards. When batch yields were sufficient, flexural beams were casted with dimensions of 100 mm by 100 mm by 400 mm. The flexural beams were subjected to third-point loading over a span of 300 mm, as shown in Figure 3.12 (c). The results, as defined in the ASTM C1609 Standard, are presented in Table 3.9. The load-deflection relationships for available specimens are presented in Figure 3.14, and they figures show that the addition of fibres improves flexural toughness, and post-cracking ductility in CRC as noted by the improvement in the post-peak stage of the specimen response.

(a) Cylinder testing machine (University of Ottawa) (b) Cylinder testing machine (McGill University) (c) Flexural beam testing machine (University of Ottawa)

Figure 3.12 Testing apparatuses used to assess concrete strength in this experimental program

Table 3.8 Concrete Properties

Column	Concrete Type	Fibre Type	Fibre Content V_f (%)	Compressive Strength f_c' (MPa)
SCC-0%-75	KING-SCC	ZP-305	0.00	51.56
SCC-0%-38		ZP-305	0.00	51.78
SCC-0.5%-75		ZP-305	0.50	53.84
SCC-0.5%-38		ZP-305	0.50	60.58
SCC-0.75%-75		ZP-305	0.75	54.67
SCC-0.75%HS-75		RC-80/30-BP	0.75	40.46
SCC-1%-75		ZP-305	1.00	46.03
SCC-1.5%-75		ZP-305	1.50	56.64
CRC-2%-75	CRC Joint Cast	OL-12/.40	2.00	144.73
CRC-2%-38		OL-12/.40	2.00	149.34
CRC-4%-75		OL-12/.40	4.00	152.60
CRC-4%-38		OL-12/.40	4.00	153.91
CRC-6%-75		OL-12/.40	6.00	165.39

Table 3.9 Results from ASTM C1609 toughness test

Mixture Name	ASTM C1609										
	P1	**δ1**	**Pp**	**δp**	**f1**	**fp**	**P600**	**f600**	**P150**	**f150**	**T150**
SCC-0%	-	-	22.81	0.070	-	6.84	-	-	-	-	-
SCC-0.5%	23.51	0.079	21.79	0.511	7.05	6.53	21.75	6.53	13.53	4.06	35.69
SCC-.75%HS	18.93	0.061	22.54	0.630	5.68	6.76	21.86	6.56	15.52	4.66	37.18
SCC-1%	22.23	0.078	22.92	0.348	6.67	6.87	22.24	6.67	13.34	4.00	36.11
SCC-1.5%	25.24	0.130	25.75	0.477	7.57	7.73	25.69	7.71	18.33	5.50	46.01

L = Span Length (300 mm), (L/600 = 0.5, L/150 =2)
P_1= First-Peak Load (kN)
δ_1= Net Deflection at First-Peak Load (mm)
P_p= Peak Load (kN)
δ_p= Net Deflection at Peak Load (mm)
f_1= First-Peak Strength (MPa)
f_p= Peak Strength (MPa)
P_{600}= Residual Load at net deflection of L/600 (kN)
f_{600}= Residual Strength at net deflection of L/600 (MPa)
P_{150}= Residual Load at net deflection of L/150 (kN)
F_{150}= Residual Strength at net deflection of L/150 (MPa)
T_{150}= Area under load vs. net deflection curve (0 to L/150), (kN*mm)
FT = Flexural Toughness Factor = $(T_{150}*L)/(L/150 *b*d^2)$

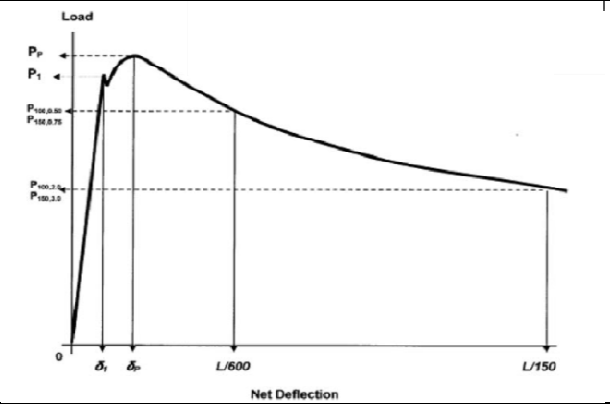

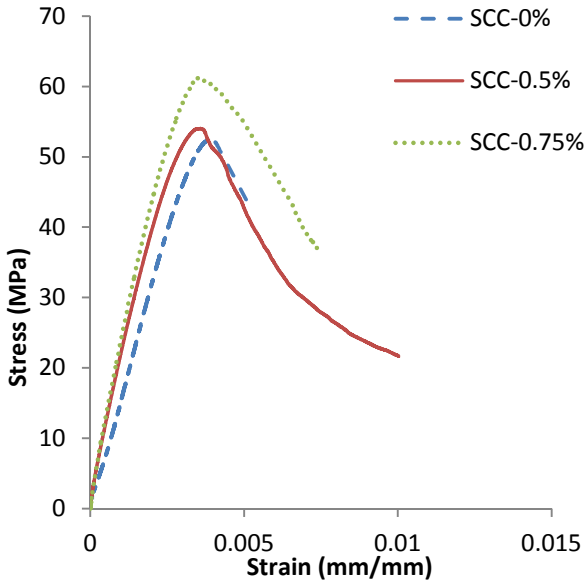

a) Concrete cylinder compression stress-strain relationship SCC 0%, 0.5%, 0.75%

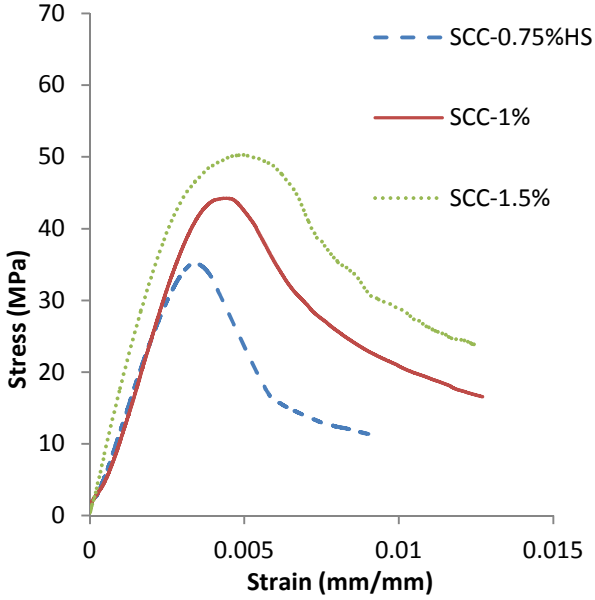

b) Concrete cylinder compression stress-strain relationship 0.75%HS, 1%, 1.5%

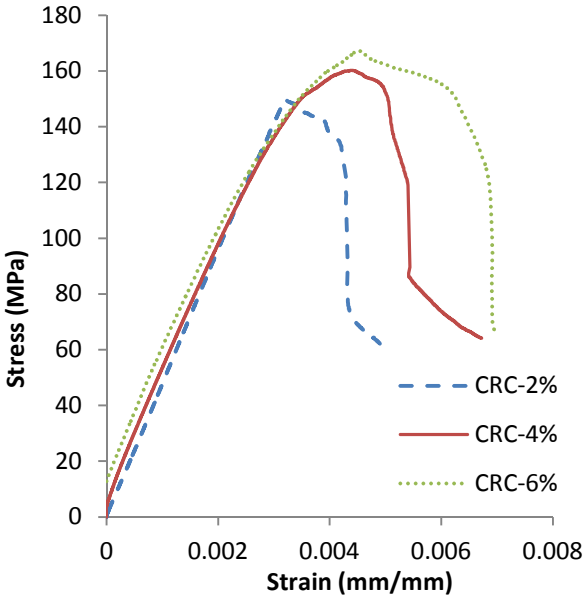

c) Concrete cylinder compression stress-strain relationship CRC 2%, 4%, 6%

Figure 3.13 Typical concrete cylinder stress-strain curves for SCC and CRC

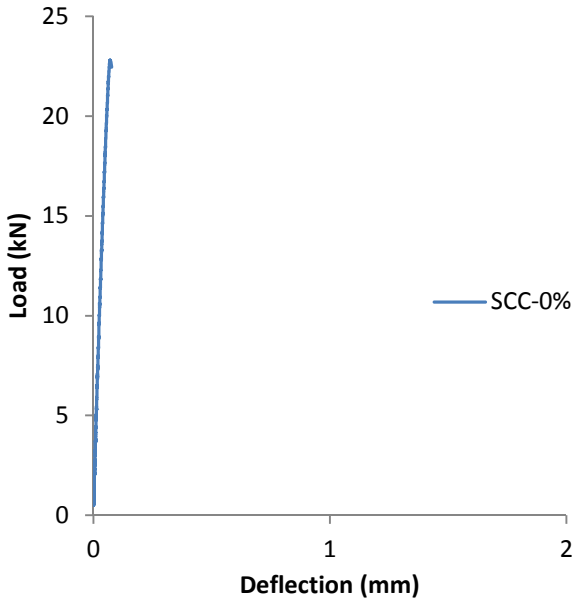

a) Flexural beam load-deflection curve SCC 0%

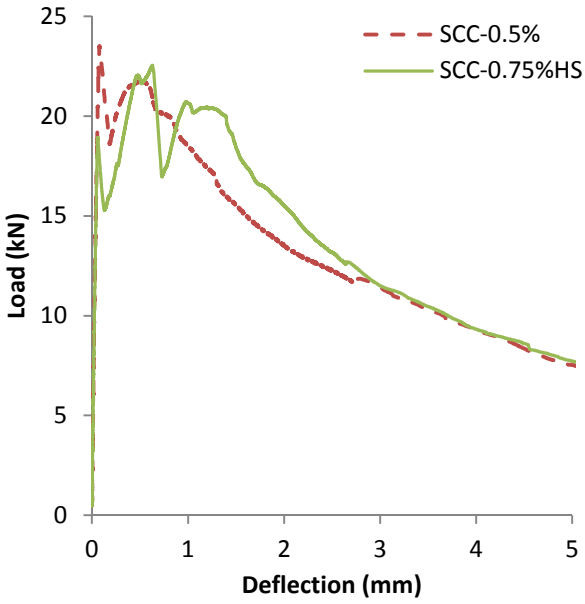

b) Flexural beam load-deflection curves SCC 0.5%, 0.75%HS

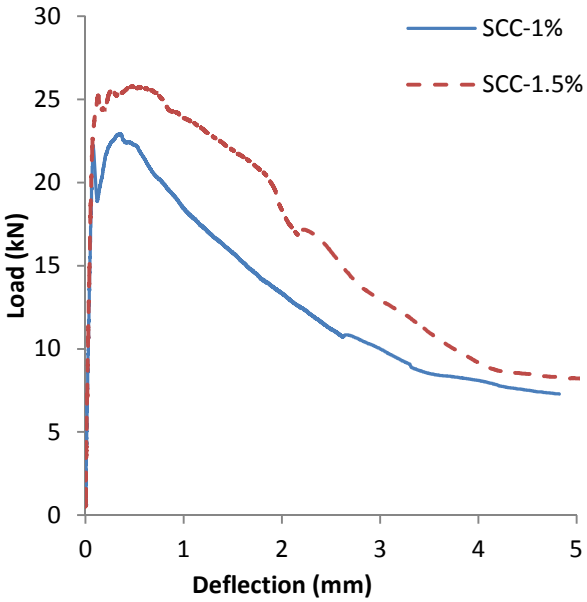

c) Flexural beam load-deflection curves SCC 1%, 1.5%

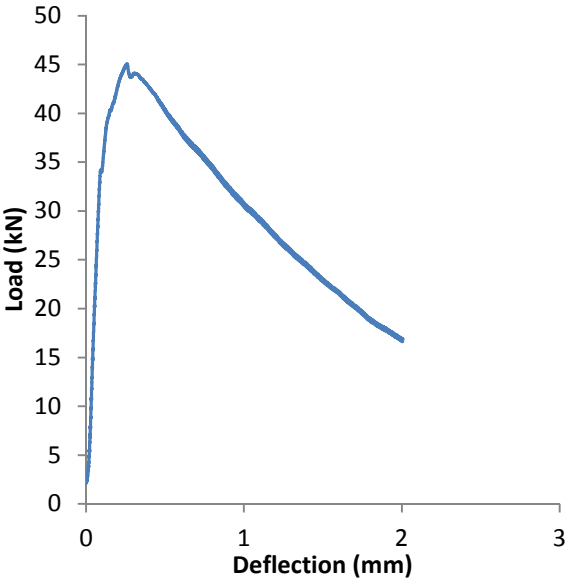

c) Flexural beam load-deflection curves CRC 2%

Figure 3.14 Typical concrete flexural beam load-deflection curves for SCC and CRC

3.4.4 Placement Difficulties

The results discussed and compared in Sections 4 and 5 of this study indicated several specimens that did not behave as expected. This is likely due to problems encountered with construction at the time of mixing and placing the specimens, related to the use of relatively long fibres (30 mm) in relatively small spaces (5 mm cover, 38 mm tie spacing). These problems are primarily due to the use of half-scale columns combined with fibres intended for full-scale construction. The test columns that did not provide expected results are SCC-0.5%-38, SCC-0.75%HS-75, CRC-4%-38, and CRC-6%-75. The following subsections endeavour to explain the missteps in casting the specimens that lead to unsatisfactory results.

3.4.4.1 SCC-0.5%-38

The key difficulty with concrete placement for this column is because the fibres used were 30 mm in length, combined with a 31 mm clear spacing between likely leading to fibres not consolidating properly in the mix due to the limited space. The tight spacing of the ties made it difficult to vibrate the specimen in all areas. Furthermore, areas where the strapping was placed across the top of the formwork (Figure 3.9) at the mid-span of the columns and near the support regions were not vibrated at all, and consequently there was improper consolidation and an increase of air voids with visible honeycombing in key areas of the column.

3.4.4.2 SCC-0.75%HS-75

There were significant challenges with the casting of this column. Due to the higher aspect ratio of the BP-80/30 fibre (l_f/d_f = 30 mm / 0.38 mm = 79), there was an increase in the number of actual fibres in the mix when compared to SCC-0.75%-75 that used the ZP-305 fibres (l_f/d_f = 30 mm / 0.55 mm = 55). The slump flow result for this batch was 390 mm, which demonstrates that it was a very stiff mixture when compared to the other specimens. This fact combined with the small spaces of the half-scale column design lead to a very poorly consolidated mixture despite significant vibration during placement. The compressive cylinder strength tests demonstrated a much weaker concrete for this column; it is noted that large air voids were observed in this column after the formwork was stripped. As noted earlier a drum mixer was used to cast this column; subsequent trials have demonstrated that the use of a pan mixer greatly improves workability of the SCC mix when BP 80/30 fibres are used.

3.4.4.3 CRC-4%-38

Similarly to SCC-0.5%-38, the difficulties in placing lie with the confined spacing of the transverse ties. In addition, while the fibres were not as long as those used in the SFRC specimens, the amount of fibres in this column were greatly increased, resulting in a much stiffer mix. Finally, it should be noted that the placing instructions provided by the manufacturer of CRC mix dictate that horizontal casting should be avoided. However, due to the limitations of available equipment, vertical casting was not possible for this experimental program. The practice of horizontal casting with the increased amount of vibration needed for this stiffer mix causes consolidation of larger particles at the bottoms of the forms, and thus may have lead to one face of the column being weaker than the other.

3.4.4.4 CRC-6%-75

A comparison of Figure 3.11 indicates that the slump flow test results of the CRC-6% mix demonstrate a very stiff batch. While this column was not seismically detailed, the use of a very stiff concrete required a considerable amount of vibration to ensure a uniform distribution of concrete within the forms. Unfortunately, the excessive vibration used in this specimen likely caused separation of the mortar, and thus a weaker column when compared to the other CRC specimens.

3.5 Test procedure and instrumentation

3.5.1 Test Setup

Figure 3.15 shows the typical test setup used in this experimental program. All columns were tested under combined axial loading and transverse simulated blast loads. The axial loading was applied using hydraulic jacks, and the transverse loading was applied with the shock tube at the University of Ottawa.

3.5.2 Axial Loading Mechanism

The columns were loaded axially with a static load to the maximum capacity of the electronic pump that activated two 6 inch^2 (3871 mm^2) hydraulic jacks. With a pump capacity of 5500 psi (37,921 kPa), an axial load of 294 kN was applied; this load level represented what is similar to what can be expected in actual structures (≈30% of pure axial load capacity) for the SFRC columns. The hydraulic jack was located below the column, and the axial load was transferred

from the hydraulic jack through the column to the 914 mm thick concrete strong floor above. The column was separated from the jack and the ceiling with steel rollers sandwiched between two bevelled steel plates.

3.5.3 Lateral Load Transferring Mechanism

In order to transfer the shockwave pressure generated by the shock tube to non-planar elements a load transferring device (LTD) must be used. In the case of the columns, the LTD collects the shock wave pressure and transfers it as a uniformly distributed load along the face of the columns. In this experimental program, the LTD consisted of a light gauge steel metal sheet connected to a series of steel beams, as shown in Figure 3.15. The eight steel beams used in the LTD were 76.2 mm × 76.2 mm × 2438 mm hollow square structural steel sections (thickness of 6.35 mm) that spanned the width of the shock tube opening, perpendicular to the height of the column. Each beam had a similar six inch long section welded to the top and bottom at mid span in order to assist with evenly distributing the blast load along the column. The beams are in turn connected to 0.71 mm thick steel sheet metal that covers the entire area of the end frame, 2438 mm by 2438 mm, for a total device mass of 209 kg. The LTD is connected to the shock tube by chains at the top, is free to rotate at the top, and completely free to move at all other locations up to the point of maximum deflection of the column.

Figure 3.15 Typical test setup

3.5.4 Supports

For all of the tests the columns were fixed to the shock tube frame using partially-fixed supports at the top and bottom that were intended for lateral restraint and to prevent rotation of the column. Figure 3.16 outlines the support configuration used for all tests at both the top and bottom. Previous experimental work with these shock tube supports determined a rotational stiffness of 903000 N*m/rad (Jacques et al. 2012). The supports were constructed using steel plates welded onto hollow structural steel sections. The supports were connected to the shock tube end-frame using a total of twelve 15.9 mm bolts per support. The clear spacing between supports was 1980 mm.

Figure 3.16 Partially fixed lateral restraint

3.5.5 Instrumentation

Each column was instrumented with ten electric resistance strain gauges, with six located on the longitudinal reinforcing bars, and four on select transverse ties near the mid-span of the columns and near the support region (350 ohm linear strain gauges, 6 mm in length). Of the six strain gauges placed on the longitudinal bars, three were placed on the bar closest to the LTD and the other three on the bar on the opposite side (named the compression side and tension side respectively, due to their behaviour at mid-span). Strain gauges were also placed on transverse ties near the support region to assess shear, and at the mid-span to assess confinement. Figure 3.17 shows the locations of seven of the strain gauges for each column (the remaining three gauges are located at the bottom of the column and are installed in a similar manner as gauges 1, 2, and 3).

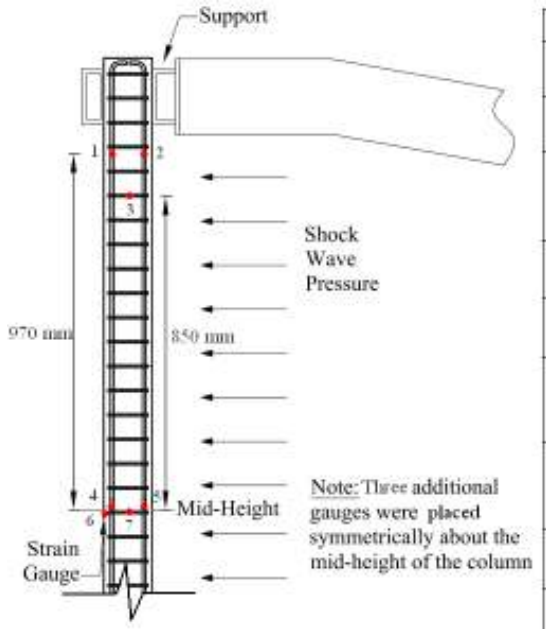

#	Name	Description	Notes
1	TT	Tension Top	Longit. Rebar, Opposite LTD, Top of Column
2	CT	Compression Top	Longit. Rebar, LTD side, Top of Column
3	ST	Strain Top	Transverse Tie, on section parallel to direction of shock wave
4	TM	Tension Middle	Longit. Rebar, Opposite LTD, Centre of Column
5	CM	Compression Middle	Longit. Rebar, LTD side, Centre of Column
6	SM2	Strain Middle 2	Transverse Tie, on section perpendicular to direction of shock wave
7	SM1	Strain Middle 1	Transverse tie on section parallel to direction of shock wave
	TB	Tension Bottom	Mirror of TT
	CB	Compression Bottom	Mirror of CT
	SB	Strain Bottom	Mirror of ST

Figure 3.17 Strain gauge locations and descriptions

Complete displacement-time histories were recorded using three linear variable differential transducers (LVDT) with a 300 mm stroke. The LVDTs were placed at 1/2 (mid-height), 1/3rd, and 1/6th distance along the clear span of the column. With a clear span height of 1980 mm, the LVDTs were 990 mm, 660 mm, and 330 mm measured from the bottom of the clear span (Figure 3.18). The use of three LVDTs allowed for linearly extrapolation to be used in the event the maximum displacement did not occur at mid-height as expected. The reflected blast pressures were measured at the base and side of the shock tube end frame using voltage differential high resolution pressure probes with 14.5 mV/kPa sensitivity capable of reading a maximum pressure of 345 kPa (5000 mV) (Lloyd, 2010).

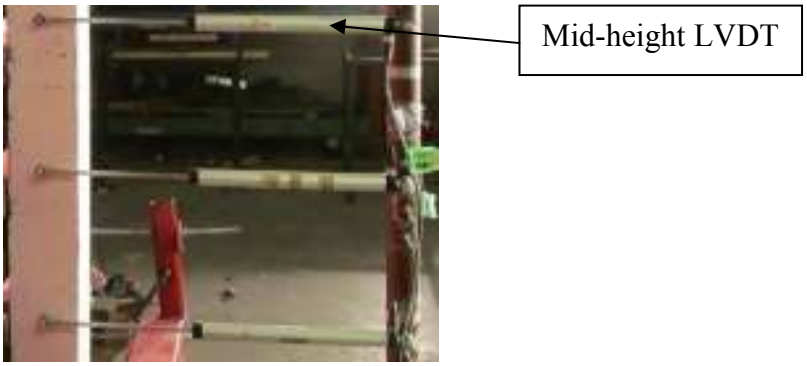

Figure 3.18 LVDT connection to column (left) and support post (right)

3.5.6 Data Acquisition

Two digital oscilloscopes recording at 100,000 Hz (samples per second) were used as the data acquisition system (DAC). Ten channels recorded strain readings, two channels recorded pressure, and three channels recorded displacement. The DAC system continuously measured and recorded strains, displacements, and pressures in an overwriting loop until a trigger signal was received on one of the pressure channels. When the pressure at the face of the load transferring system reached the preset level, the system began recording the required data, and initiated the recording of the high speed video camera (Lloyd, 2010). Pressure measurements near the load transfer device were used to record complete reflected pressure time histories for each test. The high speed camera was placed at the side of the column during testing, and recorded the column response at a frame rate of 500 frames per second, which allowed for detailed observation of column deflection at high speed.

3.5.7 Test Procedure and Loading Program

Each column was subjected to a series of varying shock tube induced shockwaves until failure. Failure was defined as either compression reinforcing steel buckling or tension reinforcing steel rupture. The shock wave pressures were selected based on a previous study by the University of Ottawa research group on traditional reinforced concrete columns having similar properties. With the exception of one shot, the driver length was kept constant at 2743 mm (9 ft) while the selected driver pressures were 69 kPa (10 psi), 207 kPa (30 psi), 552 kPa (80 psi), and 689 kPa (100 psi). The chosen pressure parameters aimed at testing the columns under elastic (Blast 1), yield (Blast 2), and ultimate loading conditions (Blasts 3, 4, 5).

Table 3.10 Blast load properties

Name	Driver Pressure kPa (psi)	Driver Length mm (ft)	Average Reflected Pressure (P_r) kPa	Average Reflected Impulse (I_r) kPa*msec	Average Positive Phase Duration (t_d) msec
Blast 1	69 (10)	2743 (9)	13.28	125.36	21.36
Blast 2	207 (30)	2743 (9)	42.75	387.47	22.95
Blast 3	552 (80)	2743 (9)	78.90	747.81	26.21
Blast 4	689 (100)	2743 (9)	96.28	892.65	25.09
Blast 5	689 (100)	4267 (9)	81.54	1355.12	33.04

4 Experimental Results

4.1 Introduction

This section compares the results from the thirteen columns tested in the experimental program. The response of the columns in terms of pressure-displacement time history, maximum and residual displacements, strains in reinforcing steel, failure mode and damage tolerance is discussed. Section 4.2 provides an overall summary of the test results, while section 4.3 summarizes the response of each individual column.

4.2 Summary of results

Overall summaries of the test results for the SFRC and CRC columns are listed in Table 4.1 and Table 4.2, respectively. The tables report the shockwave properties for each test, including the recorded maximum reflected pressure (P_r), total reflected impulse over the positive phase duration (I_r), positive phase duration (t_d) along with the response of each column, including maximum and residual mid-height displacements (D_{max} and D_{res}).

Three blasts were typically used to test the SFRC columns with non-seismic detailing at elastic, yield and ultimate conditions Blasts 1, Blast 2 and Blast 3, respectively. An additional blast was applied in the case of SFRC columns with seismic detailing (Blast 4). For the CRC columns, four blasts were typically applied (Blasts 1 to 4), with one additional blast used in the case of some specimens (Blast 4(2) or Blast 5).

Pressure values listed in Table 4.1 were those acting on the load transfer device as recorded by pressure transducers on the interior of the shock tube expansion section. Impulse values presented are the integral of the recorded pressure-time histories up to the first local maximum, this represented the point where the pressure-time curve crossed the origin (end of the positive phase). The impulse values represent the area under the pressure-time curve calculated using the trapezoidal method using the graph software *DPlot*.

Note that the displacement and rotation values reported in the tables are not cumulative since the LVDTs were re-zeroed following each blast test. The cumulative values for residual displacements are reported in Section 4.3.

The column strain gauges were also zeroed prior to each test. Furthermore, the axial strain due to the initially applied axial load is calculated from Equation 4.1:

$$\varepsilon_{axial} = \left(\frac{P}{A_T E_c}\right) \quad [4.1]$$

where P is the axial load and A_T is the transformed area of the column given as:

$$A_T = A_g + (n-1)A_s \quad [4.2]$$

where A_g gross cross-sectional area of the column, A_s is the area of the longitudinal reinforcing steel, and n is the ratio of the modulus of elasticity of the steel reinforcing steel (E_s) to the modulus of elasticity of the concrete (E_c).

The total strains (ε_{tot}, reported in parentheses) in the following subsections are the sum of the recorded maximum strains, the calculated axial strain, and residual strains from previous blasts.

Table 4.1 Summary of SFRC series test results.

		Shockwave Properties			Maximum Mid-Span Displacement	Residual Mid-Span Displacement
		P_r	t_d	I_r	D_{max}	D_{res}
		(kPa)	(msec)	(kPa*msec)	(mm)	(mm)
SCC-0%-75	Blast 1	13.66	22.18	130.01	6.42	1.77
	Blast 2	42.36	22.20	380.95	29.86	9.65
	Blast 3	87.87	25.38	780.67	126.23	108.50
SCC-0%-38	Blast 1	12.67	21.93	123.17	6.62	0.42
	Blast 2	40.87	24.35	401.35	24.98	5.76
	Blast 3	79.17	32.07	755.80	91.99	56.82
	Blast 4	108.61	28.47	963.71	340.89	308.76
SCC-0.5%-75	Blast 1	12.66	22.58	130.81	5.04	0.07
	Blast 2	41.06	21.29	399.80	21.29	4.79
	Blast 3	82.32	26.28	784.13	93.93	60.61
SCC-0.5%-38	Blast 1	13.76	21.91	143.72	6.72	0.45
	Blast 2	46.22	23.81	416.01	26.62	5.52
	Blast 3	82.63	23.70	769.47	99.67	69.18
	Blast 4	105.71	25.04	886.68	248.55	234.33
SCC-0.75%-75	Blast 1	15.52	29.29	192.64	11.46	2.38
	Blast 2	40.64	23.22	409.64	29.25	7.60
	Blast 3	86.48	23.06	675.87	81.71	56.58
SCC-0.75%HS-75	Blast 1	12.80	18.78	125.73	7.98	2.11
	Blast 2	40.12	20.62	383.83	26.98	9.05
	Blast 3	77.16	21.89	782.89	112.57	95.89
SCC-1%-75	Blast 1	12.48	22.49	127.09	5.11	0.59
	Blast 2	40.68	24.04	410.63	23.32	5.38
	Blast 3	76.62	43.60	767.32	87.72	47.56
SCC-1.5%-75	Blast 1	12.79	21.88	137.90	5.73	1.37
	Blast 2	38.52	26.30	394.98	24.13	6.04
	Blast 3	73.16	22.50	681.05	72.99	34.34

Table 4.2 Summary of CRC series test results.

		Shockwave Properties			Maximum Mid-Span Displacement	Residual Mid-Span Displacement
		P_r	t_d	I_r	d_{max}	d_{res}
		(kPa)	(msec)	(kPa*msec)	(mm)	(mm)
CRC-2%-75	Blast 1	12.57	18.58	108.45	5.15	1.60
	Blast 2	44.25	19.89	334.44	21.19	3.95
	Blast 3	82.22	25.32	735.60	67.76	21.72
	Blast 4	88.76	25.53	938.39	309.48	287.78
CRC-2%-38	Blast 1	13.62	21.05	106.29	5.15	0.74
	Blast 2	45.65	23.54	380.53	20.15	3.50
	Blast 3	71.69	23.05	693.55	47.43	8.08
	Blast 4	92.84	24.79	841.36	71.30	12.78
	Blast 4 (2)	98.44	21.14	771.21	269.53	241.79
CRC-4%-75	Blast 1	13.06	21.52	123.45	4.74	0.35
	Blast 2	46.40	22.31	398.09	21.59	3.98
	Blast 3	83.29	25.95	776.07	57.15	14.15
	Blast 4	91.08	27.99	1001.84	94.25	25.75
	Blast 5	81.54	33.04	1355.12	NO DATA	NO DATA
CRC-4%-38	Blast 1	14.97	22.14	120.63	5.05	0.13
	Blast 2	43.82	21.13	364.87	22.03	3.97
	Blast 3	75.57	22.58	730.17	69.21	22.05
	Blast 4	81.63	24.76	850.63	NO DATA	NO DATA
CRC-6%-75	Blast 1	14.34	21.23	127.07	5.33	0.34
	Blast 2	43.07	25.88	384.15	23.23	3.97
	Blast 3	75.14	22.16	716.96	56.28	16.19
	Blast 4	103.19	22.99	887.35	373.20	349.75

4.3 Description of Experimental Results – SFRC test series

4.3.1 SCC-0%-75

This column was the first of two "control" specimens constructed with SCC and without steel fibres, and the first column to be tested in the SFRC test series. This particular column had non-seismic detailing (s = 75 mm), and thus serves as baseline for comparison with the other columns in the experimental program. The shock wave data, as recorded by the shock tube pressure inducers that impinged on the load transfer device can be found in Table 4.1. Complete pressure and impulse time histories, and pressure and mid-span displacement time histories for each blast on this column are shown in Figure 4.1 to Figure 4.3. Figure 4.4 and Figure 4.5 include photographs detailing the effects of each blast on the column.

Blast 1 was intended to test the column within the elastic range. The maximum and residual displacements were 6.42 mm and 1.77 mm respectively. Strain gauge data at mid-span shows a maximum strain of 0.0007mm/mm (ε_{tot} = 0.001), which indicates the longitudinal reinforcing steel bars remained elastic. Some chipping of the concrete at the compression face and load transfer device interface occurred, which can be seen in Figure 4.4 a). There were no observable cracks in the tension face of the column; however the lack of observable cracking may have been due to the application of a thicker than usual paint layer onto this column.

Blast 2 was intended to bring the column into the plastic region, and the strain gauge data at mid-span shows a maximum strain of 0.005mm/mm (ε_{tot} = 0.0054), which indicates yielding of the longitudinal reinforcing steel bars. For this blast, maximum and residual displacements of 29.86 mm and 9.65 mm (11.42 mm cumulative) were recorded. High speed video data shows more chipping and spalling of the concrete at the compression face and load transfer device interface, and the formation of secondary blast fragments. Cracks were observed at the mid-span of the column and 75mm above, as shown in Figure 4.5 a), indicating that cracking occurred at the location of the ties.

Blast 3 resulted in column failure, as intended. The column failure was due to compression reinforcing steel buckling. Strain gauge data at mid-span is not available due to limitations of the gauge at extreme strains. High speed video data shows significant crushing of the concrete at

the compression face and load transfer device interface and the formation of secondary blast fragments. Figure 4.4 shows diagonal cracks at the mid-span extend from the location of reinforcing steel buckling outwards towards the tension face of the column. There is also significant spalling of the concrete along the tension reinforcing steel at mid-span of the column. Diagonal cracks also occur in the support region showing the formation of plastic hinges in that location. For this column, the maximum and residual displacements were 126.23 mm and 108.50 mm (119.92 mm cumulative), respectively.

4.3.2 SCC-0%-38

This column was the second control specimen in the SFRC test series. The column had identical properties to the previous column but with reduced tie spacing (s = 38 mm) to study the effect of seismic detailing on blast performance of reinforced concrete columns. The shock wave data, as recorded by the shock tube pressure inducers that impinged on the load transfer device can be found in Table 4.1. Complete pressure and impulse time histories, and pressure and mid-span displacement time histories for each blast on this column are shown in Figure 4.6 to Figure 4.9. Figure 4.10 and Figure 4.11 include photographs detailing the effects of each blast on the column.

Blasts 1 resulted in maximum and residual displacements of 6.62 mm and 0.42 mm, respectively, with the strain gauge data at mid-span showing a maximum strain of 0.0011 mm/mm (ε_{tot} = 0.0015), indicating that the longitudinal reinforcing steel bars remained elastic. There was no observable damage to the column for this blast.

Blast 2 strain gauge data at mid-span shows a maximum strain of 0.015 mm/mm (ε_{tot} = 0.01546), which indicating that the strains in the longitudinal reinforcing steel bars were within their plastic range. The maximum and residual displacements were 24.98 mm and 5.76 mm (6.18 mm cumulative), respectively, with the latter confirming that this test had brought the column into the plastic range. Vertical cracks were observed at the mid-span of the column along the compression face, as shown in Figure 4.11 a); however they follow a region of visible air voids due to improper placement of the concrete.

Blast 3 resulted in maximum displacement of 91.99 mm and a residual displacement of 56.82 mm (63.00 mm cumulative). Strain gauge data at mid-span is not available due to limitations of the gauge at extreme strains. In addition to reducing displacements when compared to specimen SCC-0%-75, reinforcing steel buckling was prevented in this column due to the seismic detailing of the column. Nonetheless, high speed video data shows significant crushing of the concrete at the compression face and the formation of secondary blast fragments. Diagonal cracks at the mid-span extend from the compression face outwards towards the tension face of the column, as can be seen in Figure 4.10 c). Diagonal cracks also appeared in the support region showing the formation of plastic hinges in that location.

Since Blast 3 did not cause this column to fail, the specimen was subjected to a fourth blast. The column failed due to tension reinforcing steel rupture after Blast 4, with the large impulse resulting is significantly large mid-span displacements [D_{max} = 340.89 mm and D_{res} = 308.76 mm (371.76 mm cumulative)]. Diagonal cracks at the mid-span increased in size, with crushing (in the compression face) and spalling (on the tension face at mid-span) were observed. High speed video data shows the formation of secondary blast fragments.

The results from this column indicate that seismic detailing results in improved control of maximum and residual displacements due to improvement confinement of core concrete, as will be discussed in Section 5. In addition, the results demonstrate that a reduction in clear distance between transverse ties is an effective means of prevention of compression reinforcing steel buckling.

4.3.3 SCC-0.5%-75

Other than for the 0.5% of steel fibres by volume, this specimen was constructed to have identical properties to specimen SCC-0%-75, and was the first of a series of specimens intended to study the effect of combined use of SCC and fibres on column performance. The shock wave data, as recorded by the shock tube pressure inducers that impinged on the load transfer device can be found in Table 4.1. Complete pressure and impulse time histories, and pressure and mid-span displacement time histories for each blast on this column are shown in Figure 4.12 to Figure

4.14. Figure 4.15 and Figure 4.16 include photographs detailing the effects of each blast on the column.

As in the previous specimens, Blast 1 kept the column within the elastic range with maximum displacement of 5.04 mm, residual displacement of 0.07 mm and strain gauge data showing that the longitudinal reinforcing steel bars remained elastic (maximum strain of 0.0008 mm/mm (ε_{tot} = 0.0011). Minor chipping of the concrete occurred on the compression face, as shown in b), and observable horizontal cracks occurred spaced at 75mm as shown in Figure 4.16 a), which indicating cracking occurred along the ties on the tension face of the concrete.

Blast 2 strain gauge data at mid-span shows a maximum strain of 0.0038 mm/mm (ε_{tot} = 0.0042), indicating the longitudinal reinforcing steel bars were strained beyond yield. No additional cracking was observed, with maximum and residual displacements of 21.29 mm and 4.79 mm (4.86 mm cumulative), respectively.

Blast 3 strain gauge data at mid-span is not available due to limitations of the gauge at extreme strains. Although maximum and residual displacements were reduced when compared to the control specimen (D_{max} = 93.93 mm and D_{res} = 60.61 mm (65.47 mm cumulative), the column failed at this blast loading due to compression reinforcing steel buckling. It is noted that maximum displacement occurred 75 mm below the centre of the column, and therefore it was necessary to compute the maximum displacements by extrapolation. Crushing of the concrete occurred at the compression face and spalling of the concrete along the tension reinforcing steel at mid-span of the column was restrained by the fibres. Diagonal cracks at the mid-span extended from the location of reinforcing steel buckling outwards towards the tension face of the column. High speed video data shows that while some secondary blast fragments occurred, this fragmentation was not as pronounced as for specimen SCC-0%-75 due to the ability of the fibres to control cover spalling.

4.3.4 SCC-0.75%-75

When compared to specimen SCC-0%-75, this column was reinforced with 0.75% fibres by volume of concrete, while all other construction remained the same. The shock wave data, as recorded by the shock tube pressure inducers that impinged on the load transfer device can be found in Table 4.1. Complete pressure and impulse time histories, and pressure and mid-span displacement time histories for each blast on this column are shown in Figure 4.17 to Figure 4.19. Figure 4.20 and Figure 4.21 includes photographs detailing the effects of each blast on the column.

Blast 1 strain gauge data at mid-span shows a maximum strain of 0.0022 mm/mm (ε_{tot} = 0.0026). In addition the column experienced maximum and residual displacements of 11.46 mm and 2.38 mm, respectively. The residual displacement and increased strain is the result of an impulse of 192.64 kPa*msec, compared to an average impulse of 130 kPa*msec for the remainder of the columns for Blast 1. This was due to an error in the selection of foils used in the spool section of the shock tube for this blast. There was no observable damage to the column post-test.

Blast 2 resulted in maximum and residual displacements of 29.25 mm and 7.60 mm (9.98 mm cumulative). The strain gauge data at mid-span shows a maximum strain of 0.006 mm/mm (ε_{tot} = 0.0078), which indicates the longitudinal reinforcing steel bars were within the plastic region. However, no observable damage was noted after this test.

As with the other specimens with non-seismic detailing, Blast 3 caused this column to fail due to compression reinforcing steel buckling. Nonetheless, the provision of steel fibres led to reduced maximum and residual displacements (when compared to SCC-0%-75 and SCC-0.5%-75 for Blast 3), which were 81.71 mm and 56.58 mm (66.56 mm cumulative) respectively. Strain gauge data at mid-span is not available due to limitations of the gauge at extreme strains. High speed video data shows slight crushing of the concrete at the compression face and significant reductions in secondary blast fragmentation when compared to the control column. Two significant horizontal cracks occurred along the tension face, the first at mid span along the tie in that location, and the other 75 mm above. Diagonal cracks at the mid-span extend from the

location of reinforcing steel buckling outwards towards the tension face of the column, as shown in Figure 4.21. Slight diagonal cracks also occur in the support region showing the formation of a plastic hinge in that location.

4.3.5 SCC-1%-75

The column was identical to the previous specimen but had an additional 0.25% of fibre reinforcement (total of 1% by volume of concrete). The shock wave data, as recorded by the shock tube pressure inducers that impinged on the load transfer device can be found in Table 4.1. Complete pressure and impulse time histories, and pressure and mid-span displacement time histories for each blast on this column are shown in Figure 4.22 to Figure 4.24. Figure 4.25 and Figure 4.26 include photographs detailing the effects of each blast on the column.

Constant with the previous test results, Blast 1 kept this column within the elastic range. Similarly, Blast 2 caused yielding of the reinforcement and resulted in permanent residual displacements after unloading. The maximum displacements for Blast 1 and Blast 2, were 5.11 mm and 23.32 mm, while residual displacements were 0.59 mm, 5.38 mm (5.97 mm cumulative), respectively. In terms of damage, no observable damage occurred after Blast 1. One small piece of concrete, approximately 10 mm in length, was chipped away at the mid-span of the column, along the compression face after Blast 2, as shown in Figure 4.26 a).

Continuing with the trend from the previous two SFRC specimens, Blast 3 resulted in reduced mid span displacements (D_{max} = 87.72 mm and D_{res} = 47.76 mm (53.53 mm cumulative) when compared to the control column, and failure occurred due to compression reinforcing steel buckling. High speed video data shows crushing of the concrete at the compression face and load transfer device interface. Although this resulted in formation of secondary blast fragments, the amount was reduced to very fine particles, as the larger fragments of concrete were restrained by fibres. Diagonal cracks at the mid-span were seen to extend from the location of reinforcing steel buckling outwards towards the tension face of the column. Spalling of the concrete along the tension reinforcing steel at mid-span of the column was restrained by the fibres, most notably a large piece that had a 75 mm width, as shown in Figure 4.26 c).

4.3.6 SCC-1.5%-75

This column was constructed with SCC and reinforced with the highest quantity of fibres used in this test series (1.5% fibres by volume of concrete). The shock wave data, as recorded by the shock tube pressure inducers that impinged on the load transfer device can be found in Table 4.1. Complete pressure and impulse time histories, and pressure and mid-span displacement time histories for each blast on this column are shown in Figure 4.27 to Figure 4.29. Figure 4.30 and Figure 4.31 includes photographs detailing the effects of each blast on the column.

For this column, the maximum recorded displacements for Blast 1 and Blast 2, and Blast 3 were 5.73 mm, 24.13 mm, and 72.99 mm respectively. The residual displacements for Blast 1, Blast 2, and Blast 3 were 1.37 mm, 6.04 mm (7.41 mm cumulative), and 34.34 mm (41.75 mm cumulative) respectively.

Blast 1 strain gauge data at mid-span shows a maximum strain of 0.0006 mm/mm (ε_{tot} = 0.001), which indicates the longitudinal reinforcing steel bars remained elastic. No observable damage occurred after Blast 1. Blast 2 strain gauge data at mid-span shows a maximum strain of 0.0046 mm/mm (ε_{tot} = 0.0051), which indicates the longitudinal reinforcing steel bars were within the plastic range. No observable damage occurred after Blast 2.

Blast 3 strain gauge data for the longitudinal reinforcing bars at mid-span is not available due to limitations of the gauge at extreme strains. As with the previous column, this column failed at this blast loading regimen due to compression reinforcing steel buckling. It is noted that while high speed video data shows crushing of the concrete at the compression face, the formation of blast fragments of concrete was prevented by the fibres. Similarly, spalling of the concrete along the tension reinforcing steel at mid-span of the column was restrained by the fibres.

The results from columns SCC-0.5%-75, SCC-0.75%-75, SCC-1%-75 and SCC-1.5%-75 demonstrate that the addition of steel fibres to a reinforced concrete column results in improvements in terms of reducing of maximum and residual mid-span displacements for blast loads causing yielding of the longitudinal reinforcing. Similarly the provision of fibres results in improved damage tolerance.

4.3.7 SCC-0.5%-38

This column aimed at studying the benefits of combined use of steel fibres and seismic detailing, and is a companion to specimens SCC-0.5%-75 (same quantity of fibres but larger tie spacing) and SCC-0%-38 (same tie spacing but no fibres). The shock wave data, as recorded by the shock tube pressure inducers that impinged on the load transfer device can be found in Table 4.1. Complete pressure and impulse time histories, and pressure and mid-span displacement time histories for each blast on this column are shown in Figure 4.32 to Figure 4.35. Figure 4.36 and Figure 4.37 includes photographs detailing the effects of each blast on the column.

Blast 1 kept the longitudinal reinforcing bar strains within the elastic range (maximum strain of 0.0012 mm/mm (ε_{tot} = 0.0016) and resulted in no apparent damage, nor residual displacements (D_{max} = 6.72 mm and D_{res} = 0.45 mm). Similar to previous results, Blast 2 brought the longitudinal reinforcing bars to the plastic range (0.0053 mm/mm (ε_{tot} = 0.0057) and resulted in some permanent displacements (D_{max} = 26.62 mm and D_{res} = 5.52 mm (5.97 mm cumulative). One horizontal crack appears along the tension face of the concrete at mid-span after this blast, as shown in Figure 4.37 a).

Similar to the companion specimen SCC-0%-38, the provision of seismic detailing in the column prevented compression reinforcing steel buckling after Blast 3. Although secondary blast fragments formed, large pieces were effectively restrained by the steel fibres. Diagonal cracks at the mid-span were seen to extend from the compression face outwards towards the tension face of the column. Diagonal cracks also occurred in the support region showing the formation of a plastic hinge in that location. In addition, the horizontal crack which formed during Blast 2 opened significantly to completely reveal the 6.3 mm tie in that location, as shown in Figure 4.37 b). Since the column did not fail an additional load (Blast 4) was imparted to the column. This severe loading resulted in rupture of the tension reinforcing steel, fracturing of the concrete on the tension face and formation of some secondary blast fragments. The maximum displacements for Blasts 3 and 4 were 99.67 mm and 248.55 mm, with corresponding residual displacements of 69.18 mm (75.15 mm cumulative) and 234.33 mm (309.48 mm cumulative).

The results from this test are inconclusive on the benefits of combining seismic detailing with steel fibres.

4.3.8 SCC-0.75%HS-75

This was the last specimen in the SFRC test series is a companion column to specimen SCC-0.75%-75. This column aimed at studying the influence of using high-strength steel fibres with a different aspect ratio (BP 80/30 fibres) on column response to shock wave loading. The shock wave data, as recorded by the shock tube pressure inducers that impinged on the load transfer device can be found in Table 4.1. Complete pressure and impulse time histories, and pressure and mid-span displacement time histories for each blast on this column are shown in Figure 4.38 to Figure 4.40. Figure 4.41 and Figure 4.42 includes photographs detailing the effects of each blast on the column.

For this column, the maximum displacements for Blast 1, Blast 2, and Blast 3 were 7.98 mm, 26.98 mm, and 112.57 mm respectively. The residual displacements for Blast 1, Blast 2, and Blast 3 were 2.11 mm, 9.05 mm (11.16 mm cumulative), and 95.89 mm (107.05 mm cumulative) respectively.

The longitudinal reinforcing steel bars remained elastic after Blast 1, however some slight chipping of the concrete compression face was observed. One significant horizontal crack occurred at mid-span of the tension face, and extended along the side of the column toward the compression face. Blast 2 strain gauge data at mid-span shows a strain of 0.02 mm/mm (ε_{tot} = 0.0206). No further tension cracks appeared at mid-span, however some initial crushing of concrete was observed in the support regions after this blast, shown in Figure 4.42 b).

As with all other columns with 75 mm tie spacing, this column failed at Blast 3 due to compression reinforcing steel buckling. Crushing of the concrete at the compression face and load transfer device occurred, but large pieces stayed in place due to the steel fibres. The horizontal crack that commenced from Blast 1 at mid span opened enough to reveal the 6.3mm tie in that location. Diagonal cracks at the mid-span extended from the location of reinforcing steel buckling outwards towards the tension face of the column. All these details can be seen in

Figure 4.42 c). Slight diagonal cracks also occurred in the support region showing the formation of plastic hinges in that location. The poor results observed for this column are likely linked to the problems mixing and placing procedures associated with the HS fibres.

4.4 Description of Experimental Results – CRC test series

4.4.1 CRC-2%-75

This was the first of five UHPFRC columns constructed with CRC and steel fibres. This particular column was reinforced with 2% steel fibres by volume of concrete and non-seismic detailing for the transverse hoops (s= 75 mm).

The shock wave data, as recorded by the shock tube pressure inducers that impinged on the load transfer device can be found in Table 4.1. Complete pressure and impulse time histories, and pressure and mid-span displacement time histories for each blast on this column are shown in Figure 4.43 to Figure 4.46. Figure 4.47 and Figure 4.48 includes photographs detailing the effects of each blast on the column. For this column, the maximum displacements for Blast 1, Blast 2, Blast 3 and Blast 4 were 5.15 mm, 21.19 mm, 67.76 mm, and 309.48 mm respectively. The residual displacements for Blast 1, Blast 2, Blast 3, and Blast 3 were 1.60 mm, 3.95 mm (5.55 mm cumulative), 21.72 mm (27.27 mm cumulative), and 287.78 mm (315.05 mm cumulative), respectively.

Blast 1 strain gauge data at mid-span shows a significant amount of signal noise affected the data, however visual interpretation shows a maximum strain of approximately 0.0006 mm/mm (ε_{tot} = 0.0008), which indicates the longitudinal reinforcing steel bars remained elastic. No observable damage occurred after Blast 1.

Blast 2 strain gauge data at mid-span shows a maximum strain of 0.0039 mm/mm (ε_{tot} = 0.0047), which indicates the longitudinal reinforcing steel was within the plastic region. Horizontal cracks developed along the tension face of the column, spaced evenly at 75mm.

Blast 3 strain gauge data at mid-span is not available due to limitations of the gauge at extreme strains. Unlike the SFRC columns with similar tie detailing, the CRC columns did not fail under

this shockwave load, and had a residual displacement of 21.72 mm. High speed video data shows a large tensile crack 75 mm below mid-span, beginning along the tension face, then extending towards the compression face of the column. Two large vertical cracks are also formed along the longitudinal reinforcing steel of the tension face from 75 mm below the mid-span (point of maximum deflection) to the mid-span itself, which can be seen in Figure 4.48 a). Converse to the SFRC columns, there is no concentration of cracking at mid span, nor are there any discernible secondary fragments from the column.

The failure mechanism of this column was tension reinforcing steel rupture after Blast 4. The CRC was able to prevent compression reinforcing steel buckling even though the column was not seismically detailed. High speed video data shows that the large crack near mid-span opening further, followed by the rupture of the longitudinal reinforcing steel on the tension face of the column. In addition, it was observed that the smooth steel fibres debonded and pulled out at the single critical crack at mid span. Observation after the shock wave load shows some crushing of concrete along the compression face in the region of maximum displacement. Two very large cracks (approximately 30 mm wide) also formed in the support regions, as well some concrete crushing.

4.4.2 CRC-4%-75

This column had identical properties to specimen CRC-2%-75 but was reinforced with 4% steel fibres by volume of concrete. The shock wave data, as recorded by the shock tube pressure inducers that impinged on the load transfer device can be found in Table 4.1. Complete pressure and impulse time histories, and pressure and mid-span displacement time histories for each blast on this column are shown in Figure 4.49 to Figure 4.53. Figure 4.54 and Figure 4.55 includes photographs detailing the effects of each blast on the column. For this column, the maximum displacements for Blast 1, Blast 2, Blast 3, and Blast 4 were 4.74 mm, 21.59 mm, 57.15 mm, and 94.25 mm respectively. The recorded residual displacements for Blast 1, Blast 2, Blast 3, and Blast 4 were 0.35 mm, 3.98 mm (4.33 mm cumulative), 14.15 mm (18.48 mm cumulative) and 25.75 mm (44.23 mm cumulative) respectively.

Blast 1 strain gauge data at mid-span shows a maximum strain of 0.00058 mm/mm (ε_{tot} = 0.00082), which indicates the longitudinal reinforcing steel bars remained elastic. No observable damage occurred after Blast 1.

Blast 2 strain gauge data at mid-span shows a maximum strain of 0.00423 mm/mm (ε_{tot} = 0.00451), which indicates the longitudinal reinforcing steel strain was within the plastic region. Horizontal cracks developed along the tension face of the column, spaced evenly at 75mm.

Blast 3 strain gauge data at mid-span shows a maximum strain of 0.0175 mm/mm (ε_{tot} = 0.0181), which indicates the longitudinal reinforcing steel strain was within the plastic region. High speed video data shows a tensile failure in the concrete, in that 4 large horizontal cracks open at 75 mm spacing centred on mid-span. One large vertical crack is also formed along the longitudinal reinforcing steel of the tension face near the point of maximum deflection. Similar to the other CRC columns, there is no distinct formation of plastic hinge cracking at mid-span, nor are there any discernible secondary fragments from the column. The mid-span effects of blast 3 are shown in Figure 4.55 a).

Blast 4 strain gauge data at mid-span shows a maximum strain of 0.0187 mm/mm (ε_{tot} = 0.0193), which indicates the longitudinal reinforcing steel strain was greater than ultimate, however rupture was still prevented. The CRC was able to prevent compression reinforcing steel buckling even though the column was not seismically detailed. High speed video data shows that previously opened cracks near mid-span simply opened further. A large vertical crack along the longitudinal reinforcing steel of the tension face can be seen in Figure 4.55 b), which indicates cover spalling.

Blast 5 involved changing the driver length of the shock tube to 14 ft, which created an impulsive load of 1355.12 kPa*msec. Unfortunately this load was much too great for the remaining resistance of the column, which caused the base of the column to completely lift out of the support, and invalidated the data of this test. The failure mechanism of this column was tension reinforcing steel rupture, and it should be noted that even at this extreme load, unlike the

SCC specimens, CRC was able to prevent any reinforcing steel buckling. As in the previous specimen the fibres pull out at a single crack at failure.

4.4.3 CRC-6%-75

This was column was constructed with CRC, 6 % fibres by volume of concrete and did not contain seismic detailing. The shock wave data, as recorded by the shock tube pressure inducers that impinged on the load transfer device can be found in Table 4.1. Complete pressure and impulse time histories, and pressure and mid-span displacement time histories for each blast on this column are shown in Figure 4.56 to Figure 4.59. Figure 4.60 and Figure 4.61 includes photographs detailing the effects of each blast on the column. For this column, the maximum displacements for Blast 1, Blast 2, Blast 3, and Blast 4 were 5.33 mm, 23.23 mm, 56.29 mm, and 373.20 mm respectively. The residual displacements for Blast 1, Blast 2, Blast 3, and Blast 4 were 0.34 mm, 3.97 mm (4.31 mm cumulative), 16.19 mm (20.50 mm cumulative), and 349.75 mm (370.25 mm cumulative) respectively.

Strain gauge data for this column at mid-span is not available due to malfunction of both the compression and tension reinforcing steel strain gauges. However, the residual displacement was 0.34 mm, which indicates the longitudinal reinforcing steel bars did indeed remain elastic. No observable damage occurred after Blast 1. After the column was subjected to Blast 2, there was a permanent deformation of 3.97mm, which indicates that, similarly to all other columns tested, the longitudinal reinforcing steel was within the plastic range. Horizontal cracks appears along a transverse ties near the mid-span of the column, spaced at 75 mm as shown in Figure 4.61 a).

In the case of Blast 3, high speed video data shows the formation of a crack at mid-span. Observation after Blast 3 simply shows that the previously noted crack at mid-span increased in size to 2 mm in width, as shown in Figure 4.61 b).

The mechanism of failure for the column was tension reinforcing steel rupture, which occurred during Blast 4. High speed video data shows that the large crack near mid-span simply opened further, and the longitudinal reinforcing steel along the tension face ruptured. Observation after

the shock wave load shows some crushing of concrete along the compression face in the region of maximum displacement. As observed in all CRC columns the fibres pullout out at a single crack at failure. Two large cracks also formed in the support regions as well. It is noted that this column did not perform better than specimen CRC-4%-75. However this may be linked to the difficulties in placing the fresh CRC in this column.

Despite the above finding, the results from these three columns demonstrate the improved blast performance afforded by the use of CRC when compared to traditional reinforced concrete.

4.4.4 CRC-2%-38

This column was the first of two specimens that aimed at examining the effect of combined use of CRC and seismic detailing. This particular column had identical properties to specimen CRC-2%-75 but with a reduced tie spacing of 38 mm. The shock wave data, as recorded by the shock tube pressure inducers that impinged on the load transfer device can be found in Table 4.1. Complete pressure and impulse time histories, and pressure and mid-span displacement time histories for each blast on this column are shown in Figure 4.62 to Figure 4.66. Figure 4.67 and Figure 4.68 include photographs detailing the effects of each blast on the column. For this column, the maximum displacements for Blast 1, Blast 2, Blast 3 and Blast 4, and Blast 4(2) were 5.15 mm, 20.15 mm, 47.43 mm, 71.30 and 269.53 mm respectively. The residual displacements for Blast 1, Blast 2, Blast 3, Blast 3, and Blast 4(2) were 0.74 mm, 3.50 mm (4.24 mm cumulative), 8.08 mm, (12.32 mm cumulative), 12.78 mm (25.10 mm cumulative), and 241.79 mm (266.89 mm cumulative) respectively.

Blast 1 strain gauge data at mid-span shows a significant amount of signal noise affected the data, however visual interpretation shows a maximum strain of approximately 0.0007 mm/mm (ε_{tot} = 0.0009), which indicates the longitudinal reinforcing steel bars remained elastic. No observable damage occurred after Blast 1.

Blast 2 strain gauge data at mid-span shows a maximum strain of 0.00416 mm/mm, which indicates the longitudinal reinforcing steel strain was within the plastic region. A hairline crack appeared along the tension face at mid-span that proceeded horizontally along one tie, and then

diagonally downward, and then ended horizontally 75mm below the aforementioned horizontal crack, as shown in Figure 4.68 a).

Blast 3 strain gauge data at mid-span is not available due to limitations of the gauge at extreme strains. Several horizontal cracks begin to form near the mid-span of the column, spaced evenly at 38mm, including a crack that bisects the diagonal crack formed during Blast 2.

High speed video data after Blast 4 shows that the cracks near mid-span simply opened further, and to the point where the fibres in the extreme tension region completely pulled out, as shown in Figure 4.68 b). The column was able to remain mostly intact, and had a residual displacement of 12.78 mm that indicates tension reinforcing steel was within the plastic range.

The column was subjected to a repeat of the shock wave load produced for Blast 4 (Blast 4(2)). The decision to repeat the loading was based on the extreme failure observed in for Blast 5 during the testing of specimen CRC-4%-75. The mechanism of failure for the column was tension reinforcing steel rupture. Continuing with the previously observed trend for CRC, failure fibre pullout occurred at a single crack at mid-span. High speed video data shows that the large crack near mid-span opened further until the tension reinforcing steel ruptured. Observation after the shock wave load shows some crushing of concrete along the compression face in the region of maximum displacement. Two very large cracks also formed in the support regions.

This test indicates the enhanced benefits of using CRC in conjunction with seismic detailing for blast resistance of columns.

4.4.5 CRC-4%-38

This column was last column tested in the experimental program and had identical to the specimen CRC-4%-75 column but contained seismic detailing. The shock wave data, as recorded by the shock tube pressure inducers that impinged on the load transfer device can be found in Table 4.1. Complete pressure and impulse time histories, and pressure and mid-span displacement time histories for each blast on this column are shown in Figure 4.69 to Figure 4.72. Figure 4.73 and Figure 4.74 include photographs detailing the effects of each blast on the

column. For this column, the maximum displacements for Blast 1, Blast 2, and Blast 3 were 5.05 mm, 22.03 mm, and 69.21 mm respectively. The residual displacements for Blast 1, Blast 2, and Blast 3 were 0.12 mm, 3.97 mm (4.10 mm cumulative), and 22.05 mm (26.15 mm cumulative) respectively. The LVDT malfunctioned while gathering data during Blast 4.

Blast 1 strain gauge data at mid-span shows a maximum strain of 0.00086 mm/mm (ε_{tot} = 0.0011), which indicates the longitudinal bars remained elastic. No observable damage occurred. Blast 2 strain gauge data at mid-span shows a maximum strain of 0.001205 mm/mm (ε_{tot} = 0.0015), which indicates the longitudinal reinforcing steel strain was within the plastic region. One horizontal crack appears along a transverse tie near the mid-span then proceed vertically downwards near the longitudinal reinforcing steel before reconnecting with the transverse tie and proceeding horizontally again along the side of the column, as shown in Figure 4.74 a).

Blast 3 strain gauge data at mid-span is not available due to limitations of the gauge at extreme strains. High speed video data shows a complete tensile failure in the concrete, in that the crack that opened in Blast 2 opens beyond the effective length of the fibres in the extreme tension region, and extends to the compression face of the concrete. Observation after Blast 3 noted that some concrete crushing occurred in the compression face at mid-span (observable in Figure 4.68 b), which indicates that the concrete for this column may not have had similar compressive properties as for the other CRC columns. As the cylinder tests for this column show good agreement with the compressive strength of other columns, this phenomenon shows that there were problems with the placement of this CRC mix.

The mechanism of failure for the column was tension reinforcing steel rupture after Blast 4 with the fibres pulling out at mid-span. High speed video data shows that the large crack near mid-span opened further, and the reinforcing steel along the tension face ruptured. Observation after the shock wave load shows some crushing of concrete along the compression face in the region of maximum displacement. Two very large cracks also formed in the support regions.

The results of this test are inconclusive regarding the benefits of combined use of CRC and seismic detailing of tie reinforcement.

4.5 Pressure, Impulse, and Displacement Time Histories & Select Photos

4.5.1 SCC-0%-75

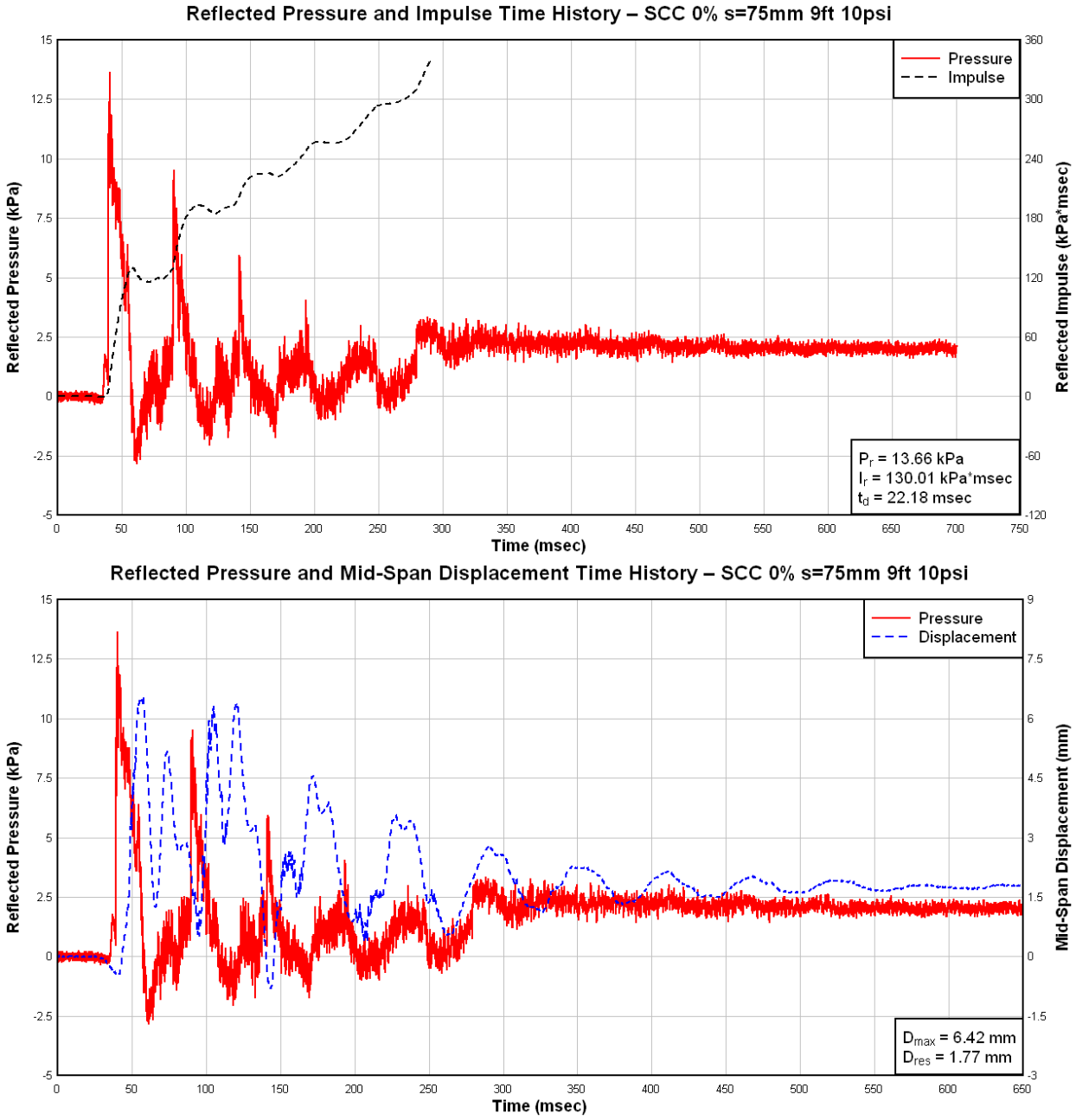

Figure 4.1 Column SCC-0%-75: recorded reflected pressure, impulse, and displacement for Blast 1

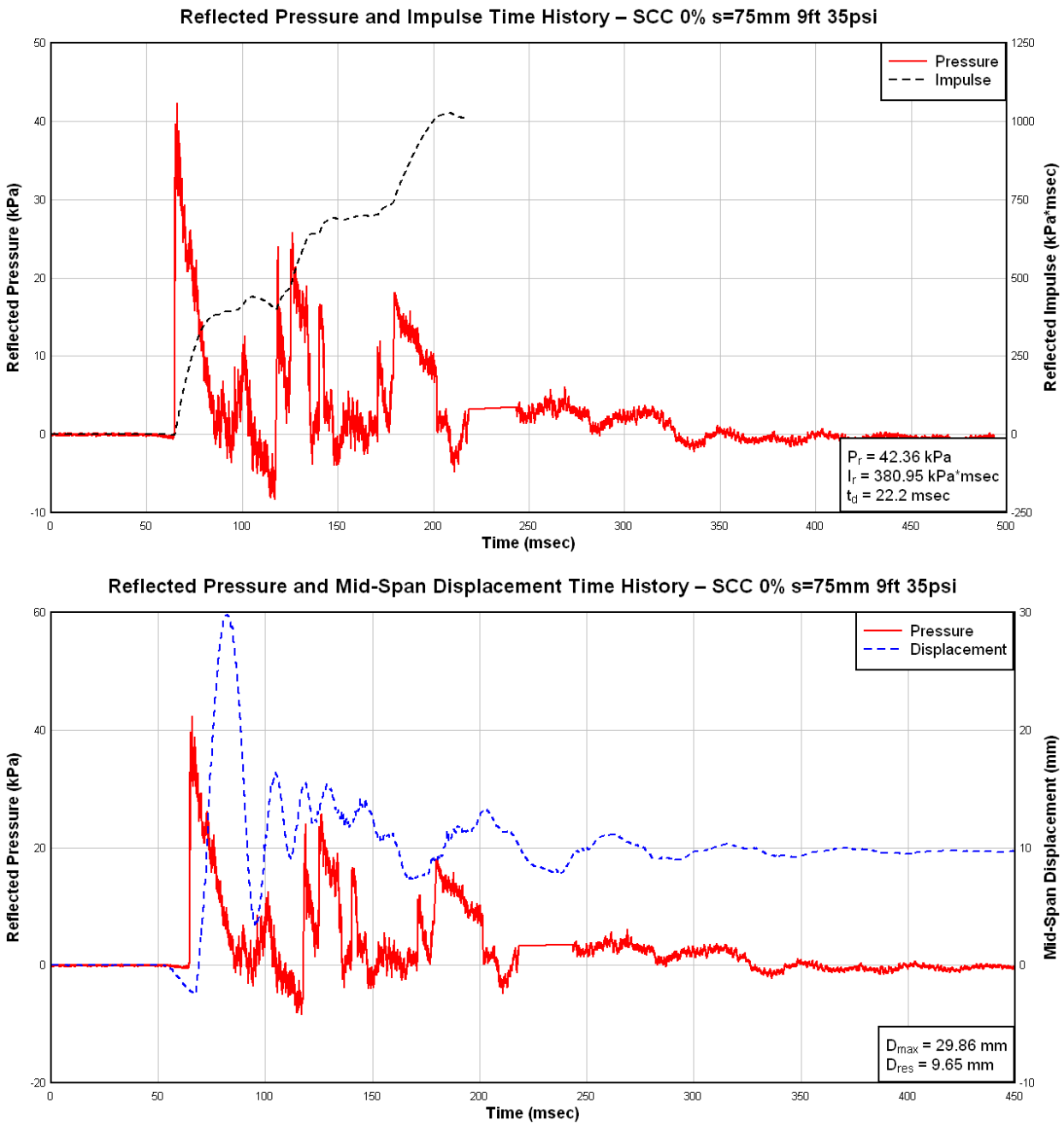

Figure 4.2 Column SCC-0%-75: recorded reflected pressure, impulse, and displacement for Blast 2

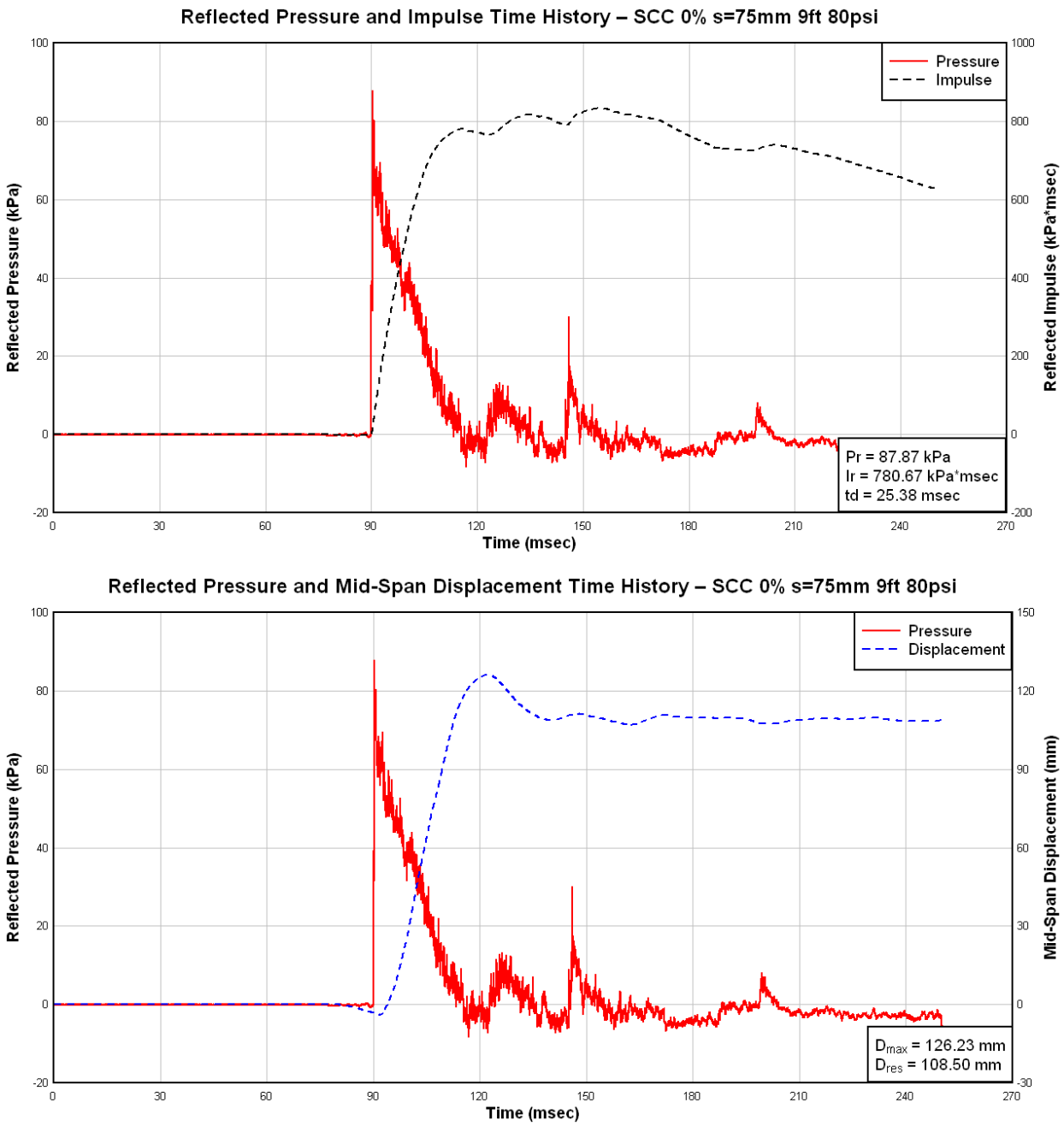

Figure 4.3 Column SCC-0%-75: recorded reflected pressure, impulse, and displacement for Blast 3

(a) Blast 1 (b) Blast 2 (c) Blast 3

Figure 4.4 Column SCC-0%-75 at the end of Blasts 1-3

(a) Mid-Span Result of Blast 2 (b) Mid-Span Result of Blast 3

Figure 4.5 Mid-span damage for Column SCC-0%-75

4.5.2 SCC-0%-38

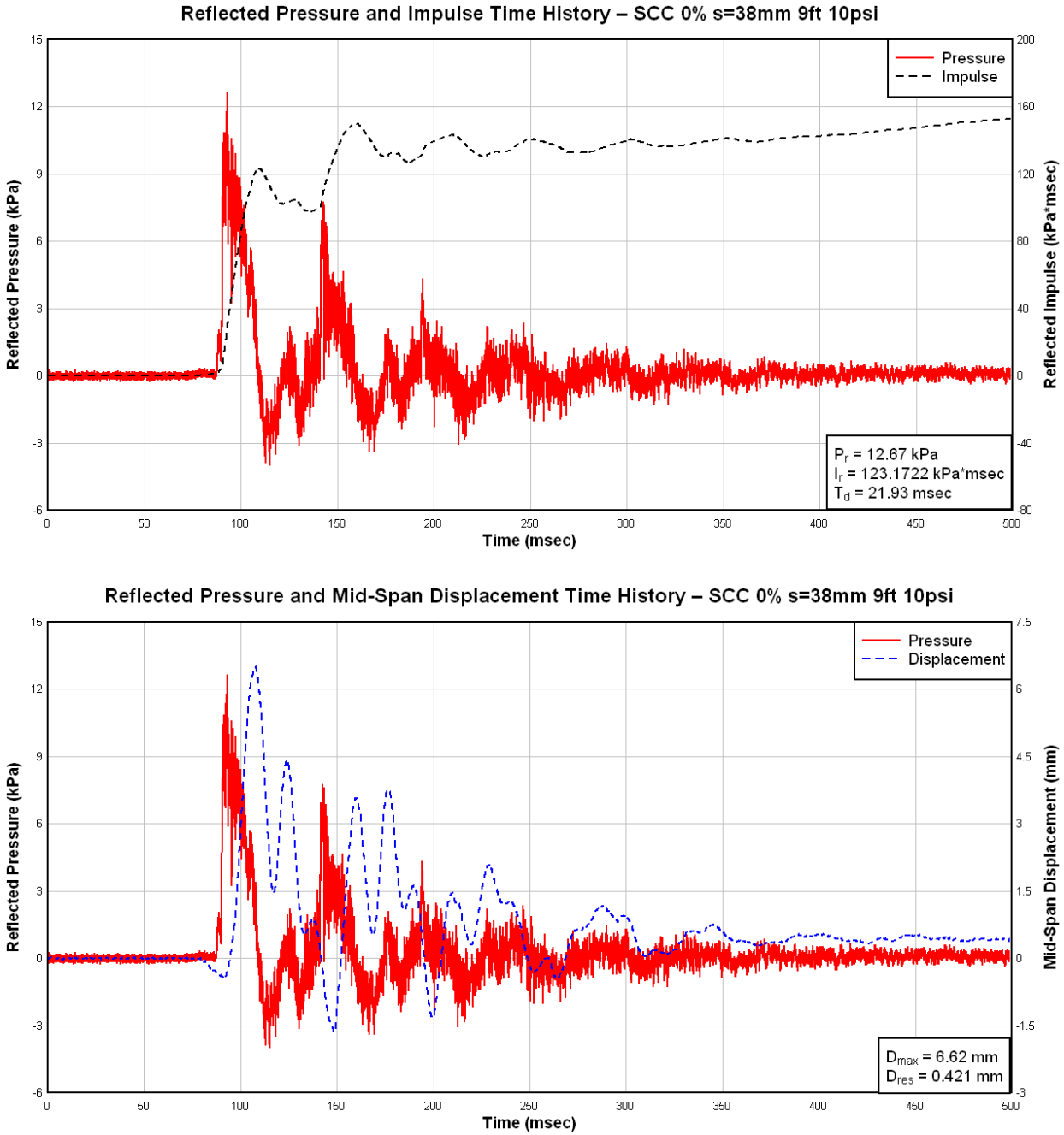

Figure 4.6 Column SCC-0%-38: recorded reflected pressure, impulse, and displacement for Blast 1

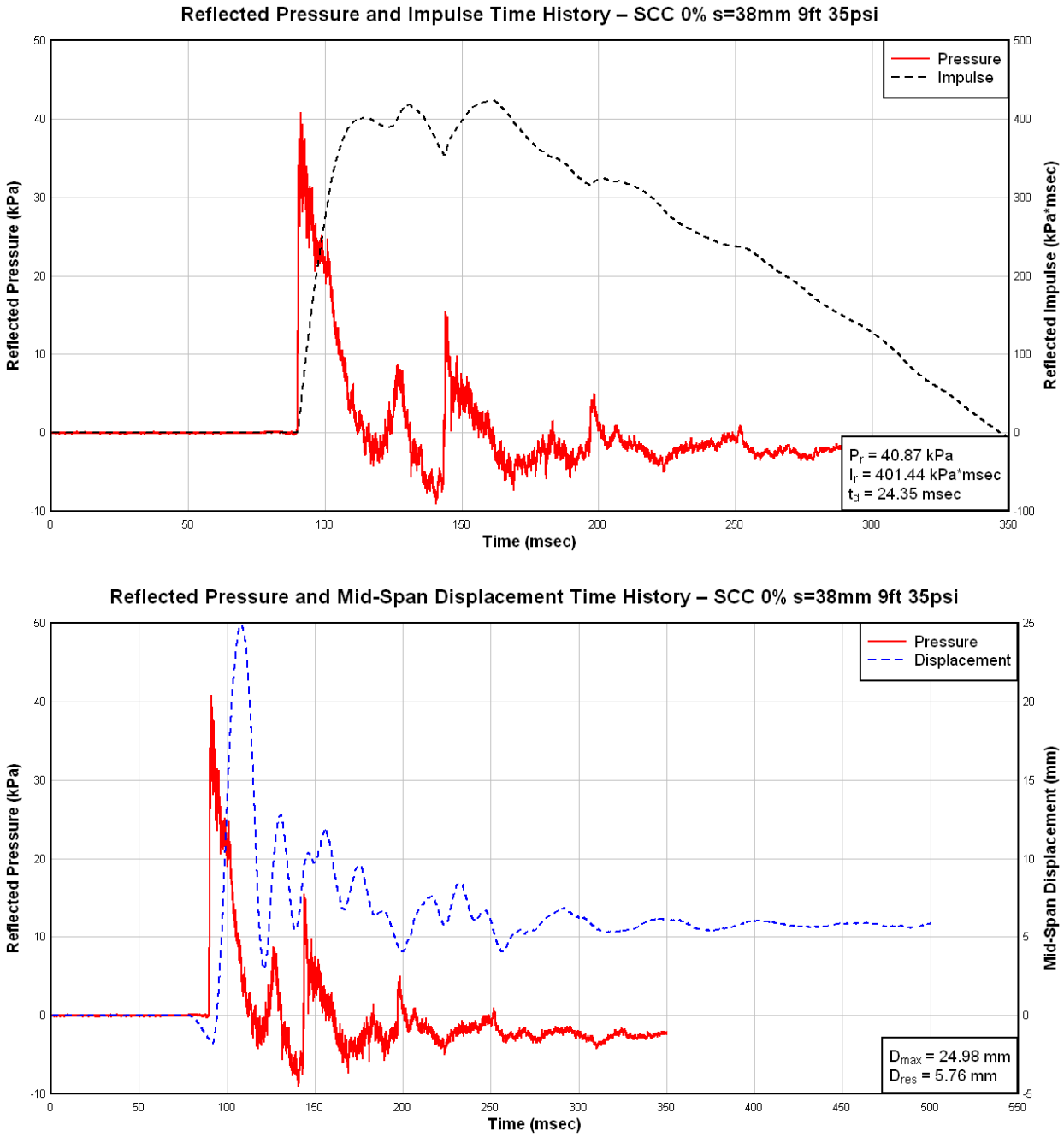

Figure 4.7 Column SCC-0%-38: recorded reflected pressure, impulse, and displacement for Blast 2

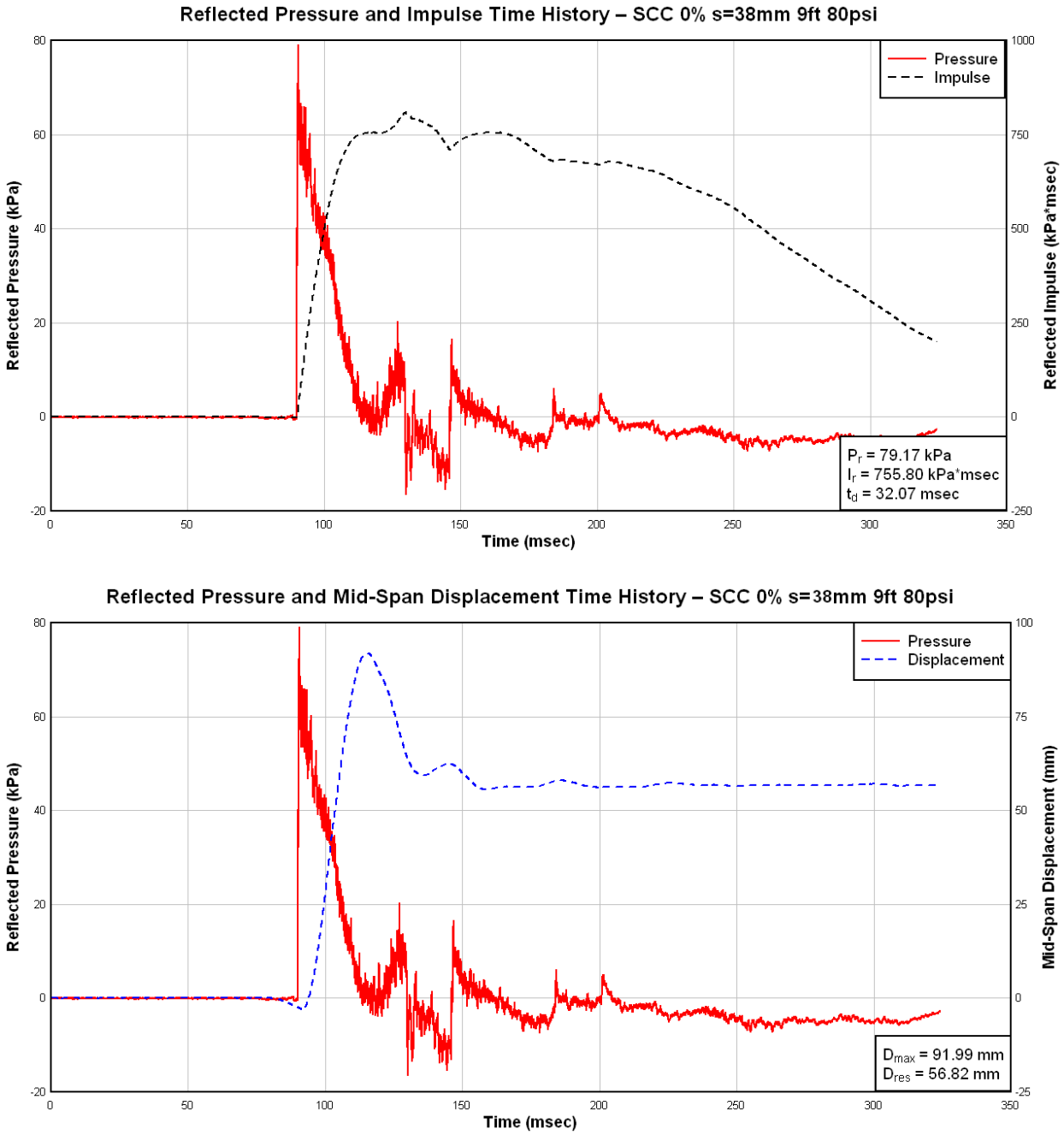

Figure 4.8 Column SCC-0%-38: recorded reflected pressure, impulse, and displacement for Blast 3

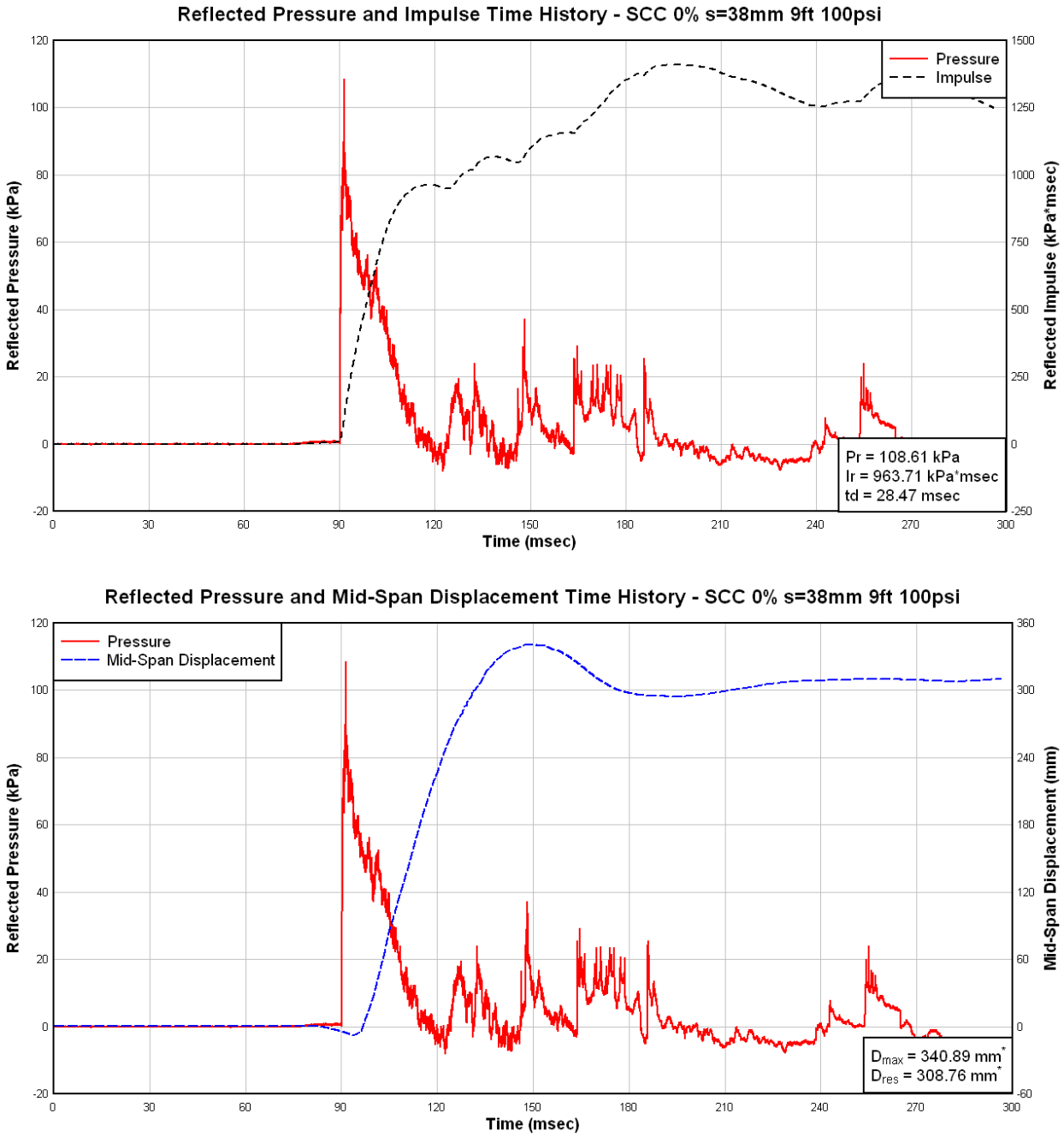

Figure 4.9 Column SCC-0%-38: recorded reflected pressure, impulse, and displacement for Blast 4

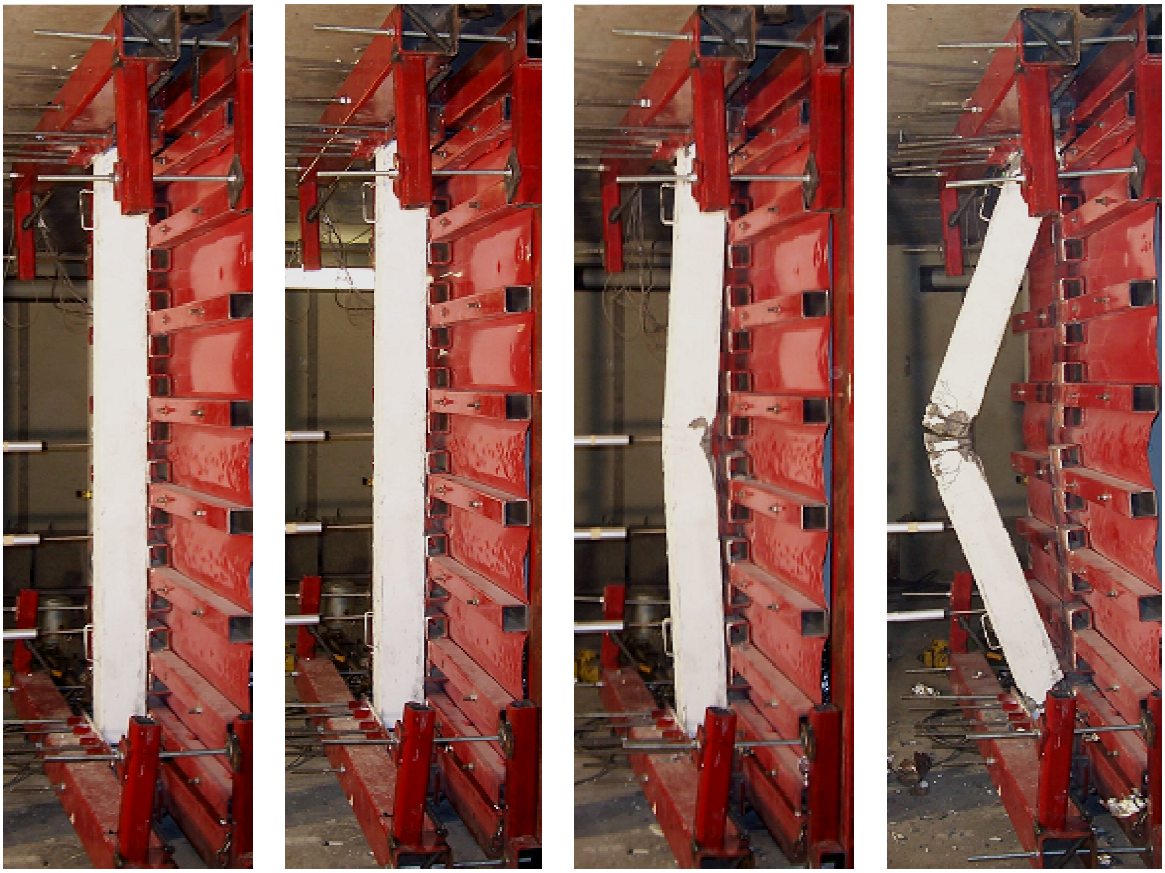

(a)Blast 1 (b)Blast 2 (c)Blast 3 (d)Blast 4

Figure 4.10 Column SCC-0%-38 at the end of Blasts 1-4

(a)Mid-Span Result of Blast 2 (b)Mid-Span Result of Blast 3 (b)Mid-Span Result of Blast 4

Figure 4.11 Mid-span damage for Column SCC-0%-38

4.5.3 SCC-0.5%-75

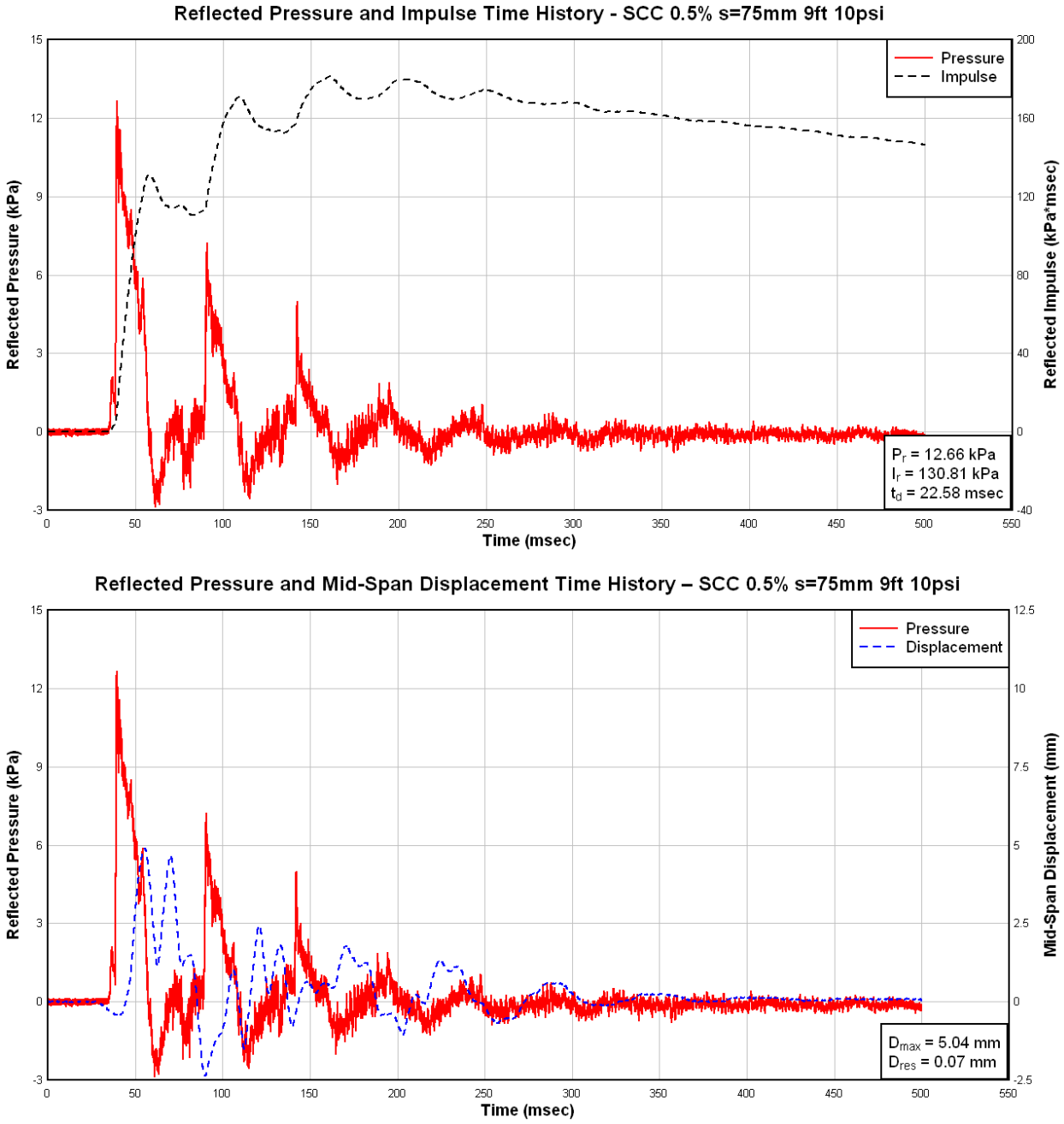

Figure 4.12 Column SCC-0.5%-75: recorded reflected pressure, impulse, and displacement for Blast 1

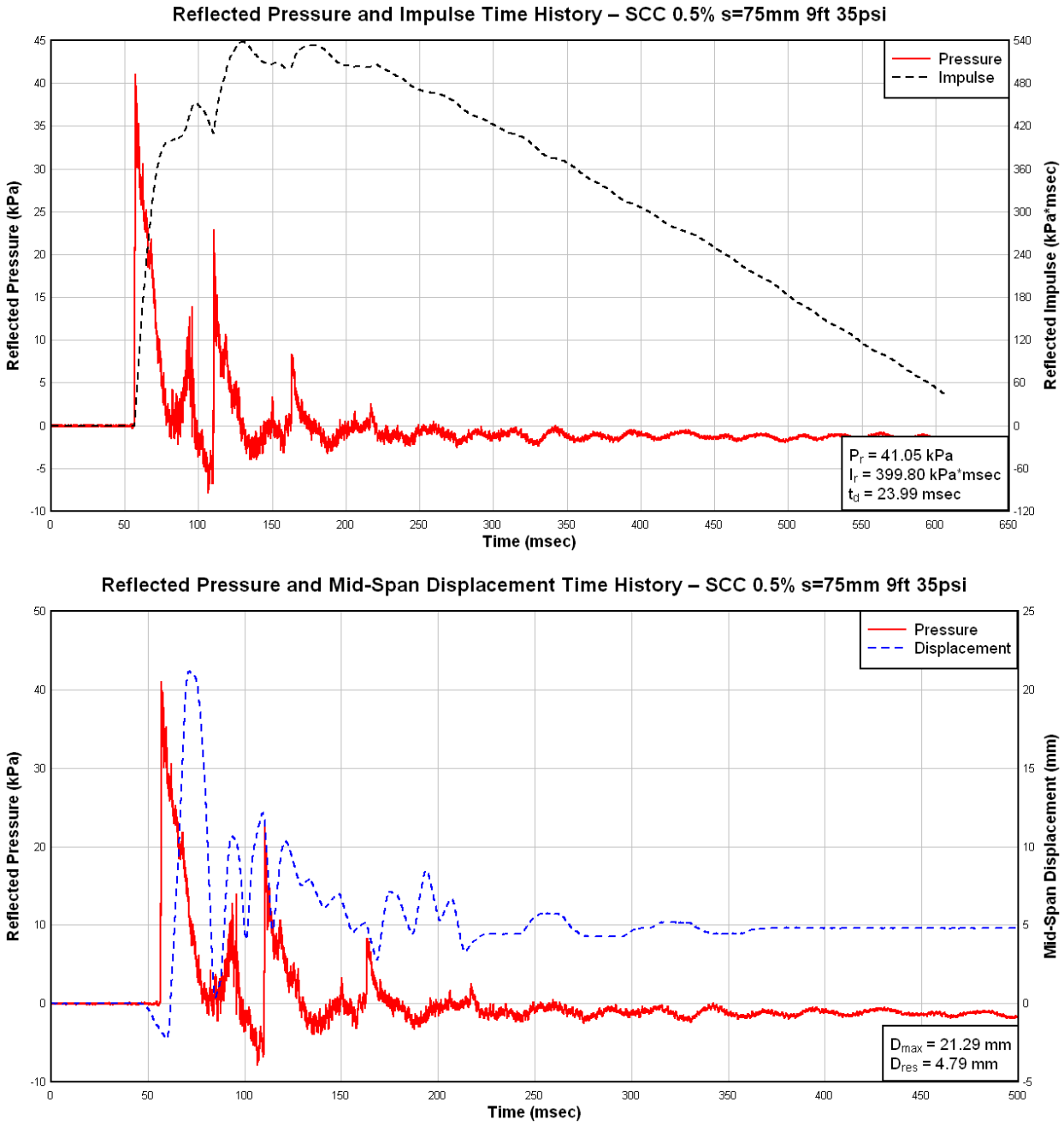

Figure 4.13 Column SCC-0.5%-75: recorded reflected pressure, impulse, and displacement for Blast 2

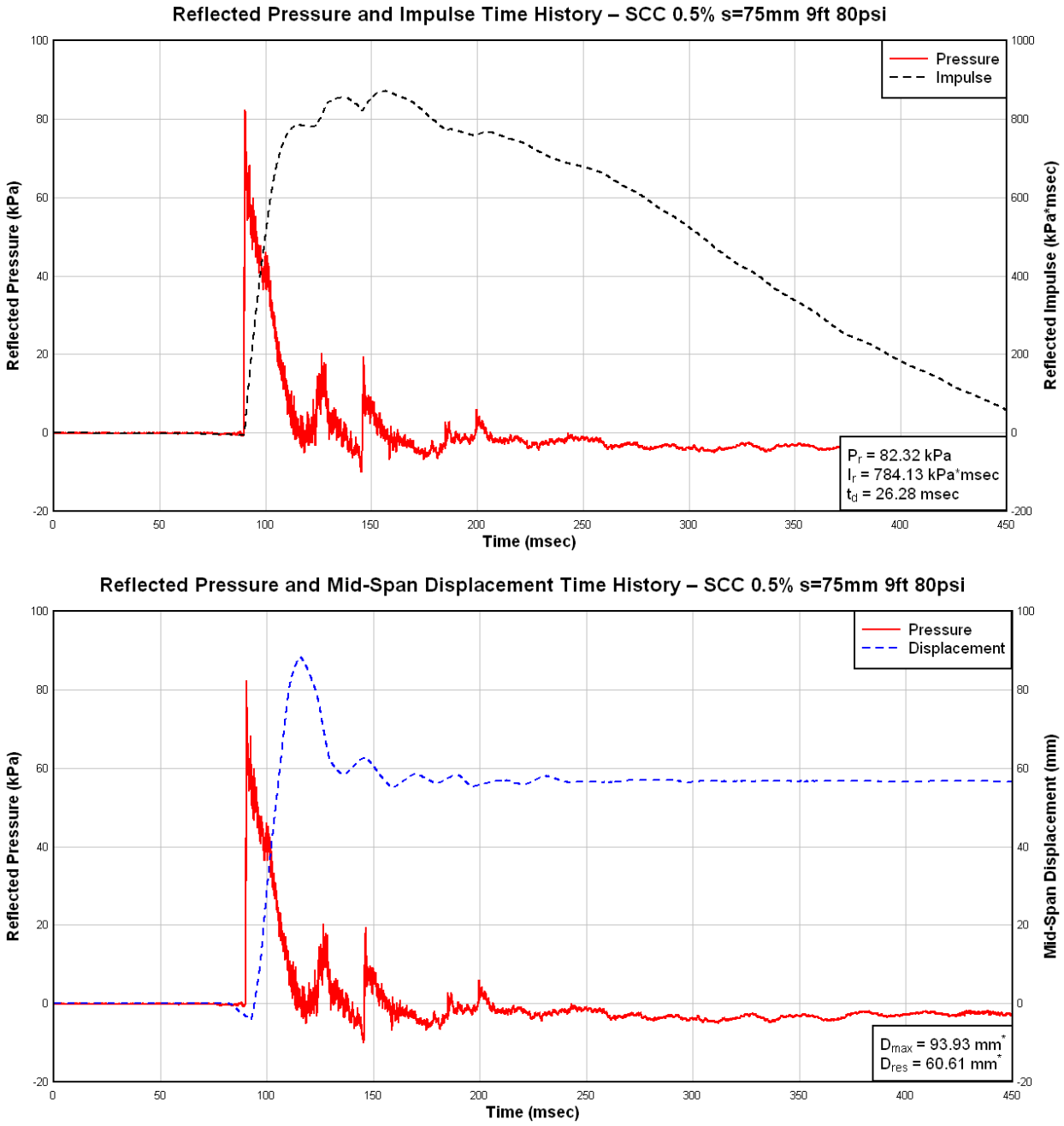

Figure 4.14 Column SCC-0.5%-75: recorded reflected pressure, impulse, and displacement for Blast 3

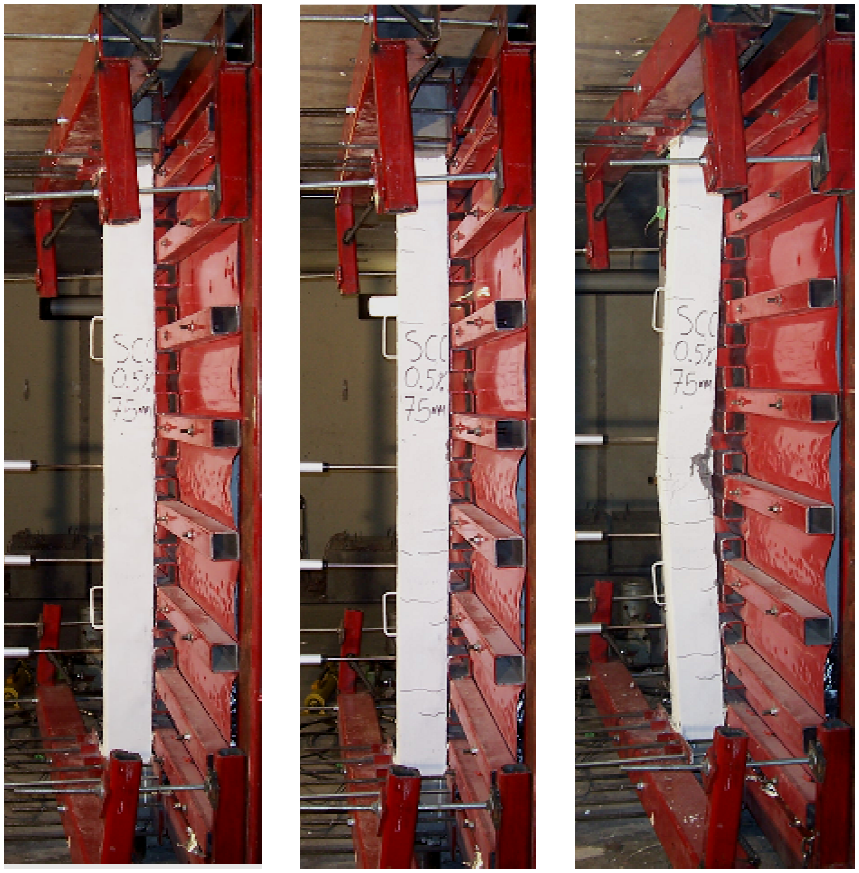

(a)Blast 1 (b)Blast 2 (c)Blast 3

Figure 4.15 Column SCC-0.5%-75 at the end of testing

(a)Mid-Span Result of Blast 1 (b) Chipping of concrete (c) Mid-Span Result of Blast 3

Figure 4.16 Mid-span damage for Column SCC-0.5%-75

4.5.4 SCC-0.75%-75

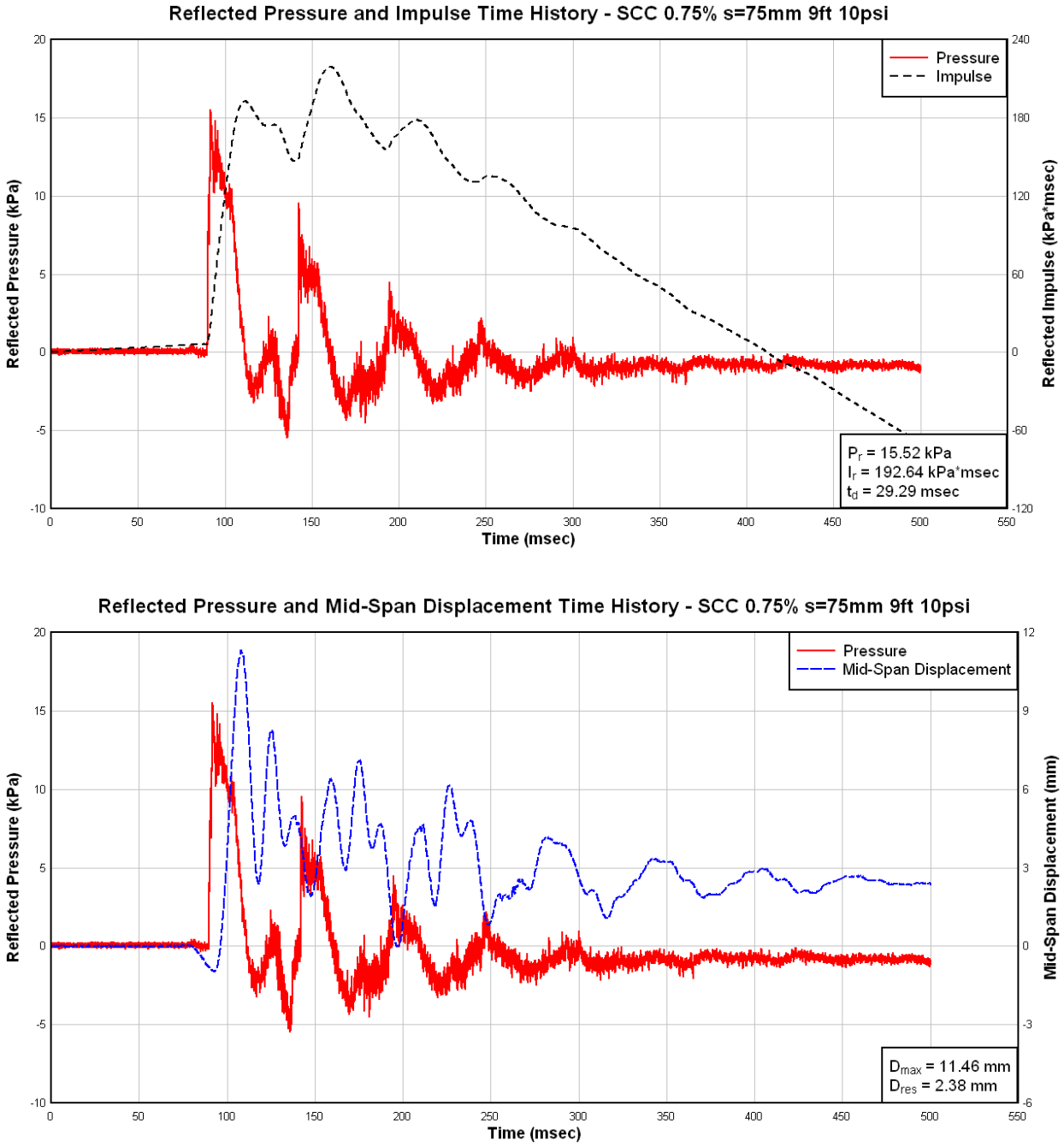

Figure 4.17 Column SCC-0.75%-75: recorded reflected pressure, impulse, and displacement for Blast 1

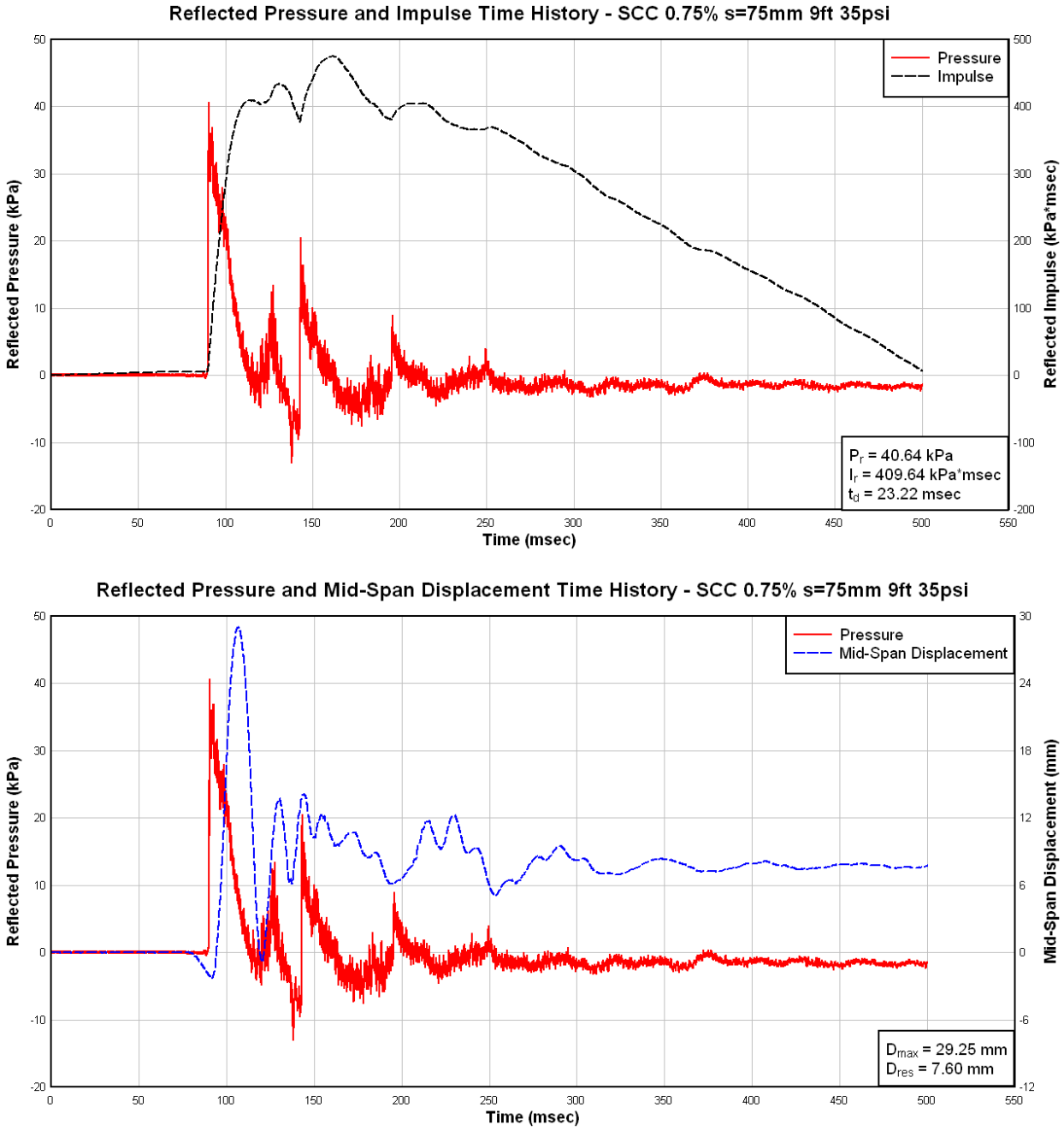

Figure 4.18 Column SCC-0.75%-75: recorded reflected pressure, impulse, and displacement for Blast 2

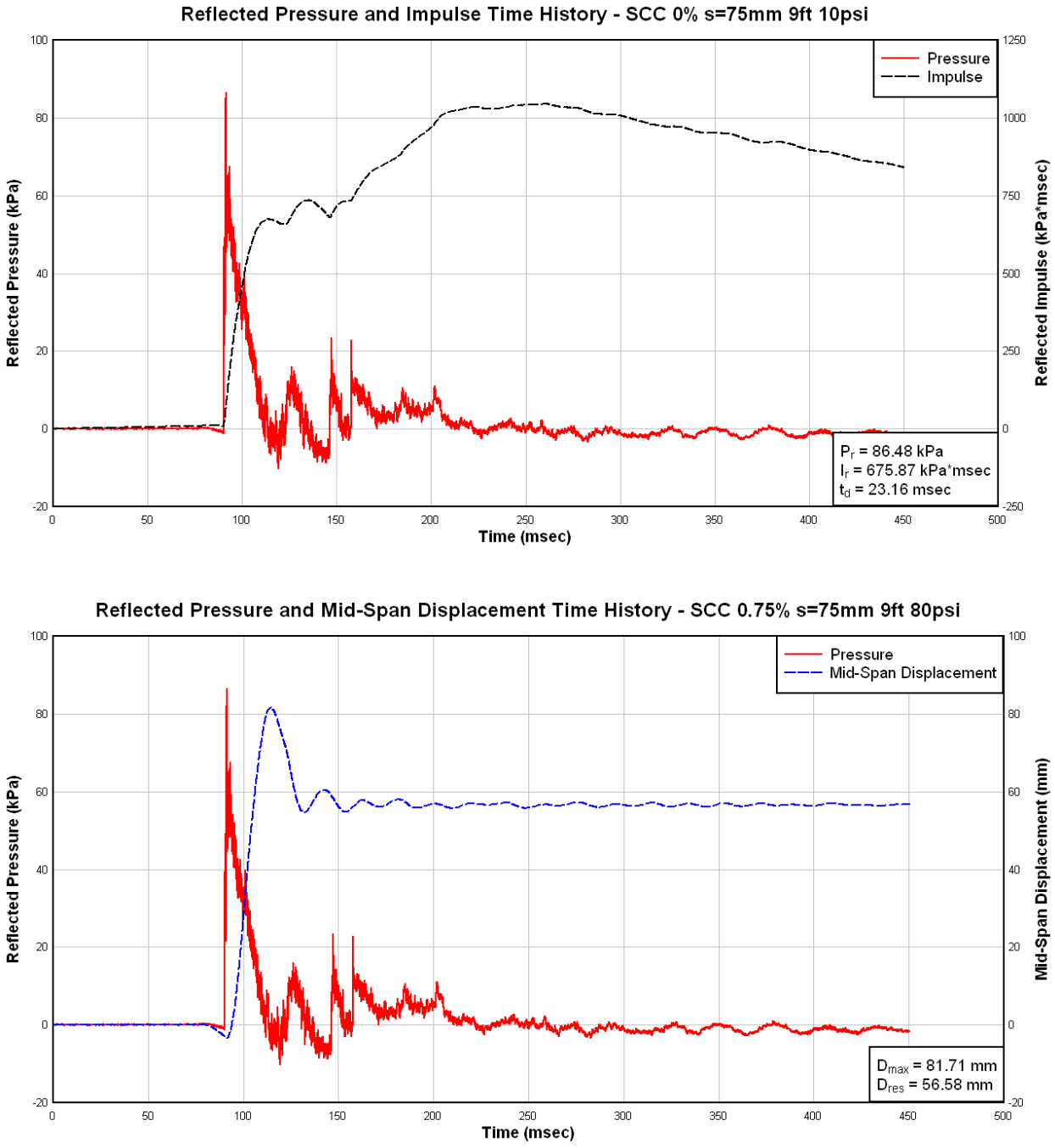

Figure 4.19 Column SCC-0.75%-75: recorded reflected pressure, impulse, and displacement for Blast 3

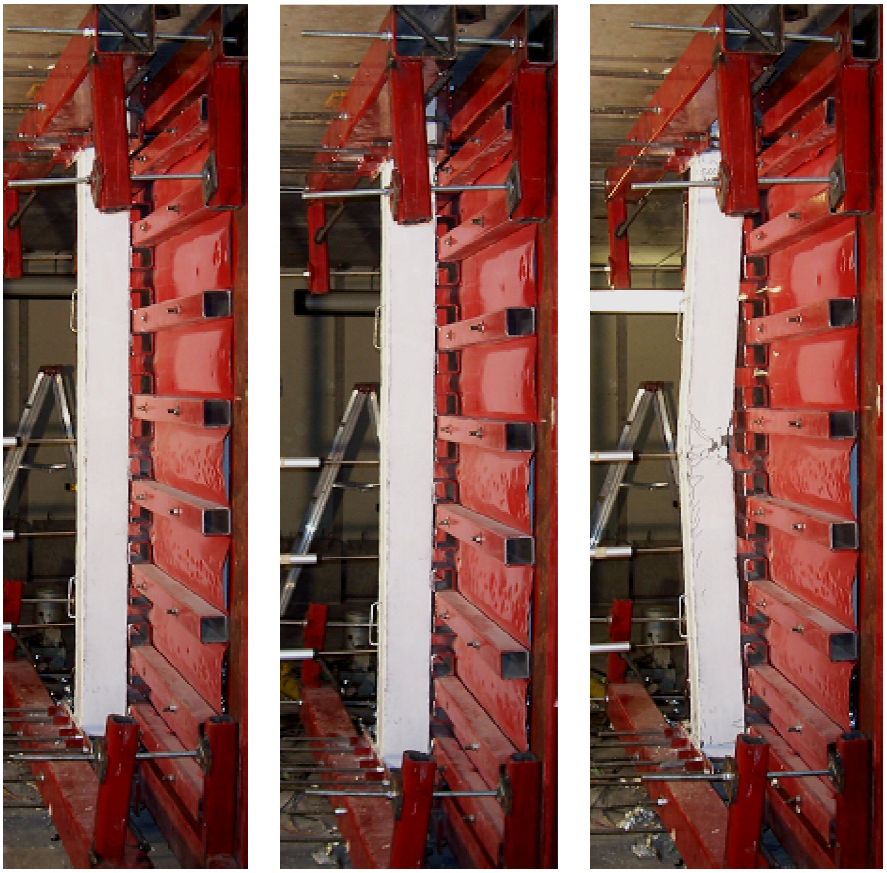

(a)Blast 1 (b)Blast 2 (c)Blast 3

Figure 4.20 Results of Shock Tube Tests for Column SCC-0.75%-75

(a)Mid-Span Result of Blast 3

Figure 4.21 Mid-span damage for Column SCC-0.75%-75

4.5.5 SCC-1%-75

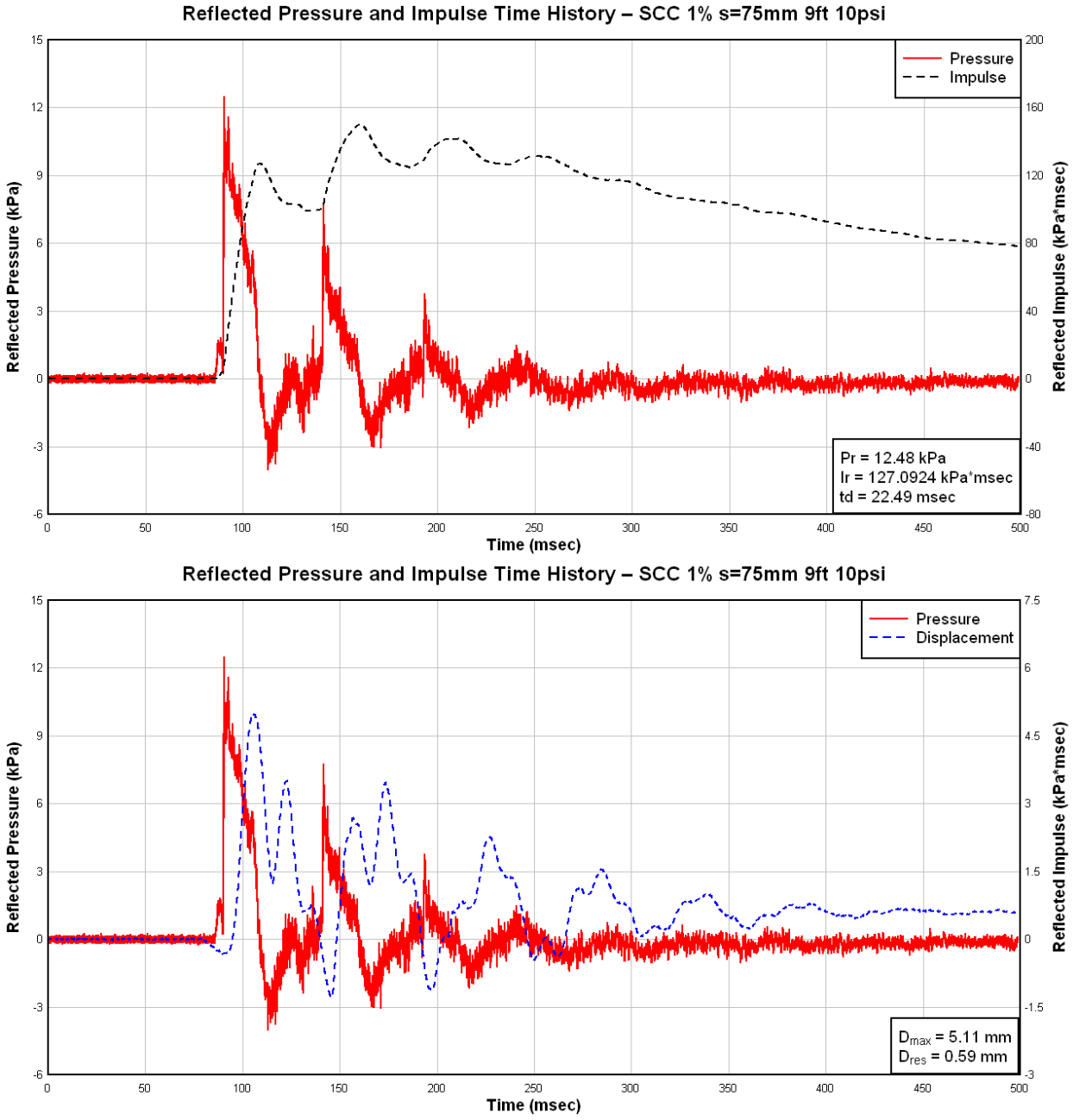

Figure 4.22 Column SCC-1%-75: recorded reflected pressure, impulse, and displacement for Blast 1

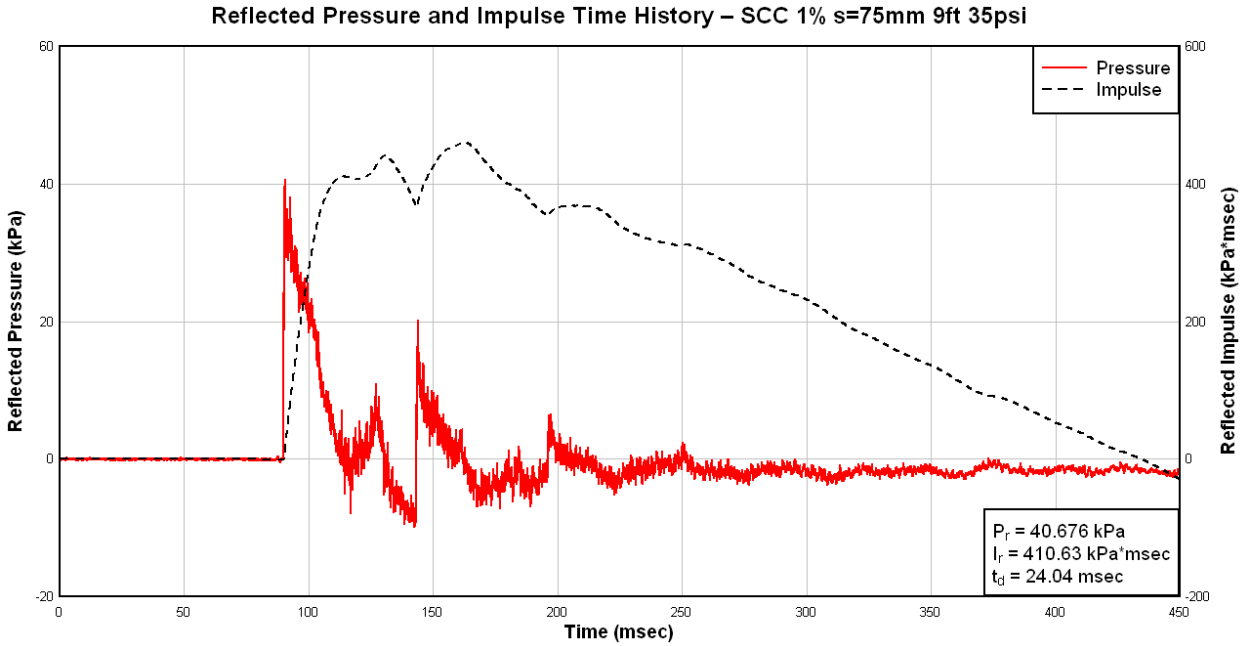

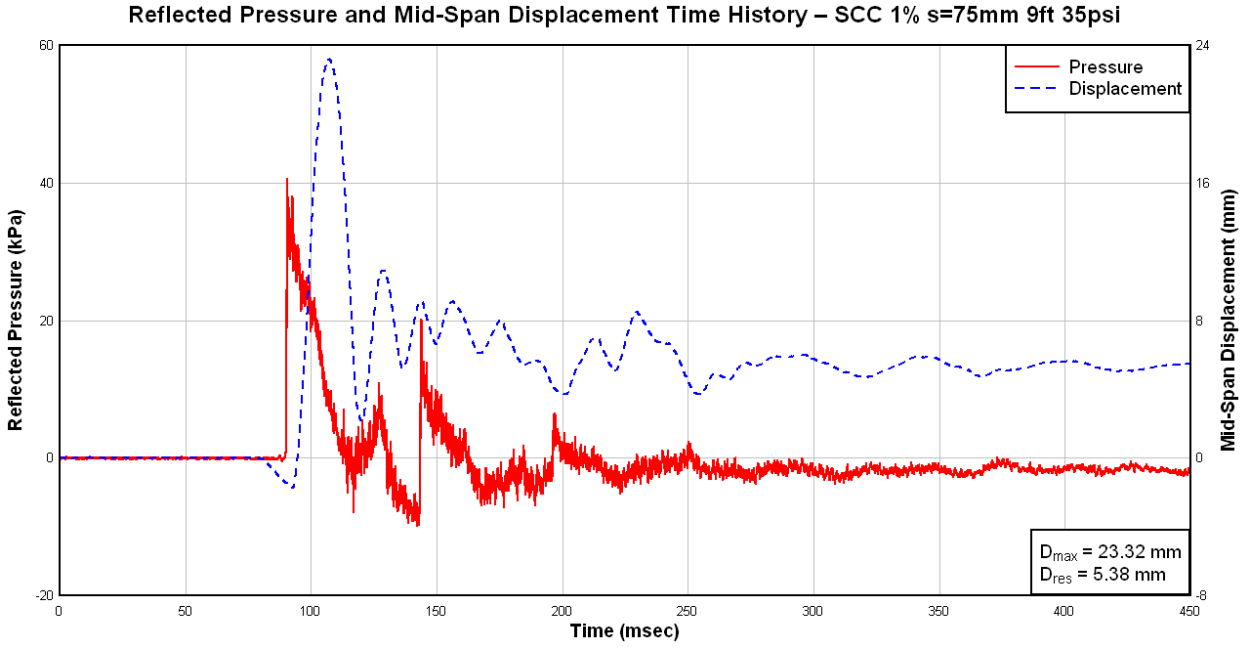

Figure 4.23 Column SCC-0.75%-75: recorded reflected pressure, impulse, and displacement for Blast 2

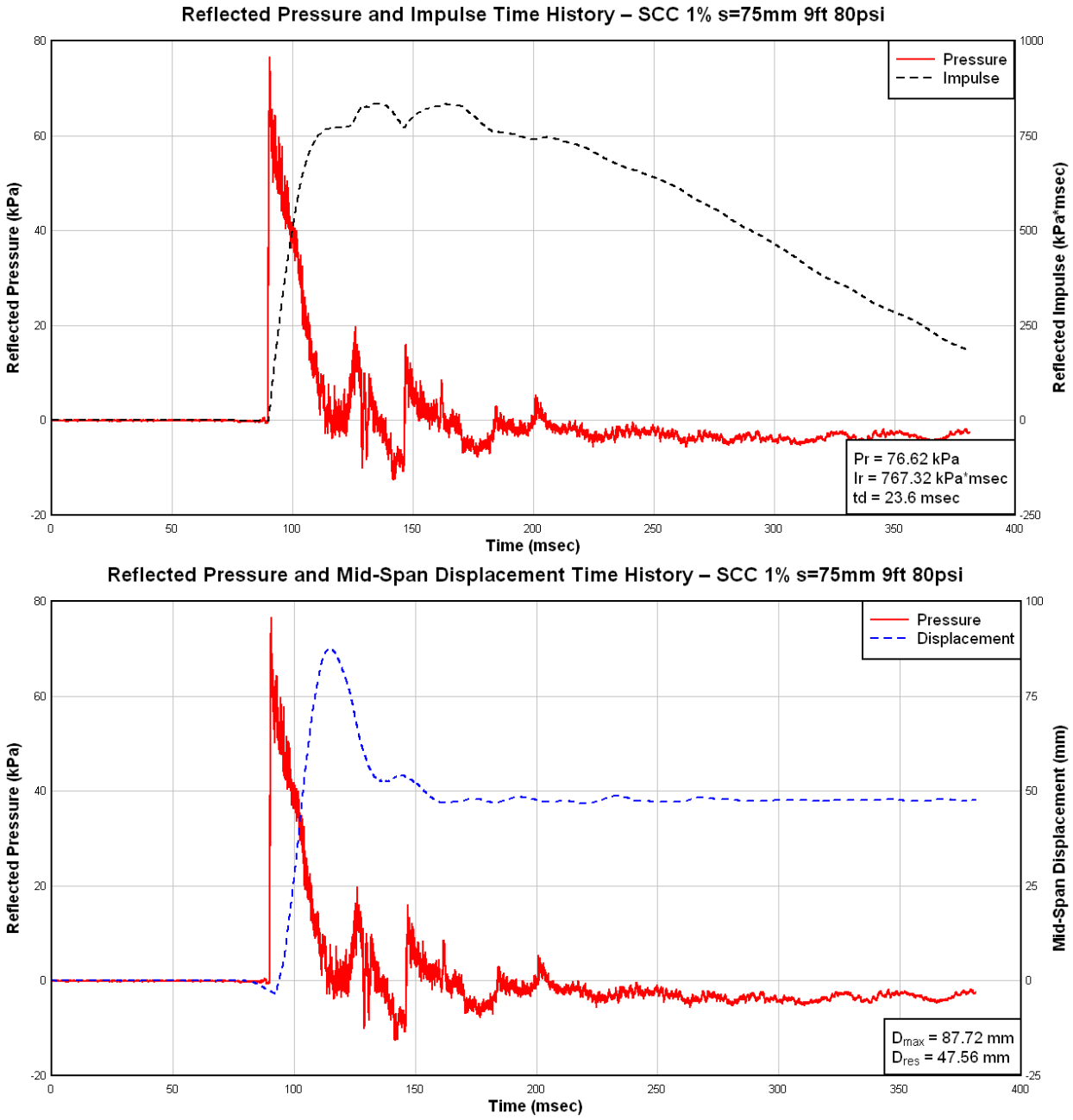

Figure 4.24 Column SCC-0.75%-75: recorded reflected pressure, impulse, and displacement for Blast 3

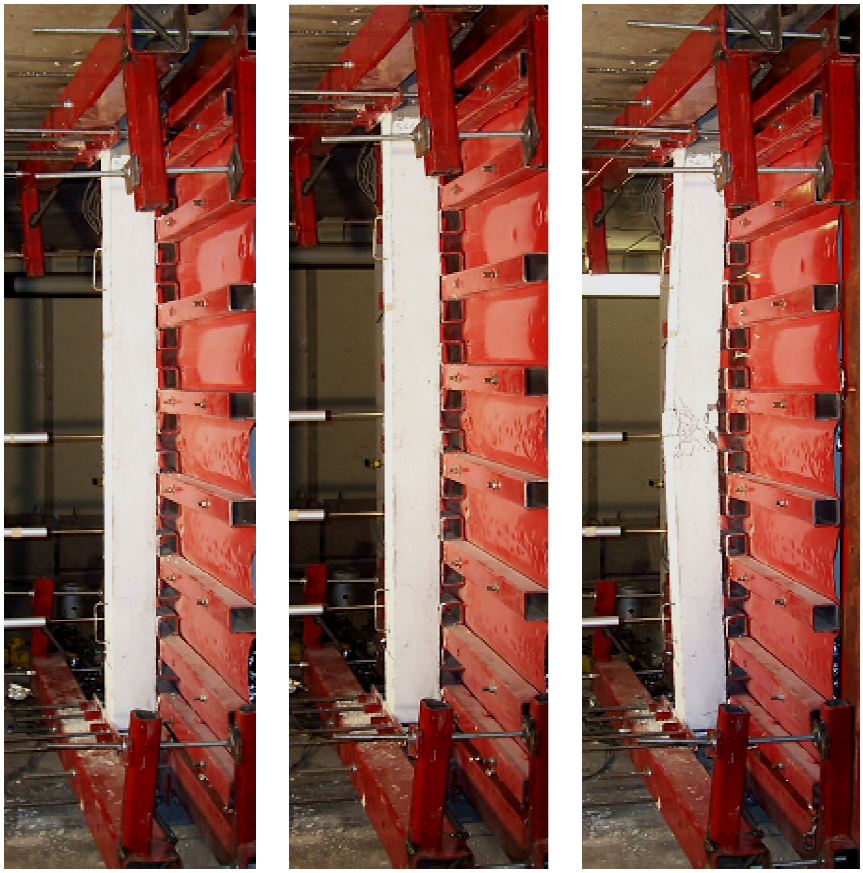

(a)Blast 1 (b)Blast 2 (c)Blast 3

Figure 4.25 Column SCC-1%-75 at the end of Blasts 1-3

(a)Mid-Span Result of Blast 2 (b)Mid-Span Result of Blast 3 (c) Tension Face of Blast 3

Figure 4.26 Mid-span damage for Column SCC-1%-75

4.5.6 SCC-1.5%-75

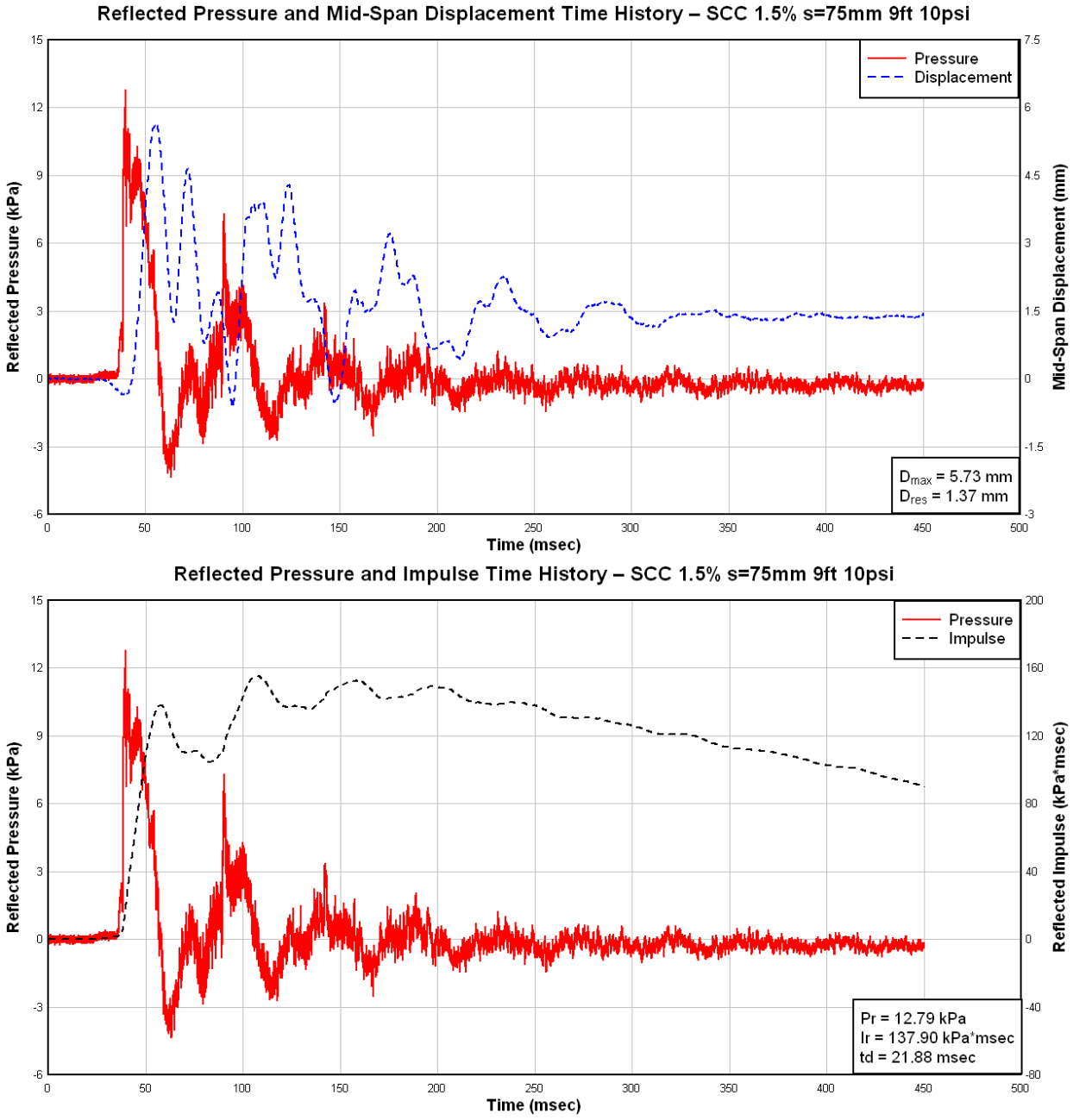

Figure 4.27 Column SCC-1.5%-75: recorded reflected pressure, impulse, and displacement for Blast 1

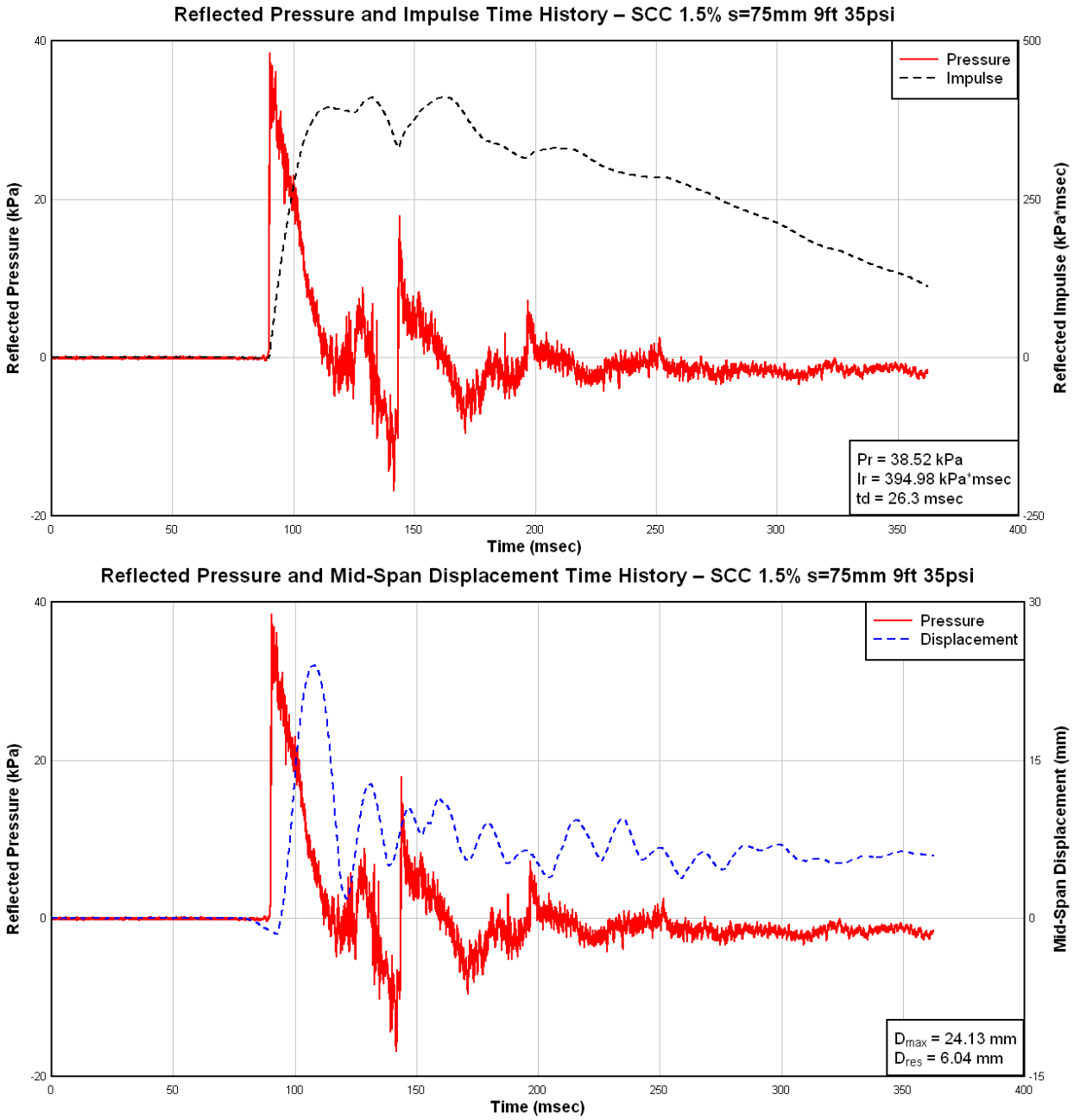

Figure 4.28 Column SCC-1.5%-75: recorded reflected pressure, impulse, and displacement for Blast 2

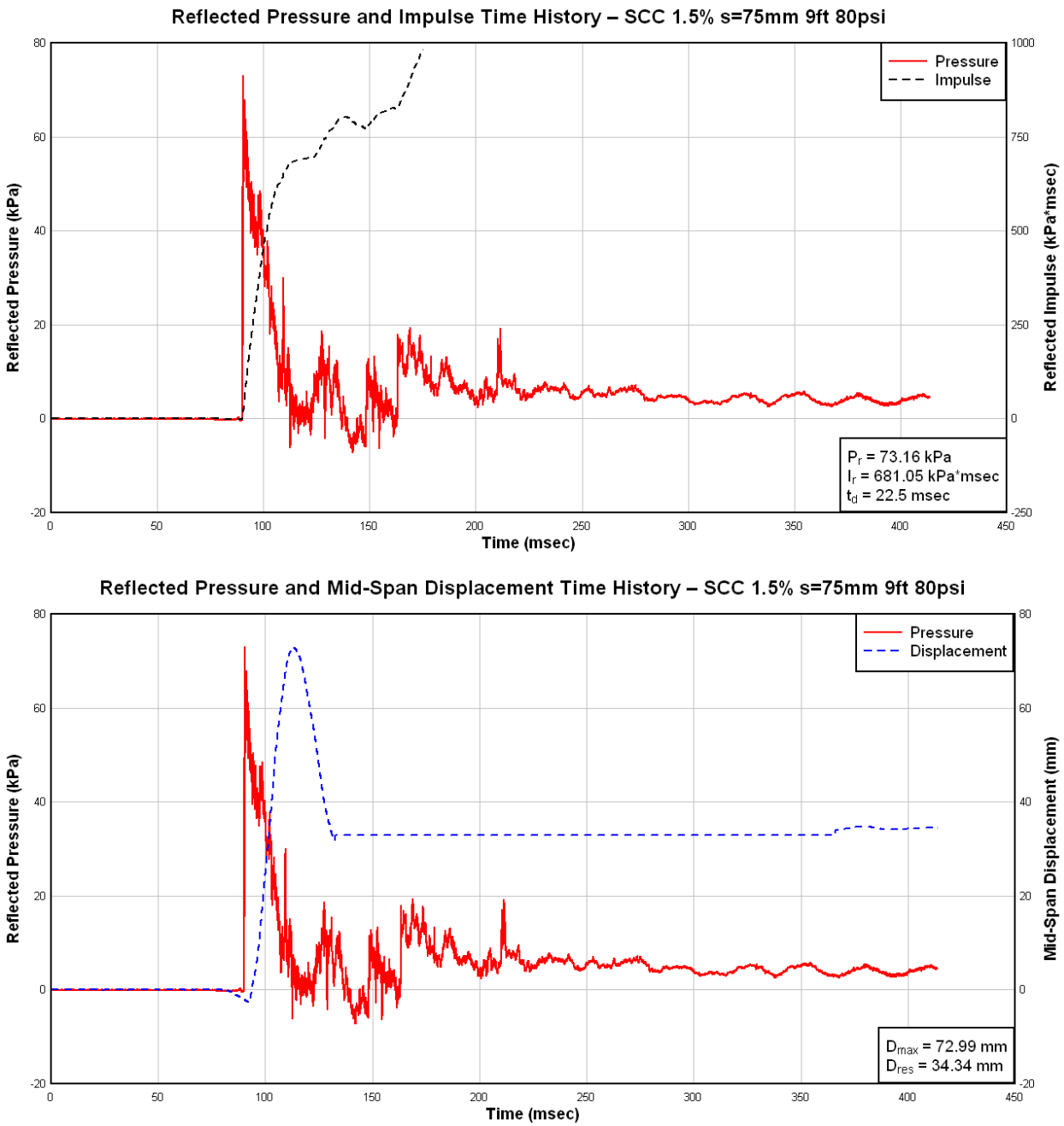

Figure 4.29 Column SCC-1.5%-75: recorded reflected pressure, impulse, and displacement for Blast 3

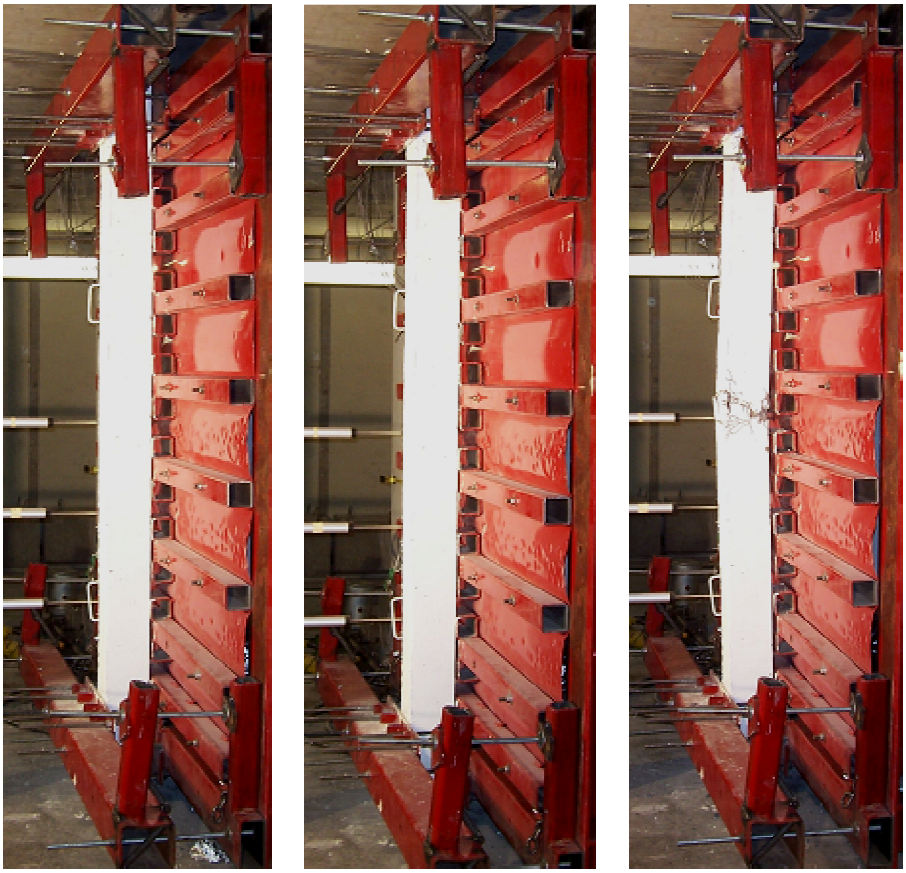

(a)Blast 1 (b)Blast 2 (c)Blast 3

Figure 4.30 Column SCC-1.5%-75 at the end of Blasts 1-3

(a) Blast 3 Tension Face (c) Mid-Span Result of Blast 3

Figure 4.31 Mid-span damage for Column SCC-1.5%-75

4.5.7 SCC-0.5%-38

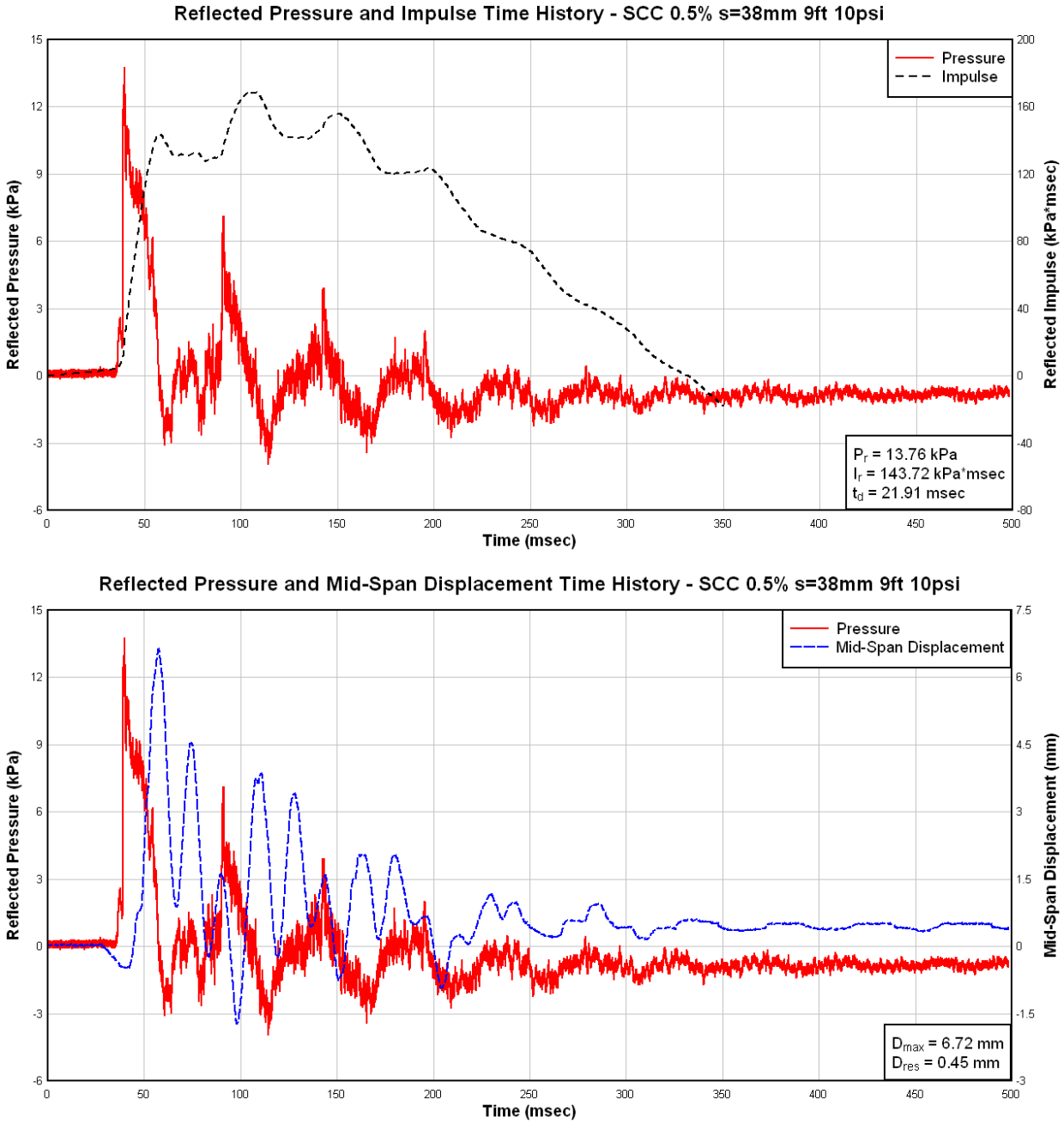

Figure 4.32 Column SCC-0.5%-38: recorded reflected pressure, impulse, and displacement for Blast 1

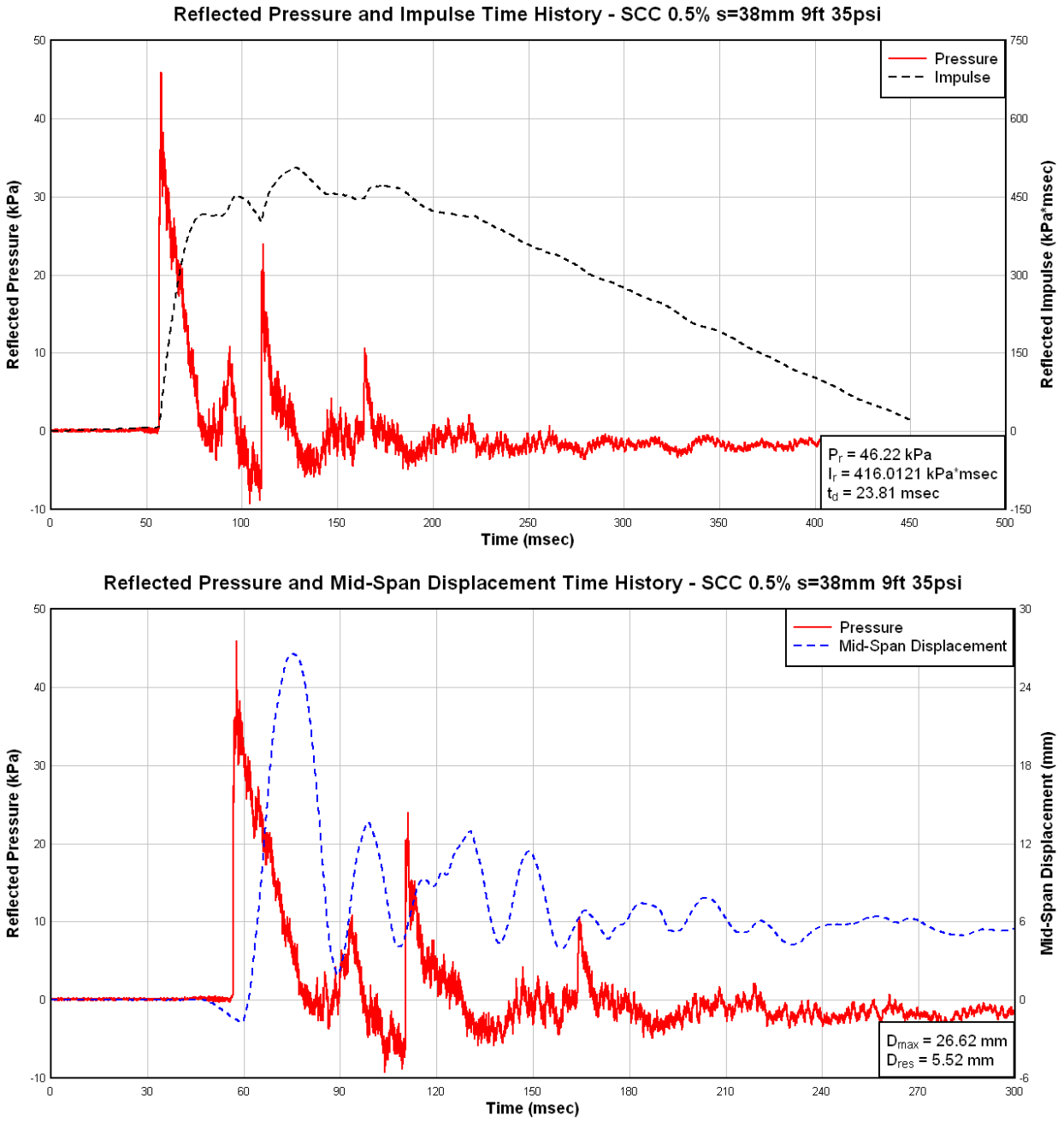

Figure 4.33 Column SCC-0.5%-38: recorded reflected pressure, impulse, and displacement for Blast 2

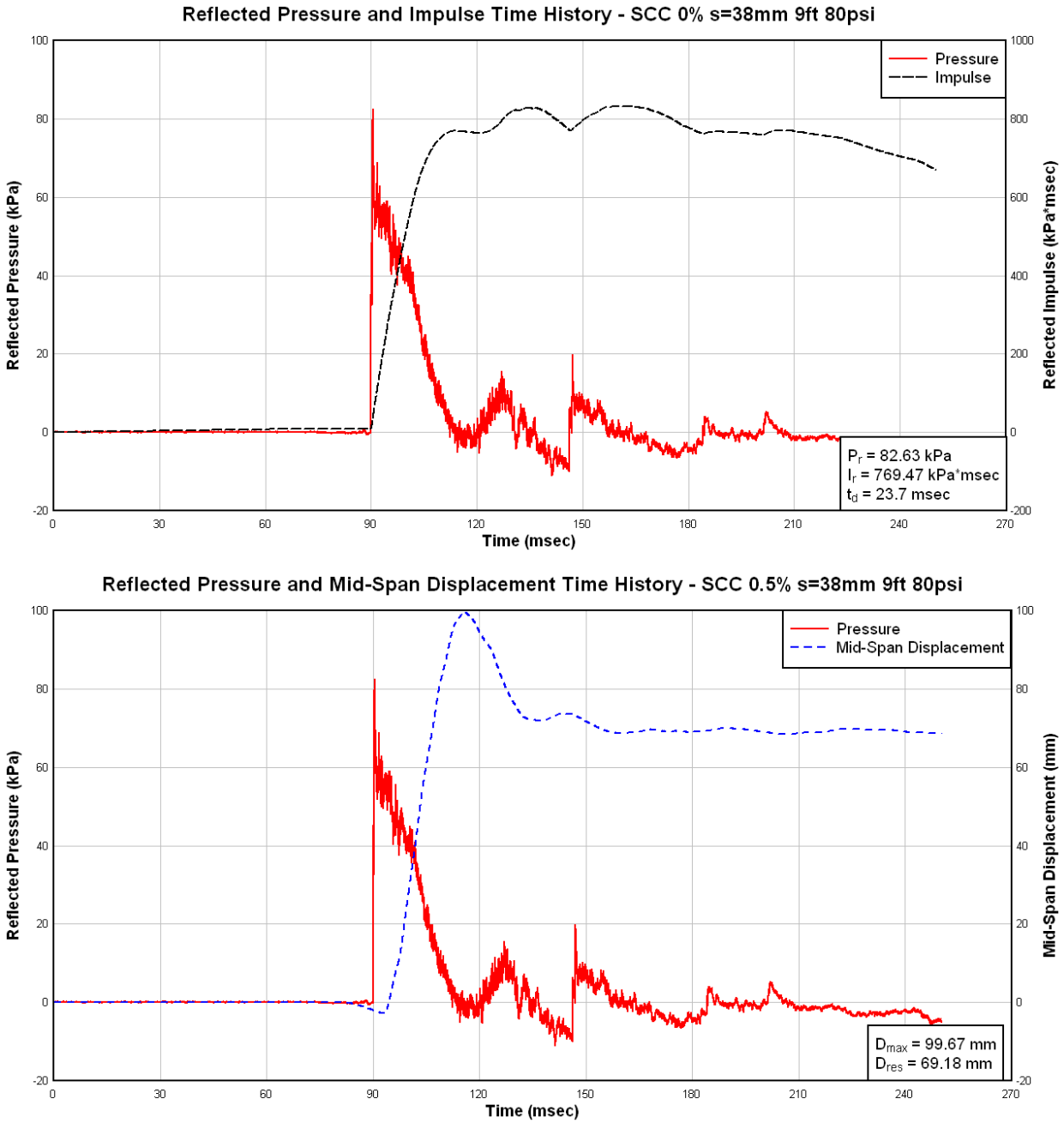

Figure 4.34 Column SCC-0.5%-38: recorded reflected pressure, impulse, and displacement for Blast 3

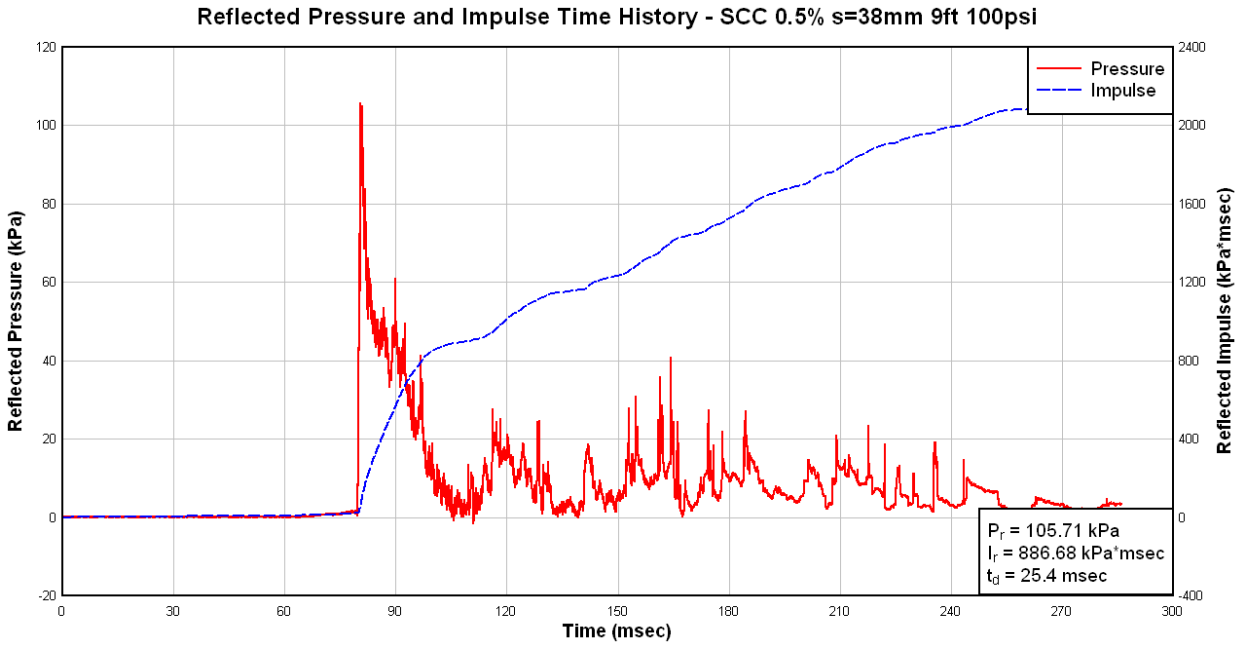

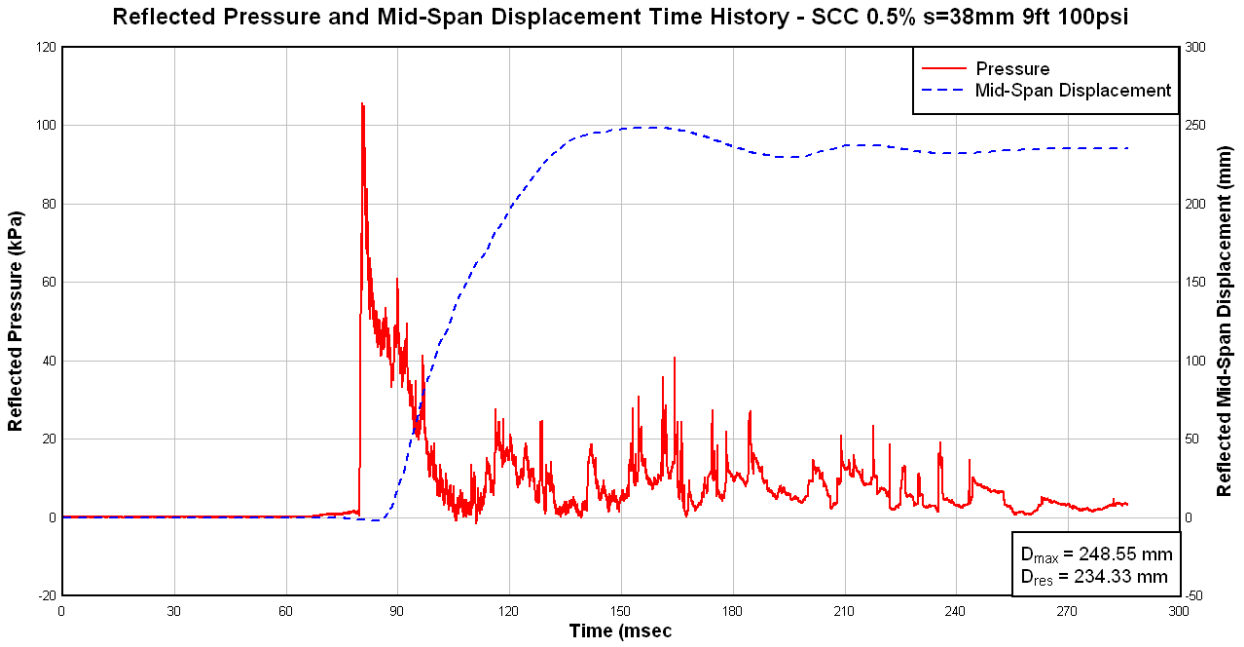

Figure 4.35 Column SCC-0.5%-38: recorded reflected pressure, impulse, and displacement for Blast 4

(a)Blast 1 (b)Blast 2 (c)Blast 3 (d)Blast 4

Figure 4.36 Column SCC-0.5%-38 at the end of Blasts 1-4

(a)Mid-Span Result of Blast 2 (b)Mid-Span Result of Blast 3 (c) Mid-Span Result of Blast 4

Figure 4.37 Mid-span damage for Column SCC-0.5%-38

4.5.8 SCC-0.75%HS-75

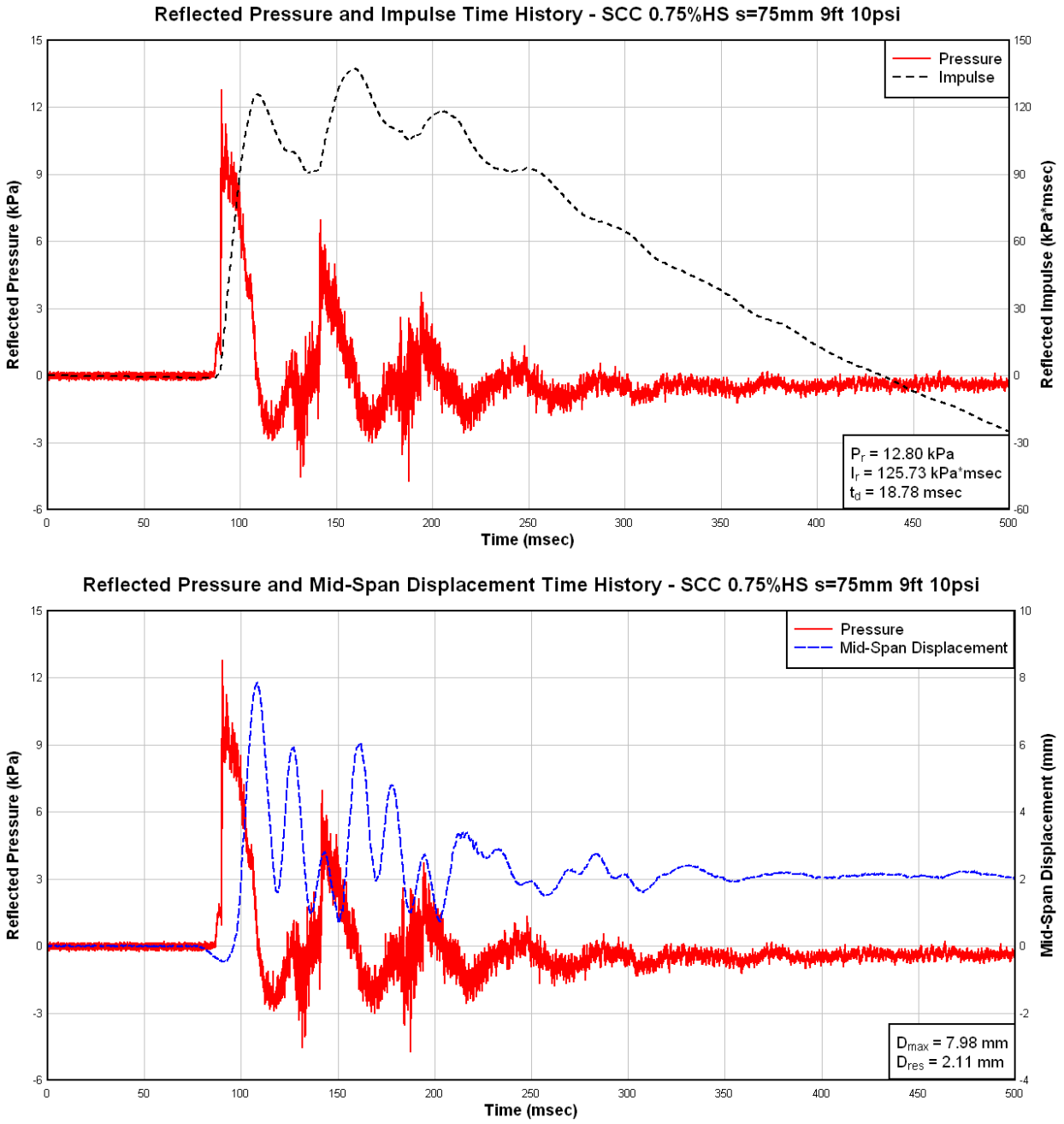

Figure 4.38 Column SCC-0.75%HS-75: recorded reflected pressure, impulse, and displacement for Blast 1

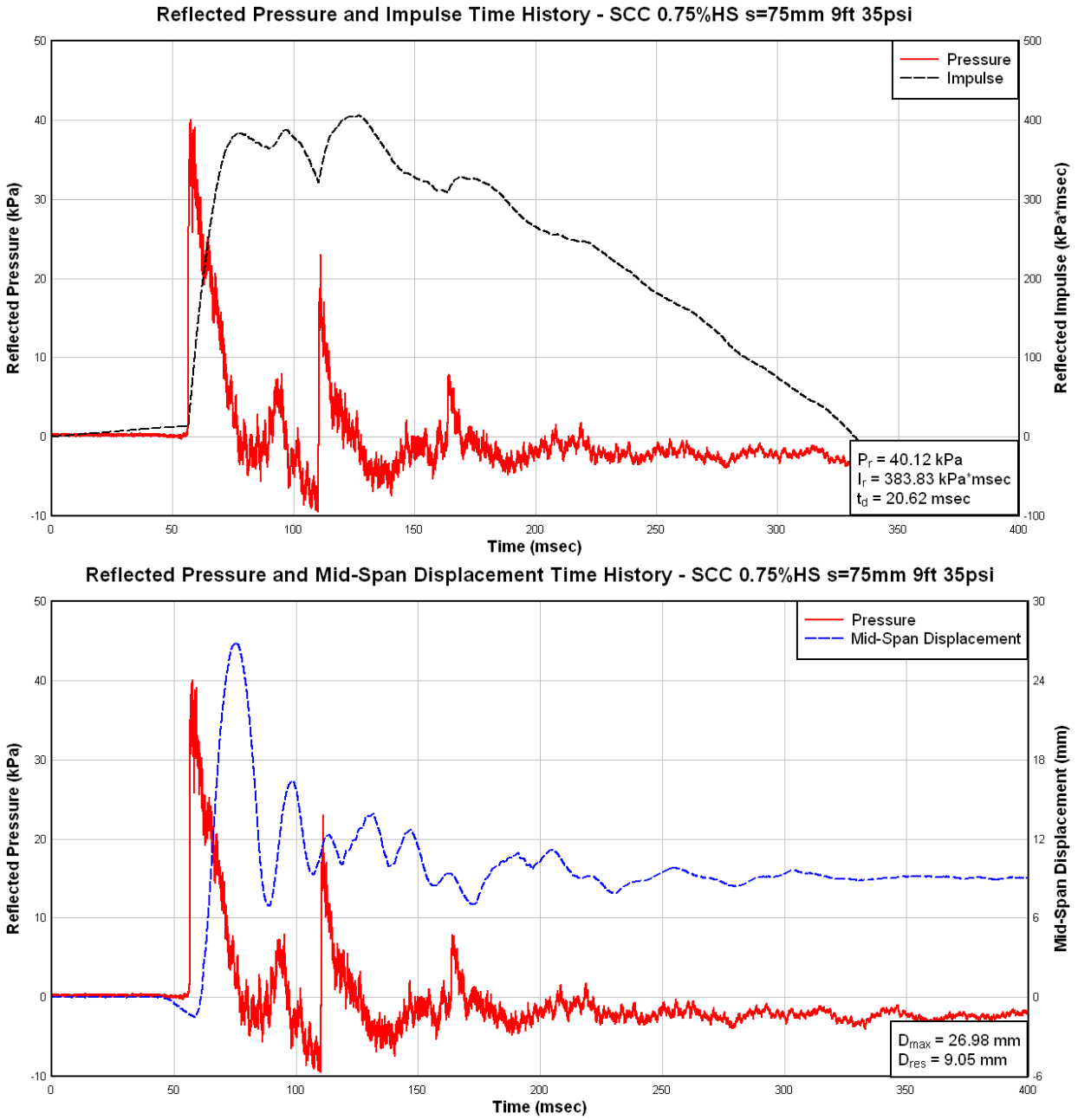

Figure 4.39 Column SCC-0.75%HS-75: recorded reflected pressure, impulse, and displacement for Blast 2

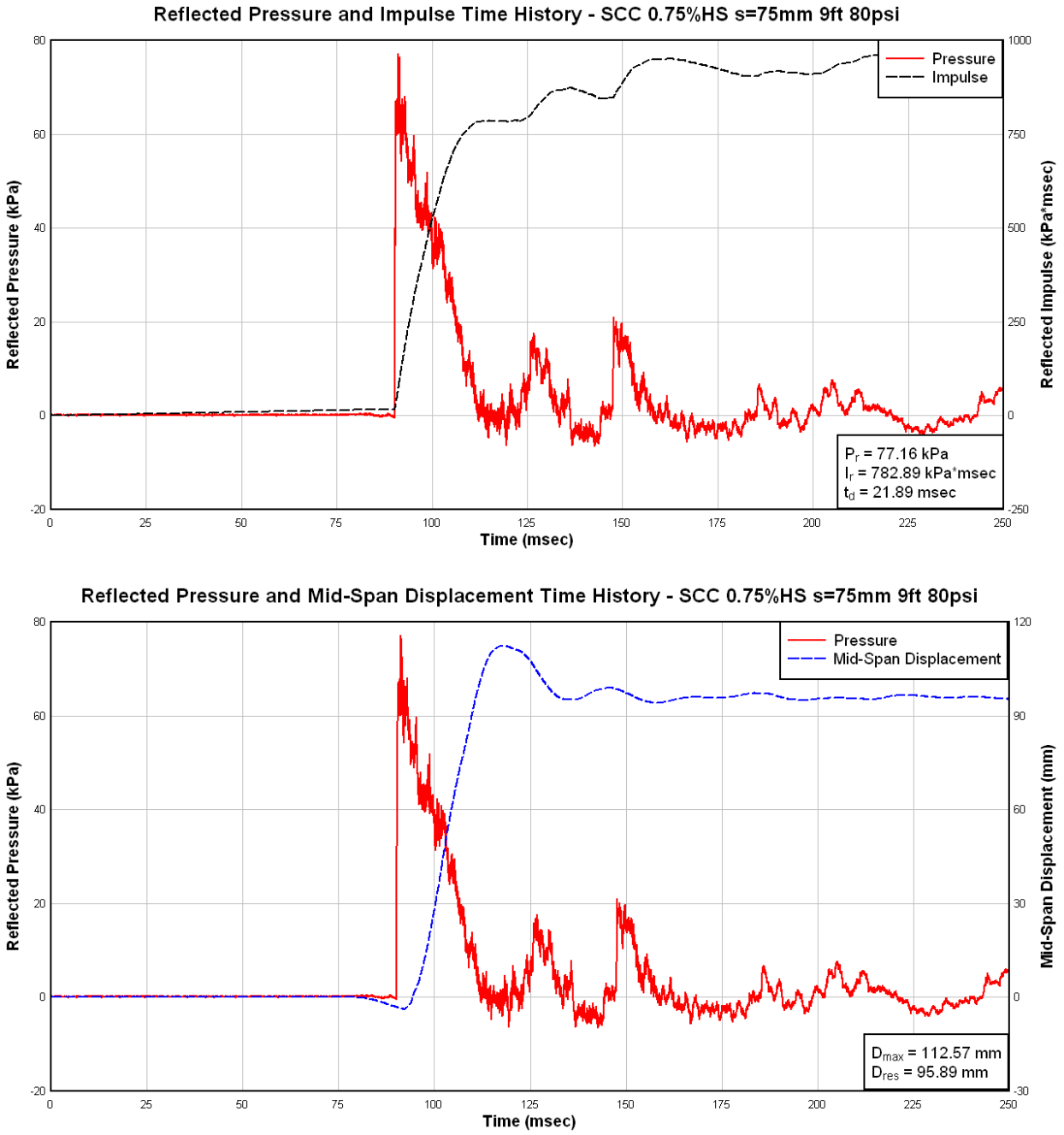

Figure 4.40 Column SCC-0.75%HS-75: recorded reflected pressure, impulse, and displacement for Blast 3

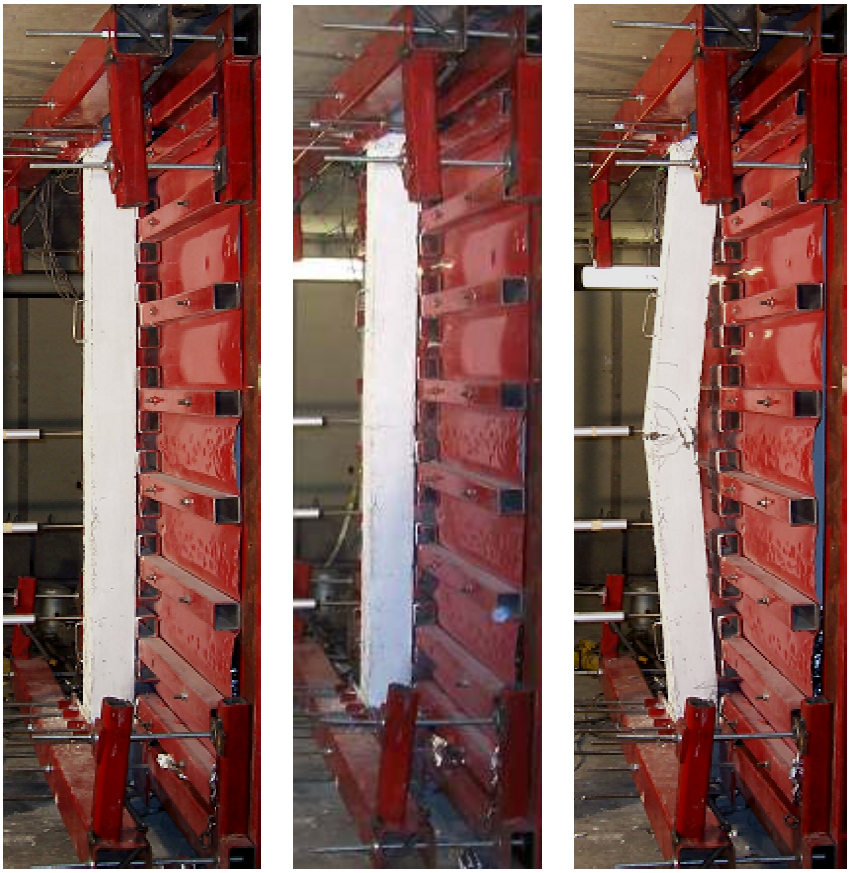

(a)Blast 1 (b)Blast 2 (c)Blast 3

Figure 4.41 Column SCC-0.75%HS-75 at the end of Blasts 1-3

(a)Mid-Span Result of Blast 1 (b) Top Support Region of Blast 2 (c) Mid-Span Result of Blast 3

Figure 4.42 Mid-span damage for Column SCC-0.75%HS-75

4.5.9 CRC-2%-75

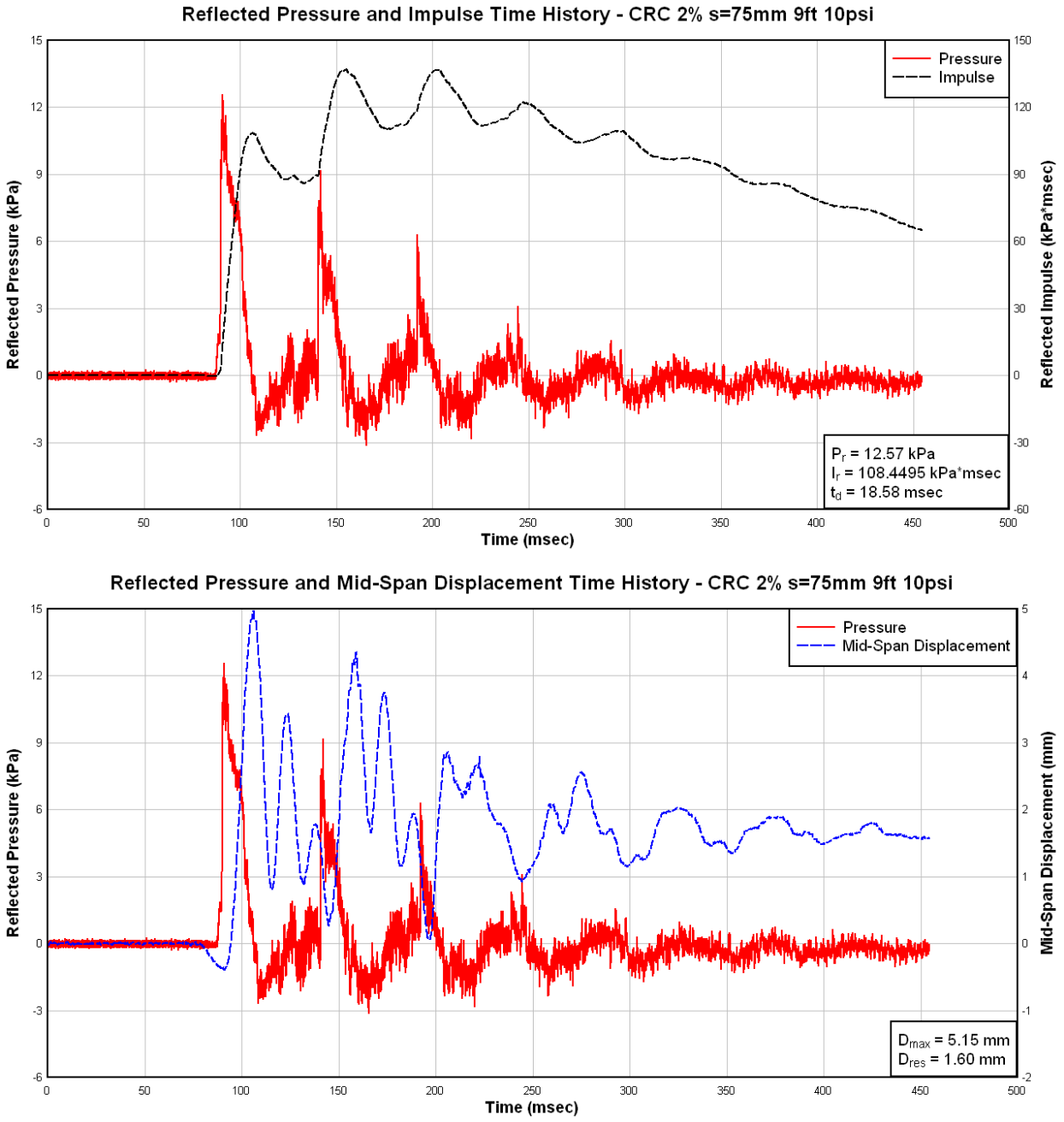

Figure 4.43 Column CRC-2% -75: recorded reflected pressure, impulse, and displacement for Blast 1

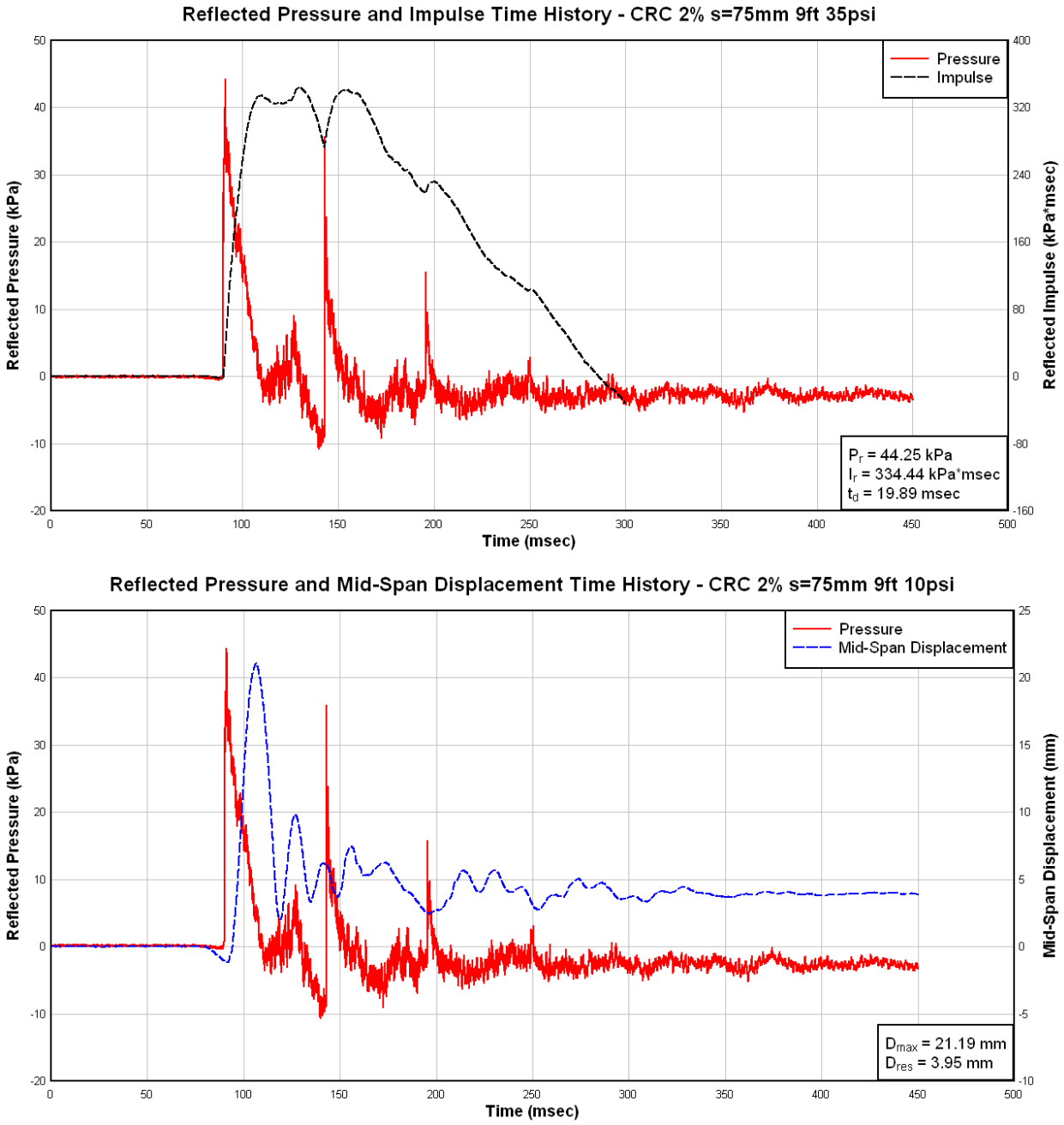

Figure 4.44 Column CRC-2% -75: recorded reflected pressure, impulse, and displacement for Blast 2

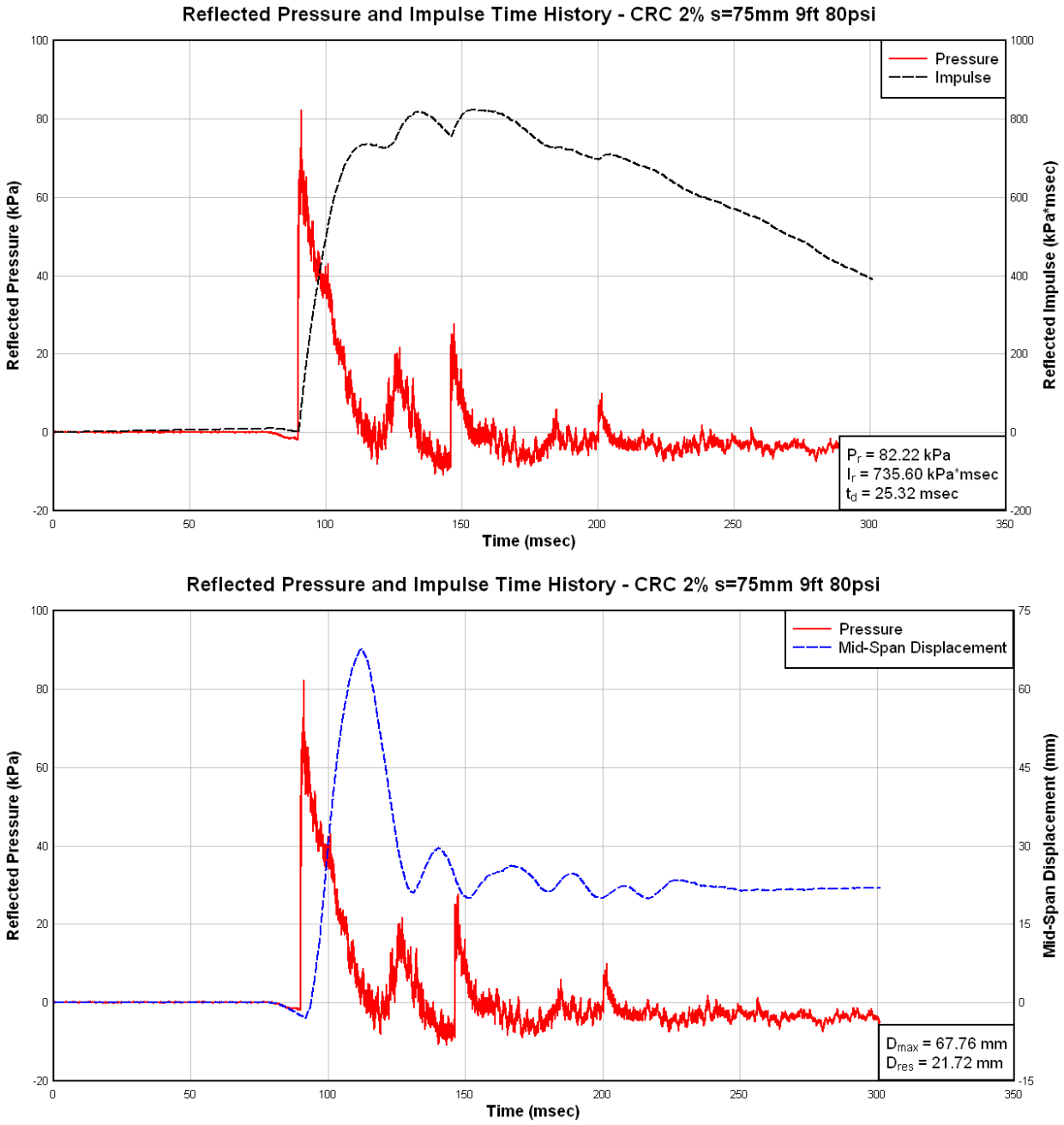

Figure 4.45 Column CRC-2% -75: recorded reflected pressure, impulse, and displacement for Blast 3

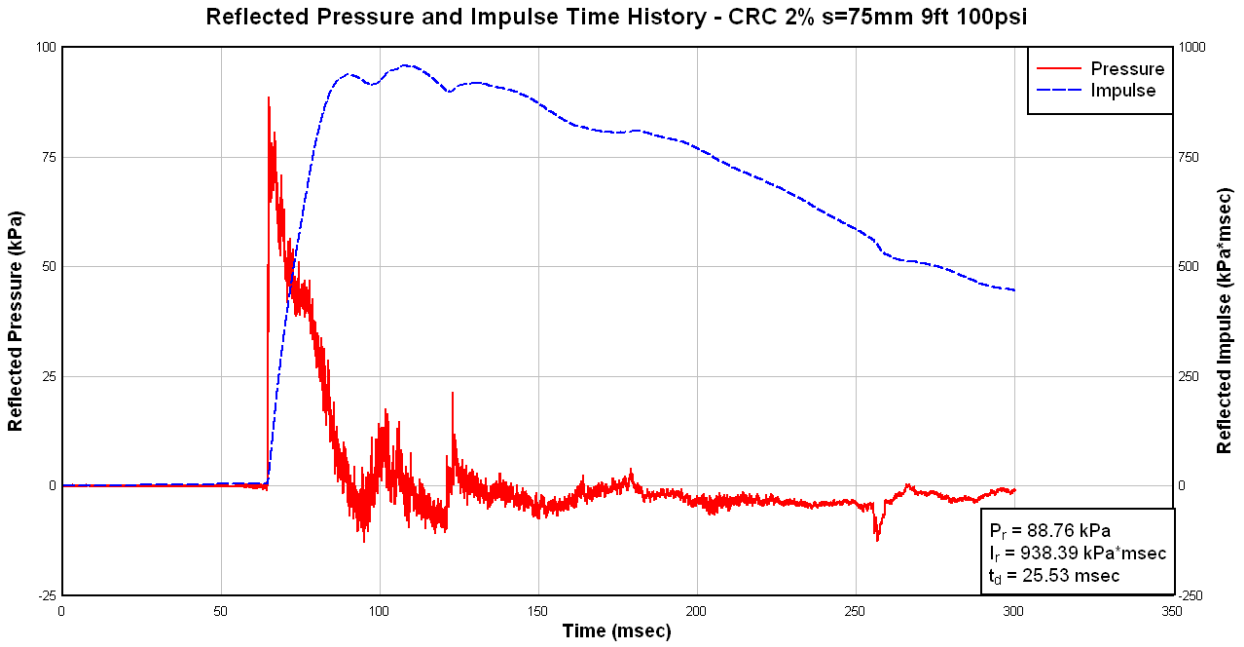

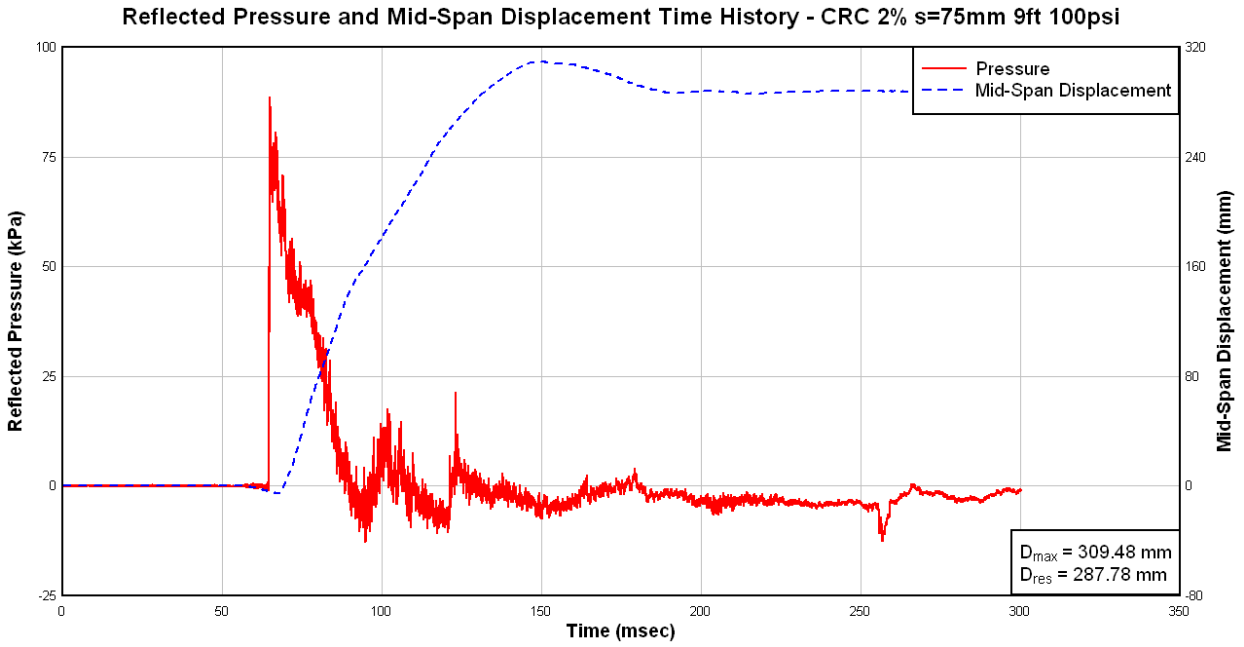

Figure 4.46 Column CRC-2% -75: recorded reflected pressure, impulse, and displacement for Blast 4

(a)Blast 1 (b)Blast 2 (c)Blast 3 (d)Blast 4

Figure 4.47 Column CRC-2%-75 at the end of Blasts 1-4

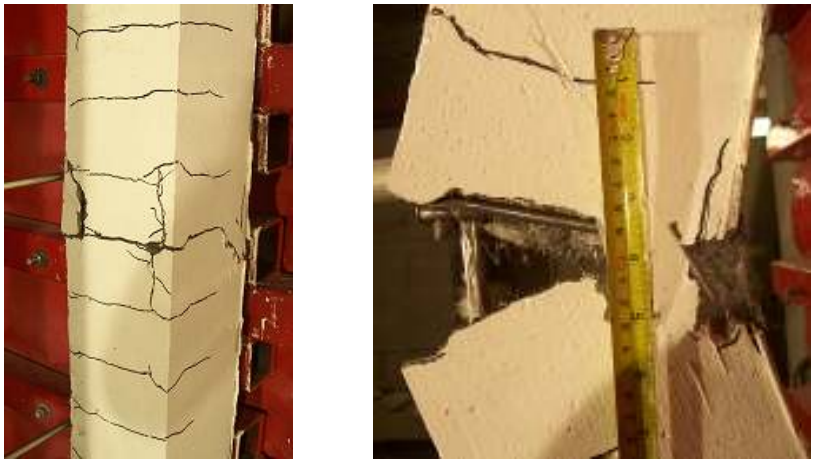

(a)Mid-Span Result of Blast 3 (b)Mid-Span Result of Blast 4

Figure 4.48 Mid-span damage for Column CRC-2%-75

4.5.10 CRC-4%-75

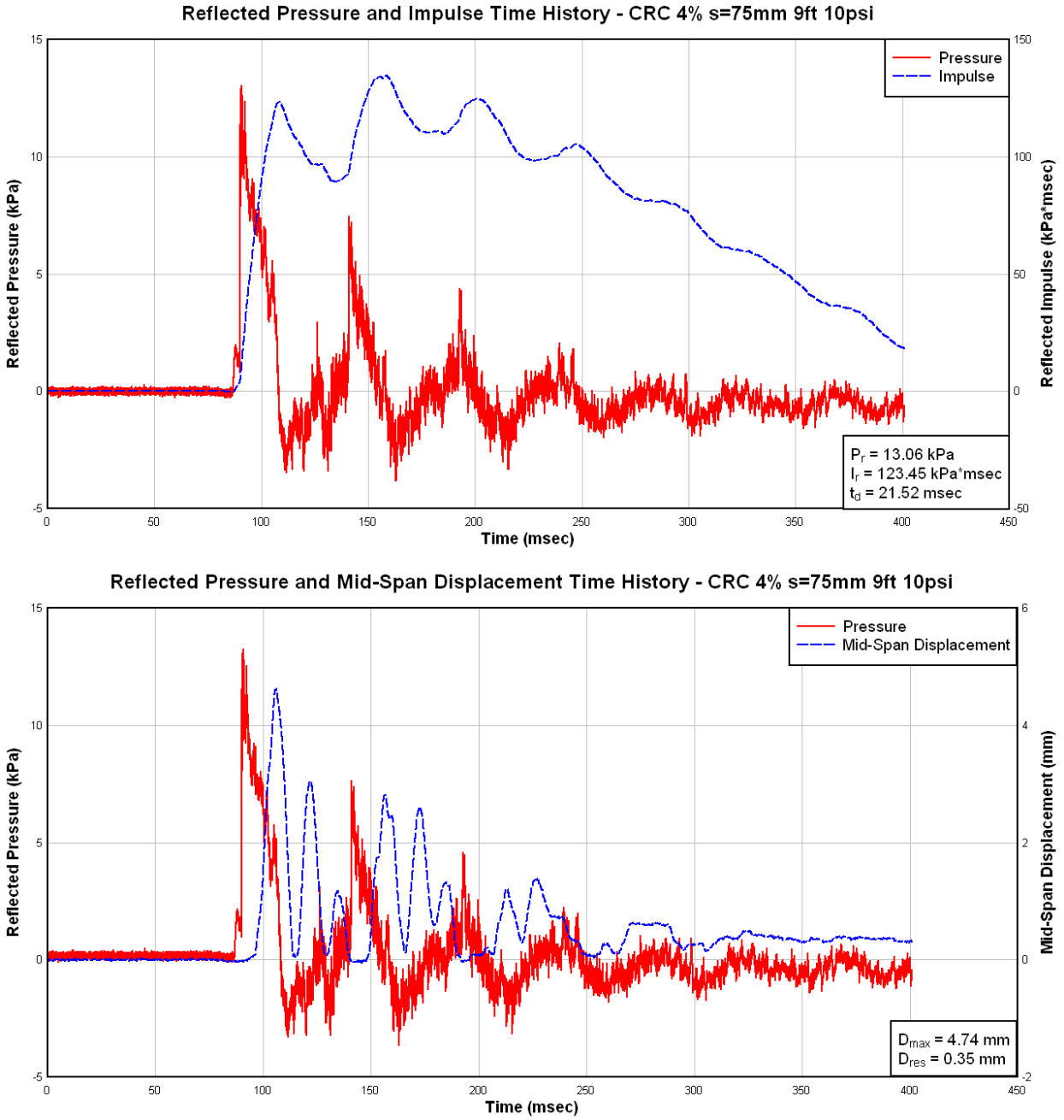

Figure 4.49 Column CRC-4% -75: recorded reflected pressure, impulse, and displacement for Blast 1

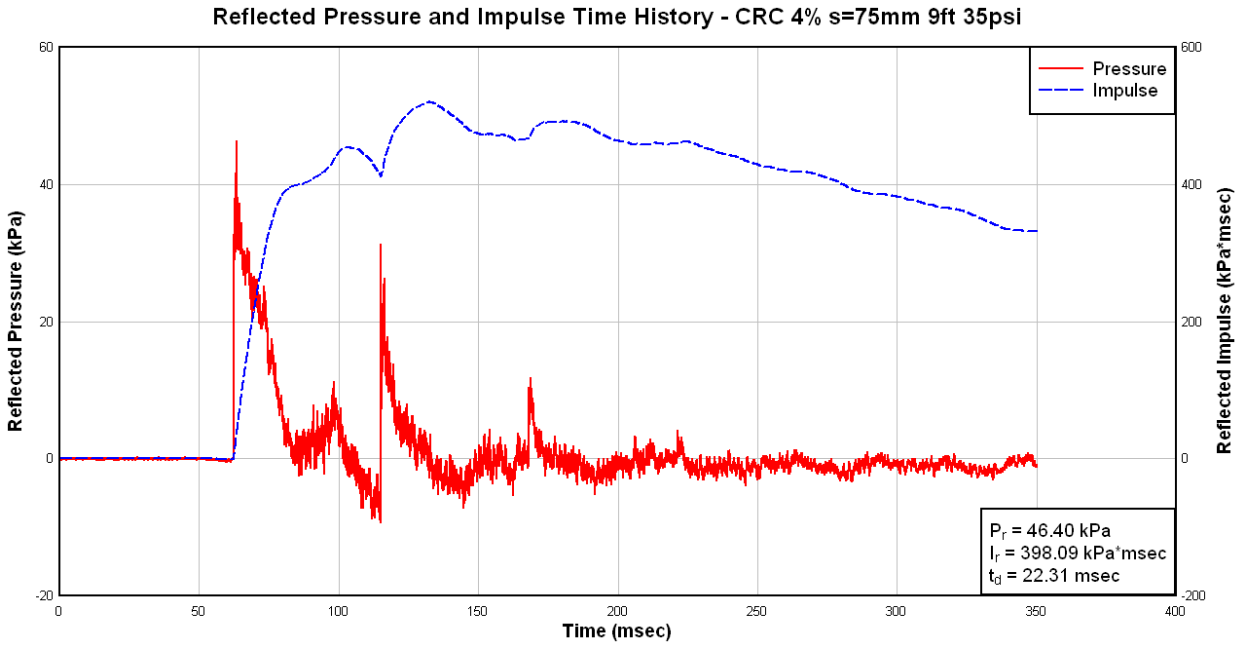

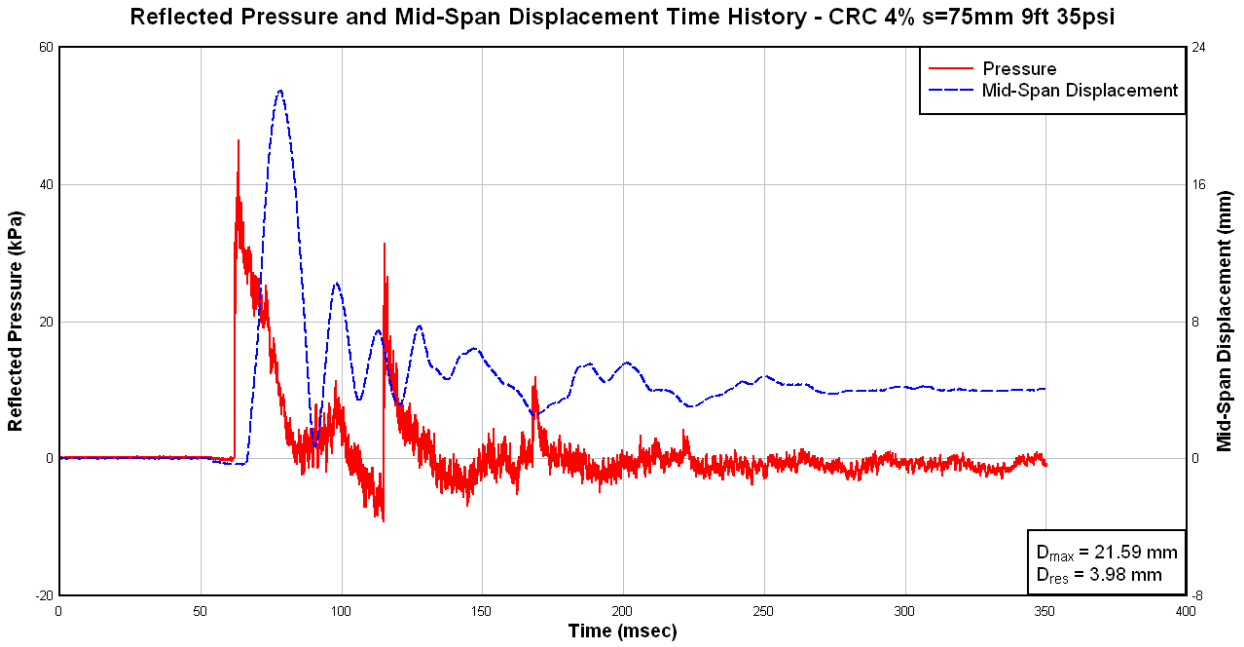

Figure 4.50 Column CRC-4% -75: recorded reflected pressure, impulse, and displacement for Blast 2

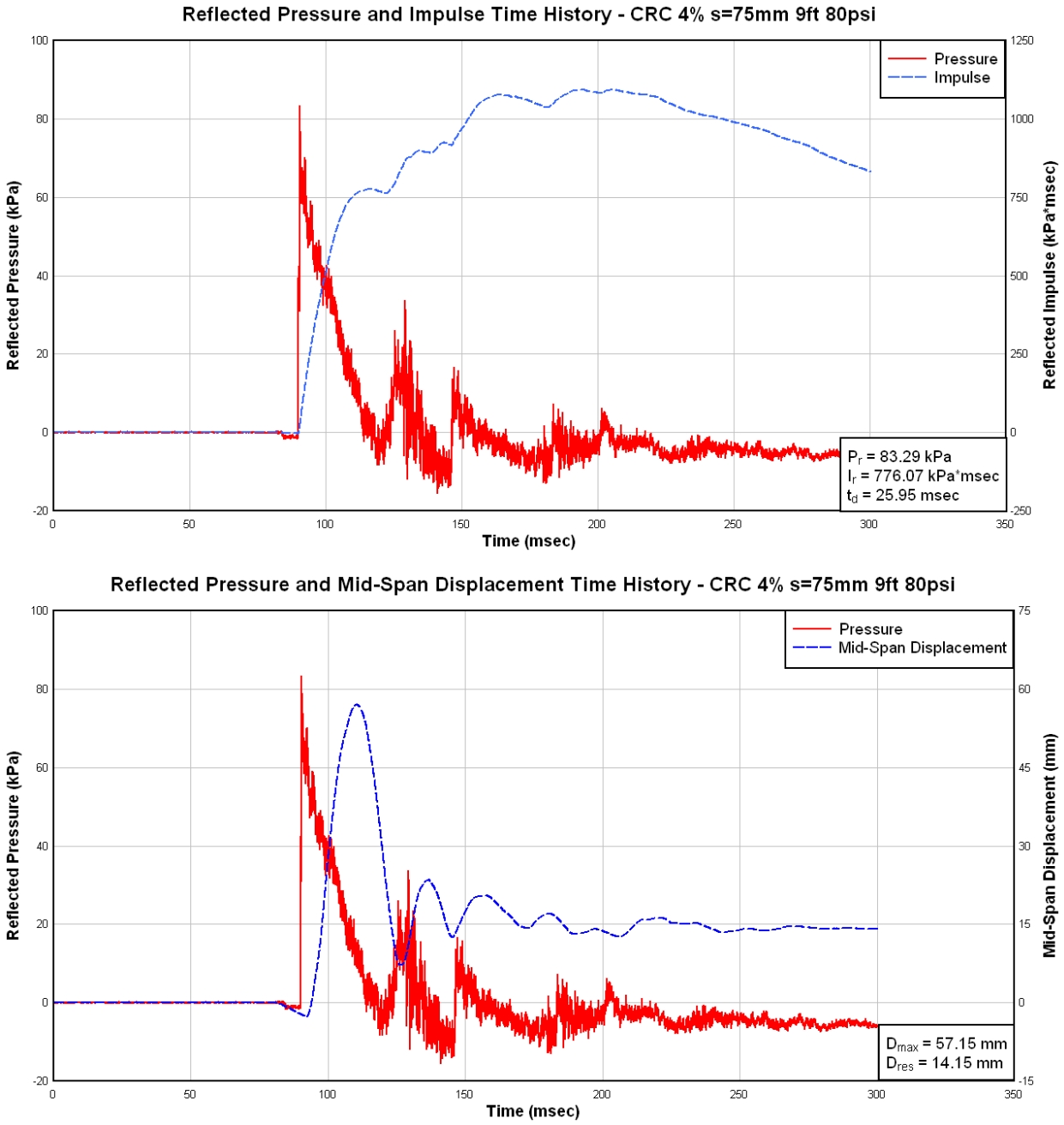

Figure 4.51 Column CRC-4% -75: recorded reflected pressure, impulse, and displacement for Blast 3

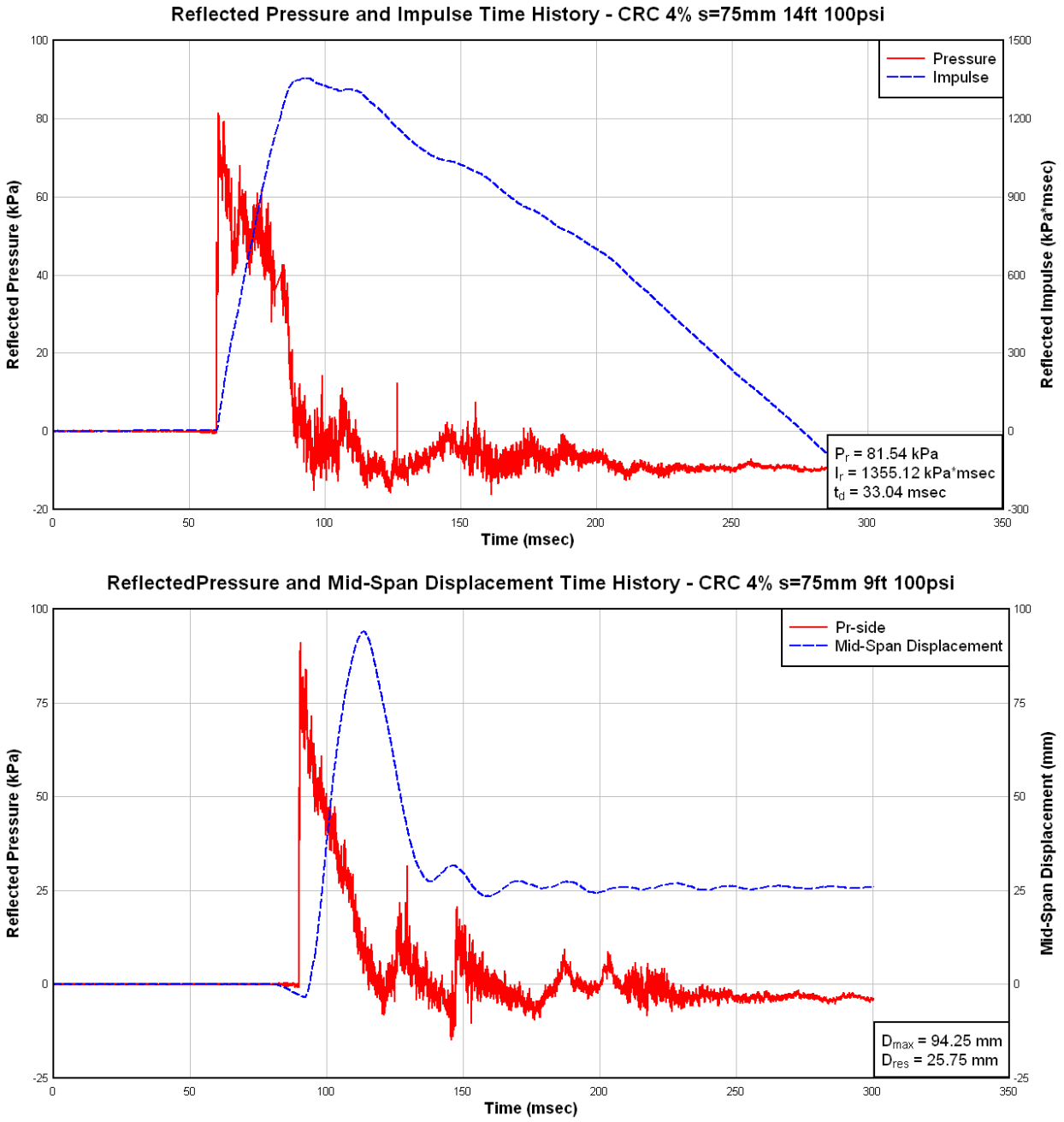

Figure 4.52 Column CRC-4% -75: recorded reflected pressure, impulse, and displacement for Blast 4

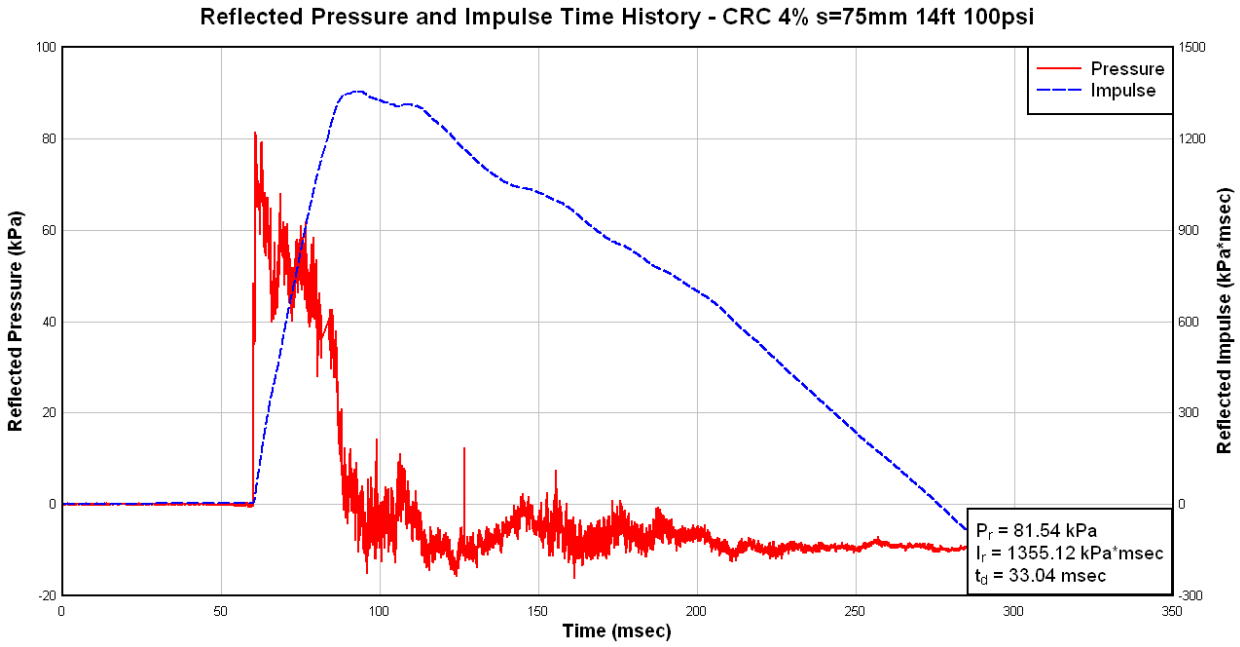

Figure 4.53 Column CRC-4% -75: recorded reflected pressure, impulse, and displacement for Blast 5

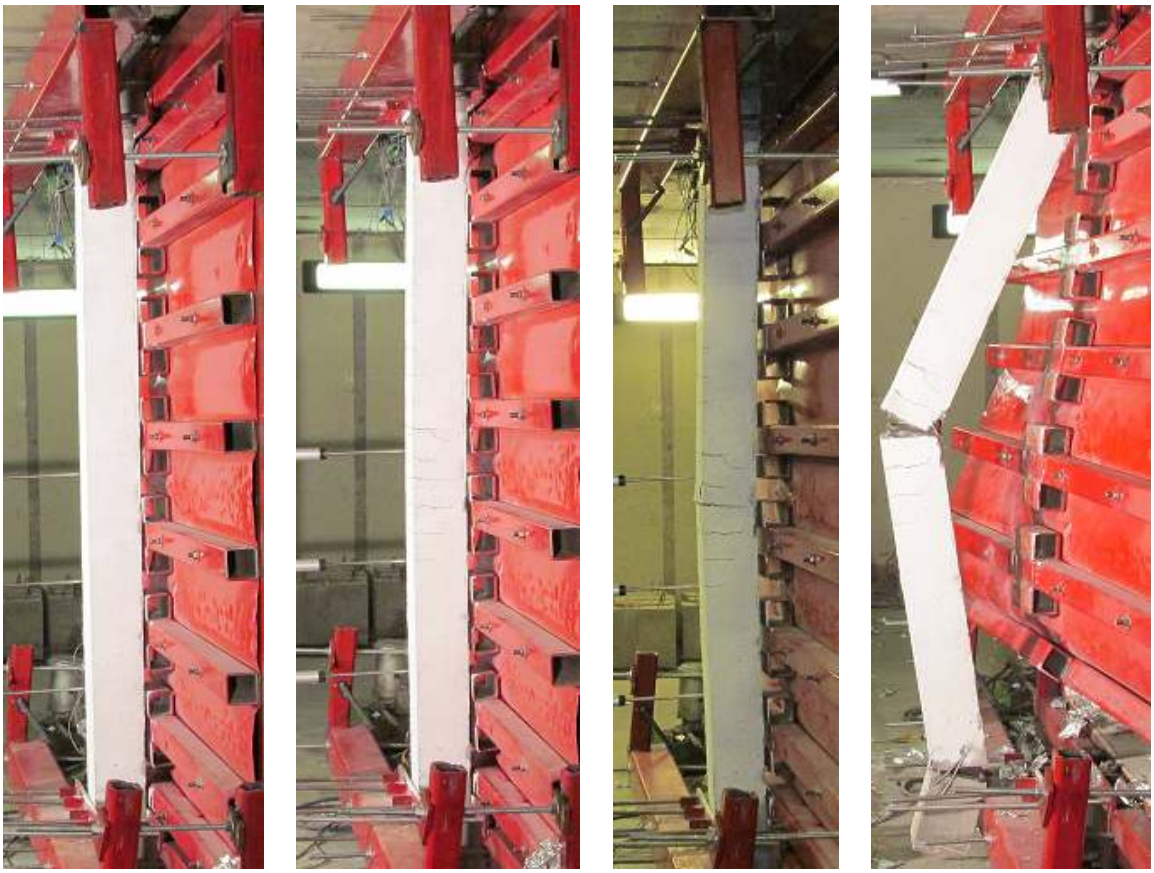

(a)Blast 2 (b)Blast 3 (c)Blast 4 (d)Blast 5

Figure 4.54 Column CRC-4%-75 at the end of Blasts 1-5

(a)Mid-Span Result of Blast 3 (b) Mid-Span Results of Blast 4 (c) Mid-Span Result of Blast 5

Figure 4.55 Mid-span damage for Column CRC-4%-75

4.5.11 CRC-6%-75

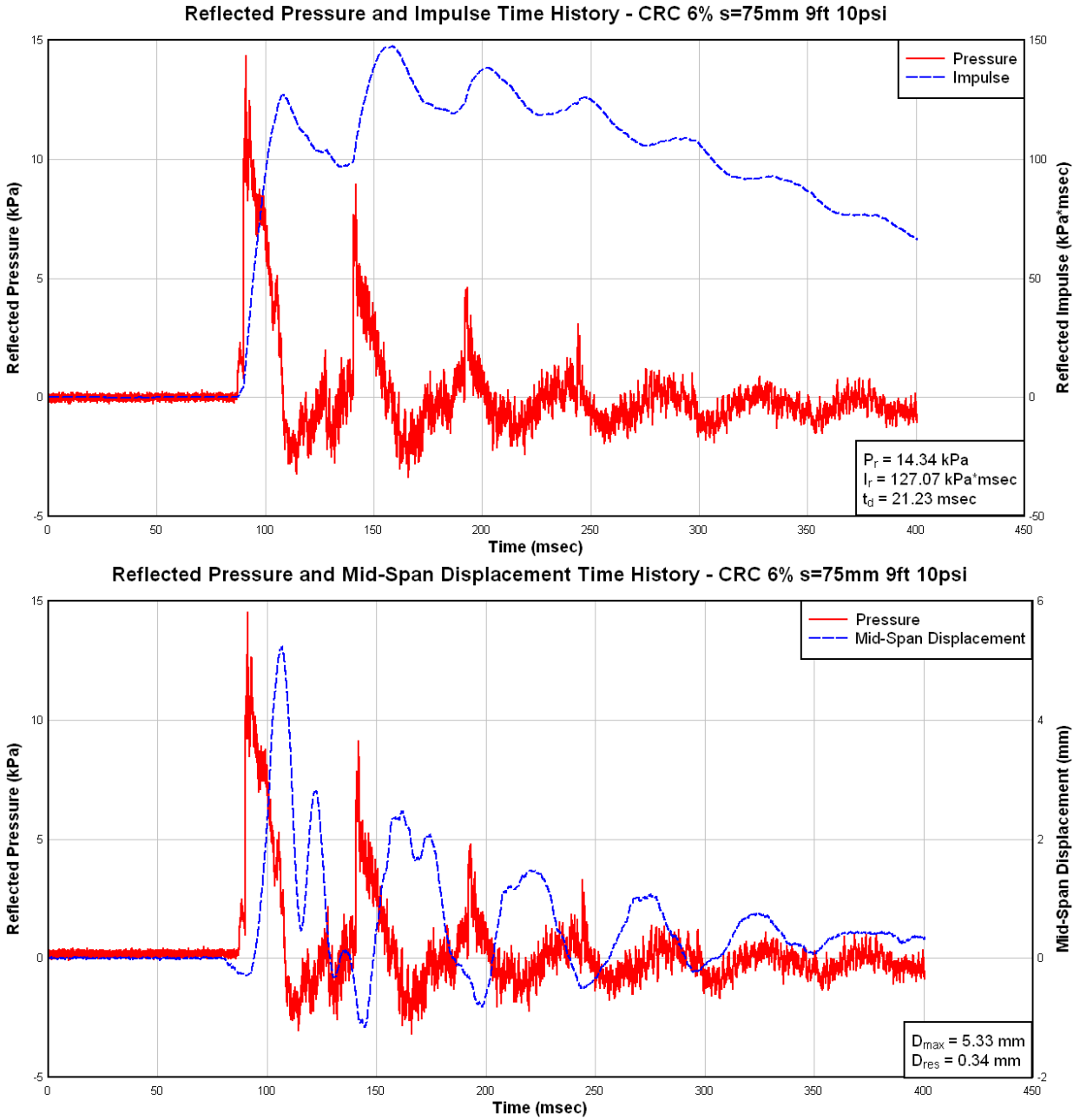

Figure 4.56 Column CRC-6% -75: recorded reflected pressure, impulse, and displacement for Blast 1

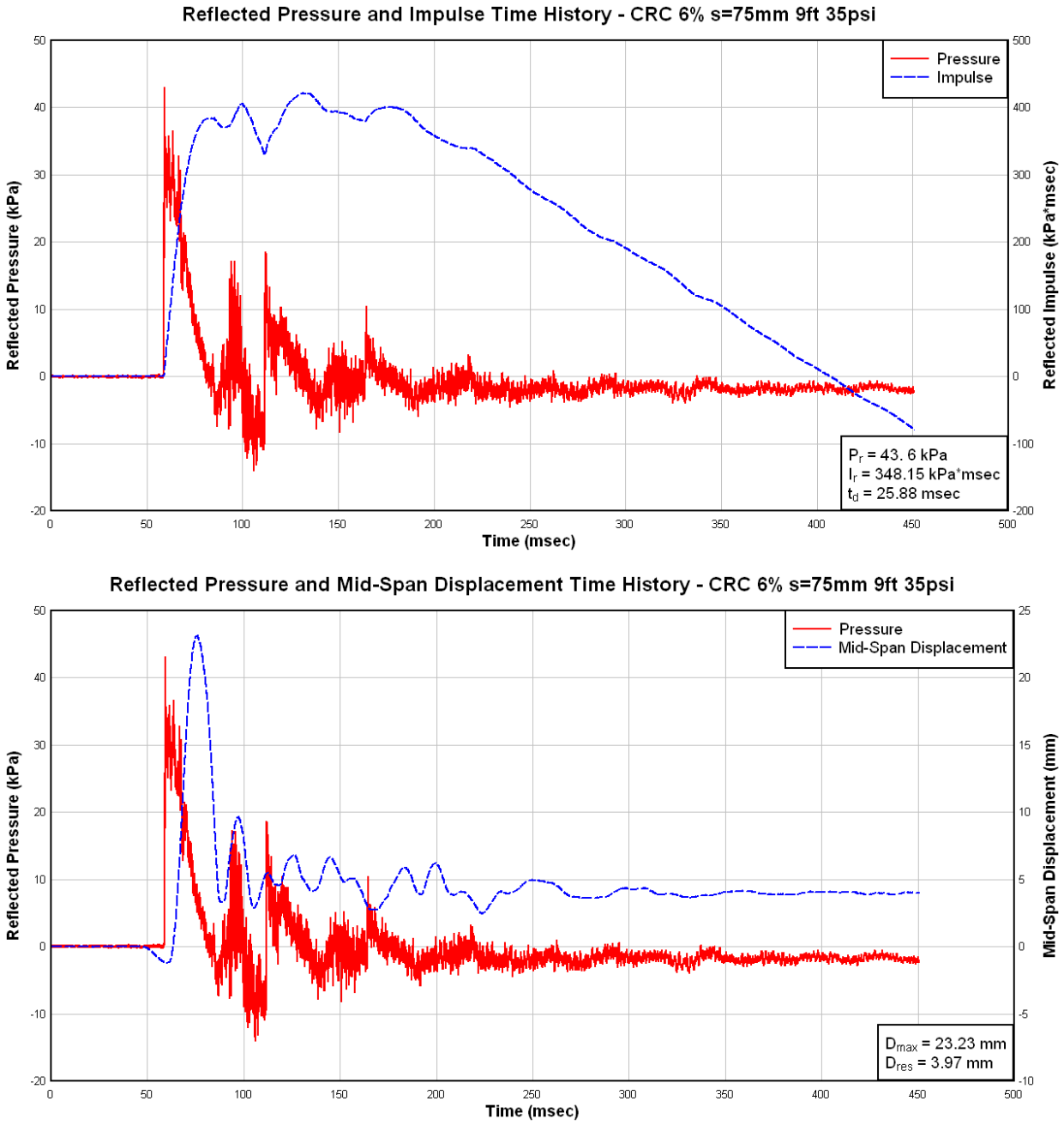

Figure 4.57 Column CRC-6% -75: recorded reflected pressure, impulse, and displacement for Blast 2

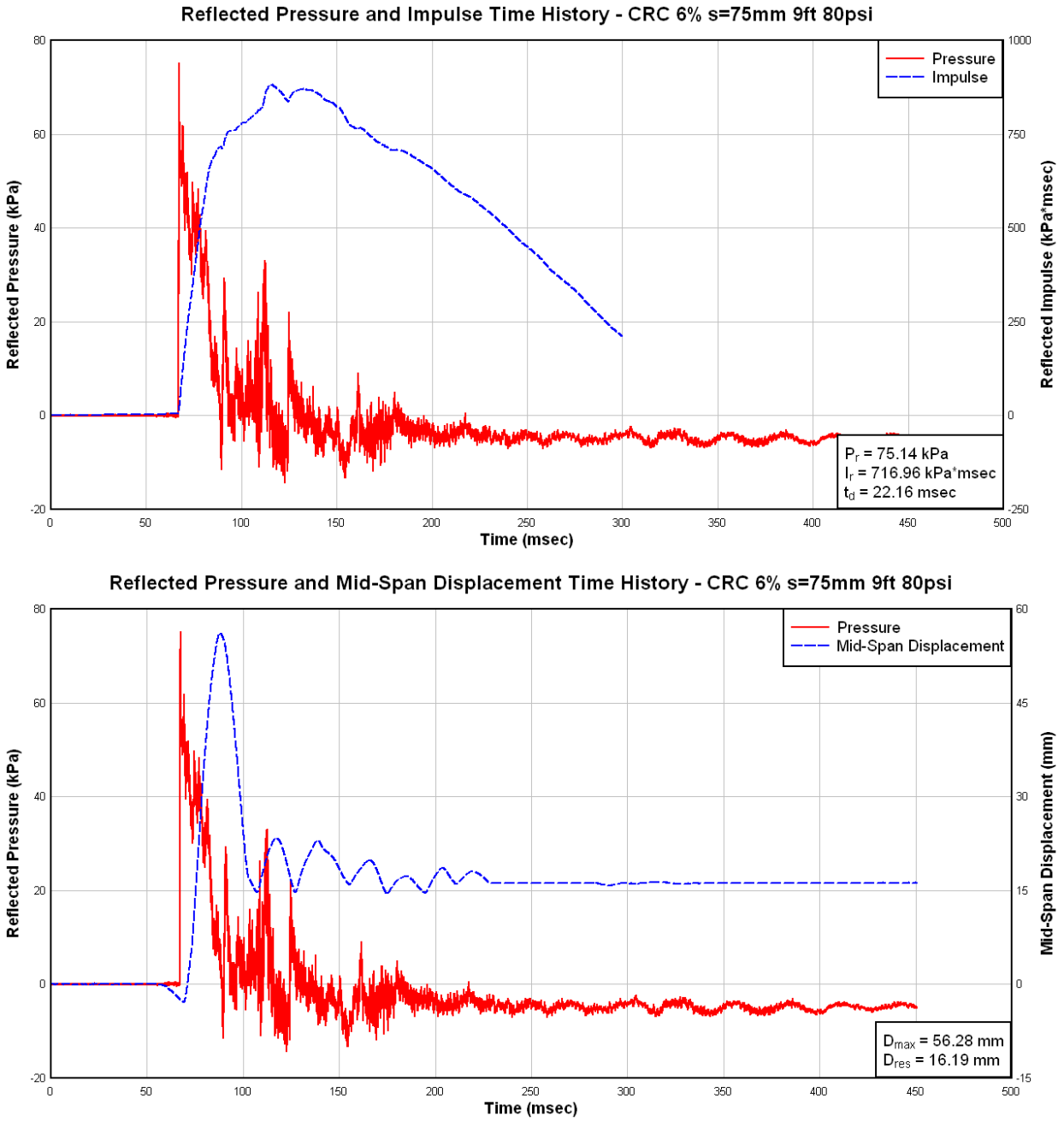

Figure 4.58 Column CRC-6% -75: recorded reflected pressure, impulse, and displacement for Blast 3

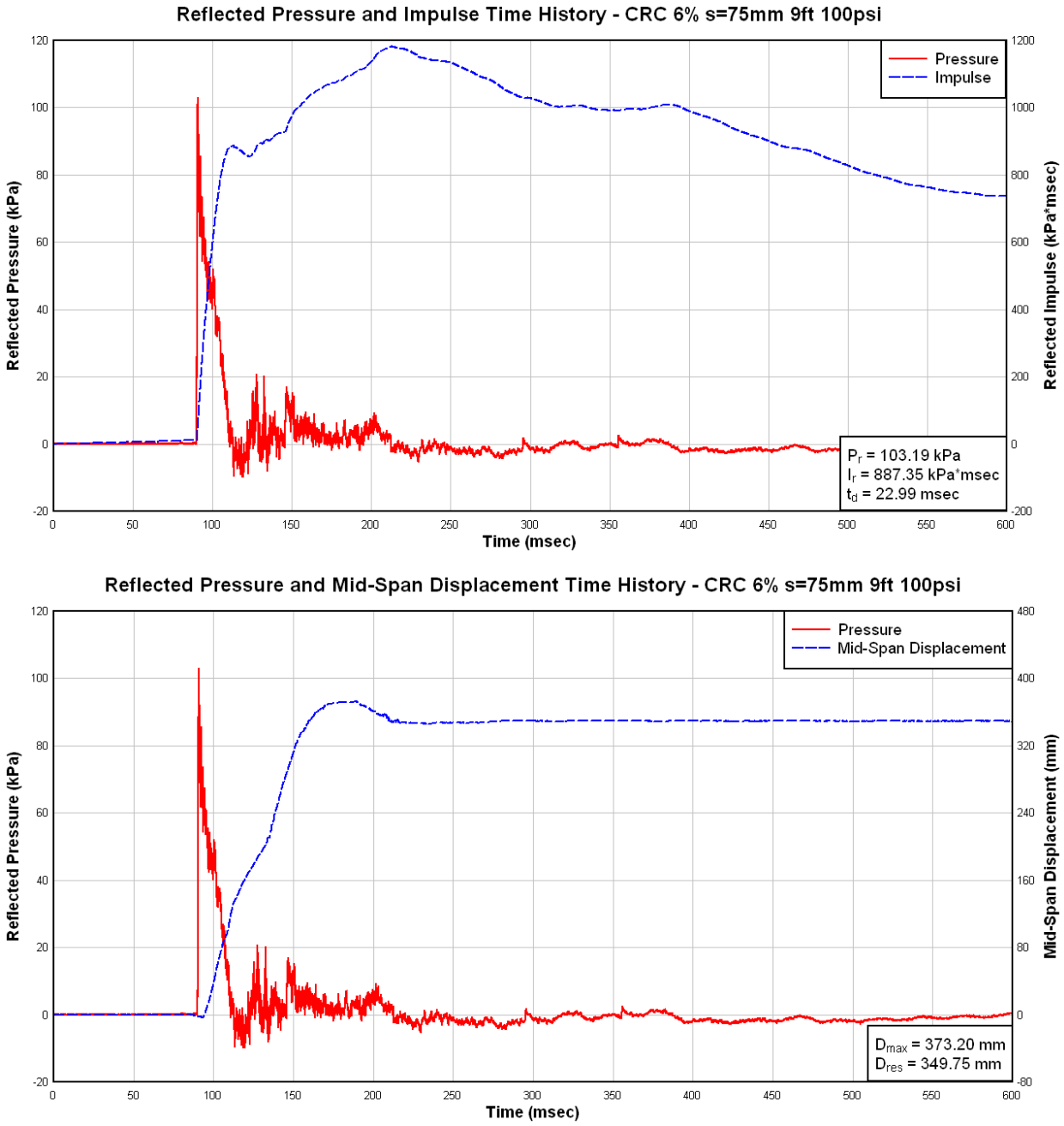

Figure 4.59 Column CRC-6% -75: recorded reflected pressure, impulse, and displacement for Blast 4

(a)Blast 1 (b)Blast 2 (c)Blast 3 (d)Blast 4

Figure 4.60 Column CRC-6%-75 at the end of testing

(a) Mid-Span Result of Blast 2 (b) Mid-Span Result of Blast 3 (b)Mid-Span Result of Blast 4

Figure 4.61 Mid-span damage for Column CRC-6%-75

4.5.12 CRC-2%-38

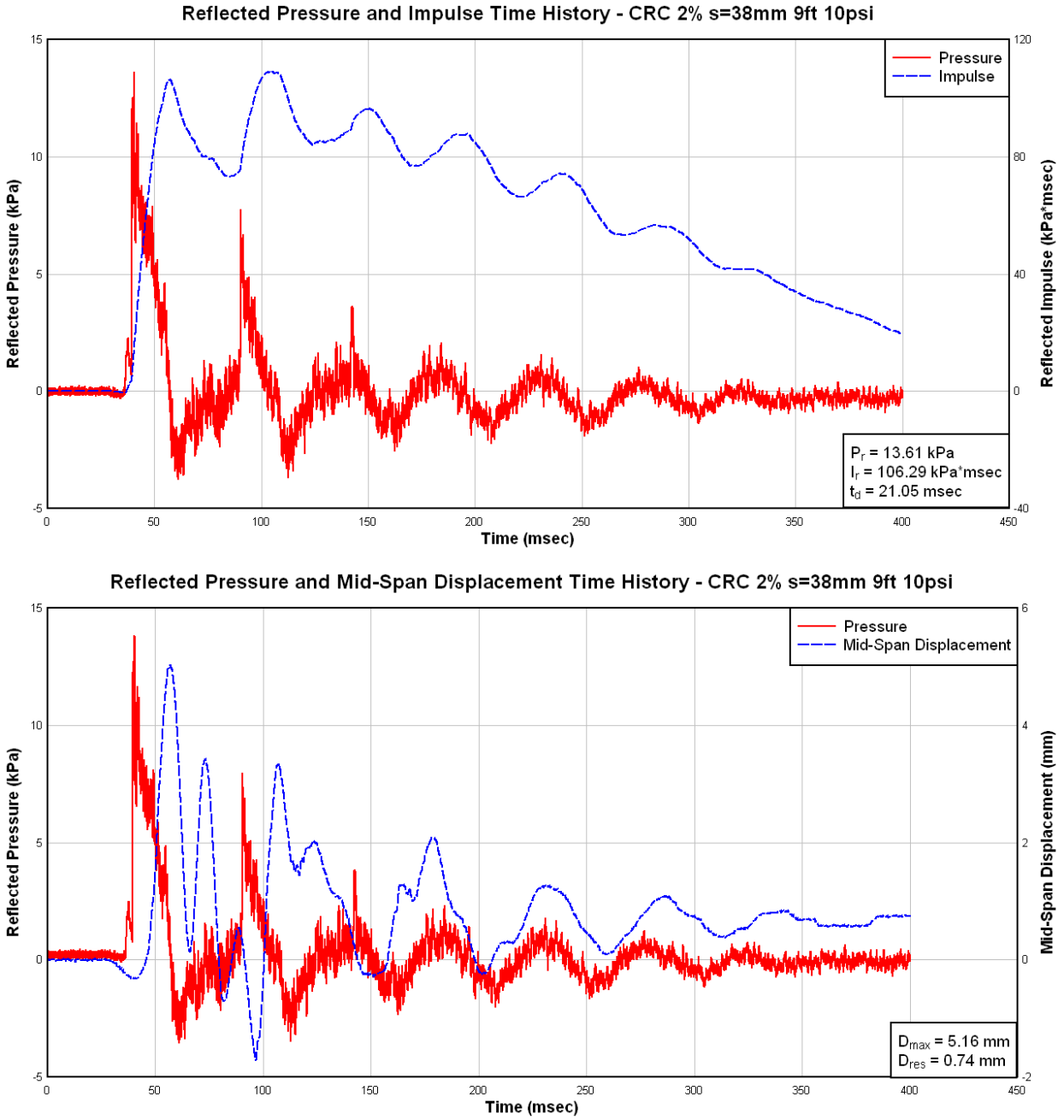

Figure 4.62 Column CRC-2%-38: recorded reflected pressure, impulse, and displacement for Blast 1

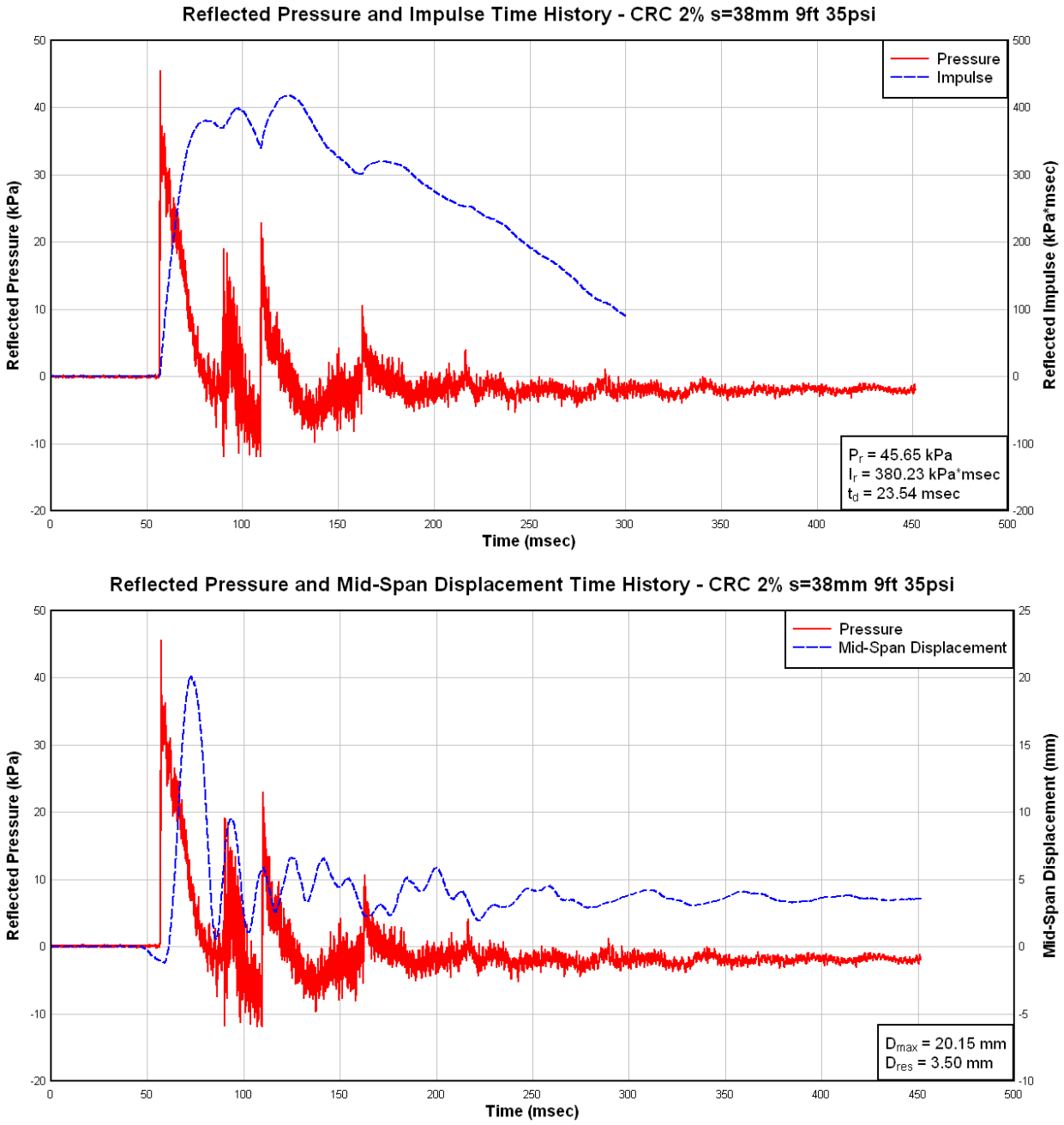

Figure 4.63 Column CRC-2%-38: recorded reflected pressure, impulse, and displacement for Blast 2

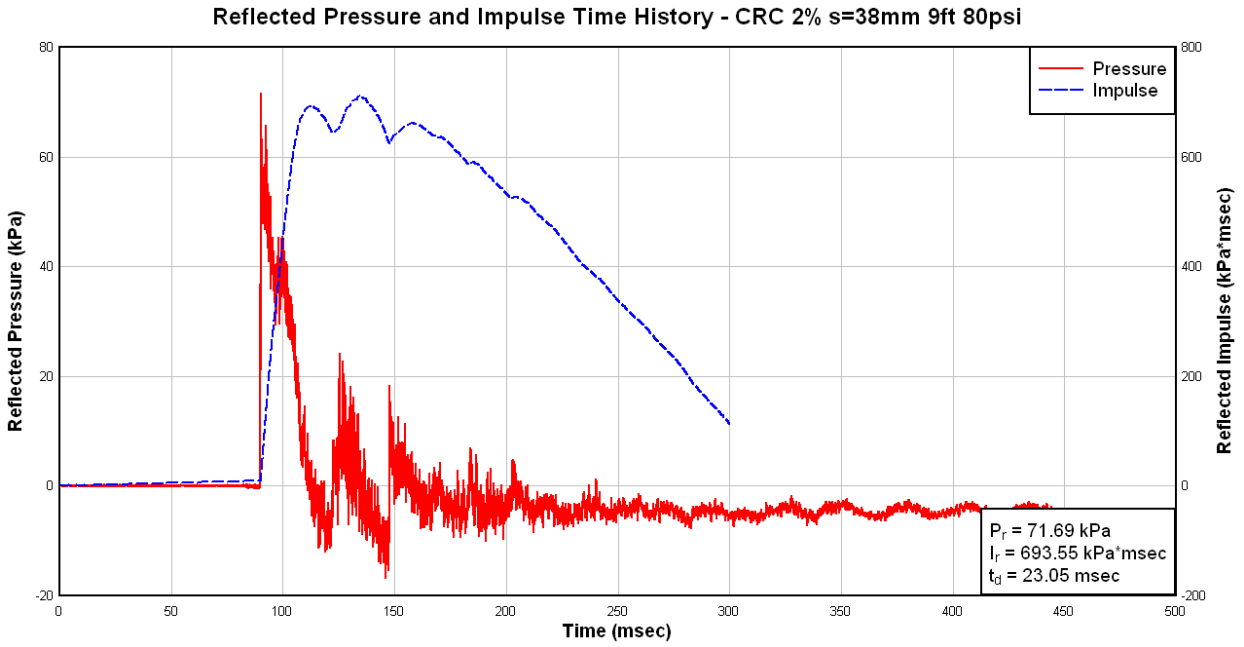

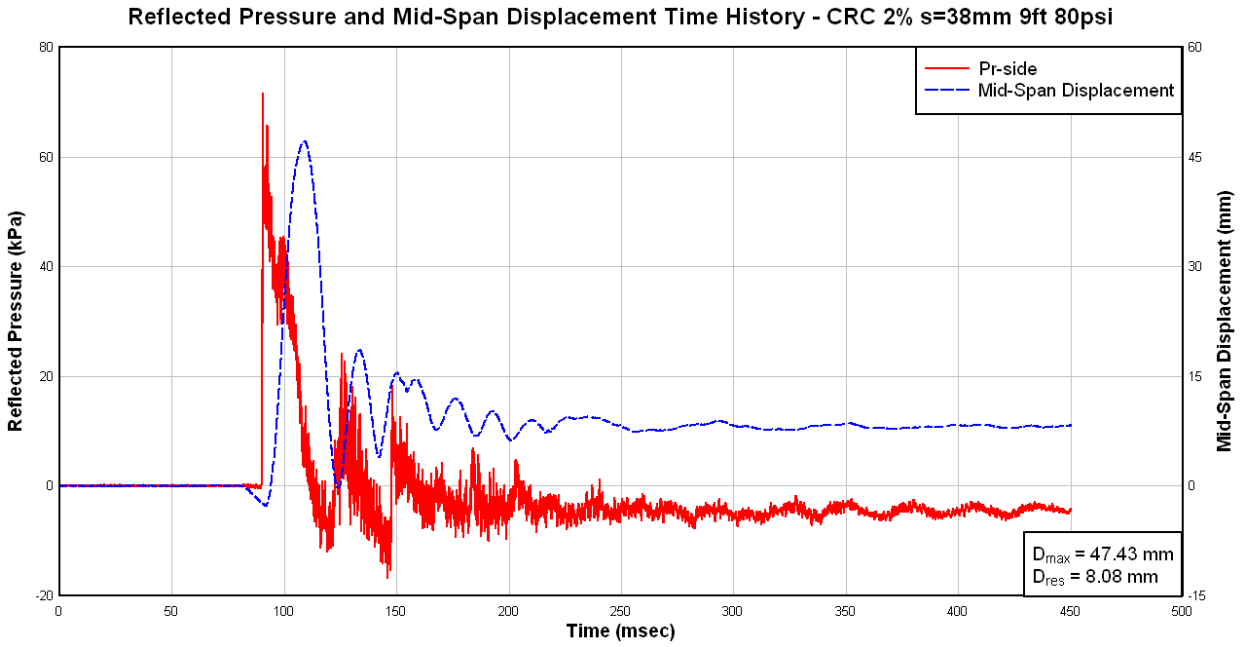

Figure 4.64 Column CRC-2%-38: recorded reflected pressure, impulse, and displacement for Blast 3

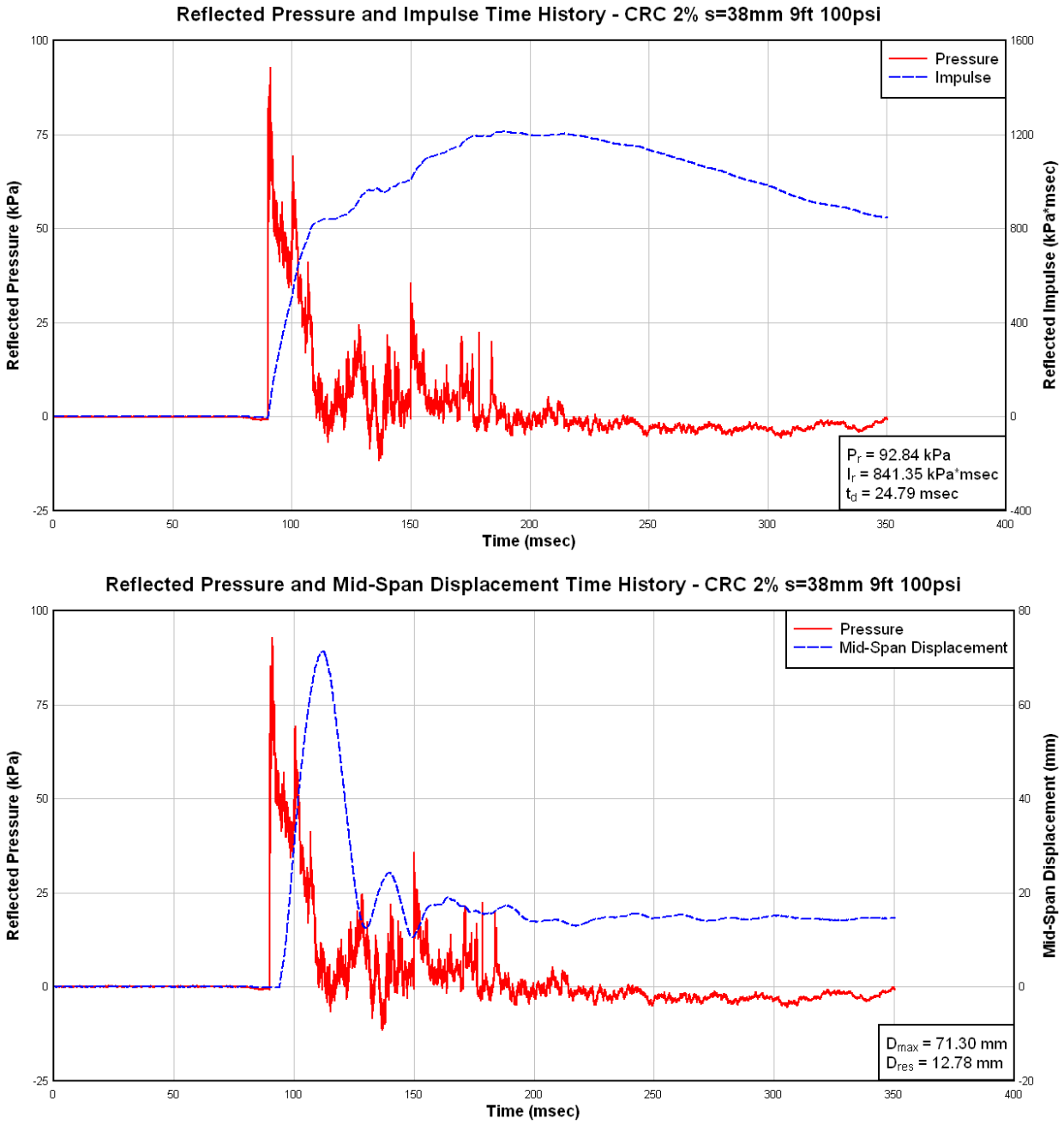

Figure 4.65 Column CRC-2%-38: recorded reflected pressure, impulse, and displacement for Blast 4

4.5.12.1 Blast 4 (2)

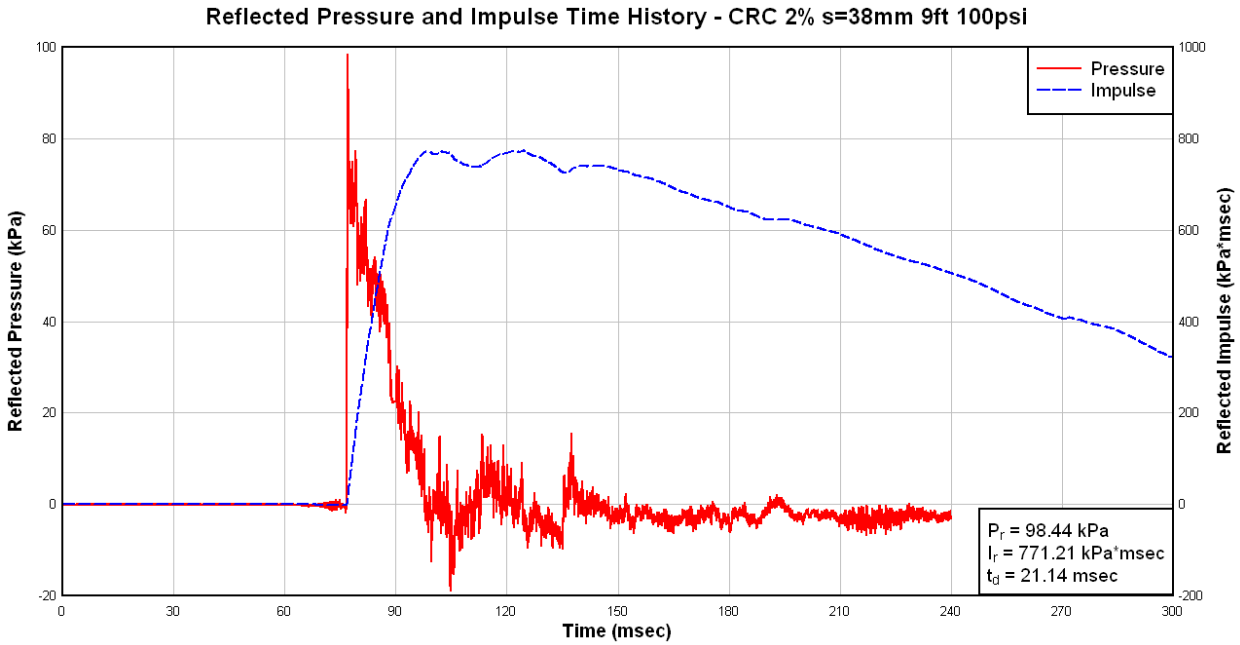

Figure 4.66 Column CRC-2%-38: recorded reflected pressure, impulse, and displacement for Blast 4(2)

(a)Blast 2 (b)Blast 3 (c)Blast 4 (d)Blast 4(2)

Figure 4.67 Column CRC-2%-38 at the end of Blasts 1-4 (2)

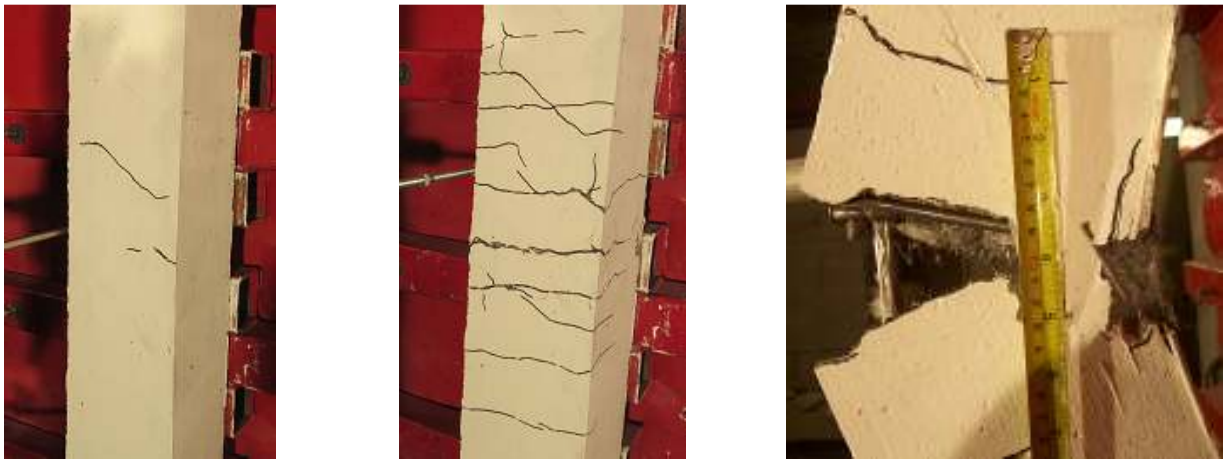

(a)Mid-Span Result of Blast 2 (b) Mid-Span Result of Blast 4 (c)Mid-Span Result of Blast 4(2)

Figure 4.68 Mid-span damage for Column CRC-2%-38

4.5.13 CRC-4%-38

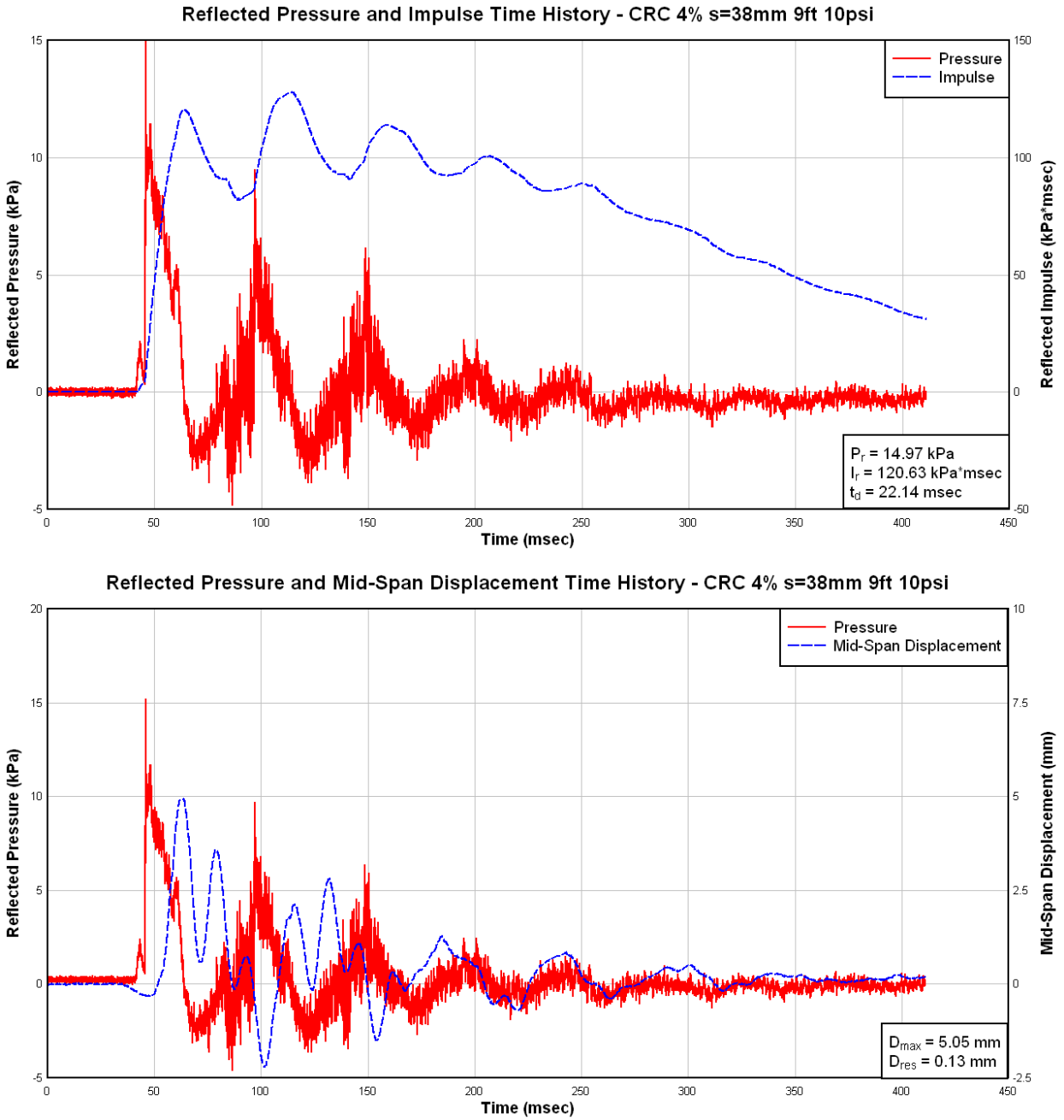

Figure 4.69 Column CRC-4%-38: recorded reflected pressure, impulse, and displacement for Blast 1

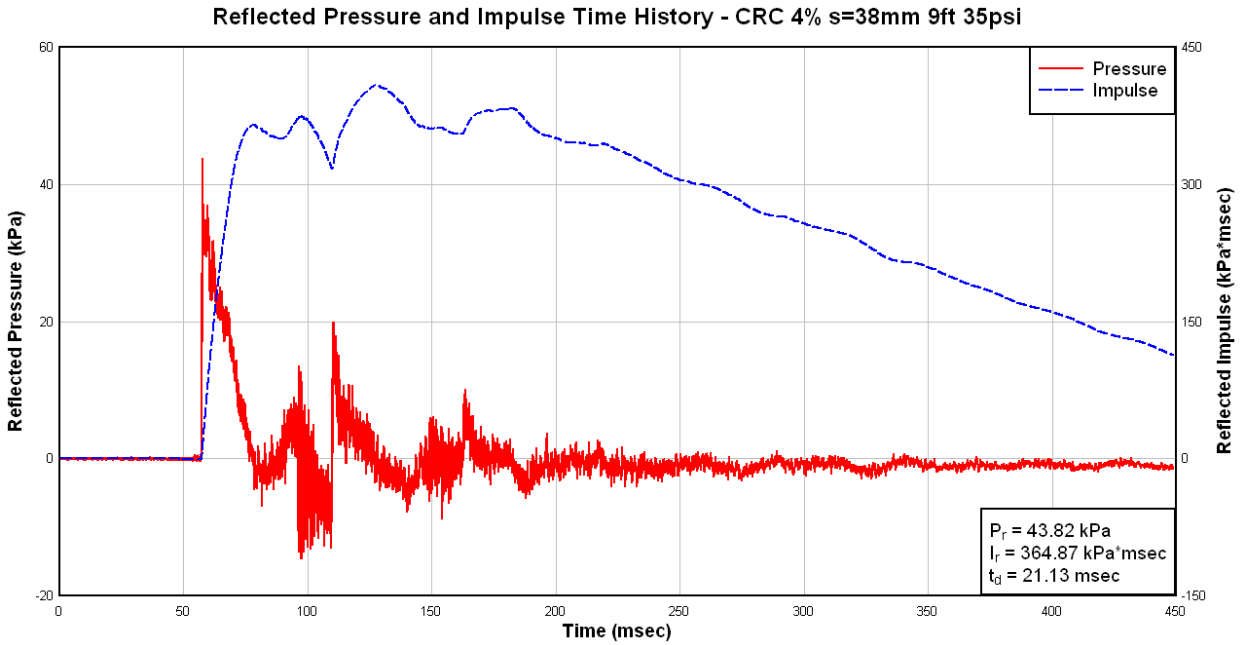

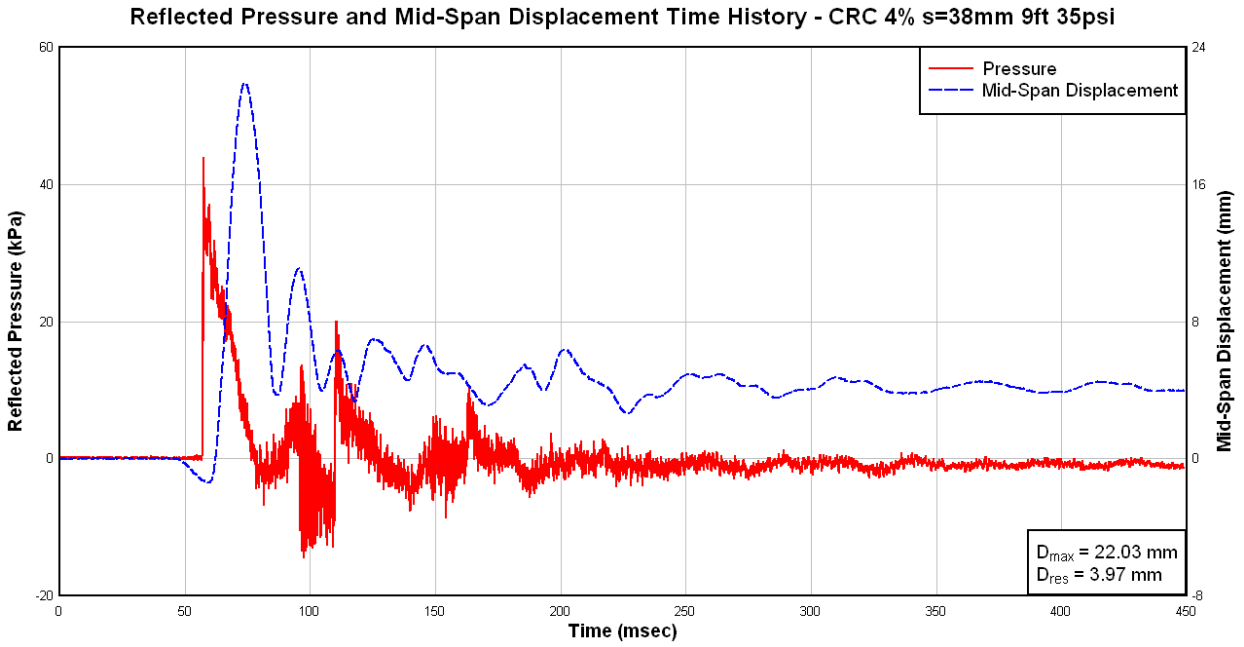

Figure 4.70 Column CRC-4%-38: recorded reflected pressure, impulse, and displacement for Blast 2

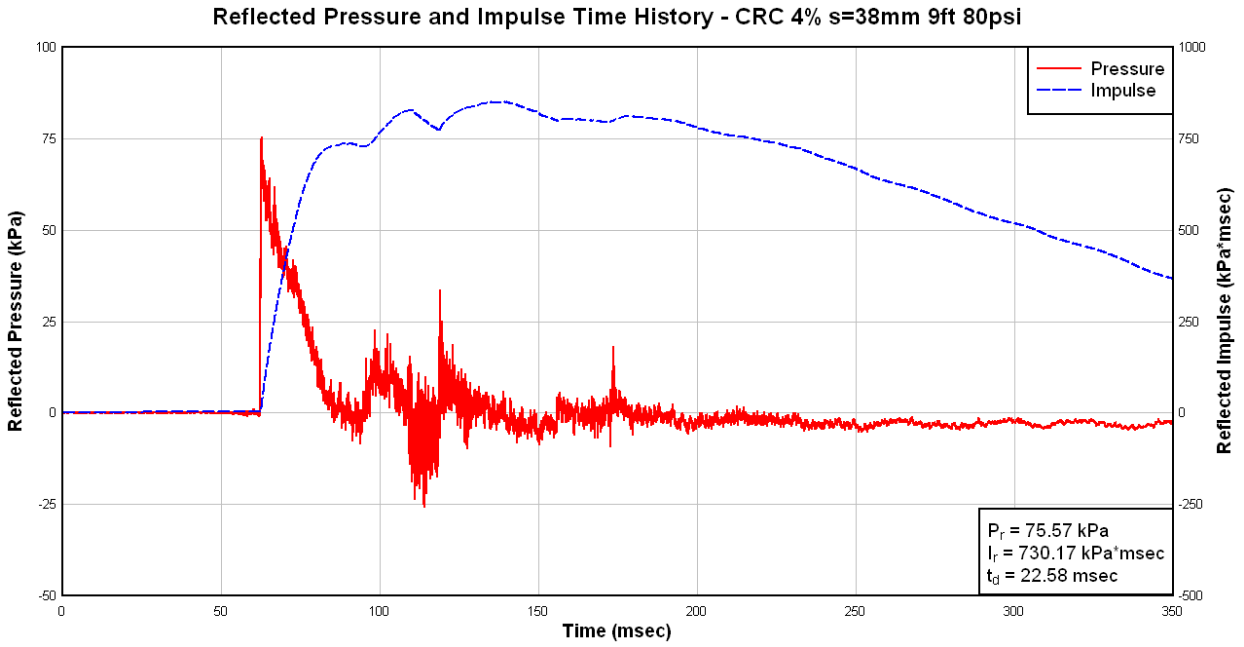

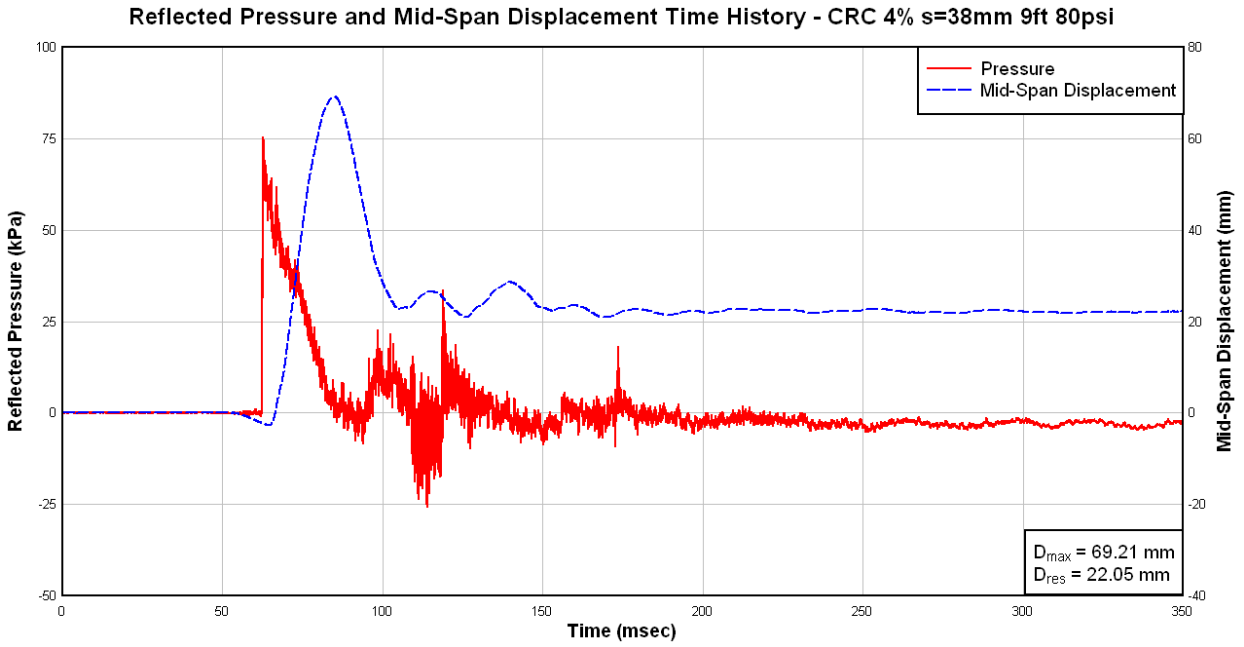

Figure 4.71 Column CRC-4%-38: recorded reflected pressure, impulse, and displacement for Blast 3

4.5.13.1 Blast 4

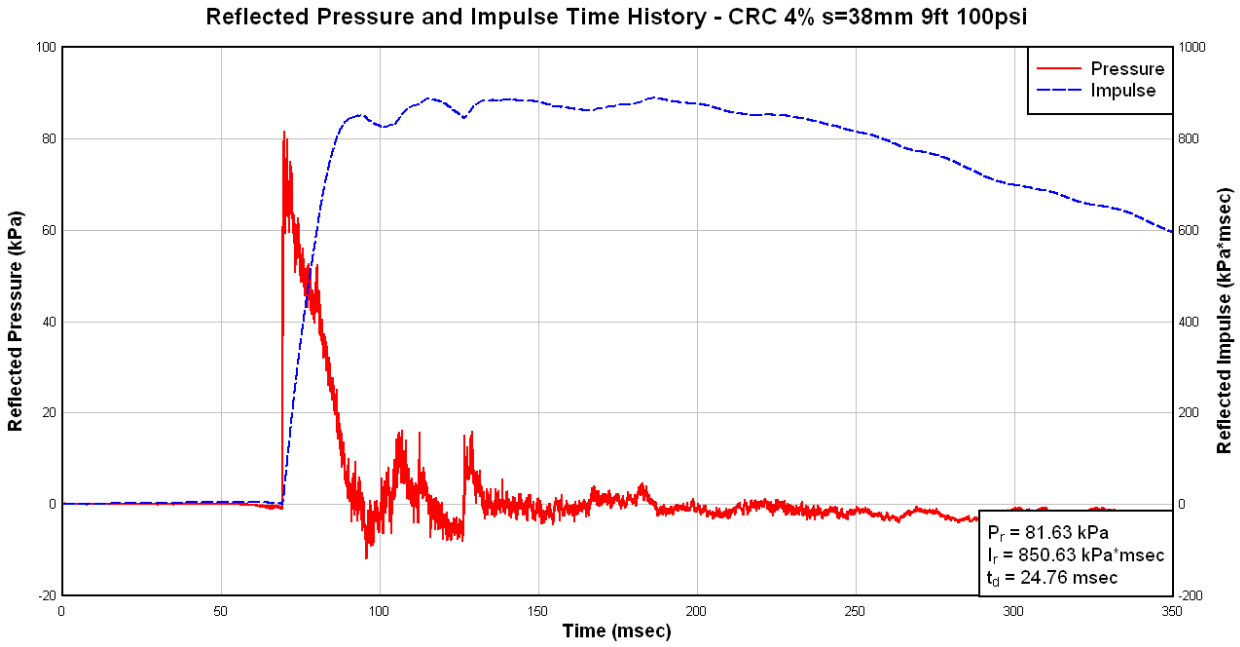

Figure 4.72 Column CRC-4%-38: recorded reflected pressure, impulse, and displacement for Blast 4

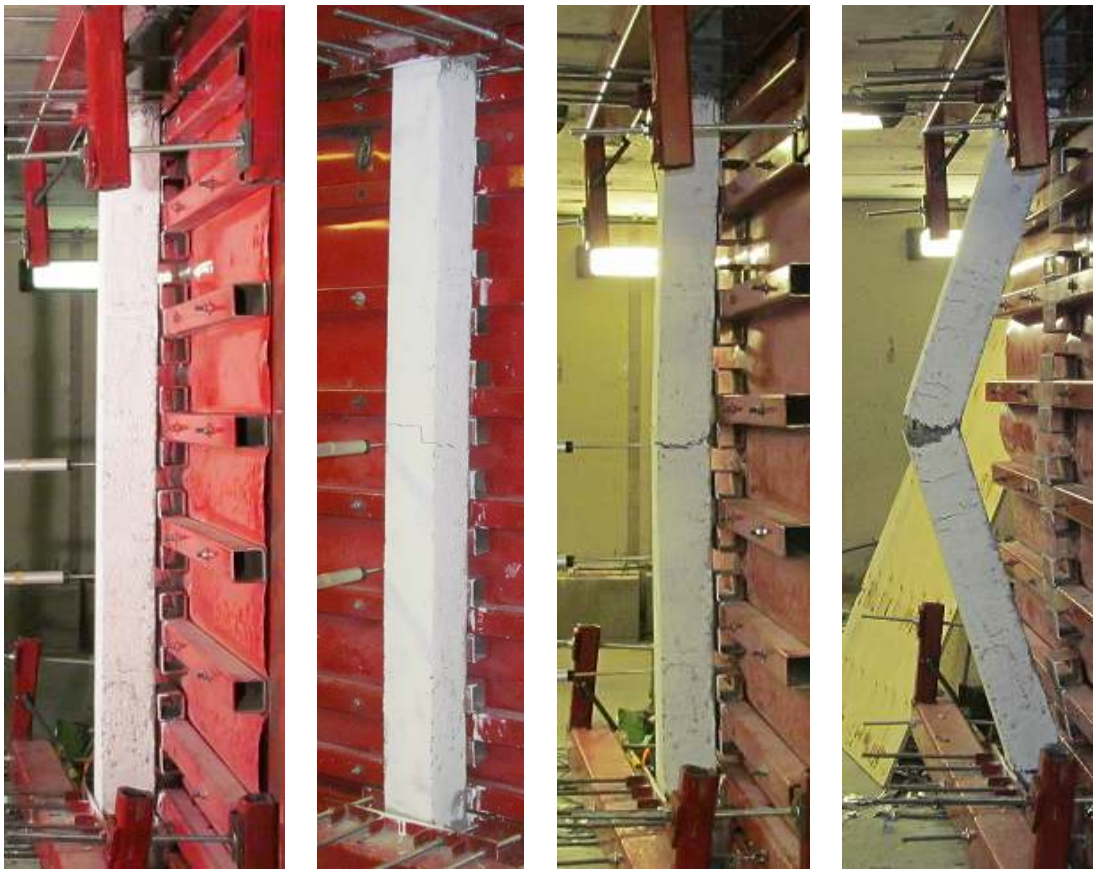

(a)Blast 1 (b)Blast 2 (c)Blast 3 (d)Blast 4

Figure 4.73 Column CRC-4%-38 at the end of Blasts 1-4

(a)Mid-Span Result of Blast 2 (b) Mid-Span Result of Blast 3 (b)Mid-Span Result of Blast 4

Figure 4.74 Mid-span damage for Column CRC-4%-38

5 Discussion

5.1 Section Overview

This section discusses and compares the results and observations of the thirteen columns tested in the experimental program. The effects of fibres, effects of concrete type, comparison of support rotation to expected degree of damage from the literature, the ability of SFRC to control secondary fragments, and the effects of seismic detailing are all considered.

5.2 Effect of Fibres on Maximum and Residual Displacements

The results indicate that all the columns behaved similarly under shock wave loading to Blast 1 and Blast 2. Blast 1 was selected to keep the longitudinal reinforcing steel in the columns within their elastic range, and based on the recorded strain gauge data, this was achieved. Correspondingly, Blast 2, the loading regime that was designed to take the column reinforcing steel beyond yield, and bring it within the plastic range was also achieved. However, no distinct trend formed for these shockwave loads. On the contrary, Blast 3 provided a trend that demonstrates the improved blast behaviour provided by steel fibre reinforcement.

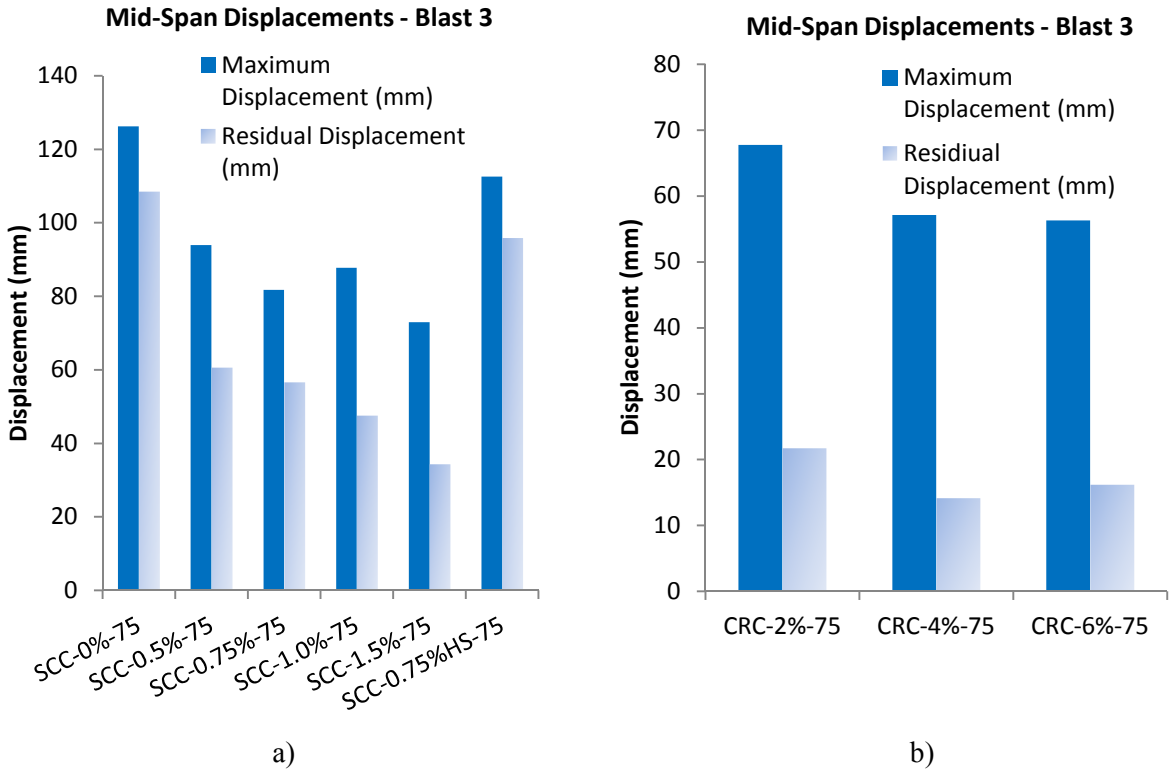

a) b)

Figure 5.1 Maximum and residual mid-span displacements recorded during Blast 3 for the non-seismic series of columns. In a) the SCC series, and b) the CRC series

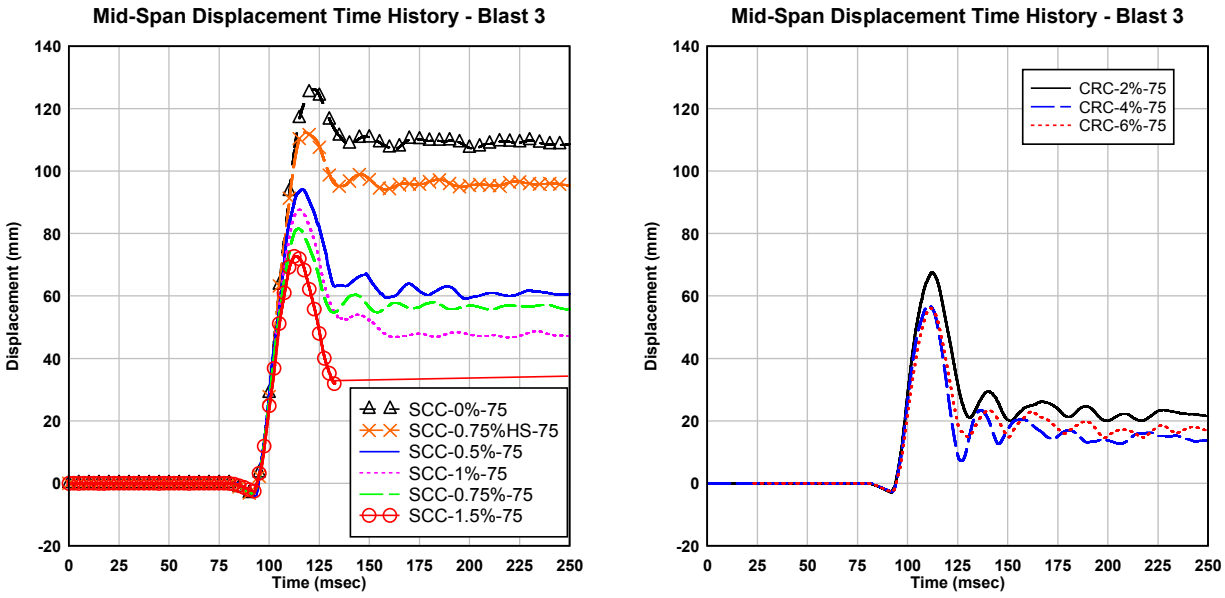

a) b)

Figure 5.2 Maximum and residual mid-span displacements recorded during Blast 3 for the non-seismic series of columns. In a) the SCC series, and b) the CRC series

Figure 5.1 a) and Figure 5.2 a) provide a comparison of the displacement responses of the control and SFRC columns after Blast 3 and demonstrates that the addition of steel fibres enhances the blast resistance of reinforced concrete columns and reduces the maximum and residual displacements under similar blast loading proportionally to the amount of steel fibres added to the mix. For instance, while the control specimen (SCC-0%-75) had maximum and residual displacements of 126.23 mm and 108.50 mm, respectively, it can be seen that the addition of only 0.5% steel fibres by volume in column SCC-0.5%-75 reduced maximum and residual displacements to 93.93 mm and 60.61 mm, respectively. The trend of reductions in maximum and residual displacements with increasing amounts of steel fibres was observed in the remaining columns; for example 0.5%, 0.75%, 1%, and 1.5% steel fibres by volume decreased the residual displacements by 44%, 48%, 56%, and 68% respectively.

While Figure 5.1 a) shows that column SCC-1%-75 had a greater maximum than what would be expected from the trend, this is because this column was subjected to an impulse of 767.32 kPa*msec, while columns SCC-0.75%-75 and SCC-1.5%-75 were subjected to impulses of 675.87 kPa*msec and 681.05 kPa*msec respectively. The increased fibre content in column

SCC-1%-75 reduced the residual displacements by 56% when compared to the control specimen, and the residual displacements follows the expected trend.

The CRC specimens, Figure 5.1 b) and Figure 5.2 b) also indicated a similar trend of decreasing maximum and residual displacements with increased fibre contents. Unfortunately only two CRC specimens verify this trend, as there were challenges with the placement of column CRC-6%-75, as discussed in Section 3.

5.3 Effects of SFRC on Failure Mode

The failure of columns without seismic detailing of tie reinforcement in the SFRC test series was compression reinforcing steel buckling after Blast 3. The degree of damage varied for each specimen in accordance with the fibre amounts: the greater the amount of fibre, the less extensive the damage. For example, while Figure 5.3 clearly shows crushing of compression concrete, buckling of compression reinforcing steel, and significant cover spalling for the SCC-0%-75 specimen, these same failure criteria were more controlled in the SCC-1.5%-75 specimen, and most of the concrete remained in place. Significantly closer observation was required to determine that the compression reinforcing steel had indeed buckled for the SCC-1.5%-75 specimen due to the significant reduction in maximum displacement. Observations indicate that structural members reinforced with steel fibres could resist greater blast pressures before failure.

a) b)

Figure 5.3 Comparison of the mid-span after Blast 3 of a) SCC-0%-75 and b) SCC-1.5%-75

5.4 Effects of CRC on Failure Mode

Contrary to the non-seismic SFRC specimens, all CRC specimens failed due to tension reinforcing steel rupture, irrespective of presence or absence of seismic detailing of tie reinforcement. This phenomenon is caused by the increased compressive strength of CRC. It is assumed that when a member is subjected to bending, the compressive forces along the cross section must be equal to the tensile forces. Since the compressive stress capacity was so high in CRC, all columns failed due to tension reinforcing steel rupture as opposed to concrete crushing and compression reinforcing steel buckling.

Bidiganavile et al. (2002) noted that CRC becomes brittle at greater stress rates with the failure mode being fibre pull-out in the tension region. This failure mode was also observed in this experimental program for the CRC columns, and this phenomenon likely the result of using smooth-straight fibres that provided no mechanical contribution to resist pull-out. Note that multiple blast pressures beyond yield were applied to each column and may have contributed to fibre pullout. If fibre debonding initiates during previously applied loads, the fibres may no longer be effective under subsequent blast loading. However, in the case of columns, ductility is provided by the longitudinal reinforcement so complete brittle failure is prevented. Since the failure mode for all CRC columns was initiated by rupture of tensile longitudinal reinforcement, the strength and ratio of this reinforcement is a factor that needs to be considered when designing CRC columns for blast resistance.

5.5 Effects of SFRC and CRC on Secondary Fragments

When compared to the two control specimens without fibres, the SFRC columns showed improved damage tolerance, enhanced control of cracking and spalling, and the ability to eliminate flying debris. As discussed in Section 4 and shown in Figure 5.4, the amount of secondary blast fragments is reduced with increasing amounts of steel fibres. Figure 5.4 shows that both SCC-0%-75 and SCC-0%-38 generate large amounts of fragments at failure of the column, while both fragment size and amount is reduced for the SCC-1.5%-75 specimen.

Although the reduction of fragmentation may not be critical in the case of columns, flying debris may pose a hazard in other types of reinforced concrete structural elements (e.g. slabs and walls).

The use of SFRC with its improved damage tolerance can be used to prevent the effect of flying debris in such elements and could thus reduce or eliminate injury to occupants in the event of an incident.

In the case of CRC columns the only noted secondary fragments are in the form of a fine powder. This trend suggests that the more fibres to retain concrete in place, the safer a structure, and also since no large aggregate is used in CRC, this reduces the probability of large fragments.

(a) SCC-0%-75

(b) SCC-1.5%-75

(c) SCC-0%-38

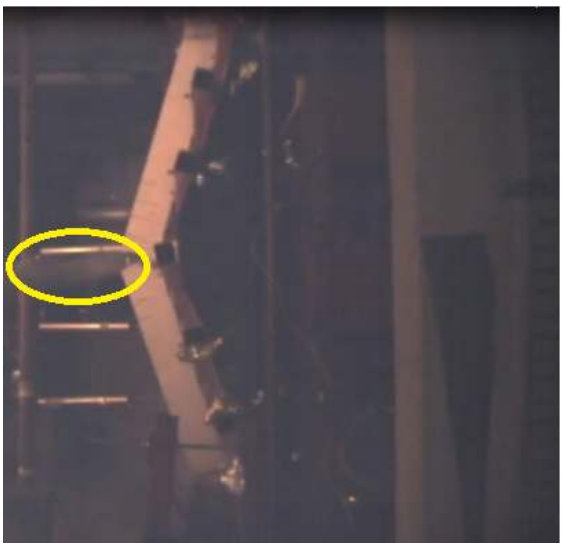

(d) CRC-2%-75

Figure 5.4 High speed video stills showing secondary blast fragments caused at the failure of each column.

5.6 Comparison of Experimental Support Rotations

As previously discussed in Section 2, the UFC-3-340-02 (2008) provides limits for reinforced concrete members in flexure, with descriptions of expected component damage, as shown in Table 5.1. Table 5.2 shows the calculated support rotations from maximum mid-span displacements for typical columns that were tested in this experimental program. The rotation in degrees at the supports is calculated from maximum mid-span displacement using trigonometric relationships. Comparing the expected component damage to the damage to the columns that was observed and described in Section 4, there is excellent correlation between the two. For example, the columns of this experimental program had less than 2° support rotation for Blast 2, and only moderate damage was observed with slight permanent deformations. However, Blast 3 for all non-seismically detailed SCC columns caused compression reinforcing steel buckling and their support rotations were greater than 5°, which Table 5.1 predicted component failure. In the case of tension reinforcing steel rupture, which was the mode of failure for all seismically detailed and CRC columns, the support rotations were calculated to be greater than 10°. This support rotation is predicted to be a complete blowout of the component, and this was observed as tension reinforcing steel rupture was a more catastrophic failure mode than compression reinforcing steel buckling. Consequently the results of this experimental program corroborates the predicted values from the literature, and also highlights that the reduced maximum displacements, caused by the use of steel fibres to increase concrete tensile strength and compressive ductility, improves the blast performance of reinforced concrete columns.

Table 5.1 Performance levels and associated deformation limits (UFC-3-340-02, 2008)

Component Level Damage	Description of Component Damage	Building Level of Protection	Limit for Reinforced Concrete Element in Flexure
Superficial Damage	Component has no visible permanent damage	High	$\mu \leq 1$
Moderate Damage	Component has some permanent deflection. It is generally repairable, if necessary, although replacement may be more economical and aesthetic	Medium	$\mu > 1$ $\theta \leq 2°$
Heavy Damage	Component has not failed, but it has significant permanent deflections causing it to be irreparable	Low	$2° < \theta \leq 5°$
Hazardous Failure	Component has failed, and debris velocities range from insignificant to very significant	Very low	$5° < \theta \leq 10°$
Blowout	Component is overwhelmed by the blast load causing debris with significant velocities	Below antiterrorism standards	$\theta > 10°$

Table 5.2 Maximum mid-span displacements and support rotations for select columns

		Maximum Mid-Span Displacement (mm)	Calculated Support Rotation (°)
SCC-0%-75	Blast 1	6.42	0.37
	Blast 2	29.86	1.73
	Blast 3	126.23	7.31
SCC-0%-38	Blast 1	6.62	0.38
	Blast 2	24.98	1.45
	Blast 3	91.99	5.32
	Blast 4	340.89	19.73
SCC-0.5%-75	Blast 1	5.04	0.29
	Blast 2	21.29	1.23
	Blast 3	93.93	5.44
SCC-1%-75	Blast 1	5.11	0.30
	Blast 2	23.32	1.35
	Blast 3	87.72	5.08
CRC-2%-75	Blast 1	5.15	0.30
	Blast 2	21.19	1.23
	Blast 3	67.76	3.92
	Blast 4	309.48	17.91

5.7 Effect of Seismic Detailing for Blast Resistance

Columns SCC-0%-38, SCC-0.5%-38, CRC-2%-38, and CRC-4%-38 were designed as seismically detailed columns, with transverse steel spaced equally along the length of the column at *38* mm, compared to their counterparts (SCC-0%-75, SCC-0.5%-75, CRC-2%-75, and CRC-4%-75) detailed with a transverse steel spacing of 75 mm. All other aspects of the two column sets were kept equal. These columns were tested under similar shock wave and axial loading regimens. A comparison between the displacements was used to draw conclusions towards the response of seismic and non-seismic detailed columns under blast loads.

5.7.1 Effect of Seismic Detailing in Reinforced Concrete Columns

The effect of seismic detailing is highlighted by comparing the response of columns SCC-0%-38 and SCC-0%-75 after Blast 3, as shown in Figure 5.5. When compared to the control specimen (SCC-0%-75), the maximum displacements for the seismically detailed column were decreased by a factor of approximately 27% (126 mm vs. 92 mm) due to the increased confinement, and ductility provided by the additional transverse reinforcement. In addition, the reduced tie spacing of SCC-0%-38 prevented reinforcing steel buckling for "Blast 3", which was the mode of failure for all non-seismic SFRC specimens. An additional blast load (Blast 4) was required to produce rupture of the tension reinforcing steel for the seismically detailed column.

The research conducted by Lloyd (2010) concluded that a column will transition into pure beam bending behaviour (no axial load) early in its response to the shock wave loading, and that it is likely that the loss of axial load negates most of the confinement benefits that may exist in columns designed for seismic regions. The research findings presented in this thesis show benefits provided by seismic detailing in traditional reinforced concrete columns, further research is required.

5.7.2 Effect of Seismic Detailing in SFRC Columns

A comparison of the results from specimens SCC-0.5%-75 and SCC-0.5%-38 allows for an investigation on the effect of seismic detailing in the SFRC columns. Although maximum and residual displacements for the two columns were not reduced at Blast 3, the provision of seismic detailing in specimen SCC-0.5%-38 prevented failure by compression reinforcing steel buckling, and allowed the column to be tested under an additional shockwave loading (Blast 4). The

findings from this research study are inconclusive about the benefits of combined use of SFRC and seismic detailing since the results of the seismically detailed columns with and without fibres are similar (SCC-0%-38 and SCC-0.5%-38). However, as noted previously in Section 3, there were some problems with placing the SFRC in specimen SCC-0.5%-38 due to confined space between the steel reinforcement, therefore further research is required.

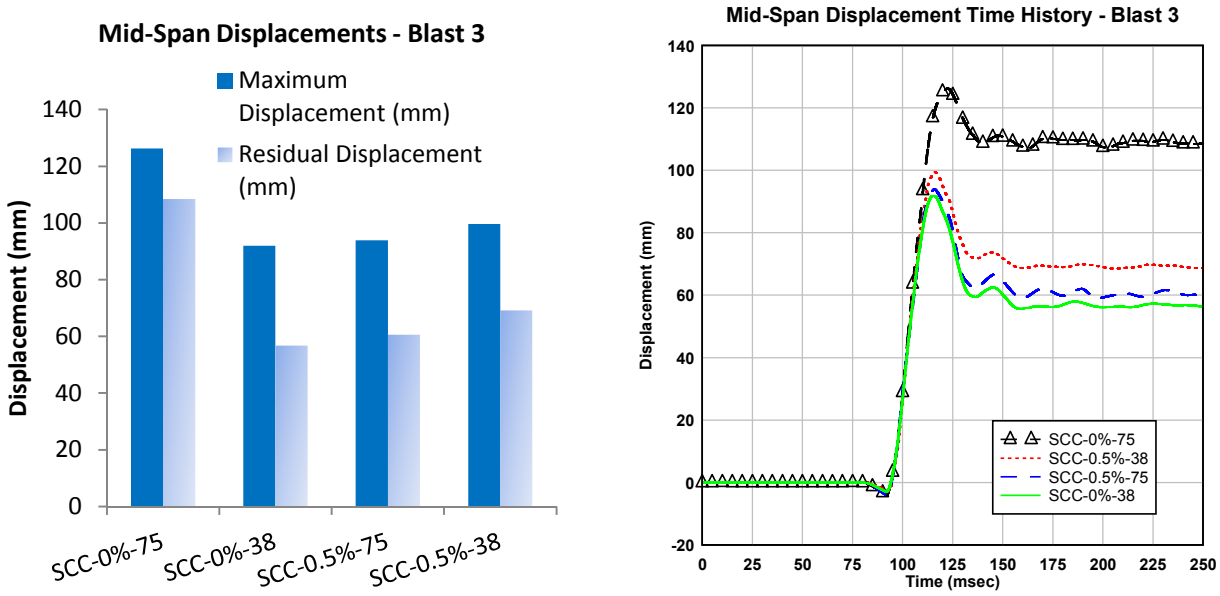

a) b)

Figure 5.5 a) Comparison of maximum and residual mid-span displacements for non-seismic and seismically detailed SCC series of columns and b) recorded mid-span displacement time histories for the columns.

5.7.3 Effect of Seismic Detailing in CRC Columns

Similarly for the CRC series of columns, the increased benefits of seismic detailing to blast loading is highlighted by comparing the response of columns CRC-2%-38 and CRC-2%-75 after Blast 3, as shown in Figure 5.6. Due to challenges with the mixing and placing of concrete for specimen CRC-4%-38, this column was not considered for direct comparison.

When compared, the maximum displacements for the seismically detailed column were decreased by a factor of approximately 30% (67.76 mm vs. 47.43 mm). Comparable to the SFRC columns, an additional blast load (Blast 4(2)) was required to produce rupture of the

tension reinforcing steel for the seismically detailed CRC-2%-38 column. Based on these four columns, it can be concluded that seismic detailing does improve the blast resistance of columns.

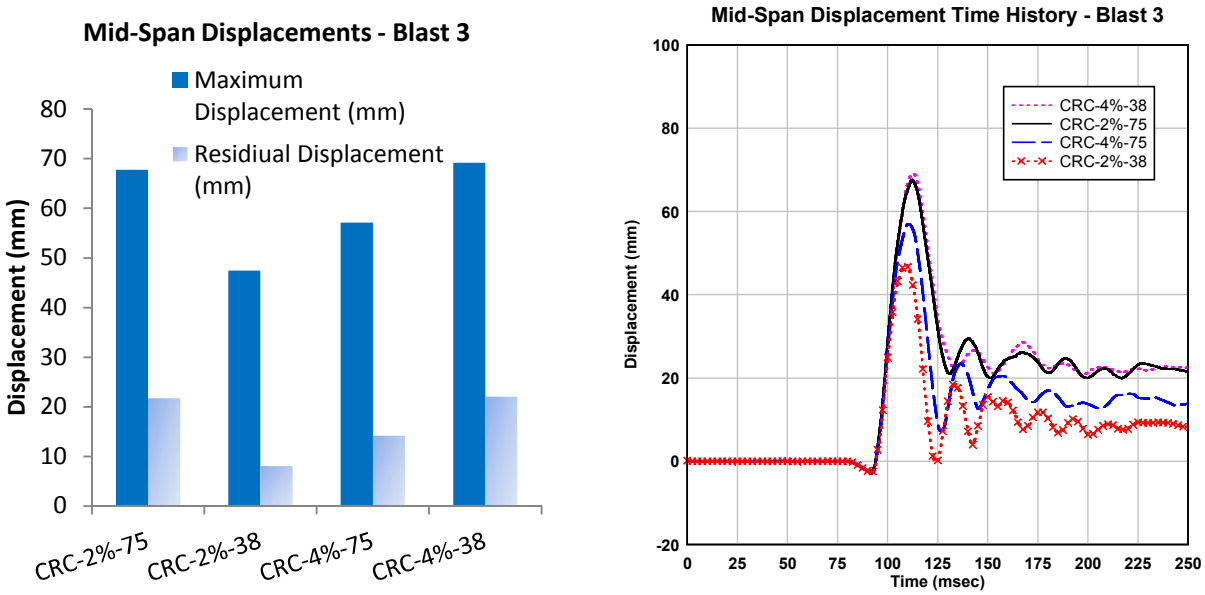

a) b)

Figure 5.6 Maximum and residual mid-Span displacements comparing non-seismic and seismically detailed CRC series of columns and b) complete mid-span displacement time histories for the columns.

5.7.4 Strain Data in Columns with Seismic Detailing

Strain data for the ties at ultimate loading is unavailable due to limitations of strain gauges at extreme blast pressures. Nonetheless, a review of the available strain gauge data for Blast 2 gives an indication of the improved level of stiffness that confinement provides through the seismically detailed columns. Figure 5.7 and Figure 5.8 show the strains from the transverse ties at mid-span for Blast 2. It is noted that the transverse reinforcement attains its maximum strain at approximately the same time as the maximum displacement of the column. In the case of the SCC and CRC series of columns, the transverse tie strains are greater for the seismically detailed columns. The data shows that while the strains remained well within the elastic region, the maximum strains in the seismic column were greater by a factor of at least 2 for the columns with seismic detailing when compared to the non-seismic columns. Similarly for the CRC columns, the strains along the transverse hoop are greater for the seismic columns, however not to the same extent as observed in the SCC columns. However, with the limited data available in this study, more research would be required to produce conclusive results.

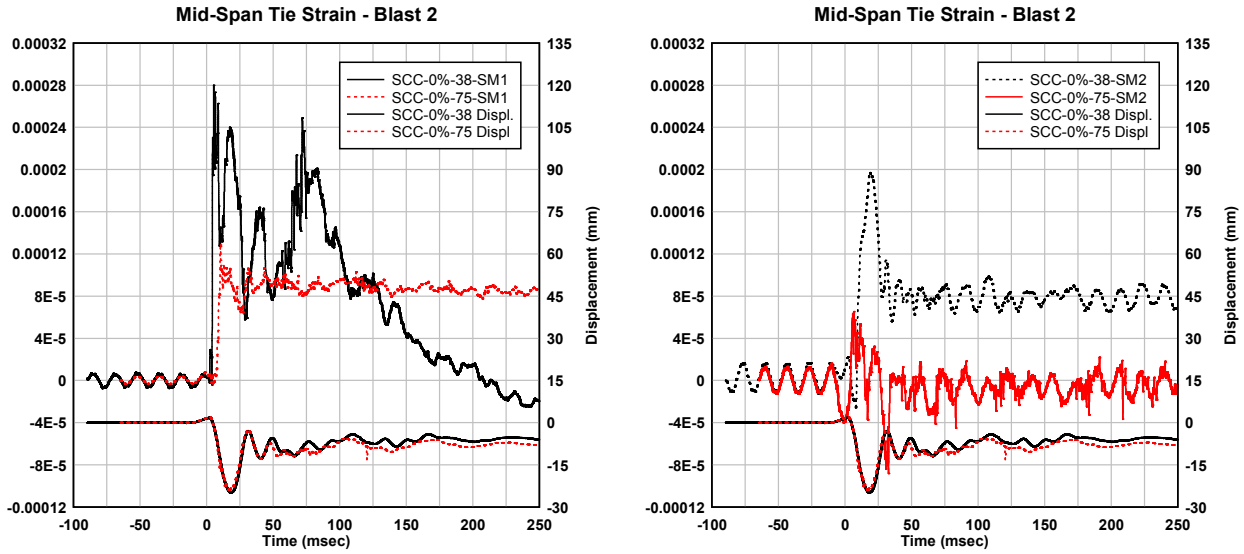

a) b)

Figure 5.7 Recorded Blast 2 mid-span transverse tie strain gauge and horizontal displacement data for SCC-0%-75 and SCC-0%-38: a) for the tie section running parallel to the shock wave; and b) for the section running perpendicular to the wave on the compression side.

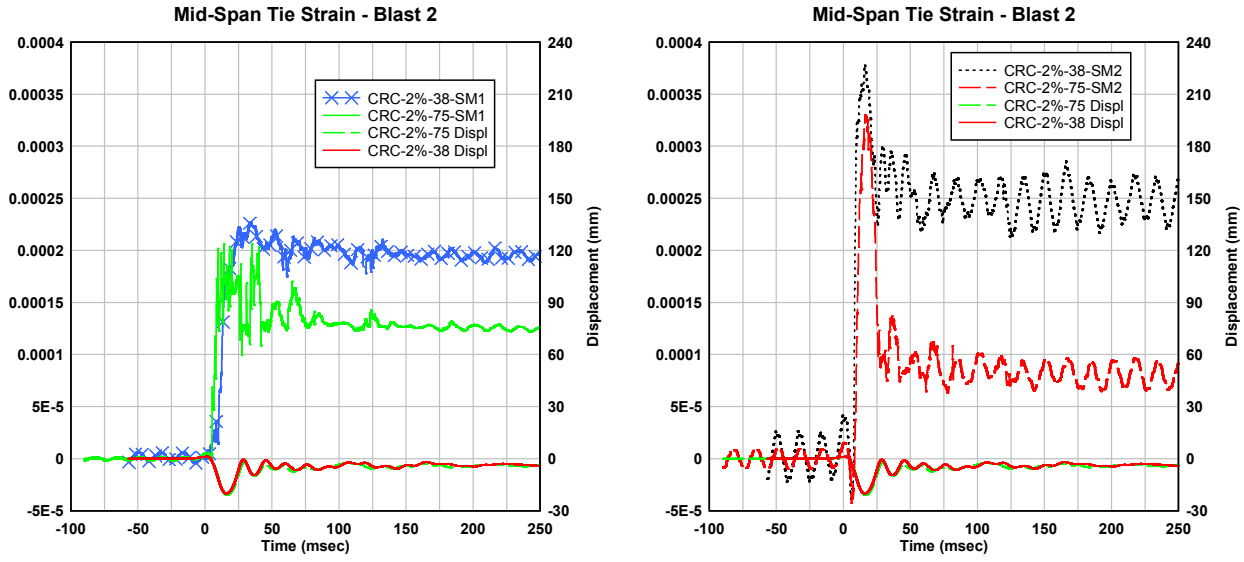

a) b)

Figure 5.8 Recorded Blast 2 mid-span transverse tie strain gauge and horizontal displacement data for CRC-2%-75 and CRC-2%-38: a) for the tie section running parallel to the shock wave; and b) data for the section running perpendicular to the wave on the compression side.

5.8 Comparison of SFRC Vs. Seismically Detailed Columns

Comparison of the data gathered during Blast 3 allows for the analysis of the fibre reinforced SCC specimens versus the seismically detailed control specimen (SCC-0%-38). The results, shown in Figure 5.9, demonstrate that the addition of steel fibres improves the performance of the columns such that the mid-span displacements are comparable to that of a heavily-congested seismically detailed column. The addition of only 0.5% steel fibres by volume in a non-seismically detailed column reduced the residual displacement to within 4 mm of that of a seismically detailed column. Also In terms of residual displacements, columns SCC-1%-75 and SCC-1.5%-75 reduced the recorded displacements by a factor of 16% and 40% respectively.

While, columns SCC-0.5%-75 and SCC-0.75%-75 were comparable, and SCC-1%-75 and SCC-1.5%-75 demonstrated improved performance when compared the seismically detailed control column (SCC-0%-38) in terms of maximum and residual displacements, the SFRC columns were not able to prevent compression reinforcing steel buckling. All non-seismic SFRC columns failed due to compression reinforcing steel buckling, but the seismically detailed columns (SCC and SFRC) prevented compression reinforcing steel buckling, and required greater blast loads in order to cause failure of the column.

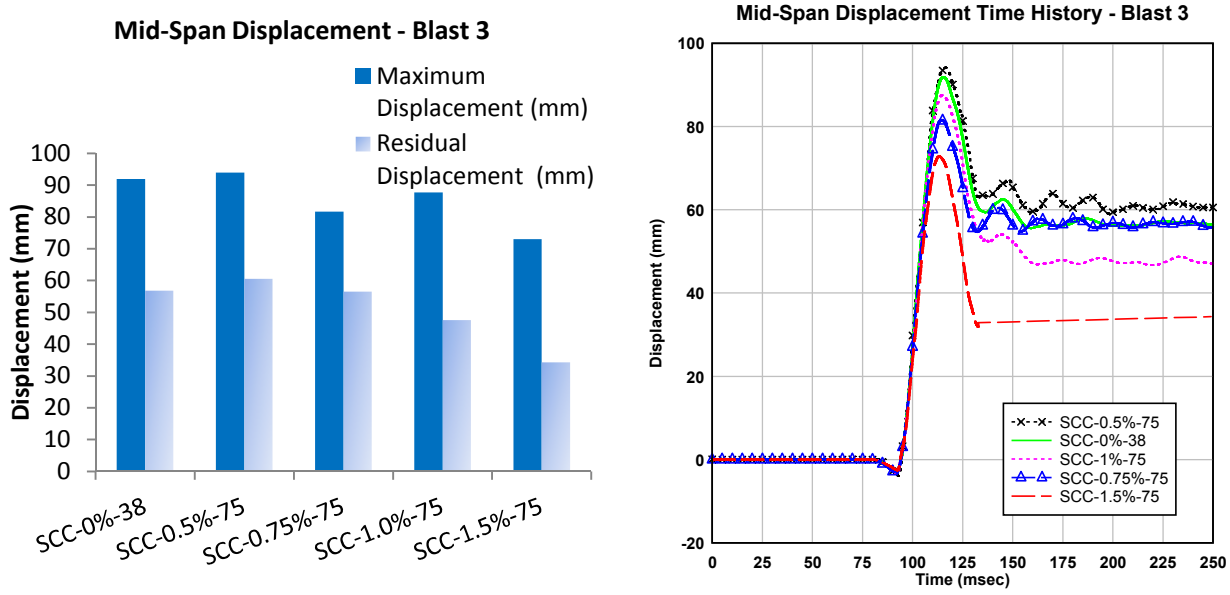

a) b)

Figure 5.9 a) Maximum and residual mid-span displacements comparing non-seismic SFRC and seismically detailed SCC columns and b) recorded mid-span displacement time histories for the columns.

Drawing from the previous section as well, the results from this experimental program suggest that a combination of steel fibres and seismic detailing may be an ideal option in order to maximize the blast resistance of reinforced concrete columns. While the results from columns SCC-0.5%-38 and CRC-4%-38 do not corroborate this finding, the results can be explained by the concrete placement issues for the specific column design used in this study, as discussed in Section 3. However, further research is required to validate this conclusion.

5.9 Effect of CRC

Figure 5.10 shows a comparison between the CRC series of columns and the control column (SCC-0%-75) for Blast 3. The results show that the use of CRC significantly improves the blast resistance of columns when compared to a control reinforced concrete column. This conclusion is not extraordinary as CRC is known to have drastically greater compressive and tensile strengths, as well as increased ductility due to very high steel fibre contents. In addition to this, CRC even has a greater density than typical SCC, and so for similar volumes of material it will have a greater mass, which inherently requires a greater blast load to cause displacements. In terms of maximum displacements, CRC-2%-75 and CRC-4%-75 improved the blast performance of columns when compared to SCC-0%-75 by factors of 46% and 55% respectively. In terms of residual displacements, these columns improved the blast resistance by factors of 80% and 87% respectively. These figures demonstrate the increased performance of CRC exhibited during impulsive loads when compared to typical concrete.

Another interesting aspect of CRC is shown in Figure 5.11. This figure shows that for columns with similar maximum displacements at Blast 2, the CRC columns had reduced residual displacements. For example, CRC-2%-75 and CRC-4%-75 each had maximum displacements of 21.19 mm and 21.59 mm respectively, while SCC-0.5%-75 had a maximum displacement of 21.29 mm. When comparing the residual displacements of these columns it is noted that for CRC-2%-75 and CRC-4%-75, the residual displacements are 3.95 mm and 3.98 mm respectively, while for column SCC-0.5%-75 the residual displacement is 4.79 mm. This phenomenon is an example of the increased elasticity of CRC to shock wave loading.

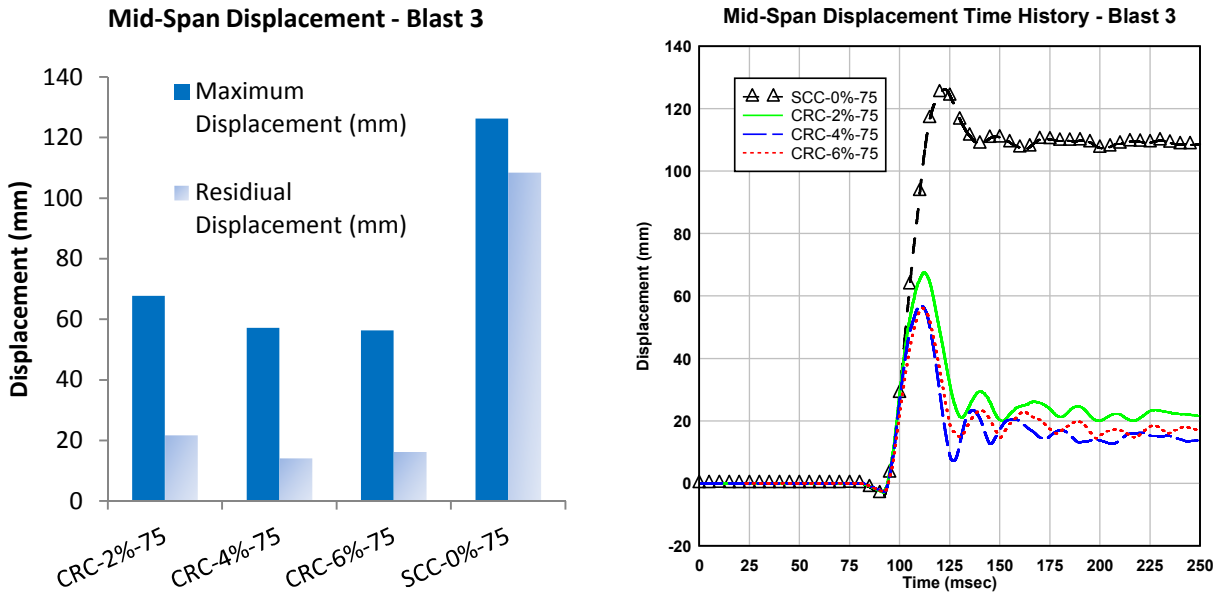

Figure 5.10 a) Maximum and residual displacements comparing the CRC non-seismic series of columns to the control column (SCC-0%-75), and b) complete mid-span displacement time histories for the columns.

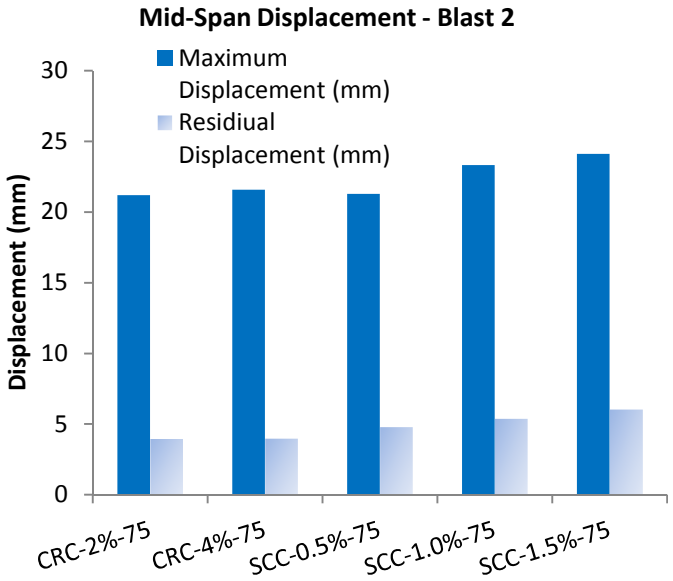

Figure 5.11 Comparison of SCC and CRC columns under similar maximum displacements

6 Theoretical Analytical Modelling of Column Response

6.1 General

This section presents the inelastic dynamic analysis of the columns tested in this experimental program. After defining constitutive material models for concrete, steel, SFRC and CRC under dynamic loading, force-displacement resistance functions are generated and the dynamic response of the columns is predicted using single degree of freedom dynamic analysis software, "RCBlast" written by Eric Jacques at the University of Ottawa. The experimental data was used to verify these analytical methods used to predict maximum displacements and time to maximum displacements for columns subjected to blast loads. The analysis shows a good ability to predict the response of SFRC and UHPFRC columns subjected to lateral blast loads.

6.2 Sectional Analysis

6.2.1 Constitutive Models used in Section Analysis

This section presents constitutive models used in the sectional analysis of the columns tested in the experimental program. For RC columns, models for unconfined and confined concrete in compression, and steel in tension and compression are summarized. In addition for the fibre reinforced concrete columns, SFRC and CRC models in compression and tension are presented.

6.2.1.1 Models Used for RC Columns

6.2.1.1.1 Unconfined Concrete Model (Hognestad, 1951)

The stress-strain behaviour of unconfined concrete in compression can be modelled using the well-known expressions developed by Hognestad (1951). For columns, the relationship can be used to model cover concrete or core concrete when confinement effects are not significant. The ascending branch of the stress-strain curve can be modelled using the expression below:

$$f_{cu} = f'_{cu} * \left(\frac{2\varepsilon_{cu}}{\varepsilon'_{cu}} - \left(\frac{\varepsilon_{cu}}{\varepsilon'_{cu}} \right)^2 \right), \qquad \varepsilon_{cu} \leq \varepsilon'_{cu} \qquad [6.1]$$

where f_{cu} refers to the stress in the unconfined concrete at a strain equal to ε_{cu}. The values, f'_{cu} and ε'_{cu} refer to the in-place static compressive strength of unconfined concrete and strain at peak compressive strain, respectively. The descending branch (for the region $\varepsilon_{cu} > \varepsilon'_{cu}$) is defined by a straight line connecting the peak stress to $0.85f'_{cu}$ at strain ε_{cu85}. A line with constant slope is then used to connect the descending branch to a maximum strain corresponding to $0.15f'_{cu}$. To account for spalling, for strains exceeding maximum the unconfined concrete stress is assumed zero.

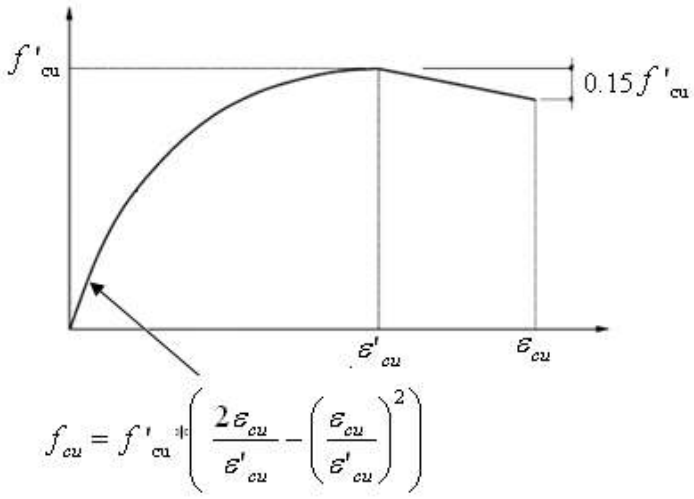

Figure 6.1 Representation of Hognestad model for unconfined concrete

6.2.1.2 Confined Concrete Model (Légeron and Paultre 2003)

Extensive research has demonstrated that confinement of concrete results in increased peak strength and an enhanced post-peak ductility. Confinement is affected by several parameters including: arrangement, spacing, yield stress and volumetric ratio of transverse reinforcement. Other parameters affecting confinement include axial load level and strength of unconfined concrete. For the purposes of this thesis, the model presented by Cusson and Paultre (1995) and later modified by Légeron and Paultre (2003) is used for confined concrete in compression. The model has been shown to accurately predict the stress-strain behaviour of confined concrete in RC columns having a wide range of concrete strengths, transverse steel tie configurations and yield strengths. In the accordance with this model, the static confined compressive strength of concrete, f'_{cc} and corresponding strain, ε'_{cc} are computed using the following expressions:

$$f'_{cc} = f'_{cu}\left(1 + 2.4\left(I'_E\right)^{0.7}\right) \quad [6.2]$$

$$\varepsilon'_{cc} = \varepsilon'_{cu}\left(1 + 35\left(I'_E\right)^{1.2}\right) \quad [6.3]$$

$$I'_E = \frac{f'_{le}}{f'_{cu}} \quad [6.4]$$

$$f'_{le} = K_e * f'_l \quad [6.5]$$

where I'_E is the effective confinement index, f'_{le} is the effective confinement pressure that acts on the core. The effective confinement pressure is a function of the nominal lateral pressure provided by the transverse reinforcement, f'_l and the effective confinement coefficient, K_e as defined in Equation 6.6 and Equation 6.7 and originally proposed by Sheikh and Uzumeri (1982). For columns having rectangular cross-section these parameters can be computed using:

$$f'_l = \frac{f_{hcc}}{s}\left(\frac{A_{shy} + A_{shx}}{c_y + c_x}\right) \quad [6.6]$$

$$K_e = \frac{\left(1 - \frac{\sum w_i^2}{6c_x c_y}\right)\left(1 - \frac{s'}{2c_x}\right)\left(1 - \frac{s'}{2c_y}\right)}{\left(1 - \rho_c\right)} \quad [6.7]$$

In which, A_{shy} and A_{shx} refer to the total cross-sectional area of transverse reinforcement perpendicular in the x/y directions, and f_{hcc} refers the stress in the transverse steel reinforcement at maximum strength of confined concrete. The quantities $s$and s' refer to the centre-to-centre and clear spacing of the transverse ties, while c_y and c_x represent the widths of the concrete core parallel to the x and y axis respectively. The parameter $\sum w_i^2$ is the sum of the squares of

the clear spacings between adjacent longitudinal bars and ρ_c is the ratio of longitudinal reinforcement in the core region.

Légeron and Paultre (2003), suggest that the stress developed in the transverse reinforcement at peak confined concrete stress is related to the amount of confinement provided to the section. That is to say, the more a column is confined, the more it is able to effectively use the full yield stress of the transverse reinforcement, f_{hy} . To account for this effect the following equations are used to calculate the stress in the transverse steel reinforcement at peak concrete stress, f'_{hcc}:

$$f'_{hcc} = \begin{cases} f_{hy} \longleftarrow\!\!\!\!\!\!- \kappa \le 10 \\ \dfrac{0.25 f'_{cu}}{\rho_{sey}(\kappa - 10)} \ge 0.43 \varepsilon'_{cu} E_S \longleftarrow\!\!\!\!\!\!- \kappa > 10 \end{cases} \qquad [6.8]$$

$$\kappa = \frac{f'_{cu}}{\rho_{sey} E_S \varepsilon'_{co}} \qquad [6.9]$$

$$\rho_{sey} = \frac{K_e A_{shy}}{sc} \qquad [6.10]$$

In the above expressions, ρ_{sey} is the effective sectional ratio of confinement reinforcement in the y direction, κ is a parameter that is used in order to determine if yielding of the transverse reinforcement occurs at the maximum strength of confined concrete, E_S is the modulus of elasticity of the transverse reinforcement. The ascending branch of stress-strain relationship for confined concrete is defined as follows:

$$f_{cc} = \frac{(f'_{cc}) * \left(k \times \dfrac{\varepsilon_{cc}}{\varepsilon'_{cc}} \right)}{k - 1 + (\dfrac{\varepsilon_{cc}}{\varepsilon'_{cc}})^k}, \quad \varepsilon_{cc} \le \varepsilon'_{cc} \qquad [6.11]$$

The above expression is based on the work of Popovics (1973), where f_{cc} refers to the stress in the confined concrete corresponding to a chosen strain equal to ε_{cc}. The values, f'_{cc} and ε'_{cc}, refer to the peak confined stress and strain of the concrete. The constant *k*, is a parameter that controls the slope of the ascending branch of the curve and is computed using:

$$k = \frac{E_c}{E_c - (\frac{f'_{cc}}{\varepsilon'_{cc}})} \qquad [6.12]$$

The descending branch of the stress-strain curve for confined concrete is defined as follows (Légeron and Paultre, 2003):

$$f_{cc} = f'_{cc} \times \exp\left(k_1 \left(\varepsilon_{cc} - \varepsilon'_{cc}\right)^{k_2}\right), \ \varepsilon_{cc} > \varepsilon'_{cc} \qquad [6.13]$$

$$k_1 = \frac{\ln(0.5)}{\left(\varepsilon_{cc50} - \varepsilon'_{cc}\right)^{k_2}} \qquad [6.14]$$

$$k_2 = 1 + 25\left(I_{E50}\right)^2 \qquad [6.15]$$

where I_{E50} is the effective confinement index evaluated at the postpeak strain ε_{cc50} as defined in the expressions below (Légeron and Paultre, 2003):

$$\varepsilon'_{cc50} = \varepsilon'_{cu50}\left(1 + 60\left(I_{E50}\right)\right) \qquad [6.16]$$

$$I_{E50} = \rho_{sey} \frac{f_{hy}}{f'_{cu}} \qquad [6.17]$$

In the above expressions, the post-peak strain measured at 50% of maximum unconfined stress, ε'_{cu50} is taken as being equal to a strain of 0.004 (Cusson and Paultre, 1995).

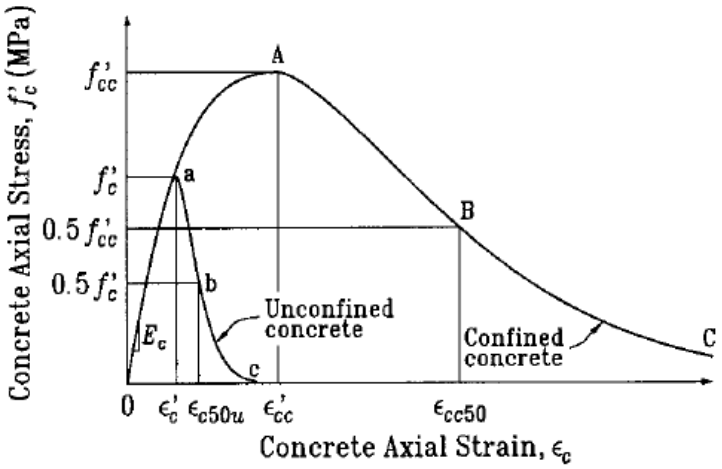

Figure 6.2 Representation of Cusson and Paultre (1995) for confined concrete

[Cusson and Paultre, 1995]

6.2.1.3 Reinforcing Steel Model in Tension

The stress-strain curves for steel in tension are typically modeled as bi-linear for the elastic and post-yield stages, and then a parabolic function to describe the strain hardening behaviour. A model of the stress-strain curve using the following equations is described in Jacques et al. (2012):

$$f_s = E_s \varepsilon_s \qquad \text{for } \varepsilon_s \leq \varepsilon_y \qquad [6.18]$$

$$\varepsilon_y = f_y / E_s \qquad [6.19]$$

$$f_s = f_y + (\varepsilon_s - \varepsilon_y)\left(\frac{f_{sh} - f_y}{\varepsilon_{sh} - \varepsilon_y}\right), \quad \text{for } \varepsilon_y < \varepsilon_s \leq \varepsilon_{sh} \qquad [6.20]$$

$$f_s = f_y + (f_u - f_y)\left[2\frac{\varepsilon_s - \varepsilon_{sh}}{\varepsilon_u - \varepsilon_{sh}} - \left(\frac{\varepsilon_s - \varepsilon_{sh}}{\varepsilon_u - \varepsilon_{sh}}\right)^2\right] \qquad [6.21]$$

where f_s is the steel stress at strain ε_s, E_s is the steel modulus of elasticity, f_y is the steel yield stress at steel yield strain ε_y, f_{sh} is the steel strain-hardening stress at strain ε_{sh}, and f_u is the ultimate steel stress at strain ε_u. However, for the analysis of all columns an average curve of the actual steel reinforcing steel coupon tests was used, and is shown in Figure 6.3.

6.2.1.4 Reinforcing Steel Model in Compression

Jacques et al. (2012) summarizes a model proposed by Yalcin and Saatcioglu to describe the behaviour of longitudinal reinforcing steel to compression, and more importantly the factors that cause compression reinforcing steel buckling. The method describes bar aspect ratio as the ratio between the unsupported reinforcing steel length and reinforcing steel diameter. When the bar aspect ratio is greater than 8.0, stability of the bar is lost upon reaching yield. However, when the bar aspect ratio is equal to 8.0, reinforcement is able to maintain some strength after yield, and when the bar aspect ratio is less than 8.0 the stress-strain behaviour of the reinforcing steel shows limited strain-hardening behaviour, which was the case for all columns in this experimental program. The stress-strain behaviour is consequently described using the following equations:

$$f_s = f_y + \left(f_{s/Du} - f_{sh}\right)\left[2\frac{\varepsilon_s - \varepsilon_{sh}}{\varepsilon_{s/Du} - \varepsilon_{sh}} - \left(\frac{\varepsilon_s - \varepsilon_{sh}}{\varepsilon_{s/Du} - \varepsilon_{sh}}\right)^2\right] \quad \text{for } \varepsilon_s > \varepsilon_s \qquad [6.22]$$

$$f_{s/Du} = f_{sh} + (f_u - f_{sh})\left[48e^{-0.9(s/d_b)}\right] \qquad [6.23]$$

$$\varepsilon_{s/Du} = \varepsilon_{sh} + (\varepsilon_u - \varepsilon_{sh})\left[6e^{-0.4(s/d_b)}\right] \qquad [6.24]$$

where $f_{s/Du}$ and $\varepsilon_{s/Du}$ are the limiting values on stress and strain respectively.

6.2.1.5 High Strain Rate Effects for Concrete and Steel

As discussed in Section 2.3.7, typical concrete and steel exhibit an increase in strength when subjected to greater strain rates, and dynamic increase factors used for design have long been established (UFC-3-340-02, 2008). In the case of concrete, the strain at peak stress remains the same regardless of strain rate, and the dynamic increase factor (selected from Table 2.4) of 1.19 is applied equally across the entire concrete compression stress-strain relationship.

However, different dynamic increase factors are used for steel along the stress-strain relationship. For steel members subjected to bending, Table 2.4 uses a DIF of 1.17 for the sections of the stress-strain curve prior to ultimate, and 1.05 for sections greater than ultimate.

However, unlike concrete the modulus of elasticity remain unchanged, and consequently there is a greater yield strain in the dynamic stress-strain curve of steel.

6.2.1.6 Summary of Constitutive Models for RC Columns

The figure below summarizes the stress-strain curves with and without dynamic effects for the reinforced concrete columns tested in this experimental program.

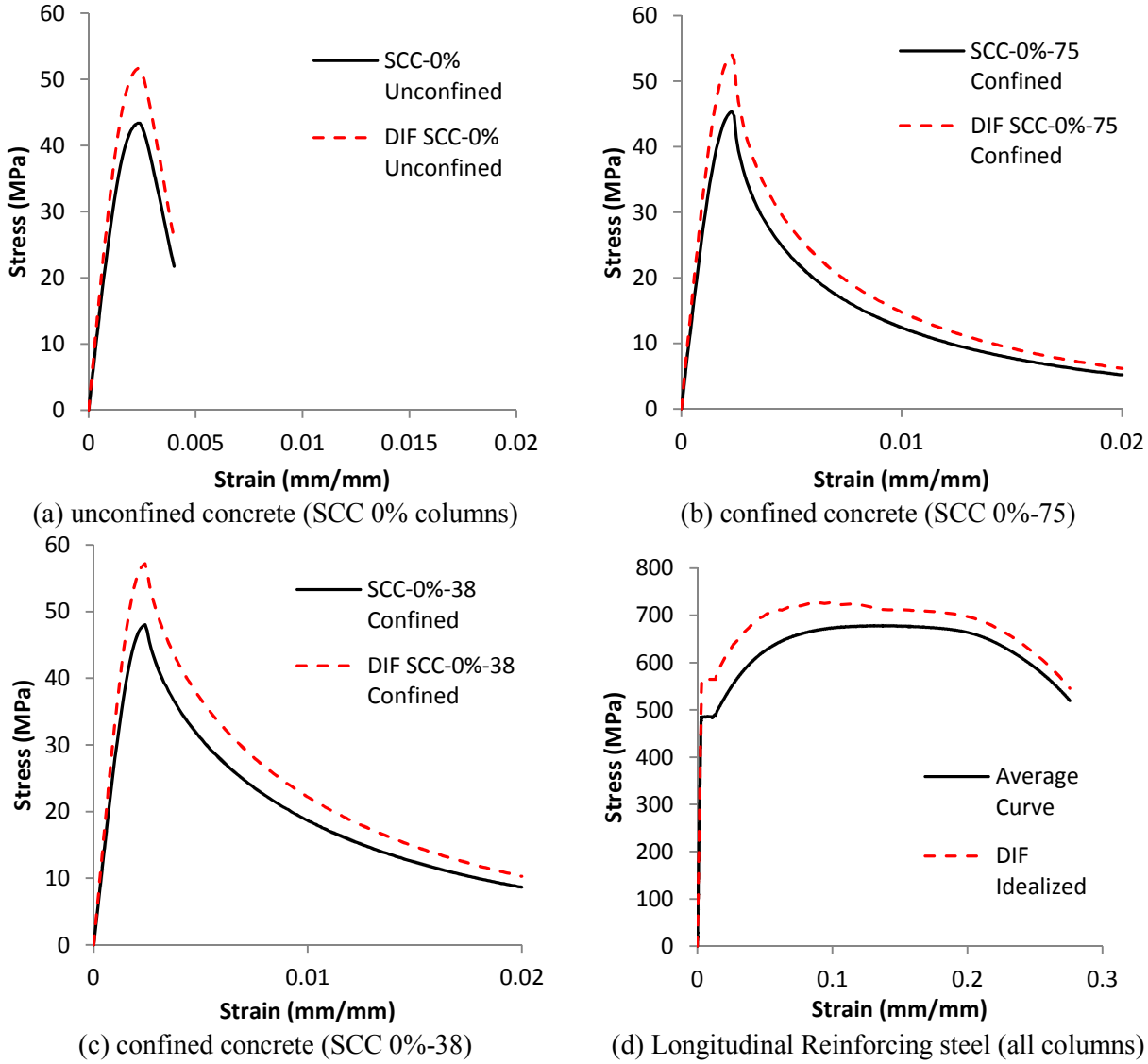

(a) unconfined concrete (SCC 0% columns)

(b) confined concrete (SCC 0%-75)

(c) confined concrete (SCC 0%-38)

(d) Longitudinal Reinforcing steel (all columns)

Figure 6.3 Material models used to generate resistance functions for reinforced concrete columns

6.2.1.7 Models Used for SFRC Columns

6.2.1.7.1 Unconfined SFRC Model (Aoude, 2007)

Over the years, several empirical models have been proposed for predicting the compressive stress-strain behaviour of SFRC. The model presented in this section is based on a model originally developed by Mansur et al. (1999) for high-strength SFRC and modified by Aoude (2007) for regular-strength SFRC. The ascending branch of the stress-strain curve of SFRC is defined by the relationship in Equation. 6.25, where $f_{cu,f}$ refers to the stress in the unconfined SFRC corresponding to a chosen strain equal to ε_{cuf}. The constant *k*, is a parameter that controls the slope of the ascending branch of the curve.

$$f_{cuf} = \frac{(f'_{\text{cuf}}) * \left(k \times \frac{\varepsilon_{cuf}}{\varepsilon'_{cuf}} \right)}{k - 1 + (\frac{\varepsilon_{cu,f}}{\varepsilon'_{cuf}})^{\text{k}}}, \qquad \varepsilon_{cu,f} \le \varepsilon'_{cuf} \qquad [6.25]$$

$$k = \frac{E_{\text{c}}}{E_{\text{c}} - (\frac{f'_{cuf}}{\varepsilon'_{cuf}})} \qquad [6.26]$$

The values, f'_{cuf} and ε'_{cuf}, refer to the peak unconfined stress and strain of SFRC. As was discussed previously many researchers have observed that SFRC does not significantly affect the ascending branch of the stress-strain behaviour of concrete in compression (i.e. no significant change in peak stress, peak strain or modulus of elasticity). The peak stress f'_{cuf} can be taken equal to f_{cu} or the 28-day compressive strength of SFRC when data is available. The peak unconfined strain ε'_{cuf} can be computed as:

$$\varepsilon'_{cuf} = 0.001684 + 0.000016 * f'_{cuf} \qquad [6.27]$$

In order to model the influence of the fibres in the descending portion of the stress-strain curve, an equation proposed by Mansur et al. (1999) for high-strength SFRC and later modified by Aoude (2007) for normal-strength SFRC can be used:

$$f_{cuf} = f'_{cuf}\left[\frac{k_{f1}\beta_1\left(\frac{\varepsilon_{cuf}}{\varepsilon'_{cu}}\right)}{k_{f1}\beta_1 - 1 + \left(\frac{\varepsilon_{cuf}}{\varepsilon'_{cu}}\right)^{k_{f2}\beta_1}}\right] \quad \varepsilon_{cuf} \geq \varepsilon'_{cu} \qquad [6.28]$$

The factors k_{f1} and k_{f2} are calculated using Equation 6.29 and 6.30 and are originally based on the work of Mansur et al. (1999). The constants were derived for normal-strength concrete by Aoude (2007) based on the results from his experimental program and are presented in Table 6.1.

$$k_{f1} = \left(\frac{C_a}{f'_{cuf}}\right)^{e_a} \times \left(1 + X_a \times \left[\frac{v_f L_f}{d_f}\right]\right)^{e_{2a}} \qquad [6.29]$$

$$k_{f2} = \left(\frac{C_a}{f'_{cuf}}\right)^{e_b} \times \left(1 + X_b \times \left[\frac{v_f L_f}{d_f}\right]\right)^{e_{2b}} \qquad [6.30]$$

Table 6.1 Constants to be used in Equations 6.29 and 6.30

Constants	For $\varepsilon_{cf} \leq 0.004$	For $\varepsilon_{cf} > 0.004$
C_a	30.2	4.62
e_a	0.49	0.47
X_a	-0.22	-7.8×10^{-5}
e_{2a}	24.9	-6.4
e_b	0.52	0.51
X_a	0.11	0.83
e_{2b}	-1.09	-0.34

6.2.1.7.2 Confined SFRC Model (Aoude, 2007)

This section presents a model for the stress-strain behaviour of confined SFRC. The model modifies the Légeron and Paultre (2003) confinement model for traditional reinforced concrete. As mentioned in the literature review, research on SFRC columns has shown that the use of SFRC in columns results in two major enhancements: an increase in peak confined concrete strength and an improvement post-peak ductility. The present model accounts for both effects.

It has long been known that the presence of lateral confinement provided by transverse steel in concrete increases the maximum compressive strength. Early research by Richart et al. (1928) demonstrated that the strength of concrete is enhanced if the concrete section is confined by an active hydrostatic pressure or passive confinement pressure (in the form of spirals). In the case of SFRC, the increase in peak stress due to the contribution of the fibres can be related to the number of fibres per unit area N_{fibres}, and the pullout resistance of the fibres. Using this same approach, Foster (2001) suggested that the confining pressure that is provided by the steel fibres, $f_{l,fib}$ can be approximated:

$$f_{l,fib} = \alpha \times \left(\frac{V_f l_f}{d} \right) \times \left[0.6 \times \left(f'_{cu} \right)^{2/3} \right] \qquad [6.31]$$

The length, l_f, that is used in the equation is taken as the length of the fibre without the hooks in the case of hooked-end steel fibres, and assumes a constant bond shear strength along the length of the fibre. Foster (2001) suggested using a value of 3/8 for the orientation factor, α. Recalling the equation proposed by Richart (1929), a similar approach is used by Aoude (2007) to approximate the expected increase in the peak concrete stress, Δf_{cf} due to the addition of steel fibres:

$$\Delta f_{cf} = 4.1 \times \left(f_{l,fib} \right) \qquad [6.32]$$

The peak confined strength of SFRC, f'_{ccf} is then taken as the sum of the confined strength of plain reinforced concrete, f'_{cc} as defined by Paultre and Légeron (2003) and the fibre contribution, Δf_{cf}:

$$f'_{ccf} = f'_{cc} + \Delta f_{cf} \qquad [6.33]$$

The influence of steel fibres on the confined concrete strain can be neglected, thus ε'_{ccf} can be taken as equal to the peak confined strain of plain reinforced concrete, ε'_{cc} as proposed by Légeron and Paultre (2003).

$$\varepsilon'_{ccf} = \varepsilon'_{cc} = \varepsilon'_{cu}\left(1 + 35\left(\frac{f'_{le}}{f'_{cu}}\right)^{1.2}\right) \qquad [6.34]$$

The ascending branch of the stress-strain curve of confined SFRC can be modelled using the same expressions used in Légeron and Paultre (2003) model but using the corresponding values of f'_{ccf} and ε'_{ccf} in lieu of f'_{cc} and ε'_{cc}:

$$f_{ccf} = \frac{(f'_{ccf}) * \left(k \times \frac{\varepsilon_{ccf}}{\varepsilon'_{ccf}}\right)}{k - 1 + (\frac{\varepsilon_{ccf}}{\varepsilon'_{ccf}})^{k}}, \qquad \varepsilon_{ccf} \le \varepsilon'_{ccf} \qquad [6.35]$$

$$k = \frac{E_c}{E_c - (\frac{f'_{ccf}}{\varepsilon'_{ccf}})} \qquad [6.36]$$

The descending branch of the stress-strain curve modifies the expression proposed by Légeron and Paultre (2003) based on the additional confinement that is provided by the fibres, $f_{l,fib}$. Research by Aoude (2007) on SFRC columns subjected to compressive axial loading has shown that the influence of the fibres in improving post-peak behaviour is directly related to the level of confinement provided by transverse reinforcement, with the fibres playing a lesser role in improving post-peak ductility in the case of well-confined columns. Aoude (2007) explained that as the ratio of "effectively confined core area", to "ineffectively confined core area" increases, the contribution of the fibres to improving post-peak behaviour reduces. Based on this concept, the effective confinement index used in the Légeron and Paultre (2003) model is modified as:

$$I'_{E,fib} = I'_E + \left(\frac{f_{l,fib}}{f'_{cu}}\right)(1 - K_e) \qquad [6.37]$$

The descending branch of the confined SFRC curve uses the same expressions defined by Légeron and Paultre (2003) but with the corresponding values of $f'_{cc\,f}$, $\varepsilon'_{cc\,f}$, $I'_{E,fib}$ and $I_{E50,fib}$ in lieu of f'_{cc}, ε'_{cc}, I'_E and I_{E50}:

$$f_{ccf} = (f'_{cc\,f}) \times \exp\left(k_1 \left(\varepsilon_{ccf} - \varepsilon'_{c\,cf}\right)^{k_2}\right), \quad \varepsilon_{ccf} > \varepsilon'_{ccf} \qquad [6.38]$$

$$k_1 = \frac{\ln(0.5)}{\left(\varepsilon_{cc50,fib} - \varepsilon'_{c\,cf}\right)^{k_2}} \qquad [6.39]$$

$$k_2 = 0.58 + 16\left(I'_{E,fib}\right)^{1.4} \qquad [6.40]$$

$$\varepsilon'_{cc50,fib} = \varepsilon'_{cu50}\left[1 + 60\left(I'_{E50,fib}\right)\right] \qquad [6.41]$$

$$I_{E50,fib} = I_{E50} + \left(\frac{f_{l,fib}}{f'_{cu}}\right)(1 - K_e) \qquad [6.42]$$

6.2.1.7.3 SFRC Tension Model (DRAMIX Stress-Strain Model)

The tension portion of the SFRC stress-strain curve was modelled using the simplified model detailed by the *Dramix Design Guidelines* provided by *Bakaert*, the company that provided the steel fibres used in this experimental program (Nemegeer, 1998). The uniaxial stress strain curve is derived using forces and deflections determined from standard 4-point bending tests used to determine the post-cracking properties of SFRC (e.g. ASTM C1609 or similar). The simplified model shown in Figure 6.4 involves three portions: an ascending branch (if tension is considered positive), a sharp descending branch to 0.1% strain, and then a less pronounced descending portion to 1% strain.

The initial ascending portion is modeled based on the modulus of elasticity of concrete, as given in CSA A23.3 (2006), and consequently has a slope in accordance with:

$$3300\sqrt{f'_{cuf}} + 6900 \qquad [6.43]$$

where f'_{cuf} is the peak compressive strength of unconfined SFRC. It should be noted that the average density of SFRC was determined to be 2300kg/m^3.

The maximum tensile stress of SFRC, $f_{fctm,ax}$ is computed based on the measured compressive strength of concrete as follows:

$$f_{fctm,ax} = 0.3{f'_{cuf}}^{2/3} \qquad [6.44]$$

The stress corresponding to 0.1% and 1% strains respectively are then given by

$$0.37\, f_{fct,eq,300} \qquad [6.45]$$

$$0.37 f_{fct,eq,150} \qquad [6.46]$$

$$f_{fct,eq,300} = \frac{F_{m300} \times l}{bh^2} \quad [6.47]$$

$$f_{fct,eq,150} = \frac{F_{m150} \times l}{bh^2} \quad [6.48]$$

F_{m300} and F_{m150} are derived from standard 4-point bending tests on SFRC flexural beams (and represent the forces at deflections of l/300 and l/150). The parameters l, b and h represent the length, width and height of the beam used in the bending test, in mm.

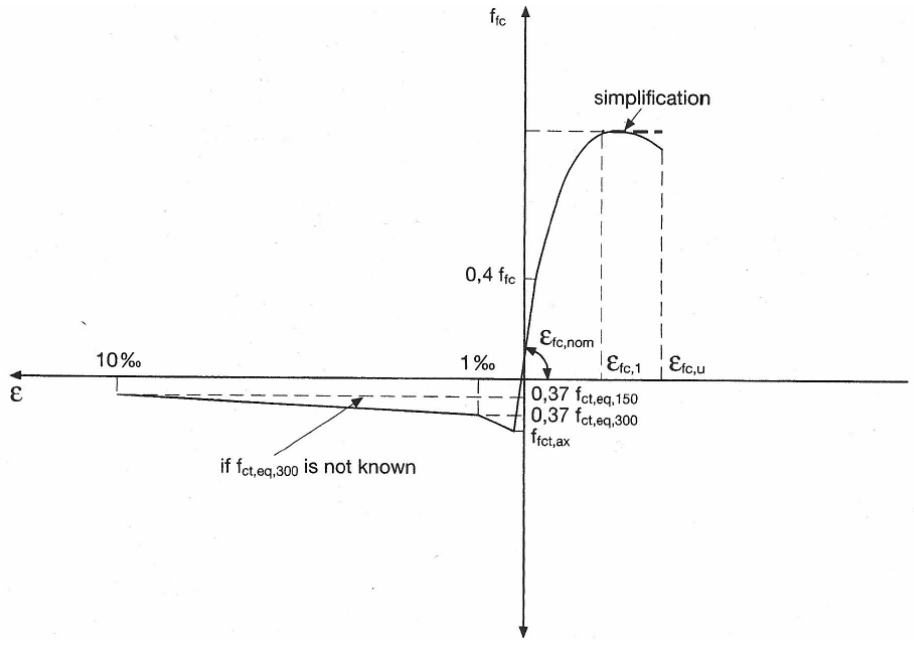

Figure 6.4 Idealized stress-strain curve for concrete reinforced with hooked-end steel fibres

(Nemegeer 1998)

6.2.1.7.4 High Strain Effects for SFRC

As discussed in the literature review, DIFs for regular strength concrete are well established, however, the development of DIFs for SFRC have not. Consequently in order to account for strength enhancement of SFRC caused by high strain rates, the long-accepted value from UFC-3-340-02 (2008) for concrete members in bending of 1.19 was applied. The dynamic stress-strain curve of the SCC columns was determined by applying the DIF to the Aoude (2007) models for confined and un-confined SFRC, as well as the tension model described in the previous section.

6.2.1.8 Summary of Constitutive Models for SFRC Columns

The figure below summarizes the concrete stress-strain curves with and without dynamic effects for the reinforced concrete columns tested in this experimental program.

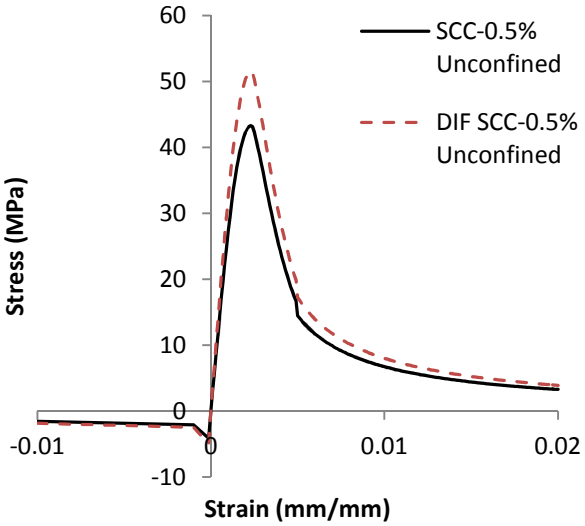

(a) unconfined concrete (SCC-0.5%-75)

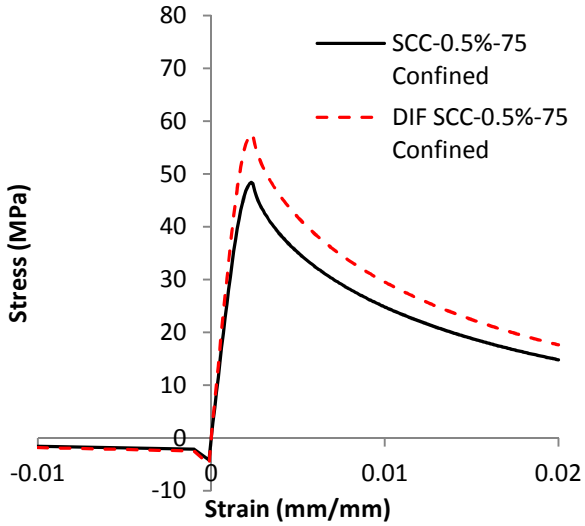

(b) confined concrete (SCC-0.5%-75)

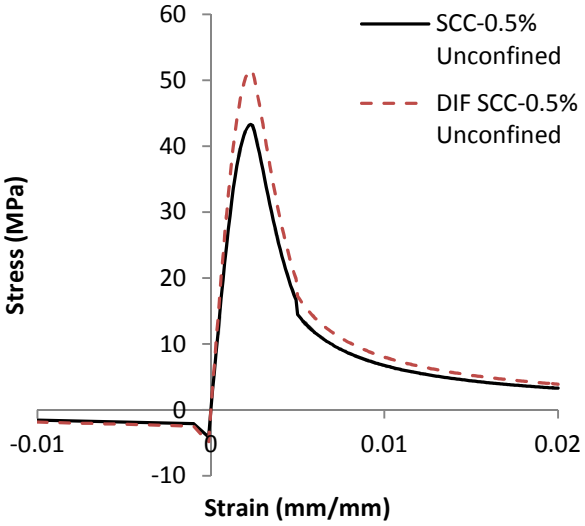

(c) unconfined concrete (SCC-0.5%-38)

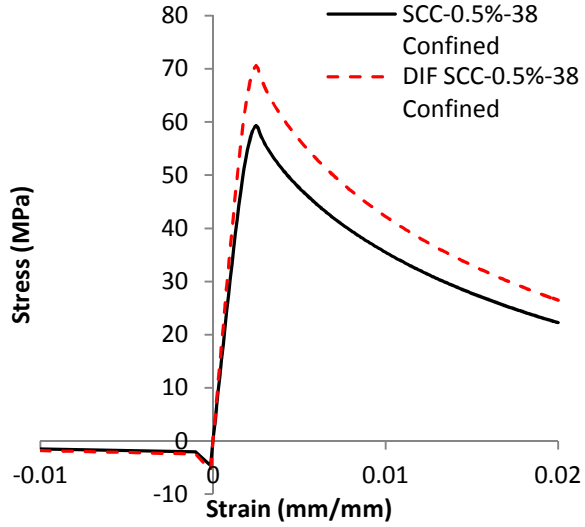

(d) confined concrete (SCC-0.5%-38)

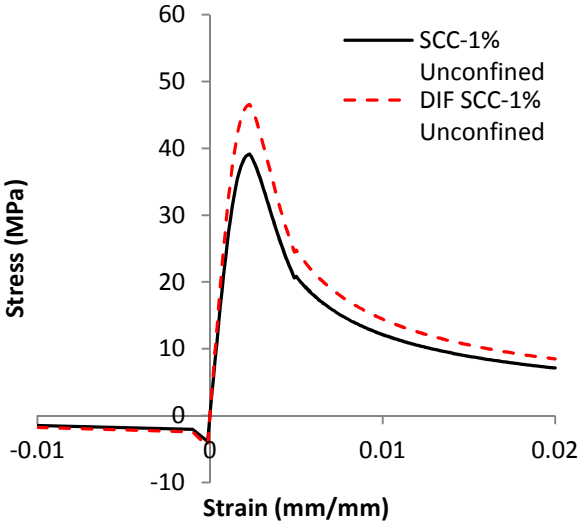

(c) unconfined concrete (SCC-1%-75)

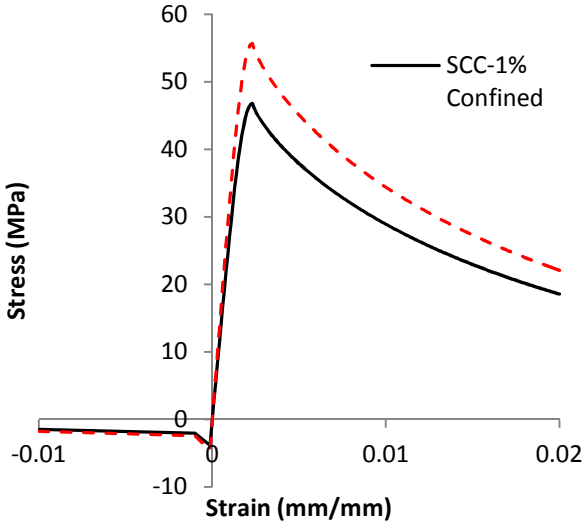

(d) confined concrete (SCC-1%-75)

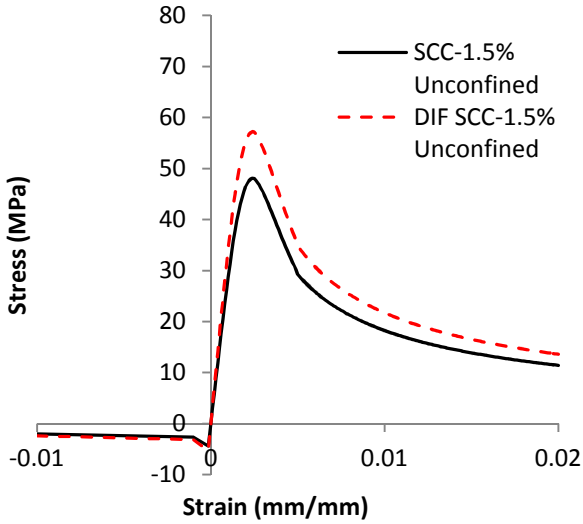

(f) unconfined concrete (SCC-1.5%-75)

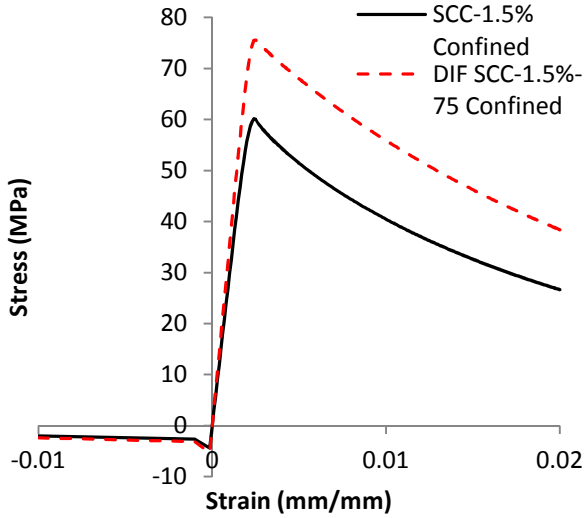

(g) confined concrete (SCC-1.5%-75)

Figure 6.5 Material models used to generate resistance functions for SFRC columns

6.2.1.9 Models Used for CRC Columns

6.2.1.9.1 Unconfined High-Strength FRC Model

In the current thesis, the curve for unconfined CRC was selected from the Carl Bro Group Report (1996). The analytical curve is a best-fit sinusoidal model based on typical tests of CRC cylinders, as shown in Figure 6.6. This figure also shows that the curve is an acceptable approximation. The sinusoidal curve is expressed using the following equation:

$$\frac{\sigma_c}{f'_c} = \sin\frac{\varepsilon_c}{\varepsilon'_{cu}}, 0 \le \varepsilon_c \le \pi\varepsilon_{c0}, \qquad \varepsilon_{c0} = \frac{f_c}{E_{c0}} \qquad [6.49]$$

where σ_c is the compressive stress, f'_c is the compressive strength, ε_c is the compressive strain, ε'_{cu} is the strain at which the curve reaches f'_c, and E_{c0} is the initial modulus of elasticity that is taken as 50 GPa (Nielsen, 1995). The descending portion of the approximation is expressed as:

$$\frac{\sigma_c}{f'_c} = \frac{4\frac{\varepsilon_c}{\varepsilon_{c1}}}{3 + \left(\frac{\varepsilon_c}{\varepsilon_{c1}}\right)^4} \qquad [6.50]$$

where ε_{c1} is the peak strain at which the sinusoidal curve reaches f'_c, and is given by

$$\varepsilon_{c1} = \pi\frac{\varepsilon'_{cu}}{2} \qquad [6.51]$$

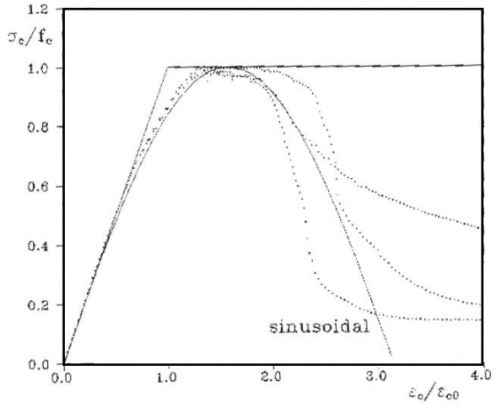

Figure 6.6 Stress-strain curve of CRC including test curves, bi-linear curve, and sinusoidal idealization

[Carl Bro Group, 1996]

6.2.1.9.2 Confined High-Strength FRC Model (Paultre et al., 2010)

The model presented by Aoude (2007) can only be used for normal-strength SFRC. Recently Paultre et al. (2010) proposed a model for the behaviour of high-strength SFRC based on tests on high-strength SFRC columns tested under uniaxial compression. The model modifies the well-established model of Légeron and Paultre (2003) to account for the additional confinement contribution provided by fibres. The expressions in the model were extracted from experimental results using regression analysis, and are based on the confinement index at peak concrete stress as previously defined by Légeron and Paultre (2003). This model was determined suitable for the stress-strain behaviour of confined CRC to predict the behaviour of the CRC columns tested in this study. The compressive stress-strain curve of confined CRC columns, and is therefore described as follows:

$$\frac{f'_{cc}}{f'_{cu}} = 1 + 2.4(I'_e)^{0.7} \qquad [6.52]$$

$$\epsilon'_{cc} = \epsilon'_{cu} + 0.21(I'_e)^{1.7} \qquad [6.53]$$

where f'_{cc} and ϵ'_{cc} is the confined concrete peak stress and corresponding strain, f'_{cu} and ϵ'_{cu} is the unconfined concrete peak stress and corresponding strain, and I'_e is the effective confinement index at peak stress, and is defined as

$$I'_e = \frac{f'_{le}}{f'_c} \qquad [6.54]$$

where f'_{le} is the effective confinement pressure at concrete peak stress due to the action of lateral steel:

$$f'_{le} = K_e \frac{A_{shy}}{sc} f'_h = \rho_{sey} f'_h \qquad [6.55]$$

where K_e is the effective confinement coefficient, A_{shy} is the cross sectional area of the transverse ties in the column, s is the centre to centre spacing of the ties, c area of the core

(centre-to-centre of the ties), f'_h is the lateral steel stress at concrete peak stress, and ρ_{sey} is the effective sectional ratio of the confining reinforcement in the y-direction.

Assuming a constant frictional bond strength, and an average fibre embedment length of l_f / 4 , as discussed in section 2.2.2.4, the confinement pressure due to fiber action, f_{lfb}, in an axially loaded column is:

$$f_{lfib} = \eta_\theta \tau_{bond} V_f \left(\frac{l_f}{d_f}\right) \quad [6.56]$$

where η_θ is the fibre orientation factor, τ_{bond} is the bond strength of fibres, d_f and l_f are the fibre diameter and length respectively, and V_f is the amount of fibres by volume.

Thus, considering the confinement effects of both transverse ties and fibres the confinement pressure can be written as:

$$f'_{le} = \rho_{sey} f'_h + \eta_\theta \tau_{fu} V_f (l_f/d_f) \quad [6.57]$$

Using the previous expression, the effective confinement index can now be computed as:

$$I'_e = \frac{\rho_{sey} f'_h}{f'_c} + \frac{\eta_\theta \tau_{fu} V_f (l_f/d_f)}{f'_c} \quad [6.58]$$

The pre-peak branch of the Paultre et al. (2010) model relies on the relationship originally proposed by Popovics (1973), and is described as:

$$f_c = f'_{cc} \frac{k(\epsilon_c/\epsilon'_{cc})}{k - 1 + (\epsilon_c/\epsilon'_{cc})^k} \quad [6.59]$$

where:

$$k = \frac{E_{ct}}{E_{ct} - (f'_{cc}/\epsilon'_{cc})} \quad [6.60]$$

where E_{ct} is the tangent modulus of elasticity of the unconfined concrete. The post-peak branch of the curve used in the current study is expressed as:

$$f_c = f'_{cc} exp[k_1(\epsilon_c - \epsilon'_{cc})^{k_2}] \text{ for } \epsilon_c > \epsilon'_{cc} \quad [6.61]$$

where k_1 and k_2 are parameters controlling the shape of the post-peak branch and defined as:

$$k_1 = \frac{\ln(0.5)}{(\epsilon_{cc50} - \epsilon'_{cc})^{k_2}} \quad [6.62]$$

$$k_2 = 0.58 + 16(I_{e50})^{1.4} \quad [6.63]$$

The post-peak strain corresponding to 50% of the confined strength, ϵ_{cc50}, is determined using:

$$\epsilon_{cc50} = \epsilon_{c50} + 0.15(I_{e50})^{1.1} \quad [6.64]$$

where ϵ_{c50} is the post-peak strain corresponding to stress equal to 50% of the unconfined concrete strength, and is assumed to be 0.004 should no experimental data be available. Paultre et al. 2010 also note that the maximum effective confinement index, I'_{e50}, that controls the strain ϵ_{cc50} and the parameters k_1 and k_2 is calculated with f'_h set to the yield strength of the transverse reinforcement, and thus:

$$I'_{e50} = \frac{\rho_{sey} f_{hy}}{f'_c} + \frac{\eta_{50}\eta_\theta \tau_{fu}\, v_f (l_f/d_f)}{f'_c} \quad [6.65]$$

where $\eta_{50} \leq 1.0$ is the parameter that takes into account the influence of fibres when the axial strain is equal to the post-peak strain ϵ_{cc50}. η_{50} = 0.5 and η_θ = 0.5.

6.2.1.9.3 General FRC Tension Model Used for CRC (Lok and Pei, 1998)

An idealized stress-strain curve of CRC under tension was not available in the literature, and due to a lack of this information, Nielsen (1995) concluded that even though the CRC matrix is found to produce very high post-cracking strengths due to fibre reinforcement, only the cracking strength of CRC under tension should be used for practical design. Unfortunately, the behaviour at increased tensile strains is important for accurately modelling the response of CRC columns at extreme blast loading, and consequently a generic model was used to model the complete tensile stress-strain behaviour of CRC (including strain-hardening at higher fibre contents).

A model proposed by Nielson (1995) for the cracking stress in conjunction with the Lok and Pei (1998) model for the post-cracking stress-strain relationship was used to predict the behaviour of CRC under tension. This was decided to be an ideal model to use since this method uses both elements based on experimental values, and also predicts the strain-hardening capacity of CRC when using significant amounts of fibre (in this study, at fibre contents ≥ 4% fibres by volume).

The pre-cracking portion of the curve is modelled linearly having a slope of 50 GPa and maximum cracking stress of 7MPa (these are the accepted modulus of elasticity and cracking stress of CRC as indicated by Nielson (1995)),. The post cracking phase is a bilinear curve with two distinct processes as described by Lok and Pei (1998). Process 1 can either be linear ascending or descending depending on whether or not strain hardening is exhibited by the matrix, and is described by the bond stress being gradually developed as the fibres are being strained. This process is expressed as linear from the point of cracking, and the maximum value is determined using:

$$\sigma_2^* = \frac{1}{2} V_f \tau_{bond} \frac{l_f}{d_f} \qquad [6.66]$$

where σ_2^* is the maximum stress for process 1, V_f is the amount of fibres by volume, τ_{bond} is the dynamic bond stress of the fibres, given by Nielsen (1995) for the fibres used in this study as 15.7MPa, and l_f/d_f is the aspect ratio of the fibres.

The corresponding value for strain is expressed as:

$$\varepsilon_2^* = \tau_{bond} \frac{l_f}{d_f} \frac{1}{E_{fp}} \quad [6.67]$$

where E_{fp} is the elastic modulus of the steel fibres, taken to be 200 GPa.

Process 2 describes the residual stress from the fibres as they are slowly being pulled out, and is a linearly descending branch to tensile strain failure (0 MPa). The strain at this point is acknowledged by Lok and Pei (1998) to be quite uncertain, however the value of 0.02 mm/mm is recommended. The complete model as proposed by Lok and Pei is shown in Figure 6.7.

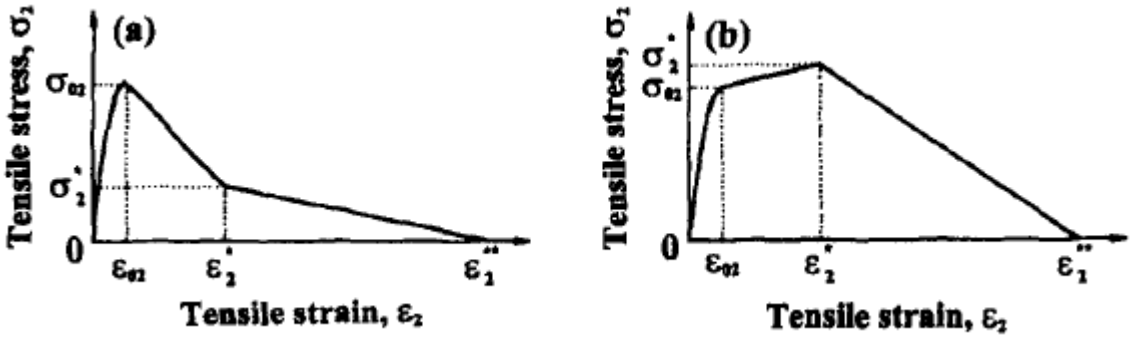

Figure 6.7 SFRC tensile stress-strain relationship as proposed by Lok and Pei (1998), showing (a) tensile softening and (b) tensile hardening.

6.2.1.9.4 High Strain Effects for CRC

As shown in Figure 2.24, DIFs are dependent on both strain rate and the material properties, and are also reduced as the strength of the concrete increases. In order to determine the DIF for UHPFRC, the CEB 1990 model, as described in Section 2.3.7 was initially used. This model uses the ratio of dynamic strain rate over static strain rate, and applies a factor to consider the compressive strength of concrete. Saatcioglu et al. (2011) noted that the tests using the University of Ottawa shock tube consistently demonstrated strain rates from 1-5s^{-1}. Assuming a dynamic strain rate of 5s^{-1} and the average experimental compressive strength of the CRC 2%, 4%, and 6% columns generated DIFs of 1.092, 1.088, and 1.081 respectively. However, Wang et al. (2012) evaluated the mechanical behavior of fibre-reinforced high-strength concrete

subjected to high strain-rate compressive loading, and concluded that the CEB model overestimates the DIF for fibre-reinforced high strength concrete. Consequently, no DIF factor was used for the CRC specimens.

6.2.1.10 Summary of Constitutive Models for CRC Columns

The figure below summarizes the modelled stress-strain curves for the CRC columns used for the analytical predictions of maximum displacements.

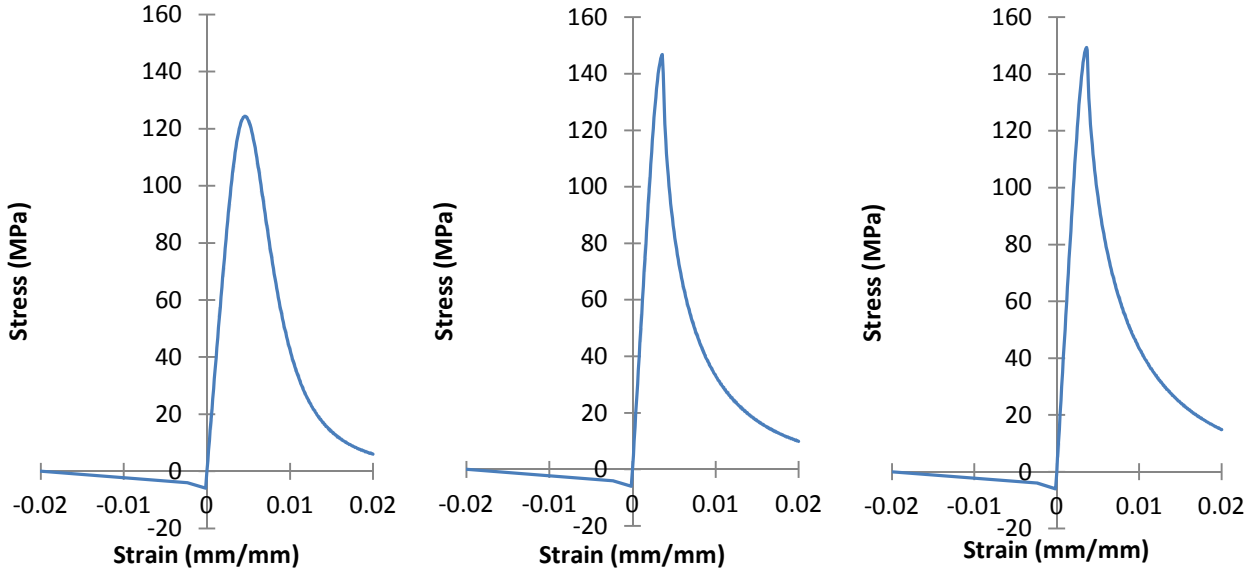

a) CRC-2% Unconfined b) CRC-2%-75 Confined c) CRC-2%-38 Confined

Figure 6.8 Modelled stress-strain curves for CRC-2% columns

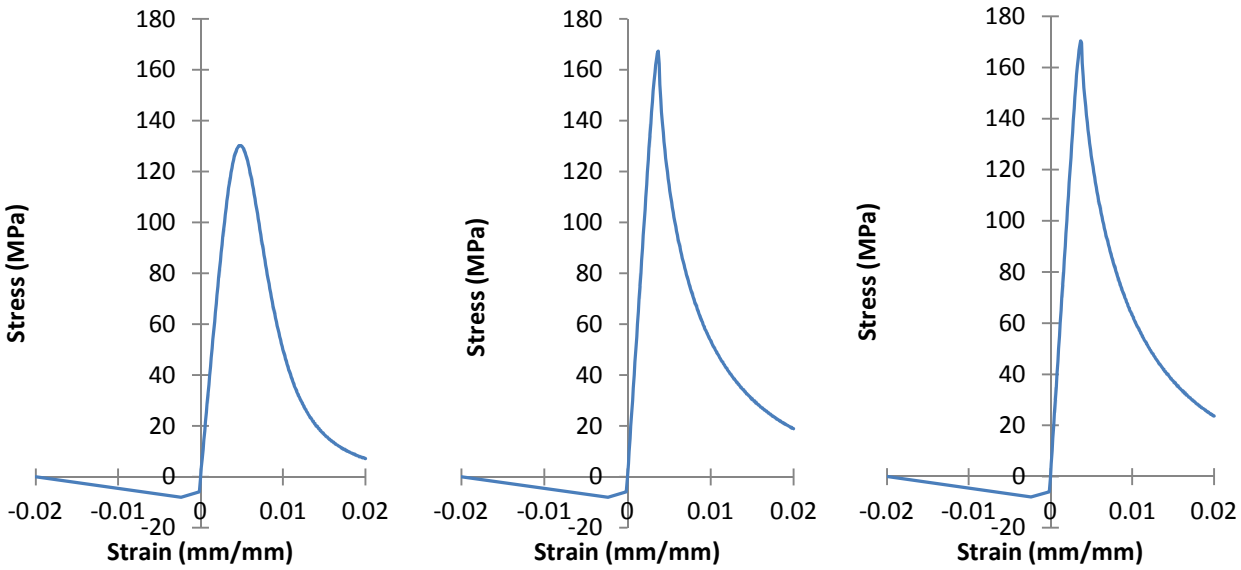

a) CRC-4% Unconfined b) CRC-4%-75 Confined c) CRC-4%-38 Confined

Figure 6.9 Modelled stress-strain curves for CRC-4% columns

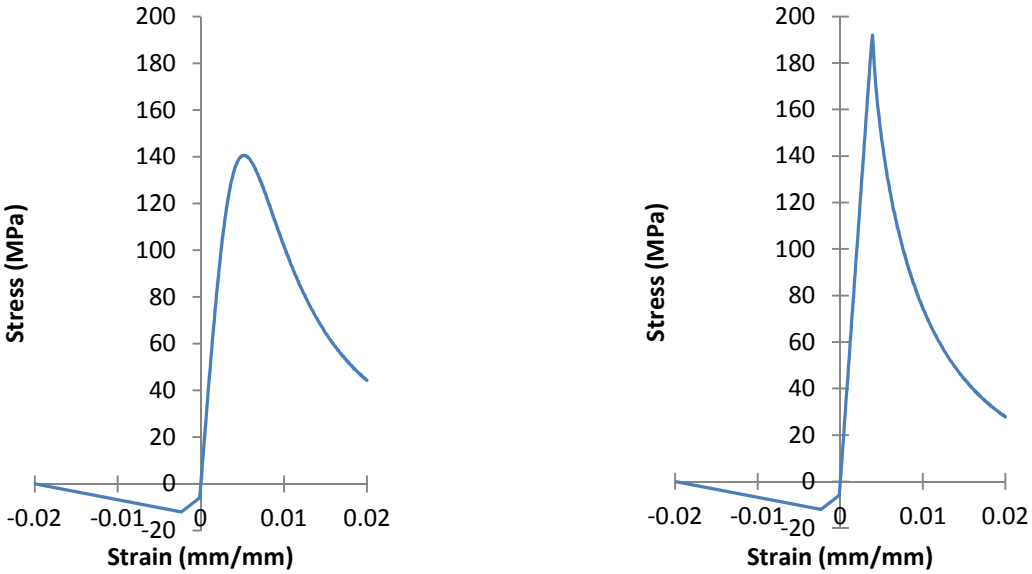

a) CRC-6% Unconfined b) CRC-6%-75 Confined

Figure 6.10 Modelled stress-strain curves fro CRC-6% columns

6.3 SDOF Analysis

6.3.1 General

All columns in this study were analyzed using RCBlast, a standalone software program written by Eric Jacques (2012) at the University of Ottawa. This sub-section will detail the computation techniques used by the program, and the specific inputs used to analyze the columns of this experimental program. The analysis using RCBlast begins with defining the cross-sectional properties of the columns, as described in section 3, and the analytical material properties, as described in the previous section. Using this data, the program then computes the moment-curvature relationship of the column section. With the moment-curvature relationship and a user-defined plastic hinge length, the resistance function and load-mass transformation factors of the columns are then computed using an elastic beam with non-linear rotational hinge analogy. The load-deformation characteristics generated by the program are then used to conduct a SDOF analysis to blast loading.

6.3.2 RCBlast Plane Section Analysis

The first step of RCBlast involves defining the material properties, the cross section dimensions of both confined and unconfined concrete, as well as the arrangement of longitudinal reinforcement. Figure 6.11 shows the input box for the stress-strain diagram of unconfined concrete. The program can consider the entire tensile and compression stress-strain diagram of composite concrete materials, and data can be directly pasted from Excel. Figure 6.12 shows the cross sectional properties input box, and in this figure the dark section shows the confined core area, while the lighter areas show the unconfined concrete. The confined area was assumed to be the area in between the centre-to-centre spacing of the column ties, in accordance with the Aoude (2007) model used for confined concrete.

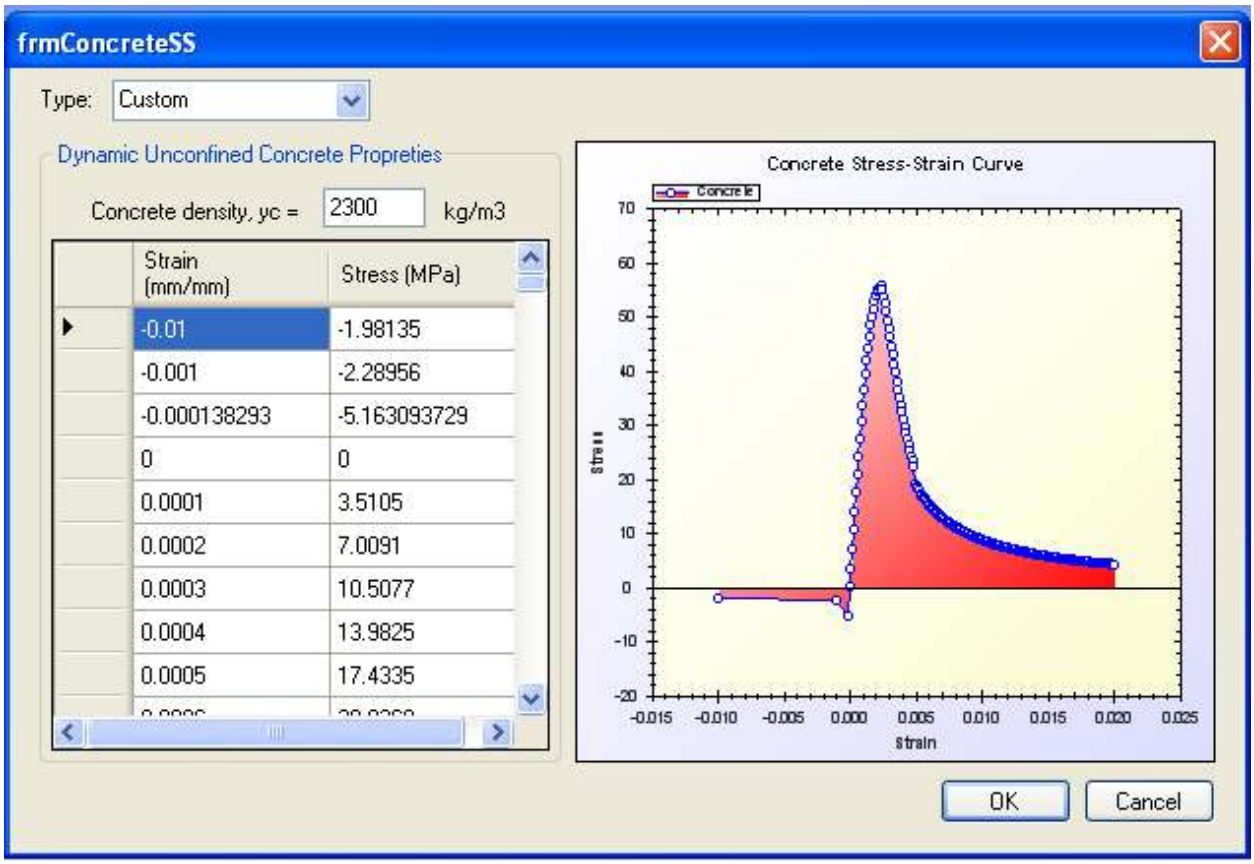

Figure 6.11 Dynamic unconfined concrete properties from RCBlast for column SCC 0.5%

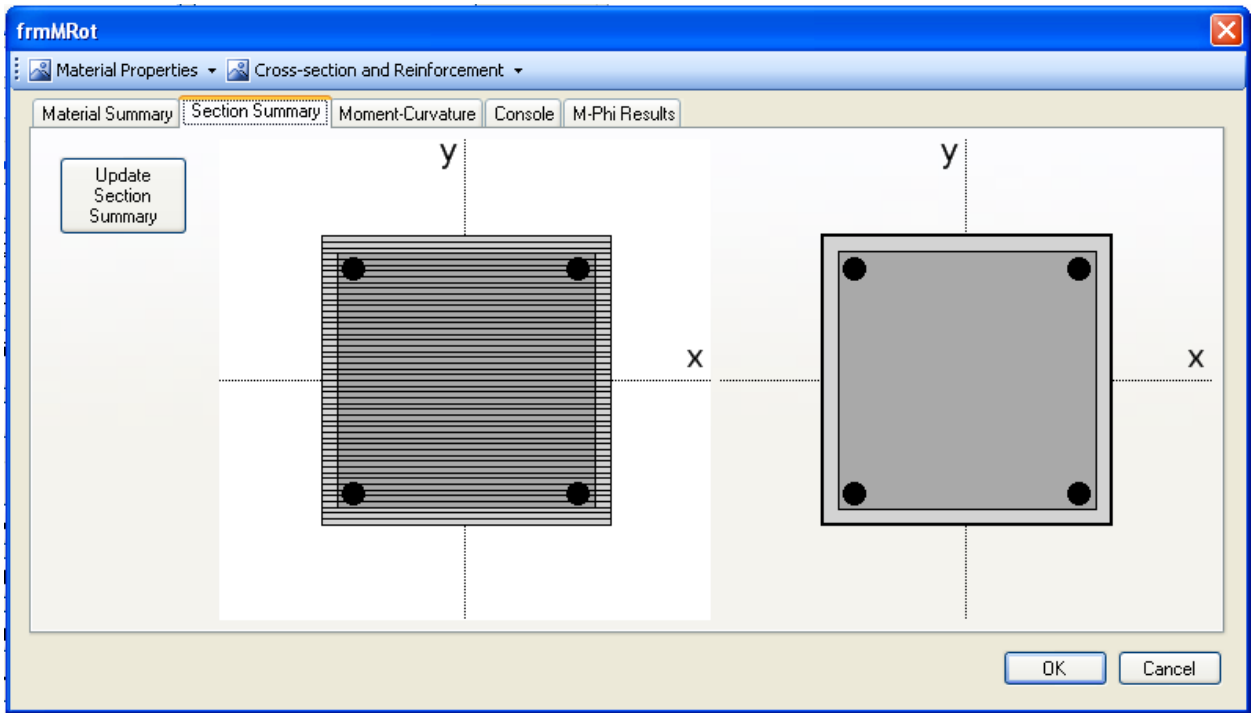

Figure 6.12 RCBlast cross sectional properties of columns

In order to compute the moment-curvature relationship of columns, RCBlast plane section analysis assumes pure flexural behaviour, no loss of bond between reinforcing steel and concrete, and that plane sections before bending remain plane after bending. The first step in analysis is to discretize the confined and unconfined areas of the defined cross section into a finite number of horizontal strips, as shown in Figure 6.12. The program then selects an extreme compressive fibre strain and initial neutral axis depth, and the strain profile within the section is generated considering the internal forces on the unconfined concrete, confined concrete, and reinforcing steel for both tension and compression. Equilibrium of internal forces and axial load is verified by the program using a root finding algorithm to select a revised neutral axis depth, and the procedure is repeated until convergence requirements have been met. To account for variable axial load caused by lateral blast loads on columns, RCBlast calculates moment curvature for several different axial loads from 0 axial load, to a maximum selected by the user. For all columns, a maximum axial load of 294 kN was used to compute the moment curvature diagrams. This axial load was selected based on the maximum capacity of the hydraulic jack, and corresponded to approximately 30% of maximum axial load, P_0, of the SCC columns in initial calculations. The program then continues sectional analysis until the complete positive and negative moment-curvature has been generated, as shown in Figure 6.13. (Jacques et al. 2012)

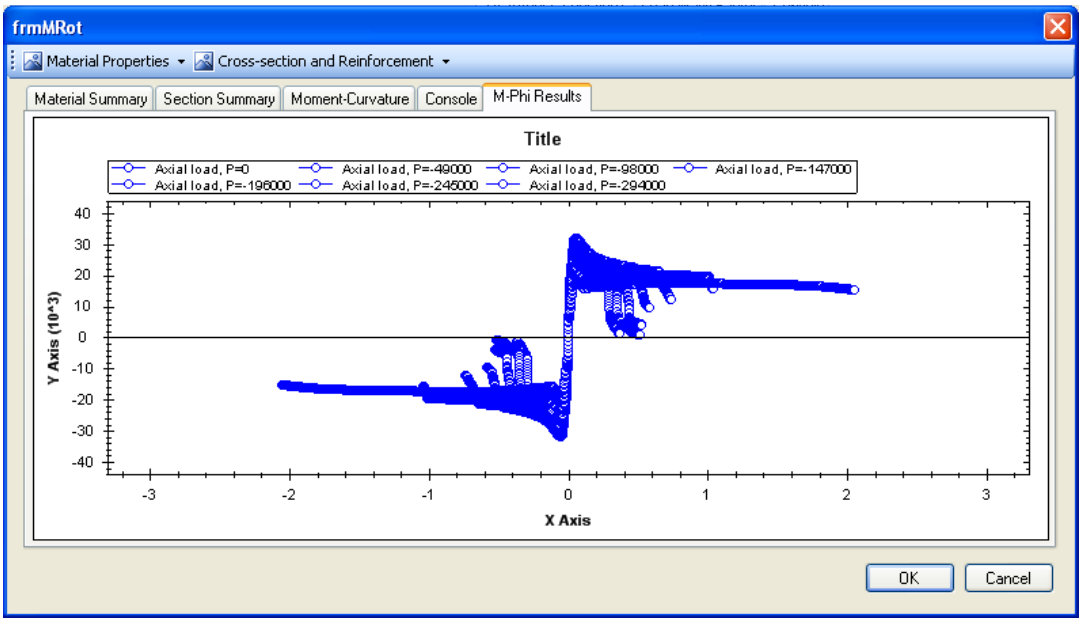

Figure 6.13 RCBlast output of moment curvature of column SCC 0.5%

6.3.3 RCBlast Member Analysis

RCBlast incrementally solves the closed form solution of a symmetric half-span beam-column with elastic material properties and nonlinear rotational springs subjected to uniformly distributed load. The real and idealized beam-column is shown in Figure 6.14. Inelastic behavior, described by the moment-rotation properties of the rotational springs, is lumped at the critical sections. The resistance and load-mass transformation factors obtained from the analysis are then used in SDOF analysis (Jacques et al. 2012). The program generates the moment-curvature relationship of the section to define the elastic and inelastic moment-rotation relationships.

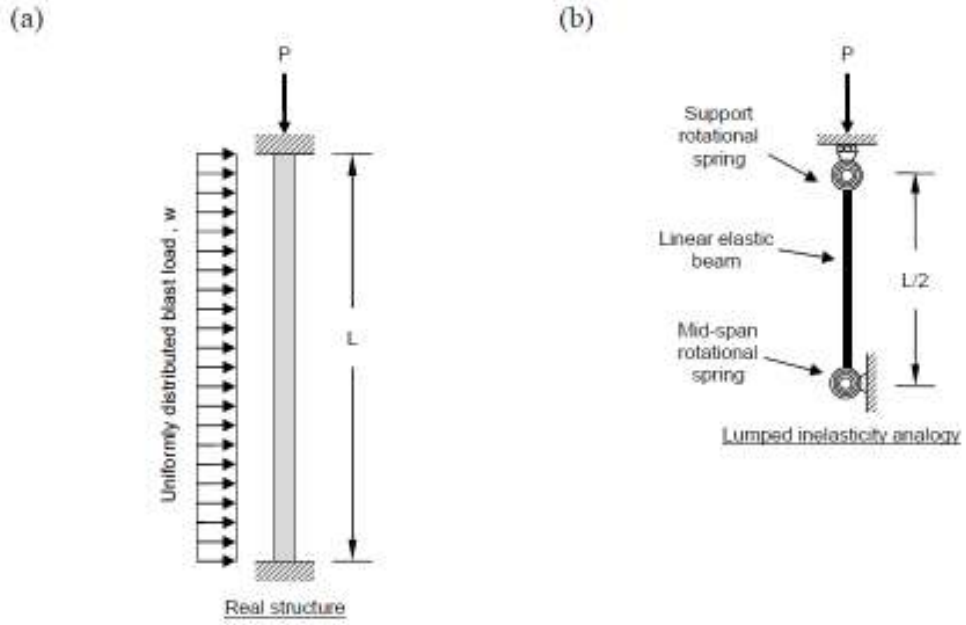

Figure 6.14 Comparison of real structure and modelling procedure used in RCBlast (Jacques et al. 2012)

An equivalent elastic rigidity, EI, of the member is computed based on the pre-yield slope of the moment-curvature relationship. The rotational characteristics of positive and negative bending springs are obtained from the moment-curvature relationship. As necessary, the pre-yield rotational stiffness of a hinge located at a support may be specified by the user. For fully fixed-fixed supports, the initial rotational stiffness of the support, k_{rot}, is infinity. However, previous experiments with the shock tube supports used in this program determined the supports to have a

rotational stiffness of 903000 N*m/rad (Jacques et al. 2012). The ultimate rotation capacity of the hinge, θ_u, is determined using the following expression:

$$\theta_u = (\phi_u - \phi_y) \times L_{pl} + \frac{M_y}{k_{rot}} \quad [6.68]$$

where φ_u and φ_y are curvatures at ultimate and yeld, L_{pl} is the plastic hinge length, and M_y is the moment associated with member yield. Plastic hinge length is a user-defined parameter in RCBlast, and was set to be the depth of column as measured from the tension reinforcing steel to the extreme compression fibre. This value was 0.13545m for all columns. RCBlast incorporates a secant stiffness solution scheme to avoid numerical instability associated with when the tangent to the resistance function approaches zero or becomes negative. The secant rotational spring stiffness for an incremental load is defined as the slope of the line from the origin of the moment-rotation relationship to the point of incremental moment and rotation, as follows:

$$k_{sp,i} = \frac{M_i}{\theta_i} \quad [6.69]$$

where $k_{sp,i}$, is the rotational spring stiffness of the hinge, and M_i and θ_i are the incremental moment and rotation respectively (Jacques et al. 2012). Figure 6.15 shows the derivation of rotational spring properties used in RCBlast, both the theoretical and idealized moment-curvature and the moment rotation relationship are shown.

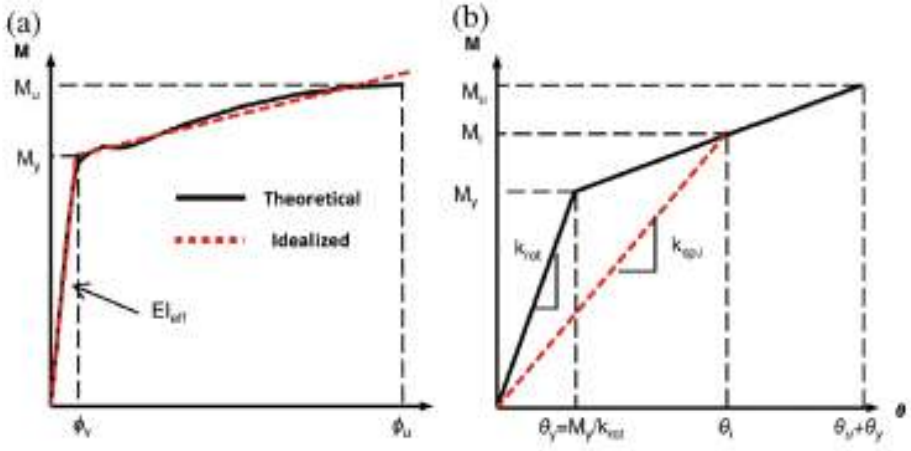

Figure 6.15 (a) Theoretcial and idealized moment-curvature relationships and (b) idealized moment-rotation relationship (Jacques et al. 2012)

In the pre-yield stage, the resistance function and load-mass transformation factors are computed from an incrementally increasing lateral load, and the consequent displaced shape. The equations used to calculate the transformation factors are discussed in section 2.3.6.1. Once yielding has occurred, the hinge responds in accordance to its moment-rotation relationship, and the inelastic rotation is also incrementally increased, and consequently a new rotational spring stiffness is obtained. RCBlast continues an iterative step-by-step process along the moment rotation curve until all plastic hinges are formed, and then all member displacements are calculated from the inelastic rotations at the critical sections (Jacques et al. 2012).

6.3.4 Variations in Axial Load

During testing, a hydraulic jack was used to apply a compressive axial load to the columns as described in Section 3.5.2. As the column is subjected to a lateral blast load, it will also deflect laterally. The lateral deflections of the column cause a shortening along its projected vertical length. The projected vertical shortening causes the piston of the hydraulic jack to expand, which in turn causes a decrease in hydraulic pressure, and thus a reduction in axial load. In order to account for the drop in axial load, a composite curve based on the resistance curves of seven intermediate axial load (0 kN to 294 kN) levels was used. An approximate method was used to develop the composite resistance curve that assumed a drop in axial load at specified deflections based on a reduction in column stiffness that could cause the hydraulic jack to expand, as shown in Figure 6.16. This method is approximate, and due to larger deflections before expected drops in axial load as reported by Lloyd (2010), it is expected that this will result in over-prediction of column stiffness.

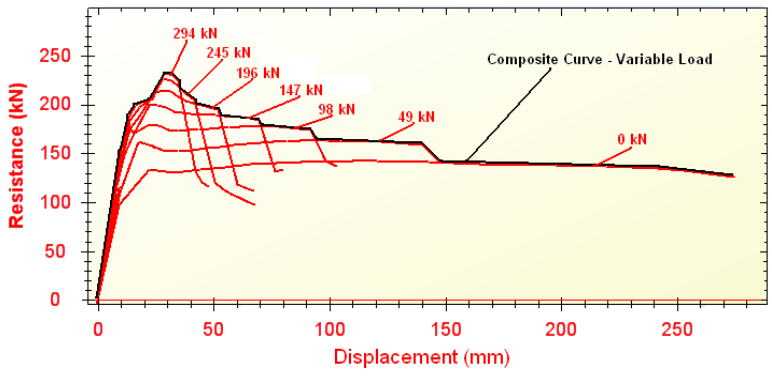

Figure 6.16 Typical resistance curve generated by RCBlast for a column subjected to variable axial load.

6.3.5 RCBlast Dynamic Inelastic Analysis

RCBlast uses SDOF analysis to predict a complete a displacement-time history at mid-span of columns up to the point of maximum displacement, as this is the point of primary interests for blast analysis of structures. The program uses the following equation of motion to describe the dynamic response of columns subjected to blast as defined in Section 2 of this thesis:

$$k_{LM}(y)m\ddot{u}(t) + R(u(t)) = AP_r(t) \qquad [6.70]$$

where u(t) and $\ddot{u}(t)$ are the displacement and acceleration of the midspan of the column, $k_{LM}(u)$ are the load mass factors as a function of displacement, $R(u)$ is the resistance function, A is the area impacted by the blast wave, in the case of this study 2.232m × 2.232m (the area of the shock tube opening, and $P_r(t)$ is the reflected pressure time history. For the analysis of all columns in this study, the reflected pressure time history was idealized in to a triangular load of equal impulse as the recorded pressure-history profile from the experimental data, as described in section 2.3.6.

RCBlast uses the equation of motion in Equation 6.71, and uses the average acceleration numerical integration solution scheme to solve for displacements of the member at any time t. The time-step is user defined, and was selected in order to ensure that the time stop was not greater than one-tenth of the natural period of the column (including the mass of the load transfer device), in accordance with Biggs (1964). The selected time step was also required to be acceptably small to negate inherent errors from the time-step method that are caused by using the resistance and load-mass factors based on displacements computed from the previous time-step (Jacques et al. 2012). A time step of 0.0001 seconds was used for the analysis of all columns. Figure 6.17 shows an example of the output screen from RC Blast SDOF analysis that computes the maximum deflection at mid-span of the columns in this study.

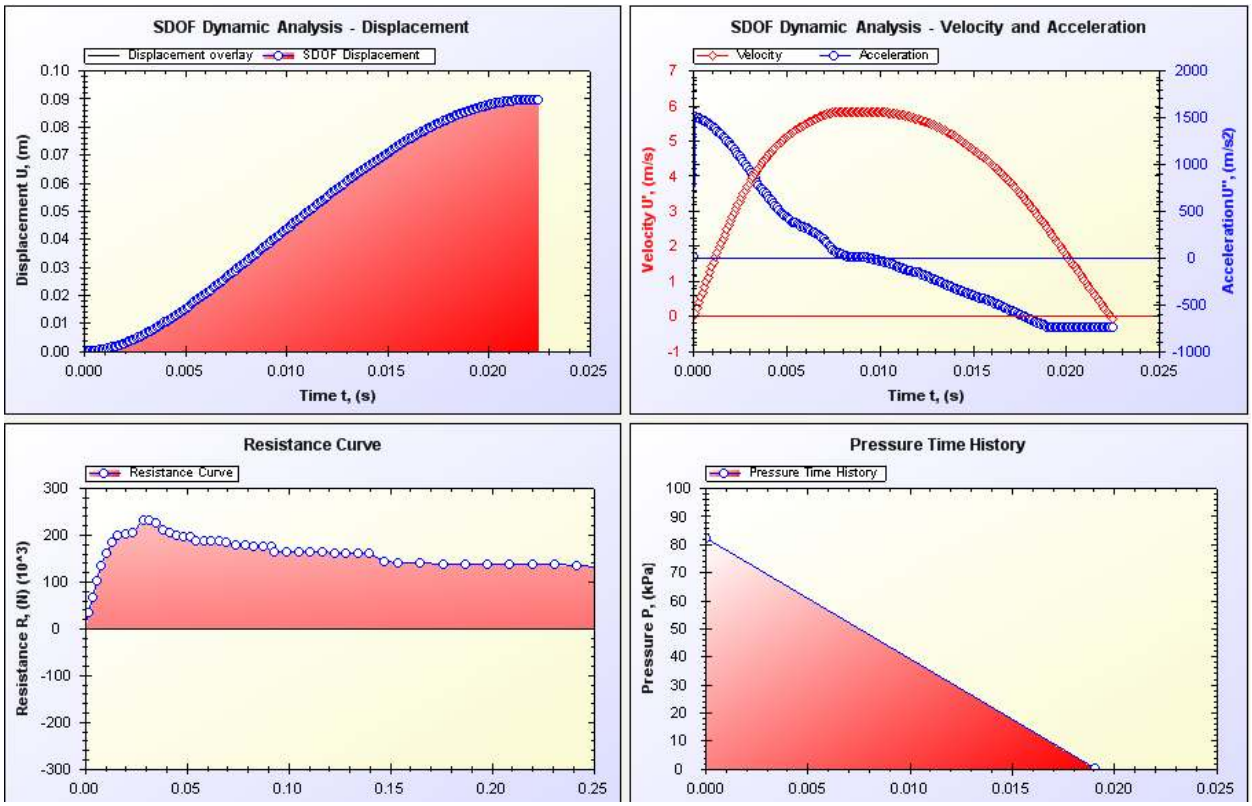

Figure 6.17 RCBlast output screen for SDOF analysis of SCC 0.5% for Blast 3. (Top left) SDOF displacement-time history, (top right) velocity and acceleration time history, (bottom left) Resistance function computed by the program, and (bottom right) idealized triangular pressure-time history.

6.4 Analytical Results

6.4.1 General

Comparisons of predicted and experimental mid-span displacement time histories, as well as the resistance functions for each column are plotted in Figure 6.18 to Figure 6.30 for selected tests. Experimental and predicted maximum displacements, as well as experimental and predicted time-to-maximum displacements for available tests are shown in Table 6.2. Summaries relating the accuracy of the predicted results to experimental results are shown in Table 6.3. The analysis indicates that the predicted mid-span displacements of all specimens are in reasonable agreement with the behaviour observed during experimental testing.

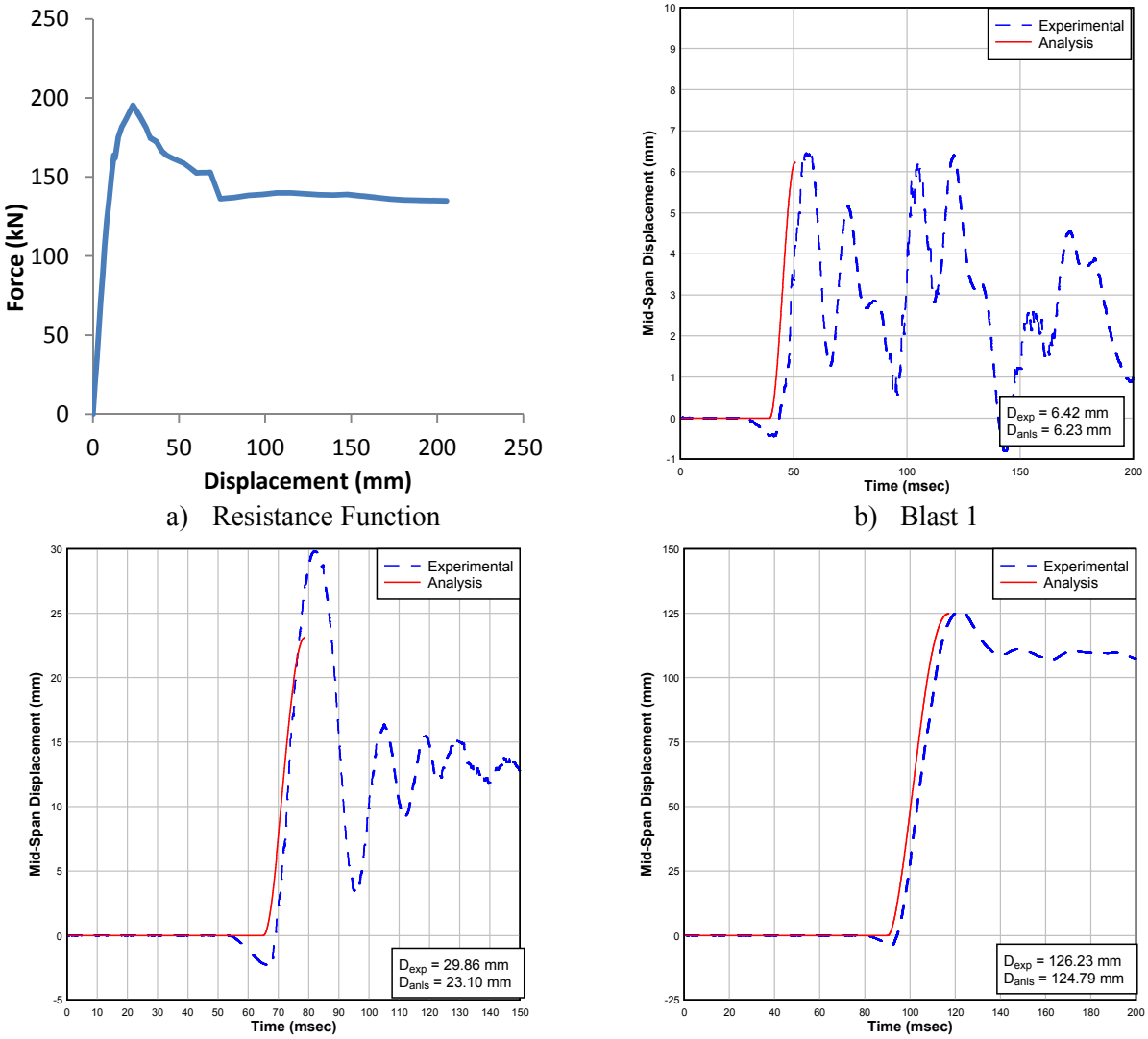

a) Resistance Function

b) Blast 1

c) Blast 2

d) Blast 3

Figure 6.18 SCC-0%-75 resistance function and displacement-time curves comparing experimental and analytical results

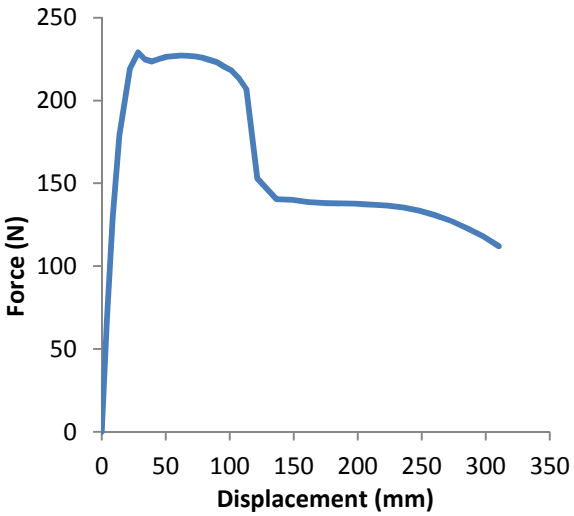

a) Resistance Function

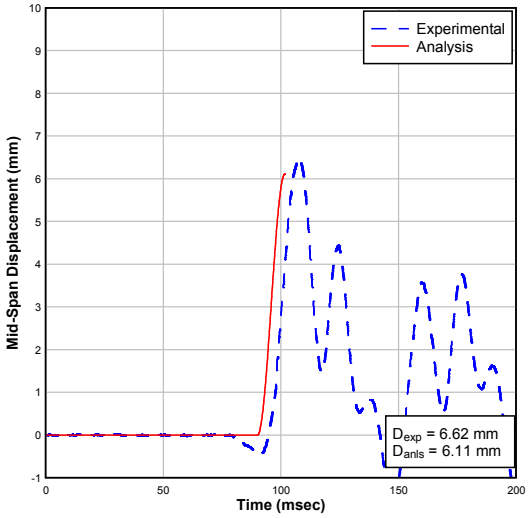

b) Blast 1

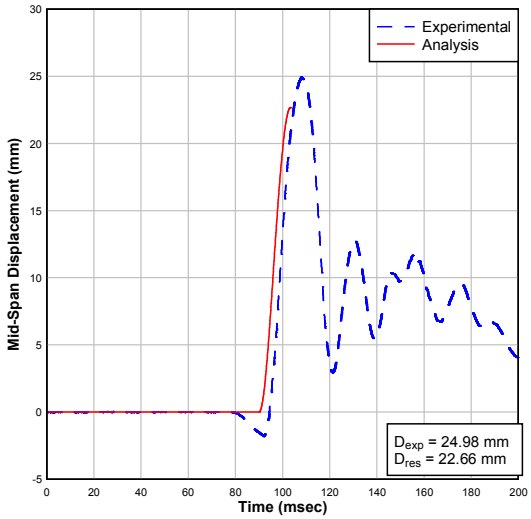

c) Blast 2

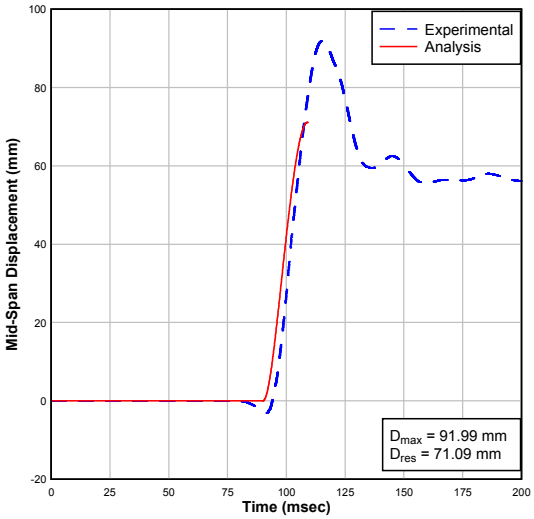

d) Blast 3

Figure 6.19 SCC-0%-38 resistance function and displacement-time curves comparing experimental and analytical results

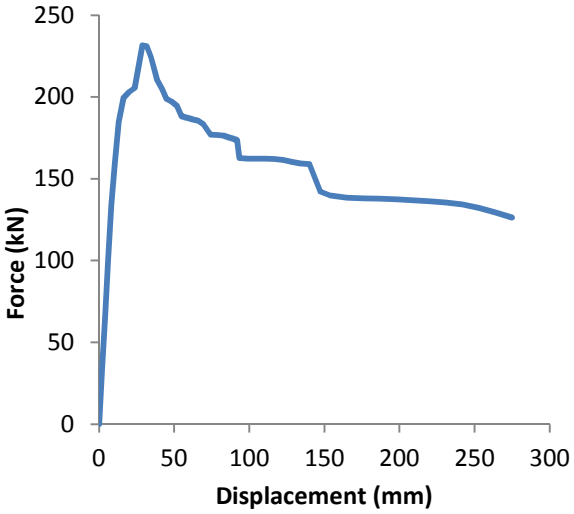

a) Resistance Function

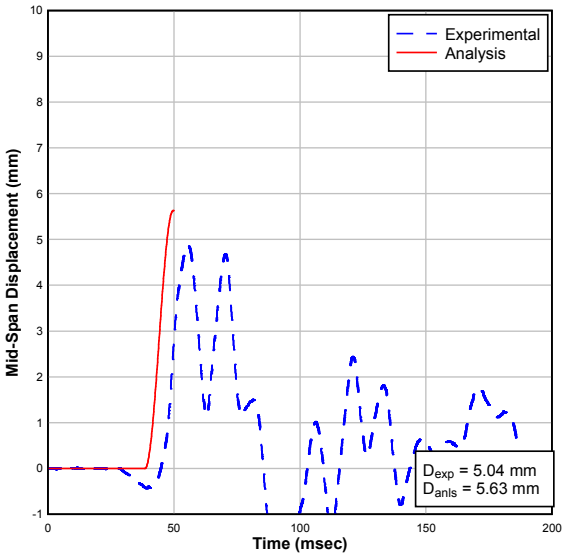

b) Blast 1

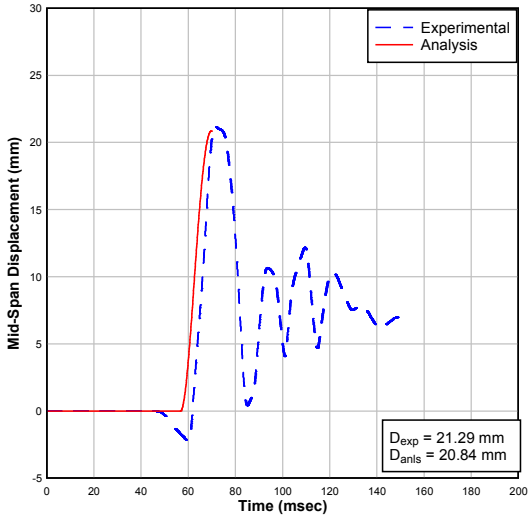

c) Blast 2

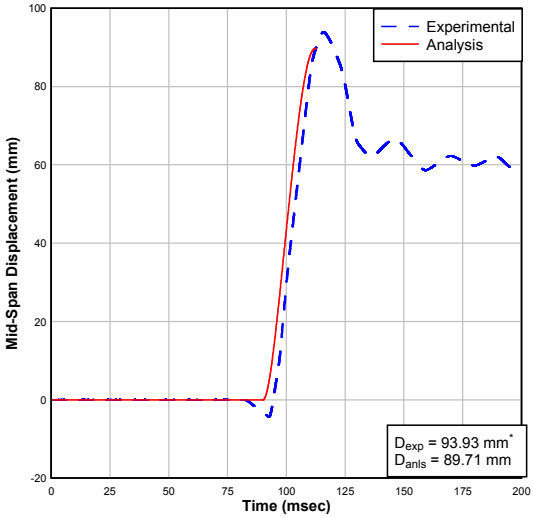

d) Blast 3

Figure 6.20 SCC-0.5%-75 resistance function and displacement-time curves comparing experimental and analytical results

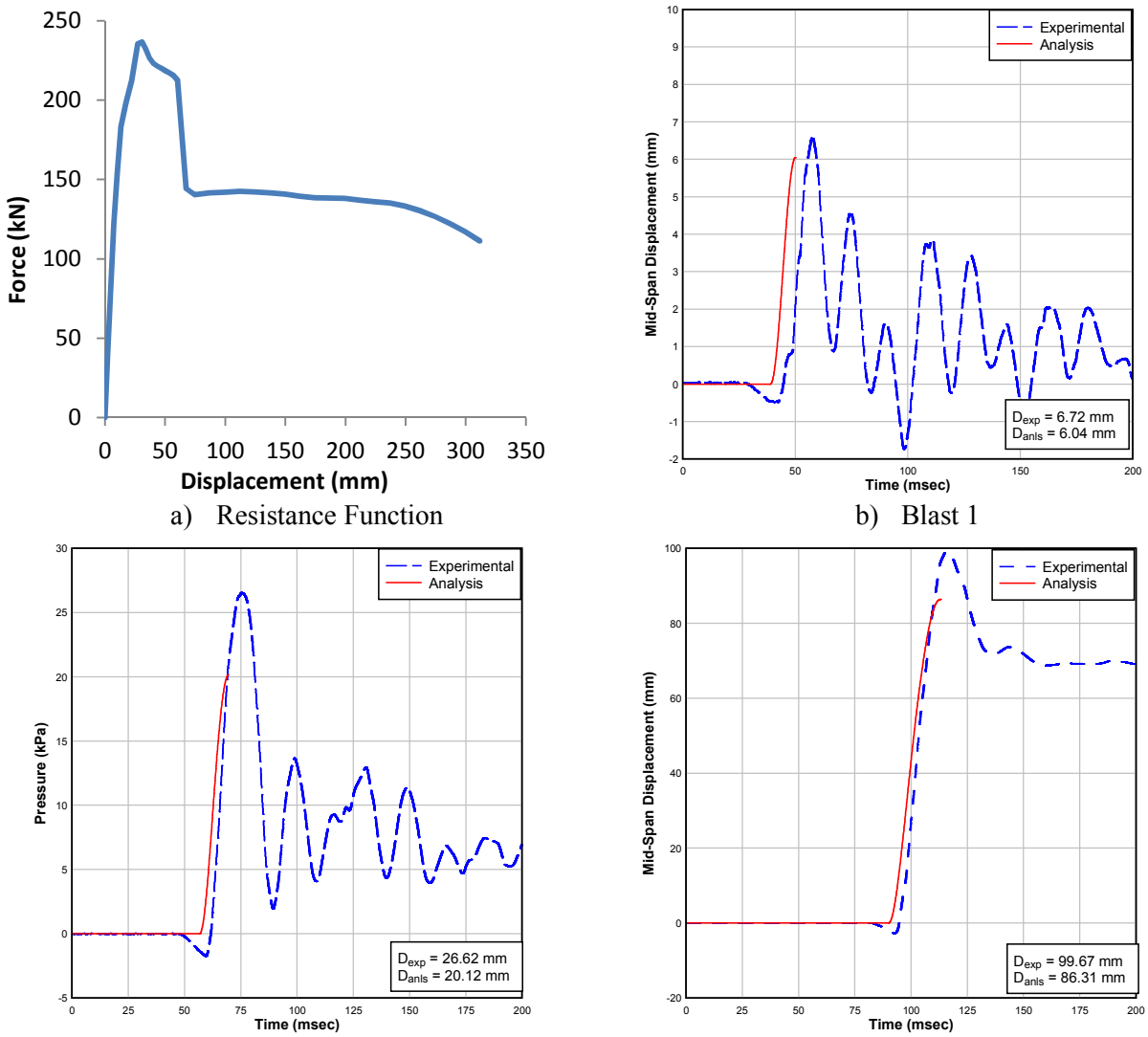

a) Resistance Function

b) Blast 1

c) Blast 2

d) Blast 3

Figure 6.21 SCC-0.5%-38 resistance function and displacement-time curves comparing experimental and analytical results

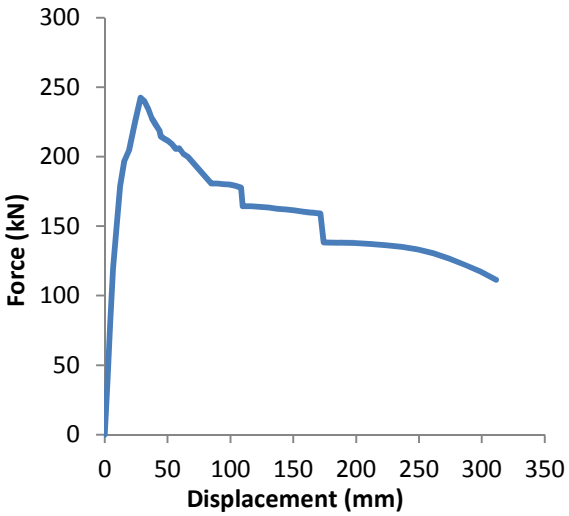

a) Resistance Function

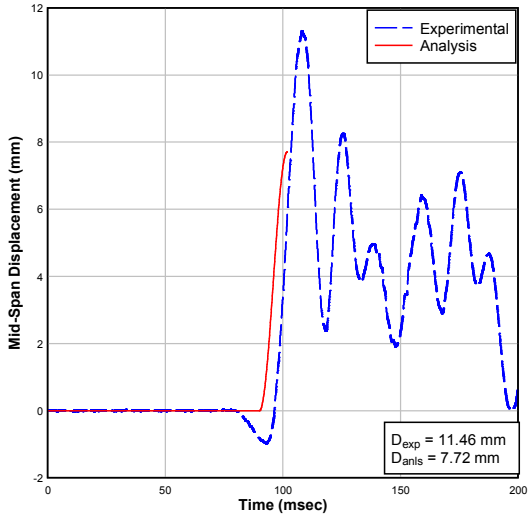

b) Blast 1

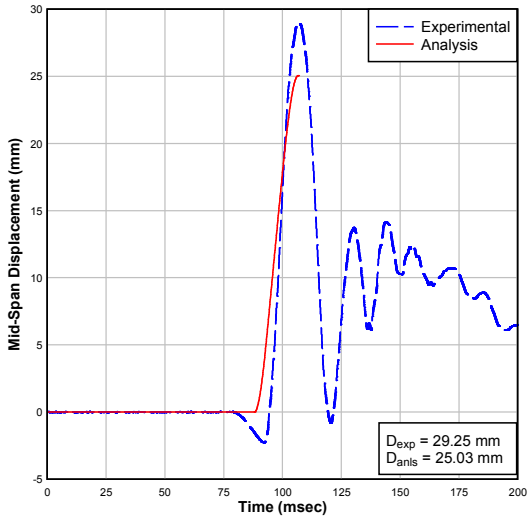

c) Blast 2

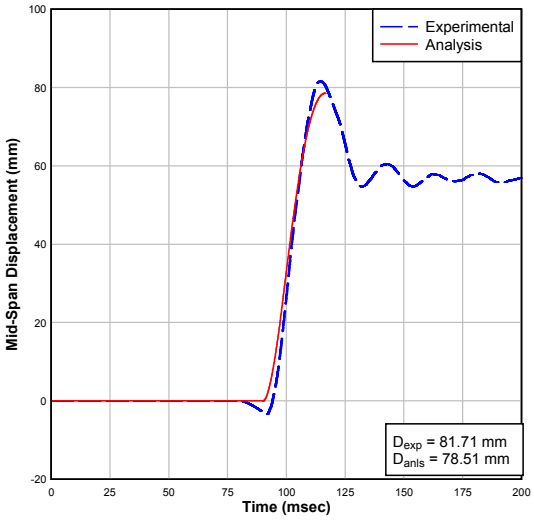

d) Blast 3

Figure 6.22 SCC-0.75%-75 resistance function and displacement-time curves comparing experimental and analytical results

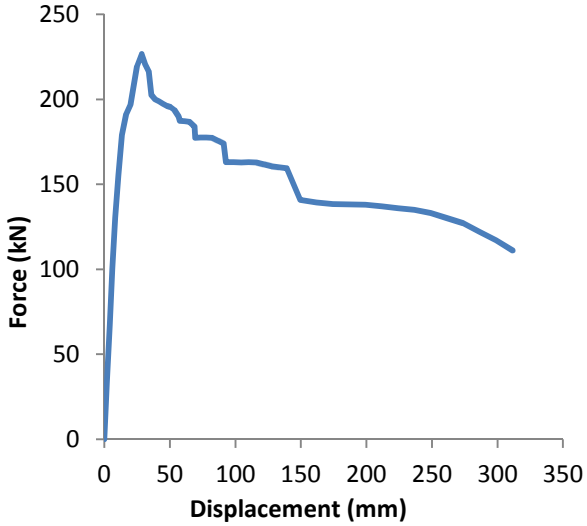

a) Resistance Function

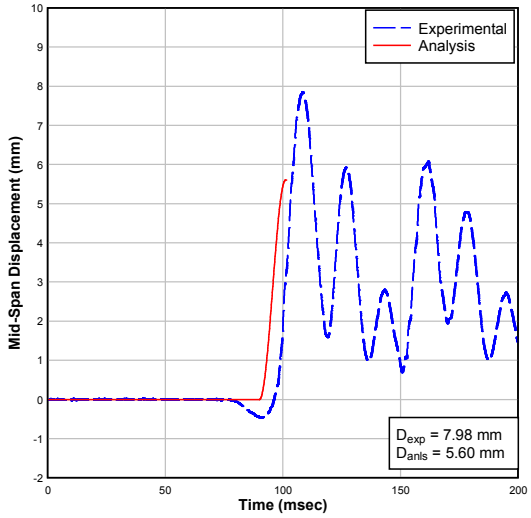

b) Blast 1

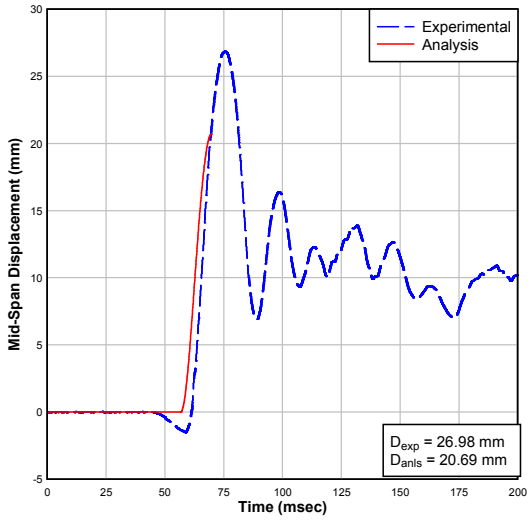

c) Blast 2

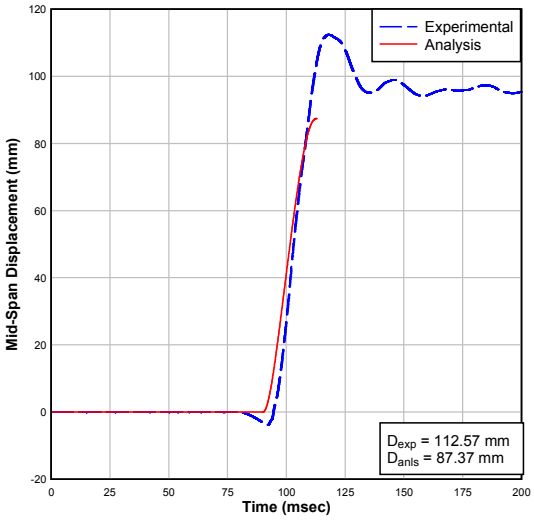

d) Blast 3

Figure 6.23 SCC-0.75%HS-75 resistance function and displacement-time curves comparing experimental and analytical results

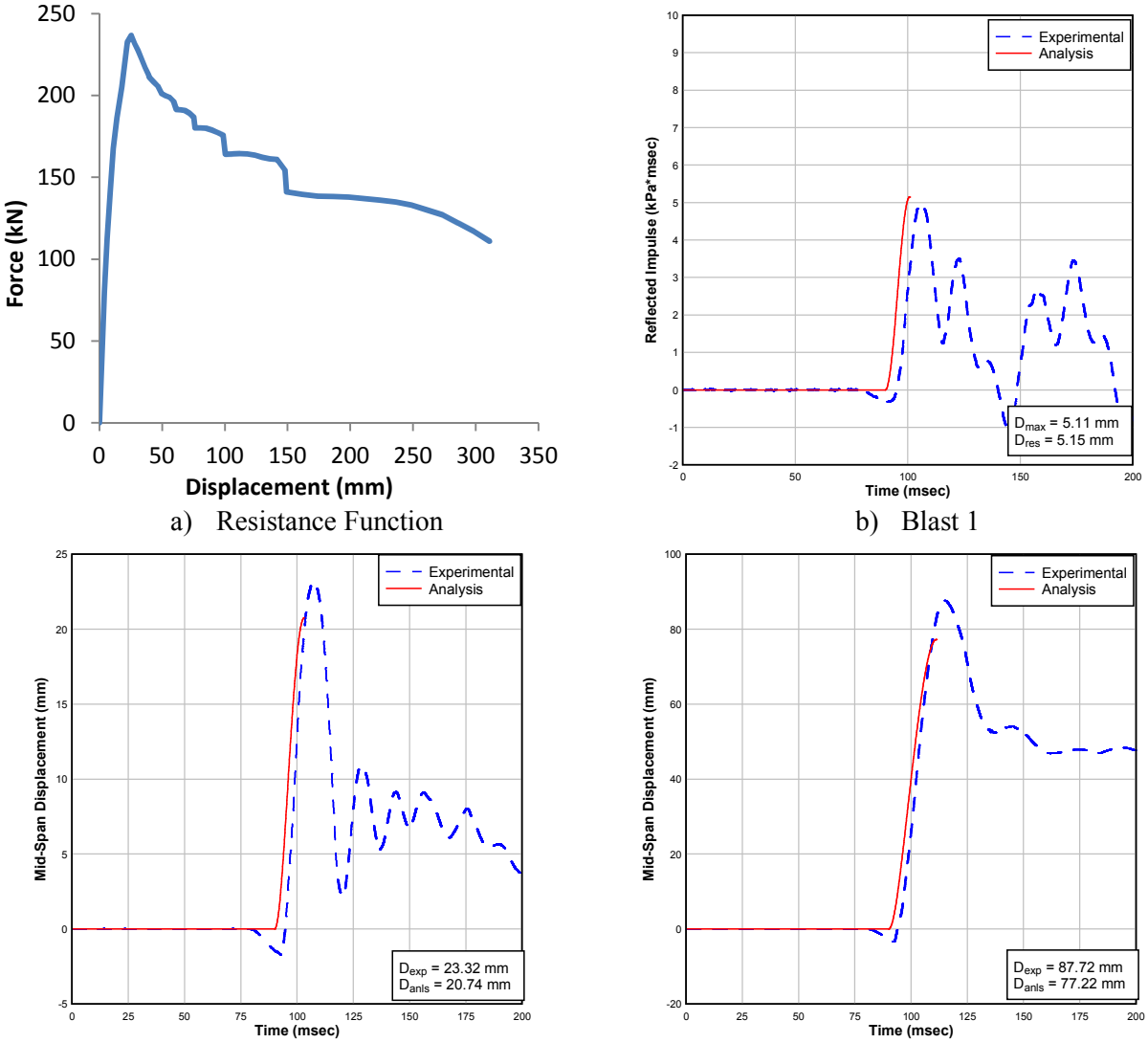

a) Resistance Function

b) Blast 1

c) Blast 2

d) Blast 3

Figure 6.24 SCC-1%-75 resistance function and displacement-time curves comparing experimental and analytical results

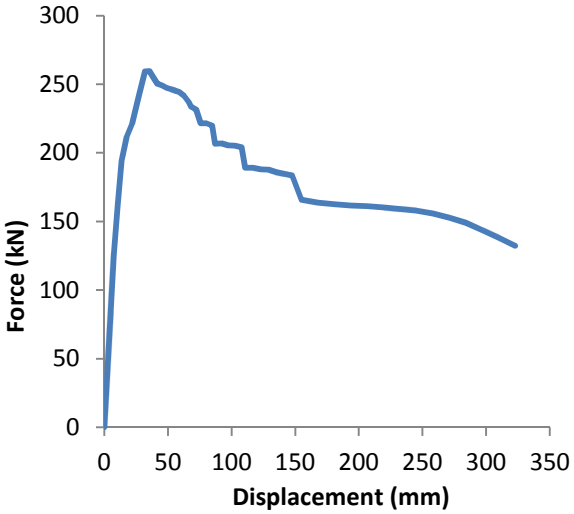

a) Resistance Function

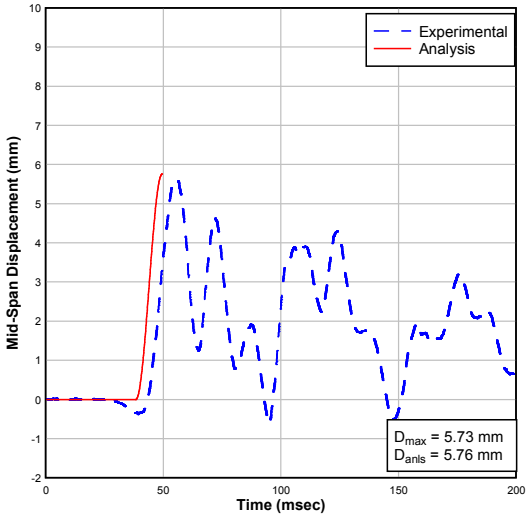

b) Blast 1

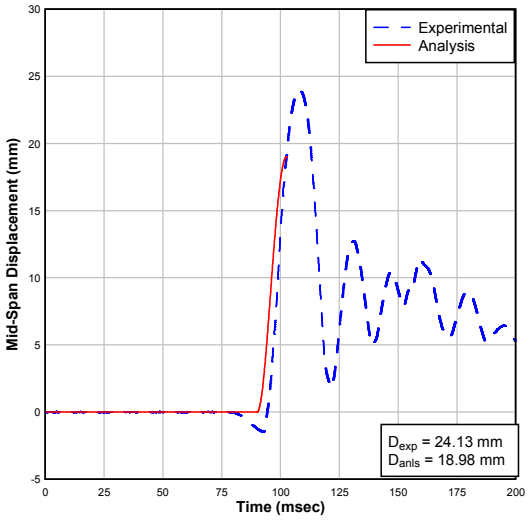

c) Blast 2

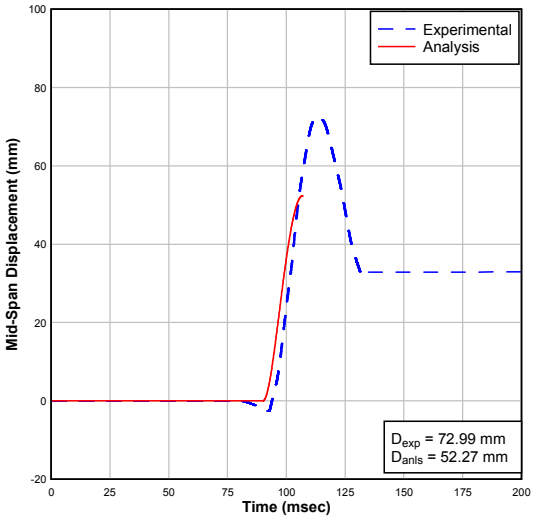

d) Blast 3

Figure 6.25 SCC-1.5%-75 resistance function and displacement-time curves comparing experimental and analytical results

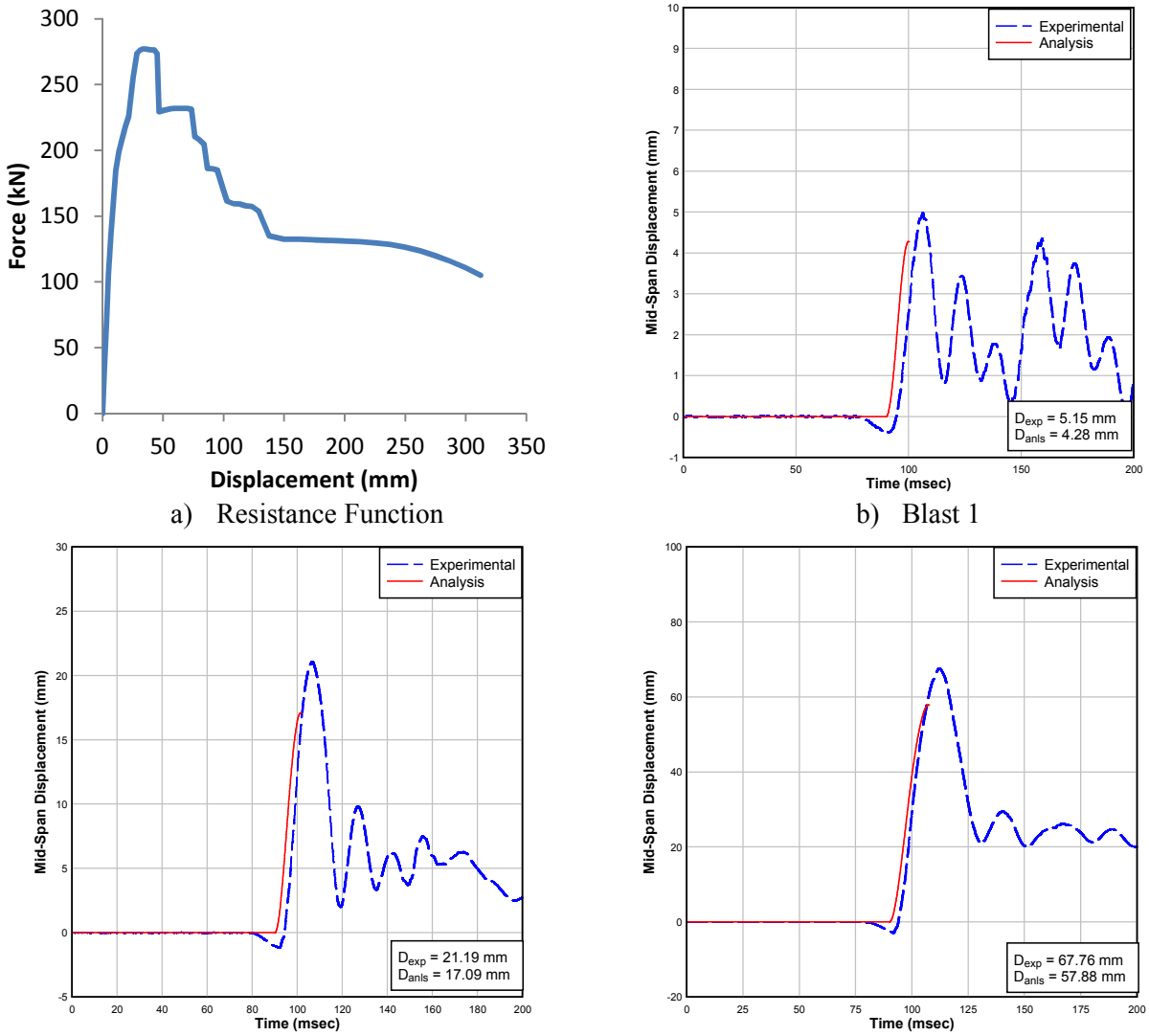

a) Resistance Function

b) Blast 1

c) Blast 2

d) Blast 3

Figure 6.26 CRC-2%-75 resistance function and displacement-time curves comparing experimental and analytical results

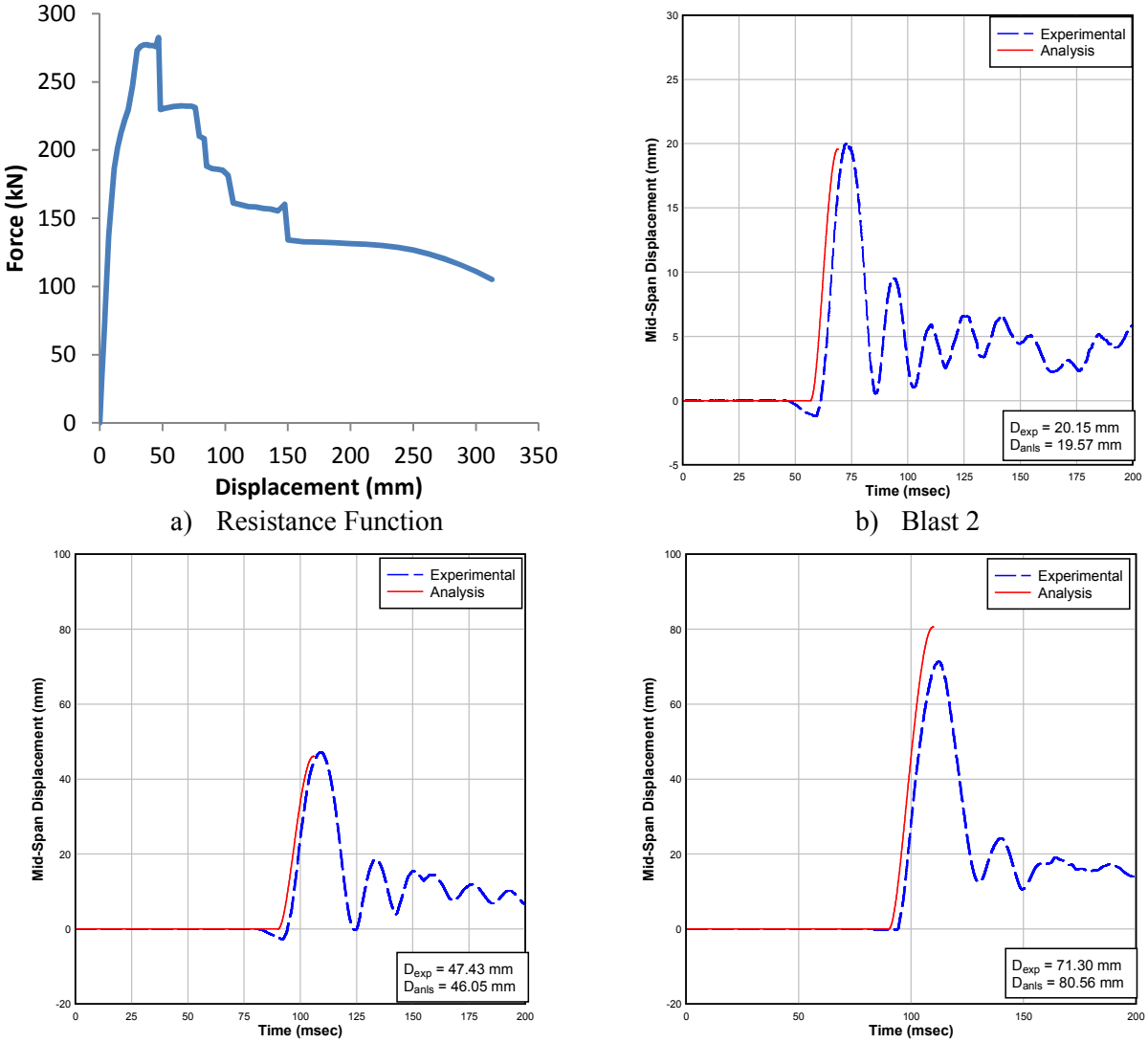

a) Resistance Function

b) Blast 2

c) Blast 3

d) Blast 4

Figure 6.27 CRC-2%-38 resistance function and displacement-time curves comparing experimental and analytical results

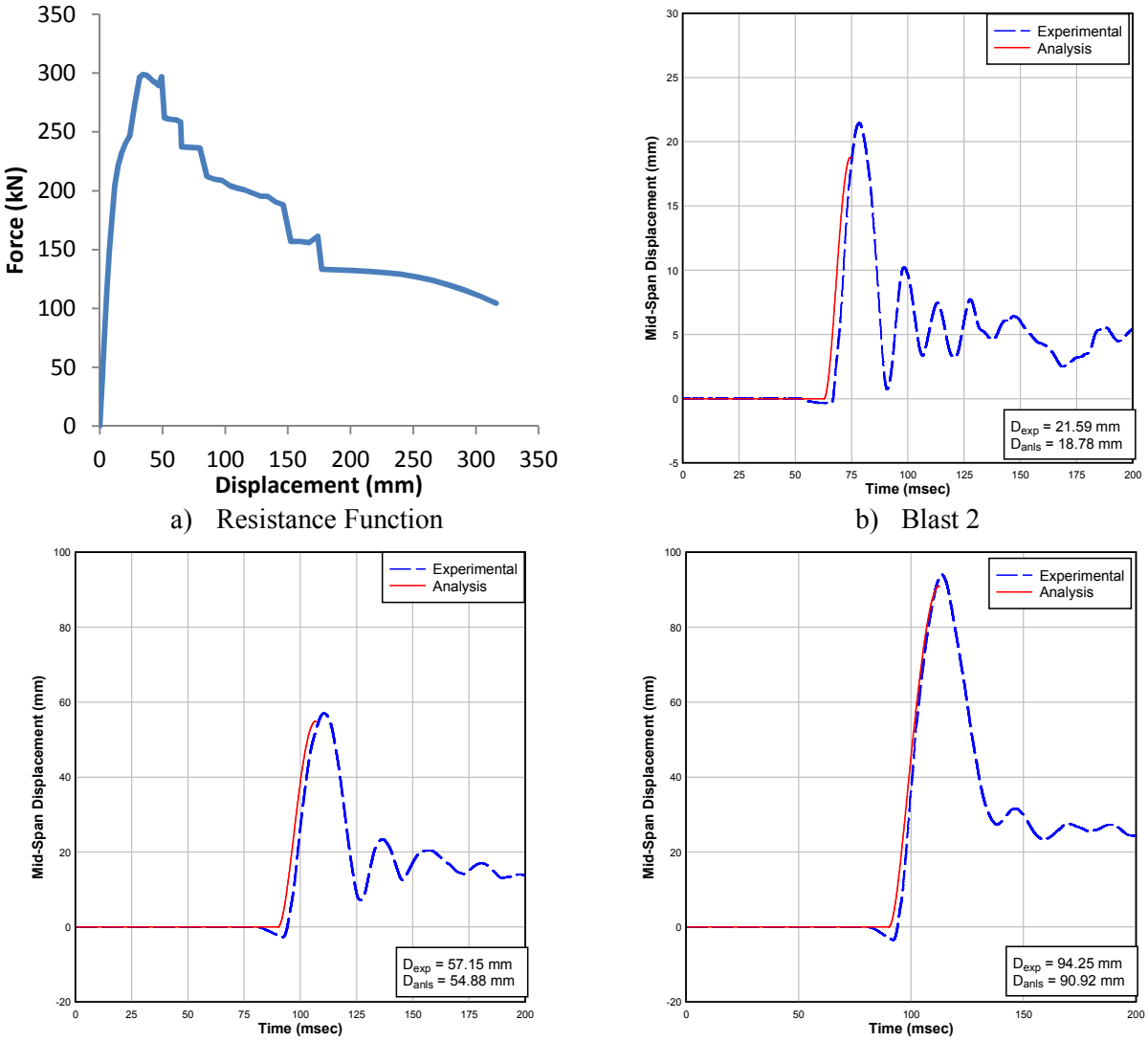

a) Resistance Function

b) Blast 2

c) Blast 3

d) Blast 3

Figure 6.28 CRC-4%-75 resistance function and displacement-time curves comparing experimental and analytical results

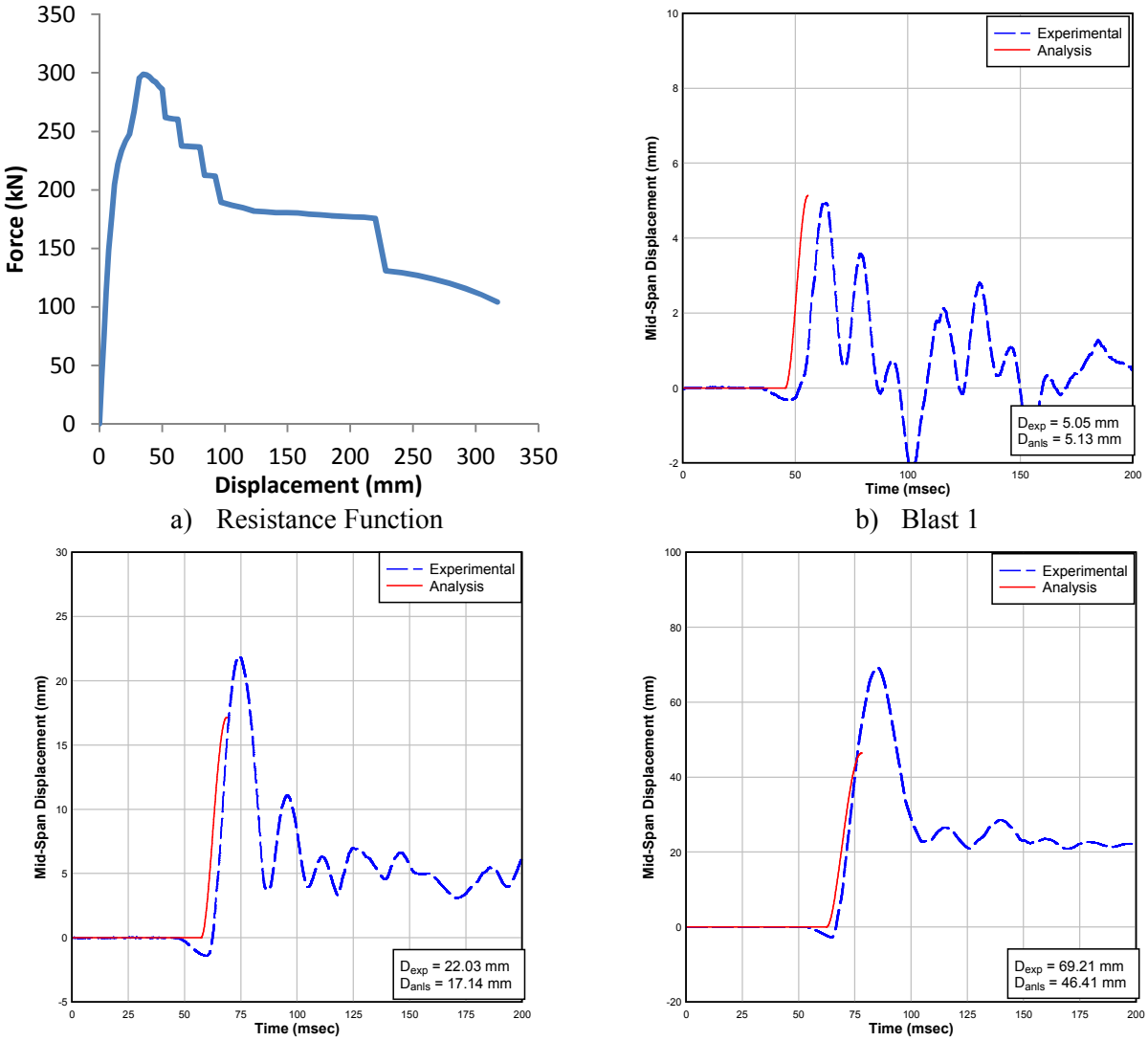

a) Resistance Function

b) Blast 1

c) Blast 2

d) Blast 3

Figure 6.29 CRC-4%-38 resistance function and displacement-time curves comparing experimental and analytical results

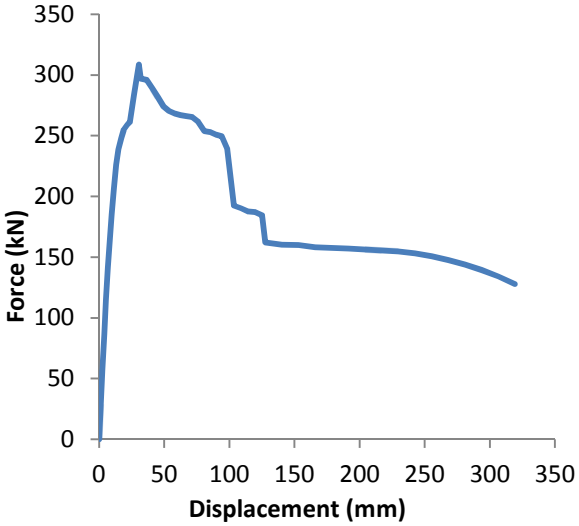

a) Resistance Function

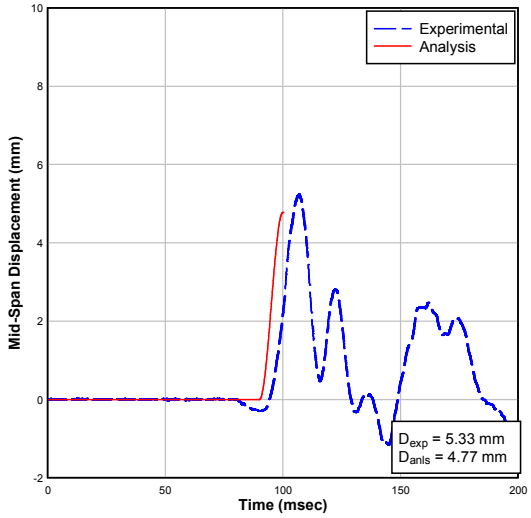

b) Blast 1

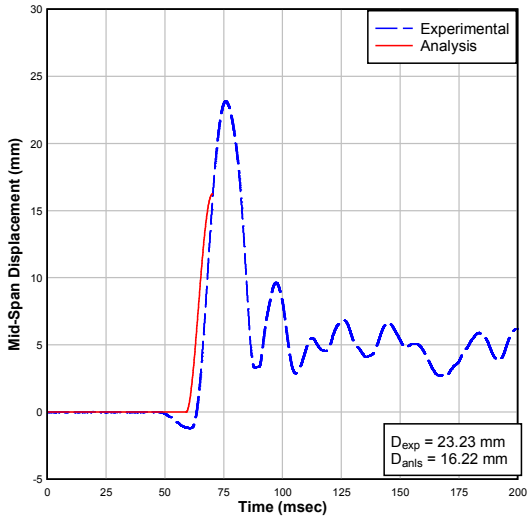

c) Blast 2

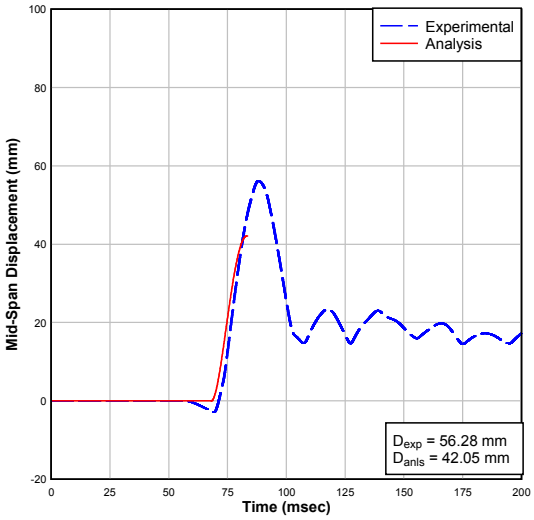

d) Blast 3

Figure 6.30 CRC-6%-75 resistance function and displacement-time curves comparing experimental and analytical results

Table 6.2 Reflected shockwave properties, idealized shockwave properties, maximum mid-span displacements, and time to maximum displacements for experimental results and SDOF analytical predictions.

		Shockwave Properties			Idealized Shockwave			Maximum Mid-span Displacement			Time to Maximum Displacement		
		P_r (kPa)	t_d (msec)	I_r (kPa*msec)	P_r (kPa)	t_{df} (msec)	I_r (kPa*msec)	Experimental (mm)	Analytical (mm)	% Error (%)	Experimental (msec)	Analytical (msec)	% Error (%)
SCC-0%-75	Blast 1	13.66	22.18	130.01	13.66	19.03	129.97	6.42	6.23	2.96%	57.92	51.91	10.38%
	Blast 2	42.36	22.20	380.95	42.36	17.99	381.02	29.86	23.10	22.64%	81.82	78.60	3.94%
	Blast 3	87.87	25.38	780.67	87.87	17.77	780.72	126.23	124.79	1.14%	122.39	116.90	4.49%
SCC-0%-38	Blast 1	12.67	21.93	123.17	12.67	19.44	123.15	6.62	6.11	7.70%	107.63	101.70	5.51%
	Blast 2	40.87	24.35	401.35	40.87	19.64	401.38	24.98	22.66	9.29%	107.88	103.40	4.15%
	Blast 3	79.17	32.07	755.80	79.17	19.09	755.73	91.99	71.09	22.72%	114.97	109.00	5.19%
	Blast 4	108.61	28.47	963.71	108.61	17.75	963.89	340.89	NO DATA				
SCC-0.5%-75	Blast 1	12.66	22.58	130.81	12.66	20.67	130.84	5.04	5.63	11.75%	53.51	50.73	5.20%
	Blast 2	41.06	21.29	399.80	41.06	19.48	399.88	21.29	20.84	2.11%	71.18	69.76	1.99%
	Blast 3	82.32	26.28	784.13	82.32	19.05	784.10	93.93	89.71	4.49%	115.74	112.40	2.89%
SCC-0.5%-38	Blast 1	13.76	21.91	143.72	13.76	20.89	143.70	6.72	6.04	10.12%	57.54	51.13	11.14%
	Blast 2	46.22	23.81	416.01	46.22	18.00	415.98	26.62	20.12	24.42%	75.14	69.46	7.56%
	Blast 3	82.63	23.70	769.47	82.63	18.63	769.67	99.67	86.31	13.40%	115.72	113.00	2.35%
	Blast 4	105.71	25.04	886.68	105.71	16.78	886.93	248.55	NO DATA				
SCC-0.75%-75	Blast 1	15.52	29.29	192.64	15.52	24.82	192.65	11.46	7.70	32.81%	107.96	103.10	4.50%
	Blast 2	40.64	23.22	409.64	40.64	20.16	409.68	29.25	25.03	14.43%	106.40	106.70	0.28%
	Blast 3	86.48	23.06	675.87	86.48	15.63	675.88	81.71	78.51	3.92%	114.44	116.50	1.80%

Table 6.3 Reflected shockwave properties, idealized shockwave properties, maximum mid-span displacements, and time to maximum displacements for experimental results and SDOF analytical predictions. (continued)

		Shockwave Properties			Idealized Shockwave			Maximum Mid-span Displacement			Time to Maximum Displacement		
		P_r (kPa)	t_d (msec)	I_r (kPa*msec)	P_r (kPa)	t_{df} (msec)	I_r (kPa*msec)	Experimental (mm)	Analytical (mm)	% Error (%)	Experimental (msec)	Analytical (msec)	% Error (%)
SCC-0.75%HS-75	Blast 1	12.80	18.78	125.73	12.80	19.65	125.73	7.98	5.60	29.81%	108.26	101.20	6.52%
	Blast 2	40.12	20.62	383.83	40.12	19.13	383.75	26.98	20.69	23.31%	75.38	69.76	7.46%
	Blast 3	77.16	21.89	782.89	77.16	20.29	782.81	112.57	87.37	22.39%	117.89	112.70	4.40%
SCC-1%-75	Blast 1	12.48	22.49	127.09	12.48	20.37	127.11	5.11	5.15	0.78%	105.57	100.90	4.42%
	Blast 2	40.68	24.04	410.63	40.68	20.19	410.62	23.32	20.74	11.06%	107.06	103.10	3.70%
	Blast 3	76.62	43.60	767.32	76.62	20.03	767.34	87.72	77.22	11.97%	115.01	111.30	3.23%
SCC-1.5%-75	Blast 1	12.79	21.88	137.90	12.79	21.57	137.92	5.73	5.76	0.52%	55.44	50.88	8.23%
	Blast 2	38.52	26.30	394.98	38.52	20.51	395.05	24.13	18.98	21.34%	107.88	102.50	4.99%
	Blast 3	73.16	22.50	681.05	73.16	18.62	681.11	72.99	52.27	28.39%	113.27	107.90	4.74%
CRC-2%-75	Blast 1	12.57	18.58	108.45	12.57	17.25	108.44	5.15	4.28	16.94%	106.10	100.00	5.75%
	Blast 2	44.25	19.89	334.44	44.25	15.12	334.50	21.19	17.09	19.35%	106.44	101.50	4.64%
	Blast 3	82.22	25.32	735.60	82.22	17.89	735.50	67.76	57.88	14.58%	112.05	107.70	3.88%
	Blast 4	88.76	25.53	938.39	88.76	21.14	938.17	309.48	NO DATA				
CRC-2%-38	Blast 1	13.62	21.05	106.29	13.62	15.61	106.30	5.15	4.78	7.22%	56.79	50.56	10.97%
	Blast 2	45.65	23.54	380.53	45.65	16.67	380.48	20.15	19.57	2.88%	72.73	68.86	5.32%
	Blast 3	71.69	23.05	693.55	71.69	19.35	693.60	47.43	46.05	2.91%	109.19	105.80	3.10%
	Blast 4	92.84	24.79	841.36	92.84	18.12	841.16	71.30	80.56	12.99%	111.97	109.80	1.94%
	Blast 4 (2)	98.44	21.14	771.21	98.44	15.67	771.27	269.53	NO DATA				

Table 6.4 Reflected shockwave properties, idealized shockwave properties, maximum mid-span displacements, and time to maximum displacements for experimental results and SDOF analytical predictions. (continued)

		Shockwave Properties			Idealized Shockwave			Maximum Mid-span Displacement			Time to Maximum Displacement		
		P_r (kPa)	t_d (msec)	I_r (kPa*msec)	P_r (kPa)	t_{df} (msec)	I_r (kPa*msec)	Experimental (mm)	Analytical (mm)	% Error (%)	Experimental (msec)	Analytical (msec)	% Error (%)
CRC-4%-75	Blast 1	13.06	21.52	123.45	13.06	18.90	123.43	4.74	4.64	2.17%	105.98	100.30	5.36%
	Blast 2	46.40	22.31	398.09	46.40	17.16	398.08	21.59	18.78	13.02%	78.15	74.45	4.73%
	Blast 3	83.29	25.95	776.07	83.29	18.64	776.26	57.15	54.88	3.97%	110.19	106.70	3.17%
	Blast 4	91.08	27.99	1001.84	91.08	22.00	1001.89	94.25	90.92	3.53%	113.30	112.40	0.79%
	Blast 5	81.54	33.04	1355.12	81.54	33.24	1355.27	NO DATA	NO DATA				
CRC-4%-38	Blast 1	14.97	22.14	120.63	14.97	16.12	120.62	5.05	5.13	1.57%	63.47	56.10	11.61%
	Blast 2	43.82	21.13	364.87	43.82	16.65	364.83	22.03	17.14	22.20%	74.24	68.70	7.46%
	Blast 3	75.57	22.58	730.17	75.57	19.32	730.02	69.21	46.41	32.94%	84.77	77.95	8.05%
	Blast 4	81.63	24.76	850.63	81.63	20.84	850.58	NO DATA	NO DATA				
CRC-6%-75	Blast 1	14.34	21.23	127.07	14.34	17.72	127.08	5.33	4.77	10.50%	106.77	100.00	6.34%
	Blast 2	43.07	25.88	384.15	43.07	17.84	384.18	23.23	16.22	30.18%	75.62	70.14	7.25%
	Blast 3	75.14	22.16	716.96	75.14	19.08	716.82	56.28	42.05	25.28%	87.98	83.03	5.63%
	Blast 4	103.19	22.99	887.35	103.19	17.20	887.43	373.20	NO DATA				

Table 6.5 Summary of accuracy of experimental response and response predicted by RCBlast.

	Maximum Displacement Ratio, $\frac{D_{anls}}{D_{max}}$					**Time to Maximum Displacement Ratio, $\frac{t_{anls}}{t_{max}}$**					**# Tests**
	Mean	**Std Dev**	**C.o.V**	**Min**	**Max**	**Mean**	**Std Dev**	**C.o.V**	**Min**	**Max**	**N**
Global	0.876	0.121	13.78%	0.591	1.130	0.949	0.029	3.04%	0.884	1.118	41
SCC	0.869	0.122	14.08%	0.591	1.118	0.952	0.029	3.05%	0.888	1.018	24
CRC	0.886	0.121	13.70%	0.671	1.130	0.9435	0.0286	3.03%	0.992	0.884	17

6.4.2 Accuracy of Theoretical Prediction

Two methods were used as indicators of accuracy of the theoretical prediction, the first of which is the calculation of the percent error, and is defined as the difference between the analytical result and the experimental result as a ratio to the experimental result, as shown in Equation 6.72.

$$\% \, Error = \frac{|Analytical - Experimental|}{Experimental} \times 100 \qquad [6.71]$$

The second method is the coefficient of variation (C.o.V), and is defined as the ratio of the standard deviation to the mean, as shown in Equation 6.73. The coefficient of variation shows the extent of variability in relation to the mean for each analytical prediction. The C.o.V is meant to be used for data measured on the ratio scale, and consequently maximum displacement ratios (D_{anls}/D_{max}) and time-to-maximum displacement ratios (t_{anls}/t_{max}) were calculated for all tests. These ratios also demonstrate the accuracy of the prediction in that the closer the value is to unity, the more accurate the prediction.

$$C.o.V = \frac{Std\ Dev}{Mean} \qquad [6.72]$$

Figure 6.31 demonstrates the experimental and analytical displacement ratios for Blast 2 and 3.

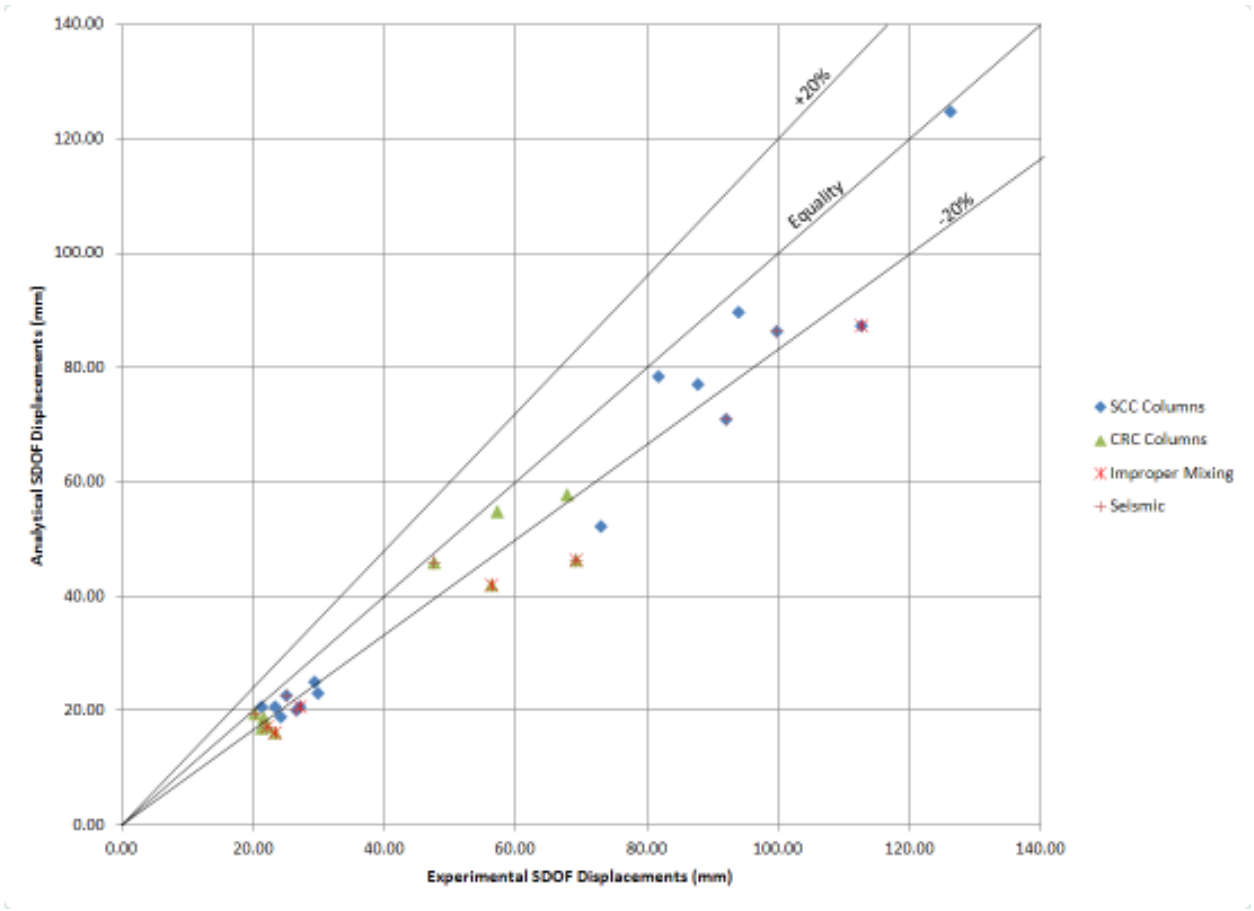

Figure 6.31 Experimental and analytical displacement ratios.

The average displacement percent error for 41 tests was 13.75%. The average maximum displacement ratio (D_{anls}/D_{max}) for 41 tests was 0.876, with a corresponding standard deviation of 0.121, and coefficient of variation of 13.78%. These results demonstrate reasonable agreement between the analytical prediction and the experimental results, and that the analytical prediction typically underestimates the maximum displacements of the columns.

The average time-to-maximum displacement percent error for 41 tests was 5.24%. The average time-to-maximum displacement ratio (t_{anls}/t_{max}) for 41 tests was 0.949, with a corresponding standard deviation of 0.029, and coefficient of variation of 3.04%. These results demonstrate reasonable agreement between the analytical prediction and the experimental results.

6.4.3 Prediction of Maximum Displacements of SFRC Columns

The SDOF predicted maximum displacements for the SFRC columns were typically lesser than the recorded experimental displacements, with the exception of three cases: SCC-0.5%-75, SCC-1%-75, and SCC-1.5%-75, all for Blast 1. For all these cases, the SDOF model over predicted the experimental result by less than 0.6 mm, as shown in Table 6.2. The mean maximum displacement ratio for all SCC tests performed was 0.869 with a corresponding standard deviation of 0.122 and coefficient of variance of 14.088%, based on 24 samples. The larger deviations from experimental data are typically consistent for all seismically detailed SFRC specimens, which indicates that the model over-predicted the ductility increases of seismic detailing. Additionally, the greatest divergence of the analysis from the experimental values of the SFRC columns is with SCC-1.5%-75, which indicates that either the model also over predicts the capacity of the fibres in the stress-strain curve at these higher fibre contents, or that the strength of the actual column did not represent what was determined from the cylinder and beam tests. Unfortunately there were not enough samples for verification.

6.4.4 Prediction of Maximum Displacements of CRC Columns

The maximum displacements predicted by the SDOF method for the CRC columns coincided with the predictions of the SFRC columns. The mean SDOF displacement ratio (D_{anls}/D_{max}) for all tests performed on CRC specimens was 0.886 with a corresponding standard deviation of 0.121, and coefficient of variance of 13.70%, based on 17 tests. Even with significant outliers in the accuracy of the results for columns CRC-4%-38 and CRC-6%-75 due to the challenges of mixing and placing of the material, as explained in Section 4, the overall accuracy of the SDOF model is demonstrated to be reasonably accurate. As demonstrated in Figure 6.31, the prediction for the seismically detailed column, CRC-2%-38, shows excellent results, which is an indicator that the stress-strain curve by Paultre et al. (2009) is an adequate model for CRC.

Similar to the observation made for the SFRC predictions, the CRC SDOF analysis did yield approximate and consistently under-predicted experimental results. Consequently, these predictions do not have the required conservatism, and would not be acceptable for design purposes. In order for the method presented in this study to be acceptable for design, material resistance factors would need to be introduced in order to yield conservative results.

6.4.5 Prediction of Time-to-Maximum Displacements by SDOF Methods

The time-to-maximum displacement ratios are tabulated in Table 6.3. The average time-to-maximum displacement ratio was 0.949, with a corresponding standard deviation of 0.029, and coefficient of variation of 3.04%. As mentioned previously, these results demonstrate excellent agreement between the analytical prediction and the experimental results. Prediction of time-to-maximum displacement is less critical than prediction of maximum displacements, as maximum displacements relate directly to the damage sustained by blast effects. Furthermore, neither over nor under-predicting time-to-maximum response has a significant impact on predicted response (Jacques 2011). The predicted SDOF displacement time-histories, generally follow the slope of the experimental displacement with a good level of accuracy.

6.4.6 Sources of Analytical Error

Predictions using RCBlast under predicted the maximum displacements of most tests. This indicates that the analytical methods used over estimated the resilience of the columns. Several factors may have led to the under predictions of displacements. These include effects of factors such as variable axial load, material models used for SFRC and CRC, choice of DIF, and assumptions regarding plastic hinge length.

One of the factors that may have caused under prediction of results is the method in which variable axial load was incorporated in the definition of the column resistance functions. In this study, the resistance functions estimated the reduction in axial load to occur at greater displacements than the default method proposed by Jacques et al. (2012) in RCBlast. The variable axial load for hydraulic jacks feature in RCBlast attempts to calculate the drop in axial load as a function of the initial strain caused by initial axial load, and the vertical displacement at the top of the column at specified horizontal displacements for axial shortening under lateral loading.

A greater axial load leads to a relatively stiffer column, and consequently greater blast resistance. For all cases, in this study the resistance functions assumed a higher axial load at greater lateral mid-span displacements than what was proposed by Lloyd (2010) and Jacques et al. (2012), and this may have affected the predictions of experimental mid-span mid-span displacements. However, the difference between the two methods is not particularly large. Figure 6.32 a) shows

an example in the difference of the two methods using SCC-0.5%-75: The composite resistance curve used in this experimental program and the resistance curve based on projected length shortening due to lateral deflections proposed by Jacques et al. (2012). Calculating the energy (area under the curve) of these two resistance curves, as shown in Figure 6.32 b), shows a 12% variation in the methods. Nonetheless, the effect of variable axial load in columns subjected to blast and modelling of this phenomenon is a subject that warrants further research.

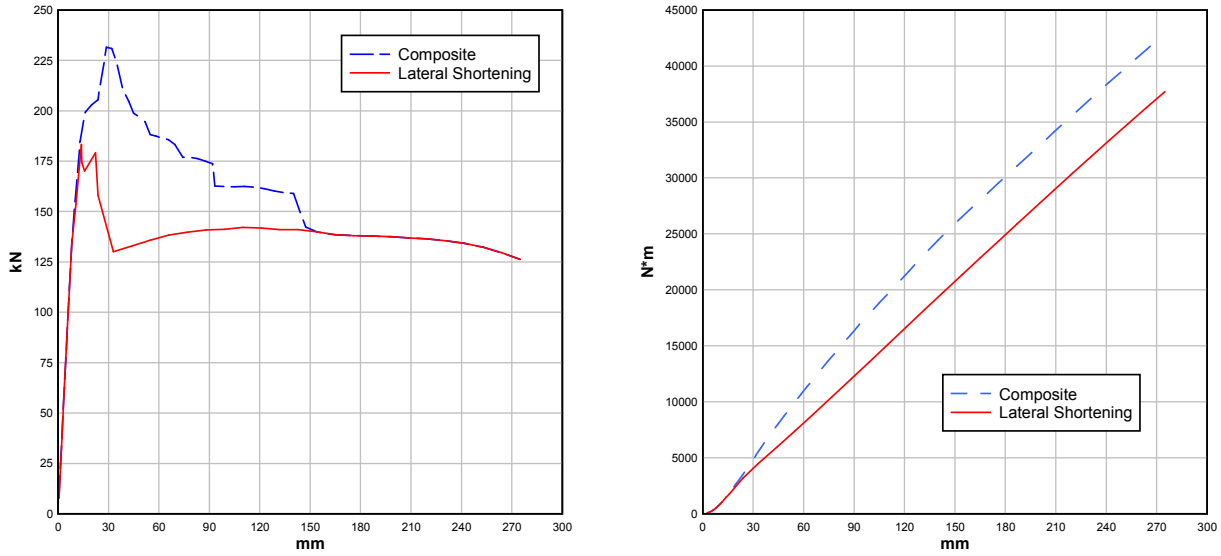

a) Resistance Curves b) Energy

Figure 6.32 SCC-0.5%-75 a) comparison of Composite and Lateral Shortening (proposed by Jacques et al. 2012) resistance curves, and b) the energy capacity of each curve

It is also possible that the analytical method under-estimated the loadings to which the columns were subjected. For example, all tests were predicted using an idealized triangular blast load. The conversion from the actual load to an idealized load using a fictitious duration alters the results of the analysis.

In accordance with Table 6.2, the maximum displacements predicted for Blast 1 had an excellent level of accuracy, and this could be due to the small displacements that lead to less experimental error. In the event that the failure mode of the specimen was tension reinforcing steel rupture, any prediction of maximum displacement was impossible since there was little to no resistance remaining in the column once the reinforcing steel had ruptured, as noted in the high-speed video footage. Also, the strength decay exhibited by severely damaged members is poorly understood

(Jacques 2011). However, in the event that the failure mode was compression reinforcing steel buckling, there is still good agreement with the predicted maximum displacements. This is due to the use of the reinforcing steel-buckling model in RCBlast, as well as the continued resistance in the compression zone from un-crushed concrete.

Other errors in the analysis may relate to the discrepancies between the models used to describe the materials, and their actual behaviour. For example, Figure 6.33 shows the variation between the experimental behaviour of columns tested by Paultre et al. (2010) and their predicted behaviour using the Paultre et al. (2010) model for high-strength SFRC. This model was used to describe the stress-strain behaviour of the CRC and thus may have led to some inaccuracies when predicting the blast response of the CRC columns. Similarly, the Aoude (2007) model, which was used to predict the behaviour of SFRC columns, uses similar parameters and could lead to inaccuracies in predictions. Similarly the models used to define the tensile stress-strain properties properties of both materials may have resulted in some inaccuracies. For example, in the case of the SFRC columns, the tension stress-strain relationship was modelled using the DRAMIX model which defines tensile parametesr based on quasi-static testing of flexural beams. Similarly for CRC, a generic tensile model was defined. Further material testing would lead to validation of these models and could result in better predictions.

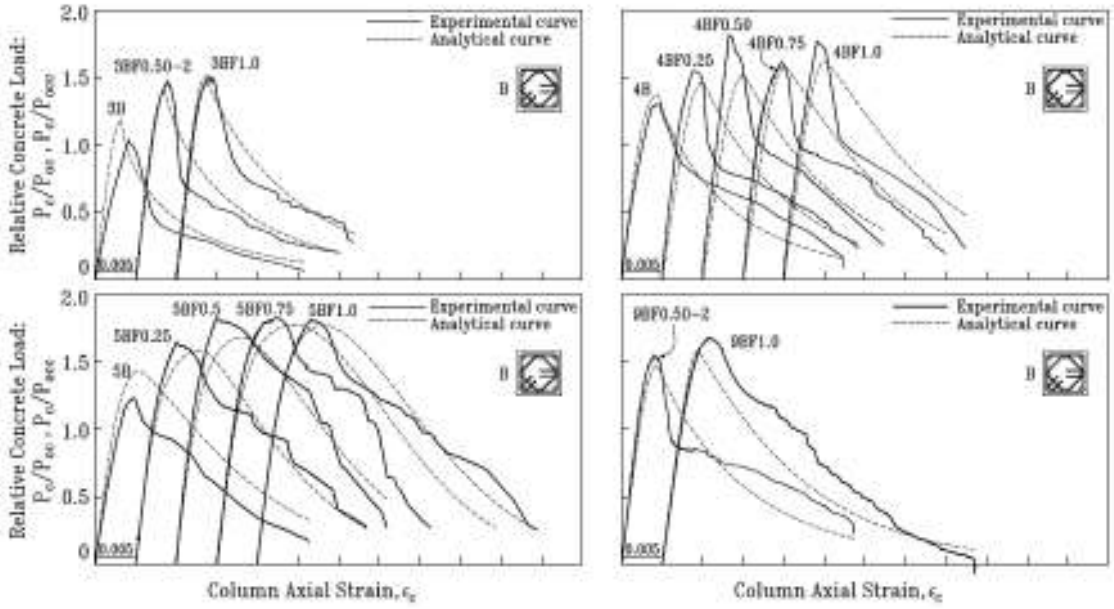

Figure 6.33 Experimental and analytical relative concrete load versus axial strain (Paultre et al. 2010)

The selection of a DIF of 1.19 for the columns could also contribute to the under-predictions of the analysis. This DIF was selected based on the accepted DIF for typical reinforced concrete. However, when evaluating the dynamic compressive toughness of FRC, Zhang and Mindess (2011) noted that most of the DIF (toughness) values for normal strength FRC are lower than 1. Consequently the selection of a DIF that is too great would contribute to the under-predictions noted in the analysis.

Discrepancies between the model and experimental results in terms of SFRC and high strain rates could also be greater when considering the tension portion of the stress strain curve. Considering the discussion in Section 6.2.1.9.4, where some authors reported that contribution of fibres at higher strain rates is absent, it is could be reasonable to assume that tensile contributions of the fibres in the stress-strain curve are over-predicting their resilience at high strain rates. In addition to this, Figure 1.15 shows that at the highest impact drop height, the flexural toughness of CRC is less than that of smaller impact loads, and demonstrates that at greater dynamic loads, specimens behave differently; this may not be captured by the assumptions made in the models. Over-predicting the contribution of fibres could explain the general under-prediction of maximum displacements calculated in this study.

The final assumption involves the plastic hinge length of the columns. This was assumed to be 0.13545m, which was the distance from the extreme compression fibre to the centre of the tension reinforcing steel. This assumption is typical for regular concrete members, however Schumacher et al. (2009) noted that the rotation at ultimate load minus the rotation at the onset of steel yielding was decreased when steel fibres were added. Consequently the plastic hinge lengths could be smaller than the length used in the analysis presented in this chapter.

7 Conclusions

7.1 Summary

This thesis presented experimental and analytical studies aimed at studying the behaviour and performance of SFRC and UHPFRC columns subjected to blast loads. The thesis provides a detailed literature review on historical examples of explosion related disasters, the behaviour of reinforced concrete columns under blast loading, results of previous experimental tests of SFRC under dynamic loading, an overview of the material properties of SFRC and UHPFRC, and a review of the modelling of blast loading and resulting structural response. A review of the literature was inconclusive on whether the addition of steel fibres provides the performance enhancements required to resist blast loads.

In order to further the research in this domain, the thesis presented the results from an experimental program examining the performance of SFRC and UHPFRC columns tested under simulated blast loads. A total of 13 half-scale fibre reinforced concrete columns were tested. The variables included effect of concrete type (normal strength SFRC, and high-strength CRC), effect of fibre type and amount, as well as the effect of transverse tie spacing. All the columns were tested under simulated blast pressures using the University of Ottawa Shock Tube. Each column was exposed to similar simulated blast loads in order to provide comparisons. The results showed clear performance enhancements with the use of steel fibres for blast resistance.

The dynamic response of the columns to the simulated blast load was predicted by defining material models for SFRC and CRC, generating member resistance functions for the various columns, and using single degree of freedom dynamic analysis using software, RCBlast. The analytical results were compared to experimental data in order to justify the analytical methodology, and it was shown to effectively under-predict the maximum mid-span displacements of the fibre reinforced concrete columns under shock wave loading on average by 13.75%.

7.2 Conclusions

Based on the findings of this thesis, the following conclusions can be made:

1. Results from this experimental program show that the addition of steel fibres reduces the maximum and residual displacements of columns subjected to similar blast loads, and enhances the blast resistance of reinforced concrete columns proportionally to the amount of steel fibres added to the mix. For example, the addition of 1.5% hooked-end steel fibres by volume reduced the residual displacement by 68% when compared to the control specimen.

2. The maximum displacements for the seismically detailed RC column were decreased by a factor of approximately 27% when compared to the non-seismically detailed specimen. This is due to the increased confinement and ductility provided by the additional transverse reinforcement. Additionally, all seismically detailed columns were able to prevent compression reinforcing steel buckling that resulted in column failure at smaller displacements.

3. While the maximum and residual displacements of SFRC columns were significantly reduced when compared to the control specimen, the addition of fibres was unable to prevent reinforcing steel buckling under similar blast loads, while seismic detailing did. An ideal solution would be to use both SFRC and seismic detailing in conjunction in columns in order to increase blast resistance. Due to issues with the placement of fresh concrete, the results of the experimental program did not verify this conclusion and further research is required.

4. The use of SFRC in structures required to resist the effects of blast loads can reduce the amount of spalling and cracking of concrete, which can render the structure significantly safer in the event of an attack or accidental explosion by reducing the amount secondary blast fragments. This experimental program observed that the amount of fragments is reduced proportionally to the amount of fibres in the mix.

5. The results clearly show that the use of CRC in columns subjected to blast loads significantly reduces the mid-span displacements when compared to a typical reinforced concrete column. This is due to the fact that CRC has drastically greater compressive and tensile strengths, increased elasticity, as well as increased ductility due to very high steel fibre contents. Due to its high compressive strength, the failure mode for all CRC columns was tension reinforcing steel rupture.

6. Proper construction procedures must be followed in order to ensure optimal structural member response to extreme loads, such as mix design of concrete, vibration, consolidation, etc...

7. Existing material models for both SFRC and UHPFRC and SDOF analysis can be used to accurately predict the response (maximum and time-to-maximum displacements) of fibre reinforced concrete columns.

7.3 Recommendations for Future Research

The following recommendations for future research would be beneficial to further the understanding on the behaviour of SFRC columns subjected to blast loads:

1. Further experimental research on the blast behaviour of SFRC and UHPFRC columns to validate the experimental results observed in this study (with investigation of effect of other variables such as fragmentation). It is also proposed to determine the post-blast axial load capacity of the columns in future studies. This would be beneficial to better quantify the performance benefits of fibres for blast resistance.

2. Determine the optimal fibre content for specific member sizes, with a view to offer recommendations for design. For example, there is a need to determine the optimal fibre amount for a given column cross section, tie spacing, and concrete properties, in order to avoid concrete placement problems, while maximizing blast resistance;

3. Investigate the effects of high strain rates on SFRC and UHPFRC members with a goal of determining a DIF that could be used for design purposes;

4. Investigate the effect of using SFRC and UHPFRC in structural members on plastic hinge length, in order to accurately calculate flexural deformation caused by dynamic loads in elements constructed with these materials;

5. Investigate the effects of fibre typology including effect of fiber anchorage properties (hooked-end, crimped, twisted) and fibre tensile strength to investigate the advantages of various types of steel fibres in columns subjected to these blast loads; and

6. Study the effects of fibres on the reduction of secondary blast fragments in planar reinforced concrete members. For example, this could be done by exposing different RC slabs or walls to similar blast loads, and using witness panels in proximity of the member.

List of References

Aarup, B. (2004). "CRC - A Special Fibre Reinforced High Performance Concrete." *CRC Technology,* Aalborg

Alwan, J. M., Naaman, A. E., and Hansen, W. (1991). "Pull-Out Work of Steel Fibres from Cementitious Composites: Analytical Investigation." *Cement and Concrete Composites,* 13(4), 247-255.

ASTM C1609/C1609M-10. (2010). "Standard Test Method for Flexural performance of Fiber-Reinforced Concrete (Using Beam with Third-Point Loading)" ASTM International.

Aoude, H. (2007) "Structural behaviour of steel fibre reinforced concrete members." Ph.D. Thesis, McGill University, Montreal.

Aoude, H., Cook W.D., and Mitchell, D. (2009). "Behavior of Columns Constructed with Fibres and Self-Consolidating Concrete," *ACI Structural Journal*, 106(3), 349-357.

Baker, W. E., Cox, P. A., Westine, P. S., Kulesz, J. J., and Strehlow, R. A. (1983). "Explosion Hazards and Evaluation*."* Elsevier Science Publishing Company Inc*,* New York.

Banthia, N. (2008) "Enhancing impact and Blast Resistance of Concrete with Fibre Reinforcement." *Resilience of Cities to Terrorist and other Threats, NATO Science for Peace and Security Series C: Environmental Security*, 3, 171-187.

Banthia, N., Mindess, S., and Trottier, J.-F. (1996). "Impact Resistance of Steel Fiber Reinforced Concrete," *ACI Materials Journal*, 93(5), 472-479.

Bao, X., and Li, B. (2010). "Residual strength of blast damaged reinforced concrete columns." *International Journal of Impact Engineering,* 37(3), 295-308.

Barthelemy, F., Hornus, H., Roussot, J., Hufschmitt, J., and Raffou, J. (2001). "Accident on the 21st of September 2001 at a factory belonging to the Grande Paroisse Company in Toulouse." *Report of the General Inspectorate for the Environment IGE/01/034,* Ministry for Regional Development and the Environment, Toulouse.

Biggs, J. M. (1964). "Introduction to Structural Dynamics," *McGraw-Hill Inc*., New York.

Bindiganavile, V., Banthia, N., and Aarup, B. (2002). "Impact Response of an Ultra-High Strength Cement Composite." *Annual Conference of the Canadian Society for Civil Engineering*, Montreal.

Braimah, A. (2010). "Blast Load Effects on Structures - Lecture Notes." Carleton University, Ottawa.

Carl Bro Group as. (1996). "MINISTRUCT Report: Design Rules, sub-task 5.1 General Structural Analysis," Aalborg.

Carriere, M., Heffernan, P. J., Wight, R. G., and Braimah, A. (2009). "Behaviour of steel reinforced polymer (SRP) strengthened RC members under blast load." *Canadian Journal of Civil Engineering,* 36(8), 1356-1365.

Cavill, B., Rebentrost, M., and Perry, V. (2006) "Ductal® - An Ultra-High Performance Material for Reistance to Blasts and Impacts." *1st Specialty Conference on Disaster Mitigation*, Calgary.

CBC News, (22 Aug 2008), "Illegal propane transfer occurred right before Toronto blast: regulator," http://www.cbc.ca/news/canada/toronto/story/2008/08/22/propane-cause.html

Colajanni, P., La Mendola, L., Priolo, S., and Spinella, N. (2008). "Experimental Tests and FEM Model for SFRC Beams under Flexural and Shear Loads," *Seismic Engineering Conference Commemorating the 1908 Messina and Reggio Calabria Earthquake*, American Institue of Physics.

Crawford, J. E., Krauthammer, T., Karagozian, J., and Hinman, E. (1999). "Structural Design for Physical Security - State of the Practice. Chapter 4. Structural Components - Analysis and Design Examples." ASCE Press, Reston.

Crawford, J.E., Malvar, J., Morrill, K.B., Ferritto, J.M. (2001). "Composite Retrofits to Increase the Blast Resistance of Reinforced Concrete Buildings." *10th International Symposium on Interaction of the Effects of Munitions with Structures*, 1-13.

Cusson, D. and Paultre, P. (1995). "Stress-Strain Model for Confined High-Strength Concrete." *Journal of Structural Engineering.* 121(3), 468-477.

(DAHS) Unified Facilities Criteria (UFC 3-340-01). (2002). "Design and Analysis of Hardened Structures to Conventional Weapons Effects." *United States Department of Defense*.

Delatte, N.J. (2009), "Beyond Failure: Forensic Case Studies for Civil Engineers." ASCE Press, Reston.

Dechy, N., Bourdeaux, T., Ayrault, N., Kordek, M., and Le Coze, J. (2004). "First lessons of the Toulouse ammonium nitrate disaster, 21st September 2001, AZF plant, France." *Journal of Hazardous Materials,* (111), 131-138.

Dupont, D., and Vandewalle, L. (2005). "Distribution of Steel Fibres in Rectangular Sections." *Cement and Concrete Composites,* 27(3), 391-398.

Foster, S.J. (2001) "On Behavior of high-Strength Concrete Columns: Cover Spalling, Steel Fibers, and Ductility." *ACI Structural Journal,* 98(4), 583-589.

Georgin, J. F., and Reynouard, J. M. (2003). "Modeling of Structures Subjected to Impact: Concrete Behaviour under High Strain Rate." *Cement and Concrete Composites,* 25(1), 131-143.

Glasstone, S. (1962). *The Effects of Nuclear Weapons. United States Atomic Energy Commission*, Washington.

Gopalaratnam, V. S., and Shah, S. P. (1986). "Properties of Steel Fiber Reinforced Concrete Subjected to Impact Loading." *Journal of the American Concrete Institute,* 83(1), 117-126.

Graybeal, B.A. (2006) "Material Property Characterization of Ultra-High Performance Concrete." *U.S. Department of Transportation, Federal Highway Administration*. Publication No. FHWA-HRT-06-103.

Grunewald, S. (2004) "Performance-Based Design of Self-Compacting Fibre Reinforced Concrete." Department of Structural and Building Engineering, Delft University of Technology, Delft.

Hognestad, E. (1951). "Study of Combined Bending and Axial Load in Reinforced Concrete Members." *University of Illinois Engineering Experiment Station –Bulletin Series*, 399.

Hughes, B.P. and Watson, A.J. (1978). "Compressive Strength and Ultimate Strain of Concrete under Impact Loading," *Magazine of Concrete Research*, 30(105), 189-199.

Jacques, E., Lloyd, A., and Saatcioglu, M. (2012). "Predicting reinforced concrete response to blast." *Canadian Journal of Civil Engineering,* 39, 1-18.

Kinney, G. F., and Graham, K. J. (1985). "Explosive Shocks in Air." Springer Verlag, New York.

Lee, Stuart M. (editor). (1993) "Handbook of Composite Reinforcements," John Wiley & Sons, New York.

Legeron, F. and Paultre, P. (2003) "Uniaxial Confinement Model for Normal and High-Strength Concrete Columns." *Journal of Structural Engineering*. 129(2), 241-252.

Li, V.C., (2002) "Large Volume High-Performance Applications of Fibers in Civil Engineering," *Journal of Applied Polymer Science,* 83 (3), 660-686.

Liao, W. C., Chao, S. H., Park, S. Y., and Naaman, A. E. (2006). "Self-Consolidating High Performance Fibre Reinforced Concrete (SCHPFRC) – Preliminary Investigation." *Rep. No. Research Report UMCEE 06-02,* Department of Civil and Environmental Engineering, The University of Michigan College of Engineering, Ann Arbor.

Lloyd, A. (2010). "Columns under Shock Tube Induced Shock Wave Loading." M.A.Sc. Thesis, University of Ottawa, Ottawa.

Lloyd, A., Saatcioglu, M., Tikka, T., Jacques, E. (2010). “Performance of Reinforced Concrete Columns under Simulated Blast Loading.” University of Ottawa, Ottawa.

Lok, T.S. and Pei, J.S. (1998). “Flexural B-ehavior of Steel Fibre Reinforced Concrete.” *Journal of Materials in Civil Engineering.* 10(2), 86-97.

Lok, T. S., and Xiao, J. R. (1999). "Steel-fibre-reinforced concrete panels exposed to air blast loading." *Proceedings of the Institution of Civil Engineers: Structures and Buildings,* 134(4), 319-331.

Lok, T. S., and Zhao, P. J. (2004). "Impact Response of Steel Fibre-Reinforced Concrete Using a Split Hopkinson Pressure Bar." *Journal of Materials in Civil Engineering,* 16(1), 54-59.

Lu, Y. and Xu, K. (2004). “Modelling of Dynamic Behaviour of Concrete Materials under Blast Loading.” *International Journal of Solids and Structures,* 41, 131-143.

Magnusson, J., Hallgren, H. (2003). “High performance concrete beams subjected to shock waves from air blast, Part 2,” FOI-R--1116--SE, Tumba.

Malvar, L.J. and Crawford, J.E. (1998). “Dynamic Increase Factors for Concrete.” *28th Department of Defence Explosive Safety Seminar*, Orlando.

Malvar, L. J., and Ross, C. A. (1998). "Review of strain rate effects for concrete in tension." *ACI Material Joural,* 95(6), 735-739.

Mansur, M.A., Chin, M.S. and Wee, T.H. (1999) “Stress-Strain Relationship of High-Strength Fiber Concrete in Compression.” *Journal of Materials in Civil Engineering*, 11 (1), 21-29.

Naaman, A. E., and Gopalaratnamt, V. S. (1983). "Impact Properties of Steel Fiber Reinforced Concrete in Bending." *International Journal of Cement Composites and Lightweight Concrete,* 5(4), 225-233.

Naaman, A. E., and Najm, H. (1991). "Bond-slip mechanisms of steel fibres in concrete." *ACI Material Journal,* 88(2), 135-145.

Nataraja, M. C., Dhang, N., and Gupta, A. P. (1999). "Stress-Strain Curves for Steel-Fibre Reinforced Concrete under Compression." *Cement and Concrete Composites,* 21(5-6), 383-390.

Nemegeer, D. (editor.). (1998). “Design Guidelines for *Dramix* Steel Wire Fibre Reinforced Concrete.” Bekaert Corp. Brussels.

Ngo, T., Mendis, P., Gupta, A., and Ramsay, J. (2007). "Blast Loading and Blast Effects on Structures - An overview." *Electronic Journal of Structural Engineering,* 7, 76-91.

Nielsen, C.V. (1995). “Ultra High-Strength Steel Fibre Reinforced Concrete – Part 1: Basic Strength Properties of Compresit Matrix”, Ph.D. Thesis, Technical University of Denmark, Lyngby.

Osteraas, J. D. (2006). "Murrah Building Bombing Revisited: A Qualitative Assessment of Blast Damage and Collapse Patterns." *Journal of Performance of Constructed Facilities,* 20(4), 330-335.

Parra-Montesinos, G.J., Wight, J.K., Dinh, H. and Librrecth, A. (2006) “Shear Strength of Fiber Reinforced Concrete Beams Without Stirrups.” University of Michigan, Ann Arbor.

Paultre, P., Eid, R., Langlois, Y., and Levesque, Y. (2010). "Behavior of Steel Fibre-Reinforced High-Strength Concrete Columns under Uniaxial Compression." *Journal of Structural Engineering,* 136(10), 1225-1235.

Perry, V. (2010). “Reactive Powder Concrete.” *PCI Journal,* July-August, 118.

Popovics, S. (1973). "A Numerical Approach to the Complete Stress Strain Curve for Concrete." *Cement and Concrete Research*, 3(5), 583-599.

Richart, F.E., Bradtzaeg, A. and Brown, R.L. (1928) “Study of the Failure of Concrete under Combined Compressive Stresses.” *University of Illinois Engineering Experiment Station Bulletin,* 26(12), 102.

Rostasy, F. S., and Hartwich, K. (1985). "Compressive Strength and Deformation of Steel Fibre Reinforced Concrete under High Rate of Strain." *International Journal of Cement Composites and Lightweight Concrete,* 7(1), 21-28.

Saatcioglu, M., Ozbakkaloglu, T., Naumoski, N., and Lloyd, A. (2009). "Response of Earthquake-Resistant Reinforced-Concrete Buildings to Blast Loading." *Canadian Journal of Civil Engineering,* 36(8), 1378-1390.

Saatcioglu, M., Lloyd, A., and Jacques, E. (2011). “Focused Research for the Development of a CSA standard on Design and Assessment of Buildings Subjected to Blast Loads.” *Hazard Mitigation and Disaster Management Research Centre Publication*. University of Ottawa.

Santamaria, N. C. (2008). "From Cold War to International Terrorism." *Prevention, Detection and Response to Nuclear and Radiological Threats*, Springer Netherlands, 3-9.

Schmidt, J. (2010). “Practical Design of Structures for Blast Effects.” *National Council of Structural Engineers Associations Webinar Series*. Chicago.

Schumacher, P., Walraven, J.C., and den Uijl, J.A. (2009). “Rotation Capacity of Self-Compacting Steel Fibre Reinforced Concrete Beams.” *HERON*, 54, 127-162.

Sheikh, S. A., and Uzumeri, S. M. (1982). "Analytical Model for Concrete Confinement in Tied Columns." *Structures,* 108(12), 2703-2722.

Smith, P. D., and Hetherington, J. G. (1994). "Blast and Ballistic Loading of Structures." Butterworth-Heinemann Ltd., Oxford.

Unified Facilities Criteria (UFC 3-340-02). (2008). "Structures to Resist the Effects of Accidental Explosions." United States Department of Defense.

Wang, Z.L., Liu, Y.S., and Shen, R.F. (2007) "Stress-Strain Relationship of Steel Fibre-Reinforced Concrete under Dynamic Compression." Construction and Building Materials, 22, 811-819.

Wang, S., Zhang, M., and Quek, S. T. (2012). "Mechanical Behavior of Fiber-Reinforced High-Strength Concrete Subjected to High Strain-Rate Compressive Loading." *Construction Building Materials,* 31(0), 1-11.

Williams, G., Batho, S., and Russell, L. (2000). "Responding to Urban Crisis: The Emergency Planning Response to the Bombing of Manchester City Centre." *Cities,* 17(4), 293-304.

Woodson, S. C., and Baylot, J. T. (2004). "Quarter-Scale Building/Column Experiments." *Structures Congress 2000: Advanced Technology in Structural Engineering, May 8, 2000 - May 10,* ASCE, Philadelphia, 1-8.

Zhang, L. and Mindess, S. (2011). "Dynamic Compressive Toughness of High Strength Fibre Reinforced Concrete." *ACI Special Publication SP-281-7*. American Concrete Institute.

Zhao, P.J., Lok, T.S., Li, X.B., and Lim, C.H. (2001). "Behaviour of Steel Fibre Reinforced Concrete Under Dynamic Load." *Proc., 4th Asia-Pacific Conf. on Shock and Impact Loads on Structures*, Singapore, 573-580.